Impingement and Impingement/Effusion Cooling of Gas Turbine Components: Conjugate Heat Transfer Predictions

By

Abubakar Mohammed El-jummah

A Thesis Submitted in Accordance With the Requirements for the Degree of Doctor of Philosophy

The University of Leeds

Faculty of Engineering

School of Chemical and Process Engineering

Energy Research Institute (ERI)

Leeds, LS2 9JT, United Kingdom

December, 2014

Copyright Statement

The candidate confirms that the work submitted is his own, except where work which has formed part of jointly-authored publications has been included. The contribution of the candidate and the other authors to this work has been explicitly indicated below. The candidate confirms that appropriate credit has been given within the thesis where reference has been made to the work of others.

All the jointly-authored publications which form part of the thesis are derived from my Ph. D research. I performed all the calculations, produced all the results and draft of the papers, dealt with all the review processes and other aspects of the publications. As it was best practice, the publications process was done under the guidance of my supervisors (or co-authors). To acknowledge my contribution as the lead authors of the papers, I am the first named author in all the publications. Details of all the published papers derived from my Ph. D work are provided in this thesis.

List of Publications

The following is a list of publications that shows 5 papers already published. Three papers completed and under review and three more that have abstract accepted and are written as draft which are also part of this Ph. D thesis. Also added are three posters that have been presented.

Papers Already Published

1. El-jummah A. M., Abdul Hussain R. A. A., Andrews G. E. and Staggs J. E. J. 2014. "Conjugate Heat Transfer Computational Fluid Dynamic Predictions of Impingement Heat Transfer: The Influence of Hole Pitch to Diameter Ratio X/D at Constant Impingement Gap Z". Trans. ASME J. Turbomachinery, 136 (12), 1 - 16.
2. El-jummah A. M., Abdul Hussain R. A. A., Andrews G. E. and Staggs J. E. J. 2014. "Conjugate Heat Transfer CFD Predictions of Impingement Heat Transfer: Influence of the Number of Holes for a Constant Pitch to Diameter Ratio X/D". *Proc. ASME Gas Turbine Conference,* GT-25268**,** 1 - 14.
3. El-jummah, A. M., Abdul Hussain R. A. A., Andrews G. E. and Staggs J. E. J. 2013. "Conjugate Heat Transfer CFD Predictions of the Surface Averaged Impingement Heat Transfer Coefficients for Impingement Cooling with Backside Cross-flow". *Proc. ASME IMECE Conference,* IMECE-63580**,** 1 - 14.
4. El-jummah, A. M., Andrews, G. E. and Staggs, J. E. J. 2013. "Conjugate Heat Transfer CFD Predictions of the Influence of the Impingement Gap on the Effect of Cross-Flow". *Proc. ASME Heat Transfer Conference,* HT-17180**,** 1 - 12.
5. El-jummah, A. M., Andrews, G. E. and Staggs, J. E. J. 2013. "Conjugate Heat Transfer CFD Predictions of Impingement Jet Array Flat Wall Cooling Aerodynamics with Single Sided Flow Exit". *Proc. ASME Turbo Expo Conference,* GT-95343**,** 1 - 12.
6. El-jummah A. M., Andrews G. E. and Staggs J. E. J. 2015. "CHT/CFD Predictions of Impingement Cooling With Four Sided Flow Exit". *Proc. ASME Turbo Expo,* GT-42256 1 - 12.

Submitted Papers Under Review

7. El-jummah A. M., Andrews G. E. and Staggs J. E. J. 2015. "Predictions of Impingement/Effusion Cooling Wall Heat Transfer ". *Proc. ASME Turbo Expo,* GT-42257**,** 1 - 9: Under Review

8. El-jummah A. M., Andrews G. E. and Staggs J. E. J. 2015. "CHT/CFD Predictions of Impingement Heat Transfer With Rib, Dimpled and Pin-Fin Obstacles". *Proc. ASME Turbo Expo,* GT-42258 1 - 14: Under Review

Papers Written and Awaiting Supervisors Approval Prior to Submission

9. El-jummah A. M., Andrews G. E. and Staggs J. E. J. 2015. "Conjugate Heat Transfer CFD Predictions of Metal Walls with Arrays of Short Holes as Used in Impingement and Effusion Cooling". *CHT'15 6th Int. Symposium on Advances in Computational Heat Transfer,* 1 - 12: Unpublished
10. El-jummah A. M., Andrews G. E. and Staggs J. E. J. 2015. "Predictions of Impingement/Effusion Cooling Wall Heat Transfer: Influence of a Reduced Number of Impingement Holes Relative to the Effusion Holes". *CHT'15 6th Int. Symposium on Advances in Computational Heat Transfer,* 1 - 12: Unpublished
11. El-jummah A. M., Andrews G. E. and Staggs J. E. J. 2015. "Flat Wall Heat Transfer Predictions for Arrays of Impingement Jets With Cross-Flow". *CHT'15 6th Int. Symposium on Advances in Computational Heat Transfer,* 1 - 12: Unpublished

Posters presented

12. El-jummah A. M., Andrews G. E. and Staggs J. E. J. 2012. "Impingement Cooling on Gas Turbine Combustor and Turbine Blade Walls: CFD Conjugate Heat Transfer Predictions". Presented at the University of Leeds, Energy Research Institute: Energy Building Official Opening Ceremony.
13. El-jummah A. M., Andrews G. E. and Staggs J. E. J. 2013. "Impingement Heat Transfer Cooling of Gas Turbine Hot Surfaces: CFD Conjugate Heat Transfer Predictions". The British Flame Research Committee in Collaboration with the Coal Research Forum and the University of Kent: Combustion Diagnostics, Control, Computational Methods and Process Optimisation Meeting.
14. El-jummah A. M., Andrews G. E. and Staggs J. E. J. 2013. "Gas Turbine Combustor Wall Cooling: Conjugate Heat Transfer Investigation using CFD". *Proc. ASME IMECE Conference*, IMECE-67014

Dedication

This entire Ph. D research work is dedicated to the memory of my beloved mother: late Hajiya Hamsatu Mohammed Biu, I lost her during the course of my first year. I never know I will never going to see her again, May Allah reward her with high palaces of Aljanna.

Acknowledgements

My gratitude to The Creator ALLAH, Who Has given me the strength, wisdom and patience to successfully complete this Research Ph. D work and defend the Ph. D thesis.

I wish to thank my supervisors Professor Gordon E. Andrews and Dr John E. J. Staggs for their motivating moral support, advice and training throughout the course of my Ph. D work. I am also thankful to the management and secretarial staffs of the Energy Research Institute (ERI), University of Leeds.

I am thankful to the members of my family: Maryam and Aisha, Farouk, Hafsa and Bilal, for their patience while I was away from them, for their prayers that I should always succeed and return back to them safely with a Ph. D certificate and for their encouraging words of advice.

To my brothers and sisters alongside their families for their good-will gesture and support.

To my friends and well-wishers, they are always in support physically and in mind.

Finally, I wish to show my esteem appreciation to the government of Nigeria and my employer, the University of Maiduguri for their financial support towards the pursuit of this research Ph. D.

Abstract

Conjugate heat transfer (CHT) and computational fluid dynamics (CFD) were combined in this work using ICEM meshing and ANSYS Fluent software. Block-structured grids with hexahedral elements were used to investigates the key features of impingement cooling of gas turbine metal surfaces, with applications to combustor wall, nozzle and turbine blade cooling. Only flat wall cooling was investigated and not any influence of surface curvature. Combustor wall and turbine blade flank cooling both approximate to a flat wall as the hole diameter and pitch are all small in relation to the combustor or blade curvature. Also the experimental data base on impingement cooling predominantly uses a flat wall. The aim was to validate the computations against experimental data from hot metal wall research facilities and then to use the validated computational methodology to predict improved cooling geometries. Experimental investigations that used hot wall rigs at 770 K cross-flow temperature and 293 K coolant were modelled to predict the overall cooling effectiveness for impingement cooling. The impingement cooling of the metal surface with an equivalent heat flux was modelled, at a hot gas value equals to 100 kW/m^2 and is an input relevant to real gas turbine combustor applications of 250 kW/m^{2}K heat transfer coefficient (HTC). Much of the experimental data base with metal walls used electrically heated metal wall experiments with relatively low wall temperatures. These were also modelled using a constant hot gas side temperature and the thermal gradient through the thickness and between impingement and effusion holes were predicted.

The work was confined to the internal wall heat transfer and did not investigate the combined film effusion cooling that is often used in combination with impingement cooling. However, the interaction of internal wall effusion cooling with impingement cooling was investigated, so that the whole internal wall cooling could be predicted. The heat transfer in a metal wall with a square array of 90^o holes is a subcomponent of impingement and effusion cooling and was part of this study, which was used to evaluate the impact of the CFD turbulence models. The standard k - ε turbulence model with standard wall function (WF) for y$^+$ values in the range 30 - 45 showed better agreement with the measured data, where all the flow features were predicted correctly. Also enhanced wall treatment approaches (EWT) were used for y$^+$ values from 1 - 5, but there was no significant improvement in the predictions compared with the standard wall function approach. All the turbulence models available in Fluent were investigated for an array of holes in a metal wall, which involves only a computation of one hole that is classic short hole or pipe entry length heat transfer. Many of the models could not predict the flow separation and reattachment within a hole L/D of ~1 and as this was fundamental to both effusion and impingement heat transfer, indicating that these models were all poor at the predictions of impingement and impingement/effusions cooling.

The experimental data base in impingement heat transfer has results that would not normally be expected and the CHT computations enabled the reason for the experimental trends to be explained. This includes the reduction in heat transfer along the impingement gap influenced by cross-flow, which would be expected to increase the heat transfer. The relatively low effect of turbulence enhancing obstacles in the impingement gap was also predicted. The influence of the number of impingement holes, which leads to methodology to choose a particular hole size has been predicted based on thermal gradients in the metal wall, this helps the designer in choosing optimum number of holes. For impingement cooling with single sided coolant exit from the cross-flow duct, it was shown that the deflection of the cross-flow onto the impingement jet wall surface was a major reason for the deterioration in the impingement target surface heat transfer along the gap. The very limited experimental database for heat transfer to the impingement jet wall surface was well predicted, thus showing that both wall surfaces were important in the overall impingement heat transfer.

The design configurations investigated were the hole length, pitch, gap, height and depth to diameter ratios L/D, X/D, Z/D, H/D and E/D respectively. The range of L/D investigated was 0.78 - 4.85, by varying the hole diameter for a fixed metal wall thickness (length) of 6.35 mm. This heat transfer was dominated by thermal and aerodynamic entry length effects including the heat transfer on the hole approach surface. The X/D range investigated was 1.86 - 21.02 by varying D at constant X and also by varying X at constant D, which varies the number of holes per surface area, *n*. The range of Z/D investigated was from 0.76 - 7.65 at varied and also at a constant Z. The main coolant flow parameter varied was the mass flux G, which is equals to G^*/P (kg/sm^2bar) in this Ph. D thesis. The requirements for each G with a fixed hole geometry, is a new CHT computation, which is time consuming compared with fairly rapid experimental determinations of the effect of G. The literature survey showed that there were no available detailed flow dynamics investigations of multi-hole impingement cooling. The key experimental measurement that indicates the correctness of the aerodynamic predictions was the pressure loss, which was as a result of the air feed to the impingement gap or effusion hole discharge. The results showed, for the range of geometries, reasonable agreement with the experimental measurements. For heat transfer the experimental measurements were all surface averaged, either for the whole wall or for each row of holes. The predictions were shown to give excellent agreement with surface average heat transfer, which also gave the surface distribution of the heat transfer. It was shown that the surface distribution of heat transfer was directly related to the surface distribution of the turbulence kinetic energy.

The experimental influence of turbulence enhancing obstacles in the impingement gap was well predicted. The experimental data base was for one obstacle per impingement hole using two flow configurations: flow parallel to the obstacles, so that the action was to increase the surface area for heat transfer at low blockage increase and flow across the obstacles, so that the action was to increase turbulence and surface area, but at the expense of higher pressure loss. Two obstacles shapes were investigated experimentally, simple

continuous ribs and slotted ribs which gave rectangular pin fins relative to the cross-flow, with both turbulence generation and surface area increased. The predictions agreed with the experiments that showed the main effect of the obstacles, for which the deterioration of heat transfer with distance was reduced, but to only have a relatively small (~ 20%) increase in the surface averaged heat transfer. The validated computational procedures were used to investigate other obstacle geometries for the same impingement configuration: surface dimples, round pin-fins and inclined ribs in a zig-zag of 'W' format. The zig-zag design predicted an improvement in overall heat transfer compared with the other designs.

Impingement/effusion internal wall heat transfer was modelled with one effusion hole per impingement hole and a fixed 8 mm gap. It was shown that the key interaction effect was to remove any cross-flow from the gap, provided all the impingement air flow went through the effusion holes. This geometry is then only viable for low coolant mass flow rates and thus the modelling was confined to low G. This limitation of coolant flow was because effusion cooling improves if the hole velocity is low relative to the cross-flow, which occurs at low mass flow rates. Also the proportion of compressor air used for film cooling of combustor walls or turbine blades increases NOx from the combustor as the air used is not available to operate the primary zone leaner with lower NOx. For impingement only cooling, most of the work was carried out at high G, close to 2 kg/sm^{2}bar, as the air in combustor application would be used for regenerative cooling and sent to the combustor low NOx primary zone at the exit from the impingement gap. Impingement/effusion cooling was shown to reduce significantly the reverse flow of the impingement jet back onto the impingement jet wall surface and hence had lower impingement heat transfer. However, the combination of the impingement and effusion wall cooling did lead to more total heat transfer than for impingement wall only cooling at the same G. Also investigated was the used of fewer number of impingement holes and more for effusion holes with a hole number ratio of 1/10. Effusion film cooling improves if the number of holes increases, whereas impingement cooling benefits from a low number of holes due to the reduced influence of the cross-flow. Also it was thought that using 10 effusion holes per impingement hole would act like a near uniform surface suction on the impingement jet leading to enhanced cooling of the effusion wall. The results of the modelling showed little benefit of this technique, which was shown to agree with experimental investigation into this effect.

This research has shown that current CHT CFD software can reliably predict experimental investigations of impingement and impingement/effusion overall wall heat transfer. It is thus considered that it can now be used as an engineering design tool for gas turbine combustor wall and turbine blade cooling optimisation. It is possible that gas turbine development in this area could be mainly using CHT CFD instead of the extensive experimental investigations that have been used to date. This work has also shown that relatively simple turbulence, wall function modelling and grid geometries are very effective and the use of more complex models is not justified.

Table of Contents

List of Tables

List of Figures

Nomenclature

A	Impingement hole porosity = $[(\pi/4)\, D^2]/X^2$
D	Diameter, m
G	Coolant Mass flux (G^*/P), kg/sm^{2}bar
G^*	Coolant mass flow per unit area, kg/sm^2
h	Heat transfer coefficient, W/m^{2}K
H	Obstacle height, m
k	Thermal conductivity of fluid, W/mK
k	Turbulent kinetic energy, m^2/s^2
L	Test wall metal thickness, m
n	Number of jet or effusion hole/unit surface area, m^{-2}
N	Number of upstream rows of impingement holes
Nu	Nusselt Number
ρ	Density of air, kg/m^3
ΔP	Pressure loss, Pa
P	Coolant supply static pressure, Pa
Pr	Prandtl number
Re	Reynolds number
t	Obstacle thickness, m
T_∞	Coolant temperature, 288 K
T^*	Normalized mean temperature
T	Temperature, K
V	Velocity, m/s
ν	Kinematic viscosity, m^2/s
W	Test plate thickness or obstacle width, m
X	Hole to hole pitch, m
y^+	Inner variable wall normal coordinate

Z	Plate to plate gap, m
ξ	Grid cell size, m
δ	Obstacle depth, m
ε	Dissipation of TKE, m^2/s^3
U	Mean velocity component, m/s
u	Decomposed steady mean velocity, m/s
u'	Fluctuating component of velocity, m/s
T'	Fluctuating component of temperature, K

Subscripts

avg	average
L	Local
C	cross-flow
j	Jet
W	Wall
s	Surface
S	Solid
∞	Coolant
f	fluid
o	Obstacle
d	Discharge
N	Number of upstream holes
1	Row of first hole
m	Mean
-	surface average
t	Turbulent
i, j, k	interval along the x, y and z coordinates

Abbreviations

RW: Ribs Wall

RP: Rectangular pin

PF: Pin-fin

ZR: Zig-zag ribs

ETSA: Enhanced target surface average

OSA: Obstacle surface average

STSA: Smooth target surface average

HTC: Heat transfer coefficient

TKE: Turbulent kinetic energy

CHAPTER ONE

INTRODUCTION

Chapter 1

Introduction

A gas turbine (GT) shown in Figure 1.1 is a heat engine that converts the energy of fuel into work by using compressed hot gas as the working medium. Energy can be extracted in the form of shaft power, compressed air or thrust or any combination of these. It usually delivers the mechanical output either as torque through a rotating shaft applicable to an industrial gas turbine (IGT) or as jet power in the form of momentum, which is relevant to an aero gas turbine (AGT). The main industrial purpose for using gas turbines are; electricity generation with the gas turbine systems operating using thermodynamic simple cycle or combined cycle gas turbine (CCGT) [1] as shown in Figure 1.2 (a and b). Other common applications of gas turbines are pipeline pumping and marine propulsion.

1.1 High Effectiveness Wall Cooling Requirements in Gas Turbine

Gas turbine thermal efficiency and carbon dioxide (CO_2) emissions are critically dependent on the combustor outlet and turbine inlet temperatures both called T_3, with higher outlet temperatures leading to higher thermal efficiencies [2]. Currently these temperatures are well in excess of the melting point of the metal material of combustor and turbine blades walls. Using the compressor air to cool the combustor and turbine blade walls is critical for their efficient operations at high gas temperatures. Further advances in gas turbine thermal efficiency rely on improved wall cooling [3] of these GT components. The use of impingement air jet and impingement/effusion cooling in gas turbine engines are classically the most effective cooling technologies [3-7], as efficient wall cooling is crucial to the achievement of the high T_3 gas turbines. This Ph. D. research work concentrates on the use of conjugate heat transfer (CHT) computational fluid dynamics (CFD) in the improvement of these cooling designs.

Gas turbine entry temperature controls the cycle thermal efficiency as Appendix A shows, modern high efficiency engines have gas temperatures above the melting point of the metal combustor and turbine blades walls. The turbine inlet temperature T_3, which increases with GT improvement in component wall cooling, is anticipated to be > 2800K [8] for aero engines in the near future. At constant T_3 the thermal efficiency is a strong function of pressure ratio, which also applies to combined cycle thermal efficiency and this is determined by the compressor pressure ratio and the fuel air ratio (F/A). Hence, the thermal efficiency is maximised at the highest T_3 or combustion firing temperature.

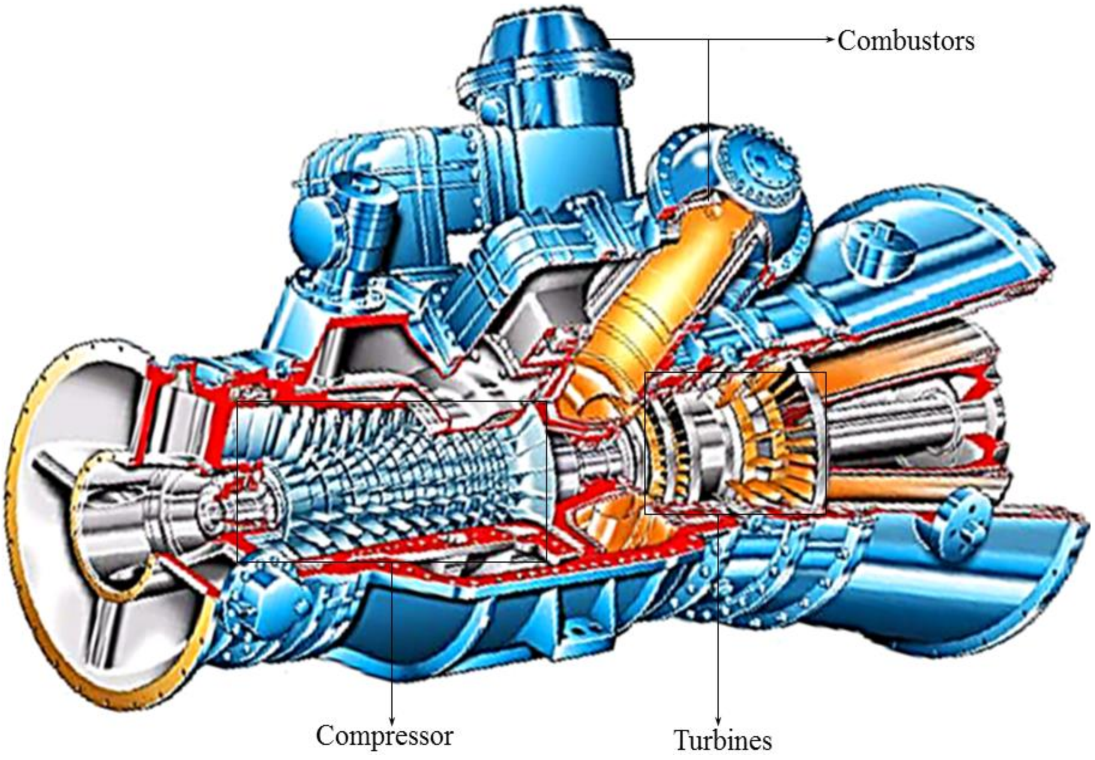

Figure 1.1: Pictorial view of gas turbine engine [9]

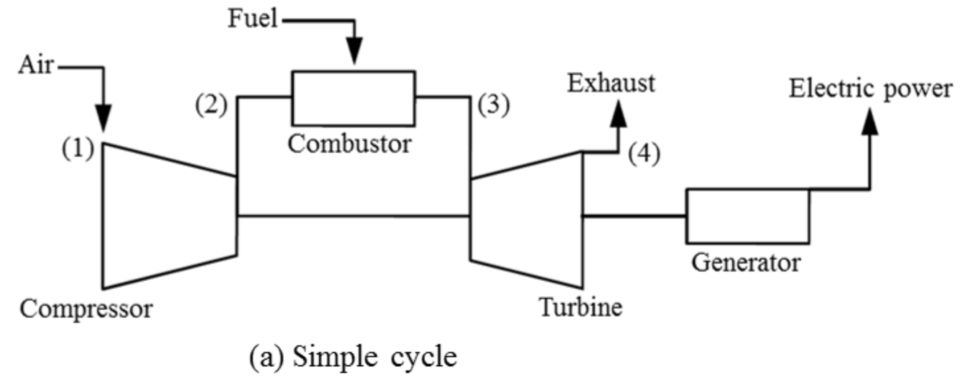

(a) Simple cycle

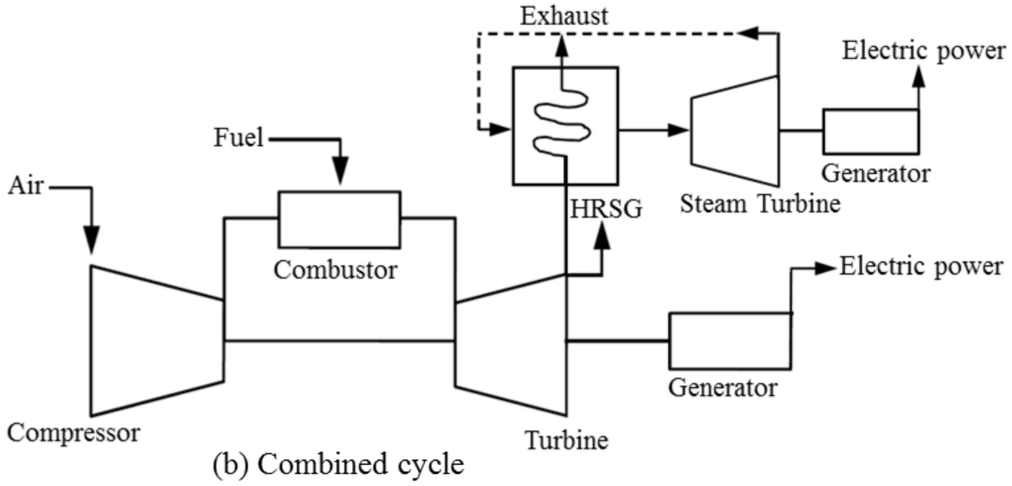

(b) Combined cycle

Figure 1.2: Gas turbine thermodynamic cycles

1.2 Gas Turbine Applications and Thermodynamics

The thermodynamic cycle or the ideal cycle for which a simple cycle gas turbines of Figure 1.2 (a) operates is discussed in Appendix A. The ideal thermal efficiency assumes that all the specific heat values at constant pressure C_p and mass values are the same. In reality the C_p for air varies with temperature and the turbine gas flow components are the products of combustion (CO_2, H_2O, N_2, and O_2), implying that mixture has a different C_p to that of air. Walsh and Fletcher [2, 8] categorized these C_p values and their variation with temperature and show that each product in the composition have a different C_p.

Gas turbine power arises from the momentum of the high velocity flow and the flow power can be related to the mass flow rate and temperature (Appendix A). It is clear that the turbine inlet temperature T_3 is increased in each generation of gas turbine, then not only will the thermal efficiency increase but also the power. Better and more efficient wall cooling techniques enable higher T_3 to be used and the present work is directed at this application so that higher power engines with a higher thermal efficiency (less CO_2/MW) can be achieved.

The gas temperature from the combustor must not exceed the allowable maximum temperature of the turbine. High combustor outlet (or turbine inlet) temperatures T_3, are achieved by advances in high temperature blade materials combined with blade cooling techniques. The future may be ceramic blades, which allow near stoichiometric combustion with the maximum possible T_3. The thermal efficiency could then be about 75% for a combined cycle. Next Generation of CCGT after the H class (1500^{o}C - 1773K) is the J class at 1700^{o}C (1973K) CCGT and the estimated thermal efficiency is 62 - 65% [10]. This will have a significant contribution to CO_2 reduction once most gas fired power stations are of this type or better by 2050.

Protecting the life of the gas turbine components in order to satisfy the requirements for high power output and low fuel consumption is necessary. This can be achieve by continuous production of entirely new alloy material or by protecting the life of the existing materials of the GT components [1, 3, 10]. Both approaches are used and the development of more barrier coatings (ceramic/metal walls) is an example of improved wall material. Cooling the walls of the gas turbine components is a reliable method of protecting the walls from hot gas core flow. This is as a result of the metallurgical limitations in withstanding the temperature of combustion in gas turbine engines. Hence, increased turbine inlet temperature relies on metal wall air cooling and this is the topic of this research project. The chemical processes that mainly influence the pollutant emissions are affected by increased turbine inlet temperature, which critically affects the air mass (Figure 1.3) used in cooling the turbine blade as little power is then extracted from this air. The solution to this problem is the use of conjugate heat transfer CHT CFD, which helps in designing geometries that

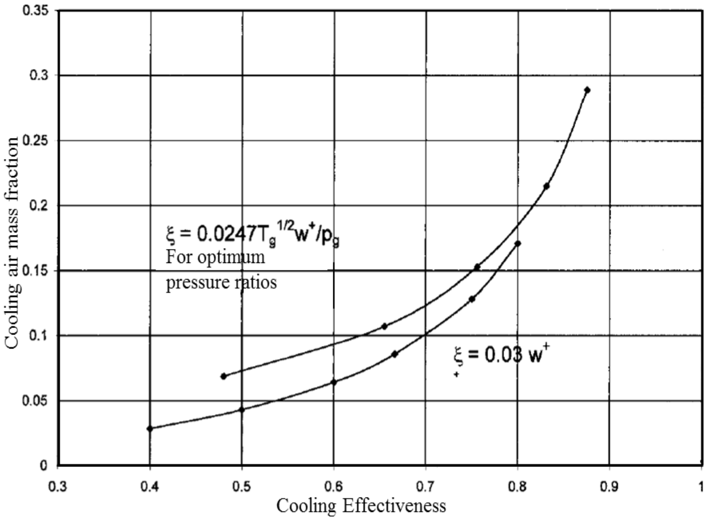

Figure 1.3: Approximation of cooling mass flow fraction expressions [8]

can minimise emissions. This work focuses towards achieving better geometries using CHT CFD software, which could not affects the design of gas turbine for minimum emissions.

1.3 Cooling of Gas Turbine Components

Air and steam (or liquid water) have been identified as major sources of cooling gas turbine component walls. Air cooling has been extensively developed and used for over 30 years [11], which is mainly based on availability, cost effectiveness and minimal influence of chemical reactions. Air is also easily extracted from the gas turbine compressor at high pressure, which influence cooling rate. However, steam is shown to be rarely used and has not proved to be practicable for many reasons, notably:

- Its associated high cost,
- It is usually unavailable or not available sufficient quantities,
- It is impossible to eliminate corrosion or formation of deposits from impurities of water,
- There are difficulties in providing adequate cooling surface area.

This work concentrates on using air for combustor and turbine blade walls cooling, which is by far the most economical source of cooling GT components.

Air cooling the turbine blade wall is achieved by either externally or internally cooling methods. Cooling the turbine blade wall externally requires the use of film cooling [8, 12-18], as shown Figure 1.4, or transpiration cooling techniques [8, 19]. However, these methods become unfeasible with increasing T_3 and with the needed cooling potentials. On the other hand, cooling by an internal method can be achieved using an impingement air jet or regenerative cooling [5, 20-22] as shown in Figure 1.5 and impingement/effusion cooling [4, 7, 23] techniques, which are the focus of the present research. It has been shown that operating gas turbine blade at high turbine inlet temperature increases the efficiency and the output power of the GT engine. Turbine inlet temperature is limited by the current turbine blade wall materials and the only better way of increasing T_3 is to use optimum cooling techniques. This will facilitate faster improvement in the performance of the GT system than the development of new techniques to improve turbine blade materials and at lower cost.

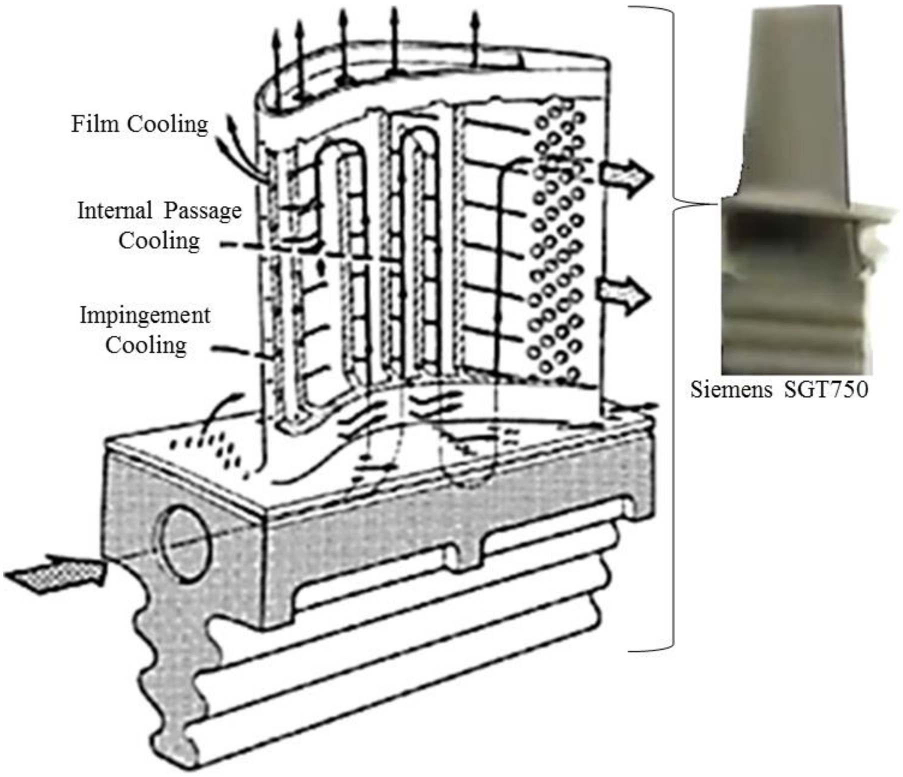

Figure 1.4: Combination of types of gas turbine cooling techniques in turbine blade [24]

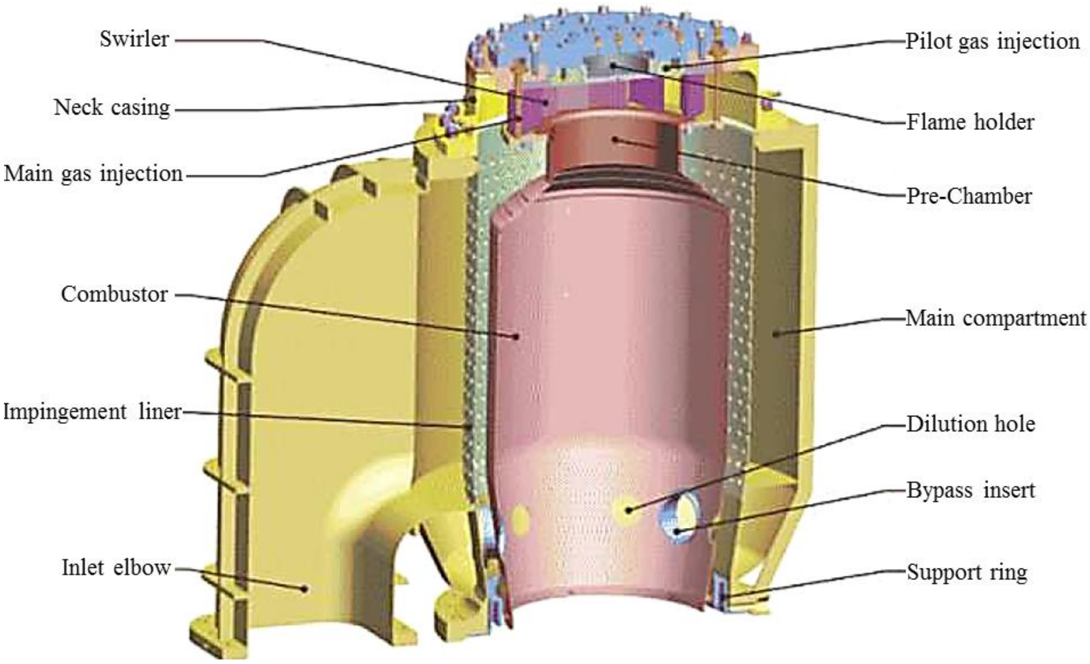

Figure 1.5: Gas turbine low NOx cooling combustor [9]

Gas turbine performance improvement is two fold: higher cooling effectiveness for the same coolant mass flow rate and reduced coolant mass flow for the same cooling effectiveness . The latter improvement is more useful as coolant air is deterimental to cycle thermal efficiency as work has been done to compress the air and the full expansion work is not being obtained if it bypasses some of the turbine blade expansion work. For combustors the minimisation of wall cooling air is necessary for the minimisation of NOx emissions, as air used for cooling is not available for lean combustion and this increases the flame stabiliser mean operating temperature which increases NOx. Hence the designer maintains the actual material used at manufacturing stage with increasing T_3 using variable improvement in the chosen cooling techniques.

The combustor liner contains the combustion process and is surrounded by a casing (or plenum chamber) with air flowing between the liner walls and the casing, this air is also the coolant. Higher engine pressure ratio as shown in Appendix A, is associated with increased inlet air temperature that raises the flame temperature T_3, which also increases the liner wall rate of heat transfer. It also reduces the effectiveness of the air as a coolant hence the requirement for a steady cooling air flow. In order to maintain the integrity of the hot sections downstream of the combustor, improvement in the pattern factor is significant.

Modifications that were shown to alleviate problems with NOx in conventional combustors invariably increase unburnt hydrocarbon (UHC) and carbon monoxide CO emissions, which also influences CO_2 emissions. Using variable geometries to regulate the amount of air entering the primary combustion zone is a solution to the problem. This requires that more air is allocated to the combustion to alleviate NOx emissions, this gives high T_3 and less fuel is require for combustion which also lower CO_2 emissions. The regeneratively cooled combustor shown in Figure 1.5 with most of the combustion air entering the head of the combustor, is a system that requires dilution air and can also be modified to be without a dilution zone [25]. This work concentrates on using CFD to parametrically study the geometrical influence of the air cooling system.

1.3.1 Materials for Gas Turbine Components

Developing new materials for gas turbine hot walls to withstand the harsh environmental conditions of high pressures and temperatures are challenging tasks that rely on the design engineer [1]. Advances in gas turbine engines is allied with developing wall materials that can withstand the initial and continuous operational temperatures of combustion that arise through the need for improved GT thermal efficiency. The application of a thermal barrier coating [26-29] and the use of alloy [10, 30, 31] materials for gas turbine combustor and turbine blade walls are typically the two most prominent approaches. The use of thermal barrier coating for example: silicon carbide (SiC), which has high thermal conductivity k_s is characterised by wall conductivity effects due to small temperature gradient[29], while alloy materials for example Nickel (Ni), Cobalt (Co), Titanium (Ti), Cobalt or Aluminium (Al) based super alloys [10, 30] (typically Nimonic-75) are found to be good wall conductive materials with lower k and realistic temperature gradients [32, 33]. This indicates that the efficient use of the cooling air, should be practically an important phenomena in addressing problems of GT combustor and turbine blade walls and the use of air jet cooling in CHT CFD could be a solution [25].

1.3.2 Emissions and Regulatory Requirements

The stringent control of products of combustion in gas turbine emissions as a result of the environmental and health concerns has become an important factor in the design of IGT and AGT systems. The significant emission products are: NOx ($NO + NO_2$) - which react in the presence of sunlight to produce smog and contributes to acid rain as well as ozone depletion, carbon monoxide CO - toxic product that reduces the capacity of blood in absorbing oxygen, unburned hydrocarbons UHCs - toxic and combines with NOx to form photochemical smog and SOx ($SO_2 + SO_3$) - are toxic and corrosive [11]. The process of combustion is complete if all the carbon is converted to carbon dioxide (CO_2), the main combustion product of any hydrocarbon fuel which is found in the exhaust of any GT system. Carbon dioxide is believed to contribute significantly to global warming due to greenhouse effect and CO_2 emissions can be reduced not only by improving GT efficiencies, but this help reduce CO_2 so that less fuel is burned. All these products of combustion are pollutant emissions that cause significant effects on human life. Improvement in the design of GT combustor and turbine blade is significant to the reduction in emissions of the combustion products.

At 62% thermal efficiency the CO_2 emissions will be 320g/kWh [10]. The best conventional coal fired plant is 44% thermal efficiency and has 840g/kWh CO_2 emissions for an output of 1.25GW. This is a 62% reduction in CO_2 or roughly a 2/3 reduction in CO_2. Practically, low NOx combustors should be the influence of wall cooling as it controls the air used for combustion. Therefore, cooling the combustor and the first stages of the turbine using air bled from the engine compressor is necessary for the metal to survive with gas temperature >1800K. Low NOx combustion requires low primary zone temperature (< 1900) and this requires a large proportion of the compression air flow (> 60%) so there is little air left for wall cooling [34]. The present requirement is to limit NOx emissions to 9ppm or less on gas fuels and 100% of compressor air enters the combustor with none available for film cooling. It is therefore necessary to develop a combustion system to achieve those requirements, which is a system where most of the combustion air is used for regenerative cooling. Figure 1.5 or Figure 1.6 (a) show the optimum design impingement wall cooling system [5, 25, 35].

A smart combustor is one that has low NOx (Figure 1.5), good flame stability and no acoustic problems, though a very expensive system if all the three problems have to be cured [36, 37]. In recent years the effect of restrictions on emissions of oxides of Nitrogen (NOx) has had a major impact on combustion design, for both industrial and aero applications [9, 38]. A low NOx solution will be possible for a firing temperature of 1900K if all the combustion air passes through the combustor with no cooling or dilution air [25], also blade cooling air must be minimized. The primary zone (Figure 1.5) must be at the overall equivalence ratio for the combustion reaction and must be stable at this condition. Also, the combustor must be regeneratively cooled using the combustor air to first cool the outer wall at high mass flow and this must be done with a low pressure loss [25, 39]. The test flow velocity or reference Mach number M will be ~ 25m/s or 0.05 and the low NOx flow conditions must be carried out at this condition. This is anticipated for the 'J' class machine that is the next generation after the H class, doing all of this within the present outer pressure casings of engines will be a challenge.

1.3.3 Cooling Techniques

Several techniques are used for cooling the gas turbine combustor and turbine blade walls as shown in Figure 1.6 (a - f), the available techniques includes [11, 40]: film cooling, transpiration cooling, effusion cooling, impingement cooling and impingement/effusion, which are briefly discussed below.

1.3.3.1 Film Cooling

Film cooling is a method of cooling applied GT components by which a coolant air forms a protective layer, as film or heat sink between the hostile combustion hot gas and the combustor wall as Figure 1.6 (a) show. With adequate design, this technique has the advantage of the cooled component being able to withstand severe pressure and thermal stresses at high temperatures. But film cooling makes no contribution to air fuel mixing in the combustor since the air flows along the liner wall. A basic limitation of this method is that it does not allow uniform wall temperatures, which result in a deterioration of the cooling potential with increasing distance.

1.3.3.2 Transpiration Cooling

Here, the surface being cooled is made porous and the coolant is forced through the wall as shown in Figure 1.6 (b). The liner material provides a large internal area for heat transfer to the air passing through it. Thus, it has the disadvantage that the cool wall is affected by intense radiation from the combustion flame and are exhausted to thermal oxidation as well as thermal stress.

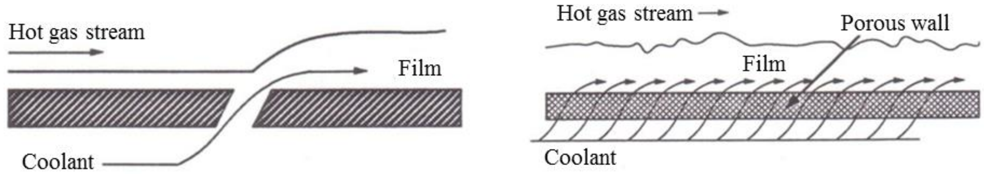

(a) Film cooling (b) Transpiration cooling

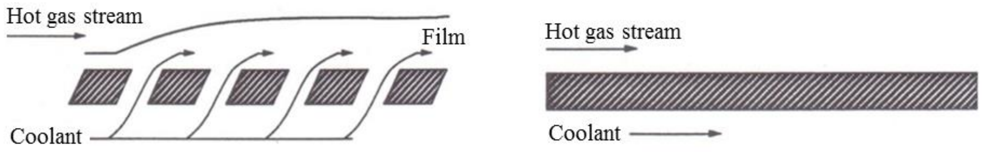

(c) Effusion cooling (d) Forced Convection cooling

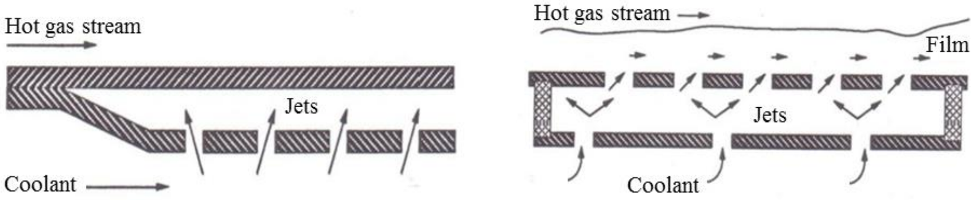

(e) Impingement jet cooling (f) Impingement/effusion cooling

Figure 1.6: Typical gas turbine cooling techniques [40, 41]

1.3.3.3 Effusion Cooling

Effusion cooling of Figure 1.6 (c) consists of large number of small holes that are in-lined or staggered, which are inclined at certain design angle and the cooling air is forced under pressure through the holes to the hot surface of the wall. The cooling air then forms a blanket over the wall surface that protects the liner from the hot combustion gas streams. The holes should be large enough to remain free from blockage by impurities and they should also be small enough to prevent the air jets penetration (or interacting with) into the combustion gas. This method is usually affected by heating of the liner walls instead of cooling.

1.3.3.4 Forced Convection Cooling

The use of a double-walled construction, whereby coolant flows between the walls, provides forced convective cooling as Figure 1.6 (d) show. This method is shown has been employed in earlier designs of turbine blade walls. The method is limited by the size of the internal passages within the blade, the effects of turbulence and availability of cooling air.

1.3.3.5 Impingement Cooling

Impingement wall cooling is a technique in which cooling air exhausts as jets from array of perforated holes, impinging on the target surface that requires cooling. The method uses convective heat transfer to cool or heat the target surface as shown in Figure 1.6 (e).

1.3.3.6 Impingement/Effusion Cooling

Impingement/effusion combines the benefits of effusion cooling and direct jet impingement cooling as shown in Figure 1.6 (f). Coolant air is forced through the impingement holes, emerging as jets and flow through the effusion holes to the flame side forming a cool layer of gas between the main stream and the target wall or effusion wall. This improves the overall cooling effectiveness of combustor and turbine blade walls.

1.4 Conjugate Heat Transfer Computational Fluid Dynamics

Computational fluid dynamics (CFD) solves the Navier-Stokes equations, together with a set of boundary and initial conditions, in a mathematically discretized form to estimate field variables quantitatively on a group of cells (grid or mesh) comprising the flow domain. CFD is commonly used to analyse complex flow dynamics also involving heat transfer and multiphase/reactive flows in many fields of engineering [42]. The combined interactions involved in the exchange of heat between fluids and solid boundaries (which may themselves move or remain static) is known as conjugate heat transfer (CHT) CFD.

Part of the conjugate heat transfer problem necessitates an accurate calculation of the heat flux at the solid/fluid boundary. This in turn is only possible if the temperature gradient normal to the solid/fluid interface is known accurately. Therefore the choice of interpolating function through the boundary layer, the structure of the grid and turbulence model are of fundamental importance.

1.5 Research Objectives

The gas turbine combustor and turbine blade walls serve to facilitate the flow of hot gases. These walls must be structurally strong to withstand the pressure differential across the walls. They must also have sufficient thermal resistance to withstand continuous and cyclic high temperature operation. These requirements can be achieved through the use of high-temperature, oxidation resistant materials combined with the effective use of cooling techniques.

An air jet impingement or impingement/effusion heat transfer cooling system may look simple, but the aerodynamics are complex, which also affects the cooling heat transfer and wall thermal gradients. The application of CHT CFD is a useful tool in visualising the air jet cooling flow fields, estimating the heat transfer and wall thermal effects. At present there are relatively few three dimensional (3D) CHT CFD studies concerned with impingement and impingement/effusion cooling techniques. This Ph. D. research investigations aims to use CHT CFD in understanding the aerodynamics and associated heat transfer effects of air jet cooling systems that are applicable to gas turbine combustor and turbine blade walls.

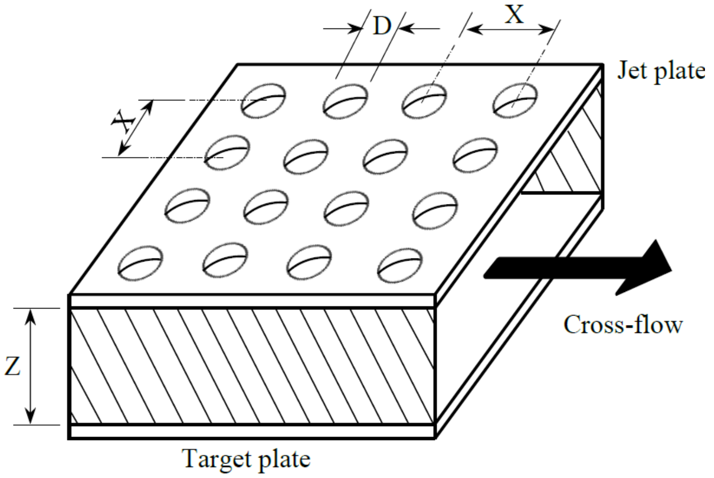

(a) Impingement jet single sided flow exit [25]

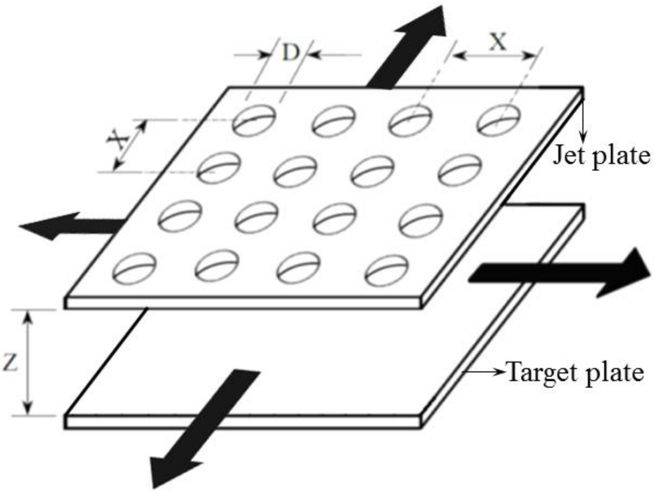

(b) Impingement jet four sided flow exit [47]

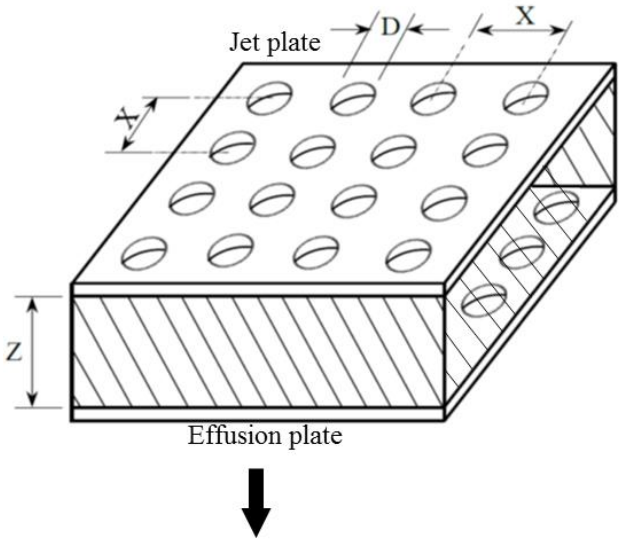

(c) Impingement/effusion flow exit through effusion hole

Figure 1.7: Gas turbine cooling flat wall geometrical setups and flow schemes

Experimental investigations were carried out in other work [3-5, 19, 22, 23, 25, 43-46] flat wall cooling with several geometrical variables and flow characteristics, on jet impingement and impingement/effusion cooling heat transfer applied to gas turbine combustor wall cooling which is also applicable to turbine blade cooling. The investigations, were performed in two different test configurations which will be referred to as the conventional test rig (or low temperature rig) and the combustion test rig (or high temperature rig). It is a primary objective of the present work, to reproduce the experimental results that have been previously published using CHT CFD methodology. The CHT CFD investigations reported here were carried out using the commercial CFD codes ANSYS ICEM (a mesh generation tool) and ANSYS Fluent (a flow solver). These CFD tools help in understanding and explaining the aerodynamics and coupled effects of conjugate heat transfer that exist in the experimental geometries that were investigated, which can also lead to new designs.

It transpire that the key parameters that significantly influence GT impingement jet and impingement/effusion heat transfer cooling are the geometrical and flow variables as shown in Figure 1.7 (a - c) and they include: the dimensionless geometrical hole pitch to diameter, impingement gap to diameter and hole length to diameter ratios X/D, Z/D and L/D respectively. By varying the number of holes N or pitch X, the number of holes/unit surface area (hole density) *n* or X^{-2} (m^{-2}) is also varied. The main flow variable is the gas turbine coolant mass flux G (kg/sm^2bar), which influences the impingement jet hole and gap velocities as well as the effusion hole flow aerodynamics and also affects the Reynolds number Re.

The effects of X/D, Z/D, L/D, *n* (m^{-2}) and G (kg/sm^2bar) for the range of hole diameter D, hole pitch X, gap Z and hole length L on impingement, effusion and impingement/effusion cooling heat transfer systems will be investigated. Changing Re implies changing either the geometrical or flow variables and these changes in values will be investigated using CHT CFD. By carrying out these investigations, the major GT aerodynamics and heat transfer components, the pressure loss ΔP and heat transfer coefficients (HTC) h (kW/m^2K) are determined. Experiments [22, 25, 46] show that for smaller X/D at high G values, the pressure loss ΔP is low and this is significant to low NOx combustions applicable in industrial gas turbine combustor, but the heat transfer values are lower due to cross-flow effects. Impingement jet geometries with high X/D values, implies that the pressure loss ΔP and heat transfer are also high. This application of high X/D or ΔP with low G values is more appropriate for use in impingement/effusion cooling systems. This present Ph. D. research work will investigates these geometries and associated flow conditions.

Experimental investigations [4, 44] show that the number of holes/square meter (or hole density) of impingement or effusion surfaces *n* (m^{-2}) does not influence the design in principle, but it does influence cross-flow for impingement jet cooling. The importance of varying *n* experimentally is usually ignored and only little work has been done on this, CHT CFD work reported here investigates the influence of *n* for which experimental data are available for validation of the CFD predictions. Validation of the CHT CFD predictions with existing experimental data leads to a better understanding and explanation of the data.

This present CHT CFD investigations will concentrate on testing the range of turbulence models, grids and influence of y^+ values, these are discussed in Chapter 3. Once agreement is reached between the CFD prediction and the experimental work, other test geometries relevant to the application of gas turbine components walls cooling will be investigated using the optimised turbulence model and grid. The specific objectives of the study are to:

1. Develop model geometries with adequate grid resolution that are capable of predicting and explaining the experimental data and the associated cooling effectiveness.
2. Investigate the aerodynamic interactions that result from the deterioration of impingement heat transfer with axial distance, which was found experimentally. This similar aerodynamic effect that result into reversed jet flow onto jet plate of an impingement/effusion or four sided impingement jet flow exit cooling systems will also be investigated.
3. Understand the heating of the impingement jet walls caused by flow recirculation within the impingement gap that has been shown experimentally.
4. Predict the thermal gradients in the target walls in order to estimate the thermal stresses that occur during GT cooling processes.
5. Understand the influence of impingement gap cross-flow velocity interaction with the trailing edge high velocity air jets and the deflection of this jets.
6. Use optimised CHT CFD calculations to predict the best air jet cooling design procedures that are capable of effectively cooling gas turbine combustor and turbine blades. This will also apply to impingement/effusion cooling designs.

A further problem is that when X/D and the impingement wall pressure loss ΔP are small the pressure gradient along the discharge duct creates a flow-maldistribution (defined as the unequal distribution of coolant air mass flow in the jet holes). This is undesirable because it leads to uneven heat transfer along the duct. A further aim of this Ph. D. work is to predict and explain the influence of the flow-maldistribution as the X/D values are varied. Other effects of jet deflection, which have deleterious effects on heat transfer will also be investigated. For example, heat transfer and thermal gradients deterioration caused by cross-flow in the axial direction on the trailing edge target walls.

1.6 Research Methodology

The overall plan to achieve the objectives stated above is as follows.

1. Construction of symmetric model geometries (from points, curves and surfaces) for a fixed computational domain around the test plates area A.

2. To represent the experimental test rigs and limit the number of nodes so that computational times are reasonable.

3. Specifying the materials for the fluid and solid bodies cell zones and the boundary (flow and energy) conditions at the surfaces. The particular surfaces at which boundary conditions will be defined includes: Inlet, outlet, symmetries and walls.

4. Computing a steady state solutions that have reached the selected convergence criteria and then running the transient solver, to verify for stability of the steady state solutions. This also helps in knowing the minimum error of the converged variables that could be reasonably acceptable.

5. Carrying out grid sensitivity tests in order to identify a low grid-sensitivity regime in which to calculate solutions.

This present CHT CFD investigations will be applying the following as a solution guides:

- Testing structured (hexahedron) and unstructured (tetrahedron) grids
- Using the following boundary conditions throughout the entire investigations: velocity-inlet (for a fixed coolant temperature, velocity, % of turbulence intensity and hydraulic diameter D_H), outflow, symmetry, hot side wall heat flux and temperature, solid/fluid coupling, adiabatic plenum and gap walls and the use of 3D surface boundaries
- The used of solid (Nimonic-75) and fluid (air) cell zones by customizing their properties
- Application of near wall treatment, energy and the use of turbulence models
- Defined and customised a convergence criteria by using the default residuals
- Post processing the predictions for surface distribution in ANSYS Fluent solver, while the data output from this solver will be plotted as xy chart in Origin Pro
- Validation of predicted results with measured work, which is significant to the actualization of new gas turbine cooling design systems.

CHAPTER TWO

LITERATURE REVIEW

Chapter 2

Literature Review

2.1 Introduction

Generally, the cooling of gas turbine (GT) combustor and turbine blade walls are usually carried out using different types of methods as was shown in the preceding chapter. The specific cooling methods that will be review here includes: Impingement and impingement/effusion cooling heat transfer systems, as these are the major concerns of the present Ph. D investigations. Since this work involves effusion geometries forming part of the impingement/effusion cooling systems, this review will briefly discuss related literature findings on effusion cooling, even though effusion alone does not form part of the research title. Therefore, in this chapter both experimental and numerical investigations on the selected cooling systems will be reviewed, whereby the major gas turbine cooling variables are discussed. These includes the heat transfer and aerodynamics dependent variables, which are typically geometrical and flow features. The specific parameters are usually dimensionless and have been shown to be influential on the GT cooling heat transfer and aerodynamics. This chapter starts with the importance of understanding heat transfer as the major tool that the present work is channelled and follow it up with the interrelated characteristics.

2.2 Heat Transfer Processes

Heat transfer (HT) is generally define as the thermal energy in transit due to a spatial temperature difference [48]. It comprises three distinct processes or modes as Figure 2.1 (a and b) shows, which includes [11, 48, 49]: Firstly, conduction heat transfer that involves the existence of temperature gradient in a stationary medium (solid or fluid), which is sustend by the atomic and molecular activity or particles interactions. This is represented by the rate equation of Fourier’s law of heat conduction shown in Equation 2.1. Secondly, heat transfer by convection for which heat transfer occurs between a surface (energy exchange due to random molecular motion or diffusion) and a moving fluid due to bulk or microscopic motion. Convective HT is represented by the expression of Newton’s law of cooling shown in Equation 2.2 that has been shown to be associated with the condition in the wall boundary layer influenced by surface geometry, the nature of the fluid motion and assortment of fluid thermodynamics and transport properties. This will be shown later to be the basis of surface and locally average heat transfer coefficients (HTC) h. Finally, the heat transfer by radiation

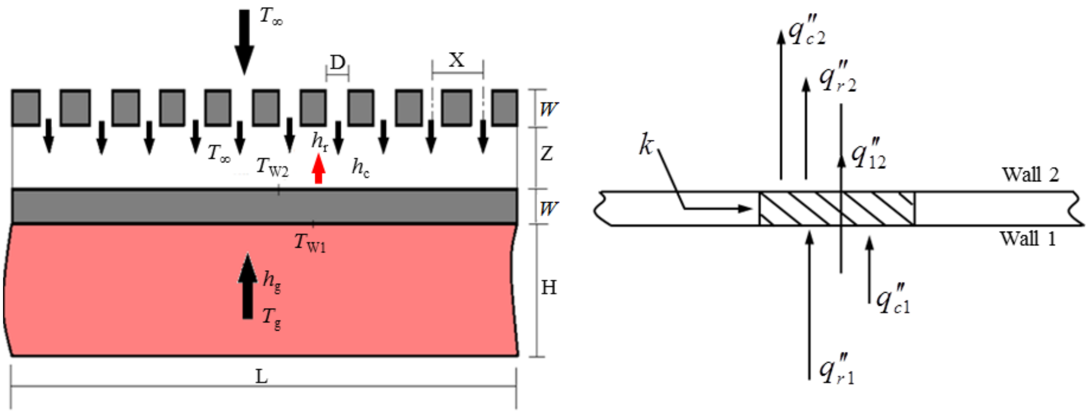

(a) High temperature test rig (b) Basic liner wall heat transfer processes

Figure 2.1: Schematic descriptions involving wall air jet cooling heat transfer

(or thermal radiation) defined as the net transfer of heat due to action of electromagnetic waves between two solid surfaces (or liquid and gases) at different temperatures in the absence of an intervening medium. Stefan-Boltzmann law gives the representation of radiation as defined by Equation 2.3 and is shown to depends on the emissive power as well as the geometry. These HT mechanisms occurs simultaneously in problems that always involves engineering heat transfer typical of the gas turbine cooling. This CHT CFD investigates the relations between wall conduction and associated convection in GT cooling heat transfer [50] as Appendix B shows, where effects of radiation are neglected [51-53]. This is because, the impingement plate to plate gap is dominated by high pressure coolant air flow and radiation influence between the plates could be neglected.

$$q''_{12} = -k_s \frac{dT}{dx} = -k_s \frac{T_{w2} - T_{w1}}{W} = k_s \frac{\Delta T}{W} = k_s \frac{T_{w1} - T_{w2}}{W} \qquad (2.1)$$

$$q''_c = h_c (T_{w2} - T_\infty) \qquad (2.2)$$

$$q''_r = \varepsilon\sigma\left(T_{w2}^4 - T_{iw}^4\right) = h_r\left(T_{w2} - T_{iw}\right) \qquad (2.3)$$

Where q''_{12}, q''_c and q''_r are the conduction, convection and radiation heat fluxes (W/m^2), respectively and are usually defined as the ratio of heat transfer rate Q (W or J/s) to surface wall area A (m^2), k_s is the wall solid material thermal conductivity (W/mK), dT/dx is the temperature gradient (K/m), T_{w1}, T_{w2}, and T_{iw} are the temperatures (K) of the liner at the combustion gas heated wall, coolant air and impingement plate surfaces respectively, T_∞ is the coolant air temperature, ΔT is the temperature difference (K), *W* is the liner wall thickness (m), h_c and h_r are the convection and radiation HTC's *h* (W/m^{2}K) respectively, ε is the emissivity - a non dimensionless quantity that defines the relative ability of material surface to emit energy by radiation and σ is the Stefan-Boltzmann's constant which is generally given by 5.67 × 10^{-8}W/m^2K^4 value [48, 49].

2.2.1 Application of Conjugate Heat Transfer

Conjugate heat transfer (CHT) has been shown in Chapter 1 to involve heat transfer analysis in a combined fluid and solid systems that deals with the interaction between the conduction inside and the buoyancy forced flow of fluid (convection) along the solid surface. This relationship can be express using the wall boundary layer concept [48], whereby at the surface energy transfer is only by conduction and is because there is no fluid motion and k_s = k_f as Equation 2.4 shows. This is by using the relation that defines Newton's law of cooling of Equation 2.2 combined with Equation 2.1 and which yields the Equation 2.4 as reference by Figure 2.1 (b), thus the basic relation that expressed CHT.

$$h = \frac{-k_f \, \partial T / \partial W \,|_{W=0}}{T_{w2} - T_\infty} \tag{2.4}$$

Figure 2.1 (a) is a typical air jet impingement cooling system applicable to gas turbine combustor wall heating by hot combustion gas. Heat is transferred from the hot target plate of L wall thickness to the coolant air at temperature T_∞ by convection and at the surface of the target plate with temperature T_{w2} when the velocity of air flow is zero (no slip condition), as the interaction between air and target surface (equilibrium state) is by conduction. This relationship is shown in Appendix B which estimates the temperature difference on the target plate surface and the opposite surface. In the impingement gap Z, the interaction between air jet particles from the hole is characterized by dimensionless hole length to diameter ratio L/D that can result into a reverse air flow causing transfer of heat from the heated fluid to the impingement plate surface by convection [4, 19]. Equally, the heat transfer from the target plate to the impingement plate can occur by thermal radiation as a result of the high temperature difference and emissive power between the plate surfaces [52]. However if the temperature difference between the target and the impingement plates surfaces is low because of the impact of jet flow that creates a barrier between the two plates, then radiation effect may be negligible [51] which this work employs.

2.2.2 Dimensionless Heat Transfer Relations

Dimensionless similarity parameters that are significant in the boundary layer (BL) of the air jet cooling shown in Figure 2.1 include: Reynolds number Re (= VL/ν) [3] related to the velocity V (m/s) and the kinematic viscosity ν (m^2/s) and Prandtl number Pr (= $C_p\mu/k$) [54] related to the air properties shown in Appendix C where C_p is specific heat at constant pressure (kJ/kgK), μ is dynamic viscosity (kg/ms) and k_f is the thermal conductivity. These have been shown to be applicable to CHT CFD investigations [22, 25] whereby results were obtained for a surface with convective conditions to geometrically similar surface with entirely different conditions [25]. They are generally represented as components of the dimensionless Nusselt number Nu which Equation 2.5 shows and is related to measure of h_c (or h) existing at the surface for a prescribed geometry [3, 5, 49], which is also explained in Appendix B.

$$Nu \equiv \frac{hL}{k_f} = + \left.\frac{\partial T^*}{\partial W^*}\right|_{W^*=0} = f\left(X^*, \mathrm{Re}, \mathrm{Pr}\right) \tag{2.5}$$

Where T^* is dimensionless temperature that will be shown later to predict wall conductive temperature of combustor and turbine blade, W^* and X^* are dimensionless independent geometrical variables (W, X and L or D or D_H are related to plate surface axial distance, wall thickness and length or hole/hydraulic diameters of the geometry), as Nu stands the universal function of X^*, Re and Pr. These are discussed in a more detailed in the experimental correlation section that is section 2.7.

2.2.3 Wall Thermal Gradients

The use of a heated wall in the experimental work and in all practical applications of impingement jets for cooling, results in heating of the impingement jets reflected as the hot impingement plate surface. Using the dimensionless temperature relations from the work of El-jummah *et al* [22, 25, 32, 33, 46] of Equations 2.6 and 2.7, this reversed jets can be determined and were shown to give the metal temperature variations predicted by the conjugate heat transfer CFD. Equation 2.6 was used when the imposed hot side condition is the temperature (^{o}C) captioned T_w, while the used of Equation 2.7 was when the hot side is the heat flux (W/m^2) shown as the only way to normalized the temperature T^* was by using the hot side mean temperature T_m (^{o}C). The used of dimensionless temperature has also been applied on effusion cooled plates by Gustafsson and Johansson [55]

$$T^* = \frac{\left(T - T_\infty\right)}{\left(T_w - T_\infty\right)} \tag{2.6}$$

$$T^* = \frac{\left(T - T_\infty\right)}{\left(T_m - T_\infty\right)} \tag{2.7}$$

2.3 Gas Turbine Cooling Systems

Improving the design of components requiring high rates of heat transfer (cooling or heating), knowledge of the parameters to that effect is important. Chance [56] reported that the parameters influencing the heat transfer coefficient (HTC) are:

1. Impingement jet velocity V_j

2. Hole area per unit surface area A
3. Plate to plate surfaces spacing or gap Z
4. Hole diameter D
5. Hole to hole pitch X
6. Spent air or cross-flow velocity V_c
7. Air jet temperature T_∞

Although average HTC $\bar{h}$ is more practical and useful in engineering application, the local HTC *h* has dependency on location, local fluid temperature, fluid properties (density ρ, velocity V_j etc.) and geometry of the system [57]. This CHT CFD work concentrates on the application of the earlier one as all the measured data are average HTC [3-5, 19, 22, 25, 46]. The heat transfer rate to or from a jet impinging onto a surface has been shown to be a complex function of several non-dimensional parameters [58]: Nusselt number (Nu), Reynolds number (Re), Prandtl number (Pr), Pitch-to-diameter ratio (X/D), jet-plate gap-to-diameter (Z/D and are essential to the design of turbine engine combustor and turbine blade walls. Investigations are usually based on the understanding that flow fields are governed by pressure gradient, development of boundary layer along transfer surface, turbulent intensity, etc., makes these characteristics with heat transfer clear with varying shape of heating surface (flat or curved), the shape of the jet (two-dimensional or axisymmetric) and the types of fluid used [59]. To obtain results, parameters that are shown to be of primary interest are the Re, D, X, Z, and Location [60].

2.3.1 Geometrical Design Considerations

Andrews and Hussain [3, 21] described two applications of impingement cooling using different design conditions and these are based on the hole pitch X, hole diameter D, non-dimensional pitch-to-diameter ratio X/D and impingement gap Z or gap to diameter ratio Z/D. Their description cited previous investigators as detailed [3], for example by varying X with varied X/D on impingement cooling using arrays of jets resulted in very high jet velocities and accompanying pressure losses for large X/D. Therefore, varying X/D influences the impingement aerodynamics [21, 61, 62]. It was concluded that X/D together with Z are major geometrical parameters by keeping X constant with varied D [61]. Generally, the ‘best’ agreeable impingement structure possess $X/D \leq 10$ [63], it gives high average heat transfer but total required coolant flow rate is also high. The impingement holes geometry can be calculated by using Equations 2.8, 2.9 and 2.10 respectively, these are useful in achieving the needed values of D, X, X/D [3, 22, 25]. The impingement wall porosity A (or hole area/X^2) is related to X/D by Equation 2.10.

$$D = \left(\frac{4}{\pi} \frac{A}{n} \right)^{0.5} \tag{2.8}$$

$$X = n^{-0.5} \tag{2.9}$$

$$\frac{X}{D} = \left(\frac{\pi}{4A} \right)^{0.5} \tag{2.10}$$

2.3.1.1 Effect of Hole Pitch to Diameter Ratio X/D

The pitch to diameter ratio X/D can be varied by varying X at constant D [64], which also changes the hole density *n* (m^{-2}) or number of holes N and the pressure loss ΔP. By varying D at constant X [25] keeps *n* fixed with varied pressure loss ΔP and by varying both X and D [22] that also varied *n* (m^{-2}) with ΔP closely remaining constant. This is the method of varying X/D used in the present CHT CFD work and in previous experimental work using four sided exit impingement cooling [21, 45, 61]. Whichever method of varying X/D is used, the main associated effect is to vary the impingement jet velocity V_j and impingement wall pressure loss ΔP/P as the total impingement air flow porosity A is varied. This is shown by Equations 2.11 - 2.14 for square array impingement holes. Increasing X/D increases V_j at constant G which also increased ΔP/P and this increases the impingement heat transfer.

Andrews *et al*. [45] and El-jummah *et a*l [22] have reviewed investigations on impingement cooling and showed that different workers investigated different ranges of *n* (m^{-2}) and are related to X/D. The lowest *n* in the literature [63, 65, 66] were in the range of 50 - 80m^{-2}, at the other extreme of *n* investigations [56, 57, 60, 67] were between 50,000 - 400,000m^{-2} have been studied. As the cost of manufacture is directly related to *n* there should be design procedures to recommend minimum values of *n* (m^{-2}), which this present work investigates.

2.3.1.2 Effect of Plate -to- Plate (Gap) to Diameter Ratio Z/D

Freidman and Mueller [68] have found that the effect of spacing on the impingement heat transfer coefficient *h* is related to the ratio of spacing to the equivalent hole diameter Z/D. El-jummah *et al* [33] showed that this Z/D affects flow-maldistribution and this will be shown later to increase the heat transfer and cross-flow effects. Arrays of impingement heat transfer tested for a smaller values of Z/D of less than five [69] showed that average heat transfer coefficient is sensitive to the impingement gap Z. A review of Z/D data was conducted for a range of values; 1 < Z/D < 10 [70] and 1 < Z/D < 6 [3], they concluded that Z/D has little influence on cooling heat transfer. They also showed similar result in their investigation for the range of Z (2 to 12 mm) values, which are applicable to a practical gas turbine combustor and turbine blade cooling. Their observation was a decrease in heat transfer as Z/D increased. The explanation they gave was that investigating for Z/D at variable Z [33, 71] has not much influence, but a greater effect was found for constant Z with variable D [21, 25, 72], which was primarily because this was achieved at constant X and hence the impingement X/D was decreased or the porosity increased.

2.3.1.3 Influence of Hole Length to Diameter Ratio L/D

The impingement jet and effusion walls thicknesses and the holes sizes depends on the hole length L to diameter D ratio L/D and is an important parameter for a short hole thermal entry effects [73, 74]. This parameter can be varied by either varying the hole size D [17] or the hole length L or both [75, 76] and it has been shown to influence the hole surface and approach heat transfer as L/D influences the aerodynamics in the hole [14, 17, 73, 77-80]. This influence of L/D will be clearly shown in sub-section 2.3.3 below.

2.3.2 Flow Design Characteristics

The impingement jet array coolant mass flux G (G^*/P) and the impingement wall pressure loss ΔP are related to the impingement X/D by Equations 2.11 and 2.12 [3, 25, 61]. The impingement jet Re is given by Equation 2.13 [3], which is proportional to the coolant flow rate/unit surface area (or mass flux) G given by Equation 2.11 and this G is related to pressure loss ΔP/P as shown in Equation 2.14 [81]. These relations are interrelated, which shows that if G is increased or decreased, V_j, Re and ΔP are also affected and all are shown to be strong functions of X/D. Where A is the total coolant flow area per square meter of wall area and *n* is the number of holes per square meter of impingement surface (m^{-2}).

$$G^* = \frac{V_j A}{RT} = C_d A\left(\frac{2}{RT}\frac{\Delta P}{P}\right)^{0.5} \tag{2.11}$$

$$V_j = \frac{G^*}{\rho A} = \frac{4G^*}{\pi\rho}\left(\frac{X}{D}\right)^2 = C_d\left(2RT\frac{\Delta P}{P}\right)^{0.5} \tag{2.12}$$

$$\mathrm{Re} = \frac{G^*}{\mu}\left(\frac{4}{\pi A n}\right)^{0.5} \tag{2.13}$$

$$\frac{\Delta P}{P} = \frac{4RT}{(\pi C_d P)^2}\left(\frac{G^*}{nD^2}\right)^2 \tag{2.14}$$

For the conditions where impingement jet deflections are likely to be significant, Andrews and Hussain showed that flow-maldistribution also becomes very important. This was as shown by the relation for the prediction of the ratio of impingement jet velocity V_j to the impingement cross-flow velocity V_C that is when this ratio approaches unity. These are related by Equations 2.12, 2.15 and 2.16, respectively and are shown to describe this ratio in Equation 2.17. The condition that the density of the air jets ρ_j is the same to the density of the impingement gap or cross-flow ρ_C here applies, hence incompressibility. This present work CFD is the application of incompressible flows to respective gas turbine cooling systems. For smaller Z/D or $V_j/V_C < 2$, cross-flow causes a flow-maldistribution as well as significant jet deflections which possibly reduce the heat transfer [20, 22, 25, 46]. Equation 2.18 defines the parameter I_C showing the influence of cross-flow, this was also correlated by Chance [56] and Kercher and Tabakoff [57]. The use of I_C to correlate the influence of cross-flow showed the insignificance of Z/D on impingement jet cooling heat transfer.

$$G_C = \left(\frac{\dot{m}_C}{ZX}\right) = \rho_C V_C \tag{2.15}$$

$$V_C = \frac{NG^*(X/Z)}{\rho} \{ for \rho_C = \rho_j \tag{2.16}$$

$$\frac{V_j}{V_C} = \left[\left(\frac{1}{N}\right)\left(\frac{4}{\pi}\right)\left(\frac{X}{D}\right)^2\left(\frac{Z}{X}\right)\right] = \frac{Z}{(NAX)} \tag{2.17}$$

$$I_C = \frac{G_C Z}{G_j D} = \frac{\rho_C V_C Z}{\rho_j V_j D} \approx \frac{V_C Z}{V_j D} = \frac{NAX}{D} = \frac{\pi ND}{4X} \tag{2.18}$$

To effectively estimate the ratio of pressure loss 'y' along the impingement plate to that of the impingement gap [20, 25], Equation 2.19 was used which shows the ratio based on the assumption that flow-maldistribution is not a factor. But if the ratio is approaching unity, the assumption is invalid. The pressure loss ratio is hence used in estimating the ratio of the mass flux at the upstream row of holes G_1 to that at the downstream row of holes G_N, for which Equation 2.20 shows. Literature findings on impingement jet cross-flow are discussed in a more detail in the impingement jet cooling section.

$$y = \left(\frac{Z}{C_d nAX}\right)^2 \tag{2.19}$$

$$\frac{G_N}{G_1} = \frac{y}{1-y} \tag{2.20}$$

2.3.3 Short Hole Aerodynamics

Gas turbine combustor and turbine blade cooling jet walls are typical of the situation where short holes in metal walls act as a heat exchanger to cool the walls [17, 25, 75, 76, 82]. The aerodynamics of short hole inlets involve hole inlet entry effects that generates inlet flow separation and reattachment in the hole [77, 78, 80, 83, 84] as shown in Figure 2.2 (a). Experiments have shown that the length and diameter ratio L/D [74, 76] is a critical parameter in the enhanced heat transfer [17, 79, 80, 83, 85-90]. A key experimental parameter is the pressure loss ΔP, which can only be successfully predicted if the inlet flow separation and reattachment is correctly predicted. It is known from flow visualisation and wall static pressure profile measurements that the flow inside short holes with a sharp edged entry is that shown in Figure 2.2 (a) [73, 79, 80, 83, 84, 90, 92], the key feature is the flow separation at the sharp edged hole inlet. This forms a vena contracto [84] which has a contraction coefficient in ideal fluid flow of 0.61 of the inlet area [83]. There is then a dump flow expansion to give a wall reattachment point about one hole diameter [73] downstream of the inlet and then a recirculation zone in the wall region that is about 1D long [76].

(a) Flow in short hole (b) Experimental short hole (c) CFD short hole

Figure 2.2: Flow features and surface patterns of short holes [25, 80, 91]

The pressure loss ΔP of the flow through the hole is critically dependent on the flow separation, as the dominant source of the pressure loss is the dump flow expansion from the vena contracto to the vessel wall plus the dynamic head pressure loss at the hole exit [73]. For an L/D up to about 0.4 the flow separation does not reattach and for an L/D of about 0.8 the flow reattaches and in between there is an unstable flow [73, 84, 93]. With flow separation the recirculation zone is a region of high turbulence [78, 85, 87, 94, 95] which occurs within an L/D of 1 and is normally centred at 0.4 - 0.5 [17, 25, 76] hole diameters from the inlet. An effusion wall has active heat transfer within the wall thickness due to short hole heat transfer and this is in addition to the film cooling effectiveness of the effusion cooling. Thus the overall cooling is the wall heat transfer plus the adiabatic effusion cooling, to give an overall cooling effectiveness [75, 96]. In practice the holes were manufactured by drilling, spark erosion or electron microscope scan, as shown in Figure 2.2 (B) and the air hole inlet would be slightly rounded. This would reduce the flow separation slightly and thus reduce the pressure loss Δp, but this rough walls of the impingement holes are not reproduced in the CFD model holes as Figure 2.2 (c) shows. This influence of hole surface will be investigated in the present CHT CFD work.

2.4 Review of Gas Turbine Experimental Cooling Techniques

The basic experimental tools that are used for any impingement jet or impingement/effusion heat transfer which are relevant to combustor wall and turbine blade cooling applications includes: The source of fluid (usually air) and the delivery loop at specified temperature and flow rate, the source of heating of the target plate (electrically or gas combustion), the design and fabrication of the impingement hole size and the interchangeable test plates with mounted thermocouples to allow for temperature measurements. The experimental apparatus are either industrially sourced for which experiments are carried out using the real practical applications [59, 97] - used a wind tunnel with nozzle of V.S. motor and turbine casing of large civil turbofan or are mainly sourced for the particular type of research, example: The large-scale model using encapsulated liquid crystals [91], the thick acrylic plastic [98], the open circuit air circulation loop or conventional rig [3], or the high temperature or combustion rig [43]. The modified conventional and combustion rigs that have been used by Andrews and Co-workers [3-5, 19, 22, 25, 43, 44, 46, 99, 100] are shown in Figure 2.3 (a - d) at University of Leeds. Typical literature based experimental methods as applied to gas turbine cooling applications are now briefly discussed:

2.4.1 Naphthalene Sublimation Techniques

The used of naphthalene sublimation has been shown to measure with some degree of accuracy heat and mass transfer data [59, 60, 79, 80, 86, 87, 101-106], but this techniques has a major restrictions that it depends critically on the accuracy of the naphthalene properties [107, 108]. This method is usually employed by several experimentalist to determine heat transfer coefficients in convective flows, by which they used the concept of analogy to replaced heat transfer problems with mass transfer problems [108]. Typically, the wall boundaries that requires cooling are substituted with the weighted solid naphthalene boundaries [60, 106, 107] whereby air flows on the new surface. The exposure of the solid naphthalene to the flowing air is characterized by loss of mass from the original body, hence for the ranged of allocated time of air flow on the naphthalene surface and the mass of weighted surface after every one flow/time the total mass transfer rate is calculated from each of the surfaces. This gives surface distributions of Sherwood numbers that is analogous to Nusselt number [102, 106, 107]. The methods employs two types of boundary conditions, which are either isothermal surface of similar uniform mass fraction to naphthalene surface hence sublimation is achieved or adiabatic surface as non-subliming as no mass exchange with air flown. Naphthalene ($C_{10}H_8$) is limited by its melting point of 80.3 ^oC and for a typical gas turbine engine that attends a temperature of > 1500 ^{o}C, this techniques will be inappropriate for use in actual GT wall conductive heat transfer. The present CHT CFD studies is chosen as the preferred method that incorporate real GT wall conductive materials directly.

2.4.2 Electrocalometry Methods

The electrocalometry technique has not been usually used and will only be shown here by work of Dyban *et al* [109], where the specific heat fluxes were determined and local heat transfer are found. They formed a heat transfer surface using a 25 nickel heater strips and pasted onto a Tufnol slab at 0.5 mm spacing in lateral direction to the exit flow. Temperature that does not exceed 350 K was measured and the coolant air taken at room environment conditions, with all measurements taken at steady state thermal conditions. Taken into account the heat losses due to the thermal conductivity k_s of Tufnol, the local HTC h was therefore found.

2.4.3 Transient or Thermochromic Liquid Crystals Methods

A transient liquid crystals (TLC) experimental technique have been employed [12, 13, 110-119], which was shown to measure HTC h in GT blade cooling passages [120, 121] and it has also been extended to combustor wall using different types cooling applications [122, 123]. Ireland and Jones [110, 114] introduced and have shown numerous ranged of descriptive properties of liquid crystals with its usage for time response on thermometer surface, while Baughn [124] reviewed types of application methods and these are not discuss here. Ireland and Jones [116] showed that by using a hot air flow on a Perspex model of blade, surface temperature are monitored using a charge-coupled device (CCD) camera for ranged of time, whereby the internal HTC was determined from this. They showed that the wall of the models can be thin and thick, hence the surface temperature was measured using liquid crystal thermochromic colour indicators. A different but similar in its application is the temperature indicating coating with transient cooling techniques used by Bunker and Metzger [125] and Metzger and Bunker [16], but are not discussed here. The TLC technique have also been shown to attract impingement air jet cooling investigations [91, 119, 123, 126-137], for which low conductive adiabatic wall materials [111] were used to measured heat transfer.

The used of liquid crystal coating that displayed colour over two distinct temperature ranges on a Perspex (with k_s = 1/100th of a GT blade alloy) surface have been carried out [111]. They used a direct development of the technique that was applied on a coated model of grains (not specified) and the liquid crystal film was used in monitoring the step changed in gas temperature of the surface, hence the local cooling HTC h values were obtained. A thin layer of black ink was also shown to be applicable on film surface of the liquid crystal material, this helps to stop light transmission [128, 131, 138]. The used of coated thermochromic liquid crystal on Perspex that showed peak intensity at 313.3 K was also carried out [127, 130], while Lee and Lee [139] used Gold coated film. These investigations have been shown to be applicable to single impingement jet [129, 139] and multiple impingement jets [91, 112, 119, 122, 126, 132-137]. Facchini and Surace [123] investigated the used of liquid crystals for both steady and transient state applicable to multiple impingement jet flow, whereby an Aluminium combined with a high conductive coated and black paint wall target plate was used. This present CHT CFD investigates the influence of a typical GT wall conductive material that show the significances of cooling effects as X/D is varied, hence the used of TLC will not be an appropriate techniques.

2.4.4 Steady State Segmented Wall Electric Heating

Several investigators [56, 57, 98, 140-146] have found the used of segmented isothermal block walls for the steady state determination of heat transfer as useful technique. This experimental method was shown to be applicable to only multiple impingement jets cooling systems and investigators either employed the used of copper [56, 57, 146] or Aluminium [98, 144] wall blocks, which both materials were found to give near uniform wall temperature [32]. Metzger *et al* [140] showed that the choice of segmented blocks was mainly to give chord-wise spatially resolved HTC *h* and also provides control of thermal boundary conditions at the heat transfer surfaces. Gardon and Akfirat [144] argued that the choice of high conductive Aluminium segmented plates was to suppress the lateral temperature differences in the wall, which enabled them determined a steady state HTC *h* on the top surface. Bunker and Metzger [125] and Metzger and Bunker [16] used segmented acrylic plastic test material that was coated with sprays and the test was run as a thermal transient, where locally surface HTC was determined.

Chance [56] methods of heating was by individually heating the copper blocks using cartridge type heater and embedded within the blocks. This method has similar jets cooling and heating of the target plate procedures with steady state lumped capacitance that is discussed later. While the latter is a continuous plate using a mat heater that covers this plate, the earlier is a segmented plate with heaters that covers individual plates. Each segmented walls were shown to be insulated at the hot side and edges, hence between two plates was an insulator and this is anticipated to affects continuous wall conduction.

2.4.5 Lumped Capacitance Flat Wall Techniques

The methods of heating the impingement target continuous flat test walls using a steady state lumped capacitance technique, are rarely used experimentally and only few investigators have been found [3, 5, 22, 25, 43, 46, 61, 63, 64, 147-150]. The used of copper [63, 64] and polystyrene [151] for one flat target test walls has been experimentally shown to give measured heat transfer data. While the earlier one was for high thermal conductivity k_s (~ 401 K) of high melting point (~ 1400 K) has been shown for a similar wall (Aluminium) by El-jummah *et al* [32], to give too high HTC at near uniform temperature throughout the target wall length due to internal conduction, cannot be use as a real combustor wall material. The later was for $k_s = 0.033$ W/mK and melting point of 515 K, has too low k_s that could give a very high Biot number β which has been shown to exceeds experimental conclusions of $\beta > 0.2$ [5, 33, 46], which is also calculated in Appendix B. The used of Nimonic-75 materials [3, 19, 23, 25, 43, 99] as a common industrial gas turbine combustor wall has thermal properties typical of other GT wall materials. This Nimonic-75 wall material was chosen as the present impingement jet and target or effusion approach test walls, whereby the lumped capacitance technique is employed.

2.4.5.1 Steady State Continuous Wall Technique

Andrews and Hussain [3, 61], El-jummah *et al* [22, 25, 46] and Andrews *et al* [19, 23] used the experimental equipment shown in Figure 2.3 (a - c) and are called conventional rig, they consisted of an air supply to a thermally insulated plenum chamber feed to the impingement holes. The 152.4 mm square Nimonic-75 impingement test plate was bolted to the plenum chamber and the impingement gap Z was set. For single sided exit impingement flow the gap was formed using a Teflon spacer flange and other three sides blocked, for a four sided exit impingement flow all the gap sides are open, while for an impingement/effusion all the sides were completely blocked and the flow was through the effusion holes. For the effusion rig shown in Figure 2.3 (a), the impingement target wall was removed and all the air flow was through the impingement air plate. The Teflon spacer has a low thermal conductivity and this minimized the transfer of heat between the two metal walls made of Nimonic-75 material.

The thermally insulated target test wall was electrically heated, in the absence of any impingement coolant flow to about 80 ^{o}C (353 K) and then the electrical heating was switched off and the impingement flow established. The target wall was instrumented with grounded junction mineral insulated thermocouples brazed to the Nimonic-75 wall with the thermocouple junction flush with the impingement jet target surface [25]. There were six thermocouples at 25.4mm intervals placed on the centreline between the impingement surface jets and thus at the most remote places relative to the high local convective cooling of the impingement points. Conductive heat transfer within the wall smoothed out the strong gradients in surface convective heat transfer, as the Biot numbers for all conditions were < 0.2 and < 0.1 for the lower coolant flows, with ± 10 % maximum error for *h* and 5%

for G [5, 46]. The thermocouples thus measured a surface averaged temperature and were located at the lowest local convective heat transfer position and hence would give slightly higher temperatures than the mean and thus result in conservative measurements. The target wall thermocouples were used to determine the steady state locally surface averaged HTC *h* that will be shown later using the lumped capacitance method [5, 22, 25, 46]. Conductive heat transfer in the metal wall occurs in practical engines, this present CHT CFD work investigates this using the lumped capacitances methods as most experimental and CFD investigations of impingement heat transfer are for adiabatic wall conditions.

2.4.5.2 Continuous Wall Transient Techniques

The use of hot gas flow in order to heat up the impingement or effusion approach test plates has not been mostly applied in the gas turbine cooling applications, as only very few work have been found in the literature. Gauntner *et a*l [67] carried out their investigations using a real life turbine cascades at an average hot side temperature of 1255 K and air coolant temperature of 290 K for staggered array of holes. Nakamata *et al* [152] investigations were for single jet hole using a hot side temperature of 633 K and coolant air at room temperature 298 K, they used the manufactured rig of Japan Aerospace Exploration Agency (JAXA).

The experimental facilities tagged "Combustion" rig of Abdul Hussain and Andrews [5, 43] shown in Figure 2.3 (d), is the only literature based designed laboratory equipment that used the hot side heating of the impingement test plate with hot gas flow temperature T_g of ~ 600 K and a coolant air at room temperature T_∞ of ~ 298 K, with their ratio typical to a gas turbine applications. The hot gas duct were externally air cooled and the flow rate was controlled to achieve an equal temperature as the test wall, which also minimised the radiation heat transfer effects from this wall. Their experimental test rig coolant air supply system was the same as that used in the preceding sub-section for conventional rig, hence the major differences is with the heating of the impingement test plate. This rig have been used and applied for the experimental investigations of impingement, effusion, impingement/effusion and transpiration gas turbine cooling.

In order to effectively determine HTC *h* of the work by Abdul Hussain and Andrews [5], a transient cooling technique was used using the combustion facility, at a low coolant flow rate whereby an equilibrium temperature was achieved. The coolant flow was forced to a step changed at a higher value, which allow for changes in the measured test wall temperatures that was used in the determination of HTC and cooling effectiveness η. This CHT CFD gas turbine cooling investigations, will not model explicitly the hot gas flow in the duct below the target test wall. Instead, a constant heat flux of 100 kW/m^2 [32, 33] will be applied as the boundary condition along the target wall and was because it approximately reproduces the conditions of the hot rig of Abdul Hussain and Andrews [5, 43]. This gives coolant to hot gas temperature difference of ~ 450°C and convective heat transfer coefficient at the cooled surface of ~ 200 W/m^{2}K. The heating application of an imposed heat flux q'' (W/m^2) that has the same HTC with a typical gas turbine combustor wall hot side.

2.4.6 Infra-red Thermography Camera Technique

The infra-red thermography camera (IR) technique [120, 153-157] captures surface heat transfer when the emissivity of the wall materials is known [153]. This techniques employed the used of constant heat flux electrical heater that are embedded with thermocouples at selected locations [120]. The heater generate temperature distribution and the IR is used to measure the inside temperature of the heater that has to be checked by the thermocouples. Oh *et al* [155] used a black paint to increase the emissivity of the stainless steel wall and the

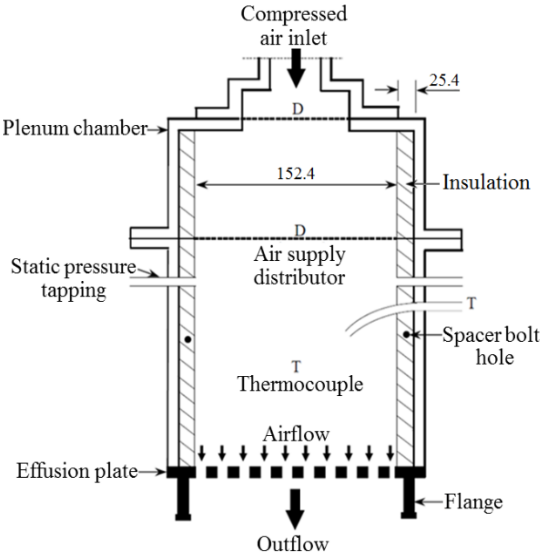

(a) Effusion rig

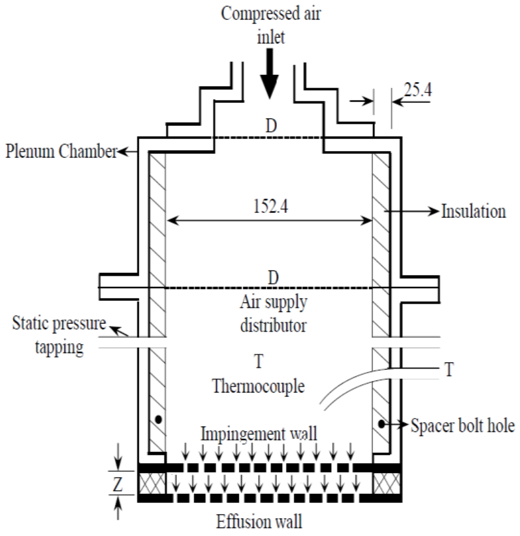

(b) Impingement/effusion rig

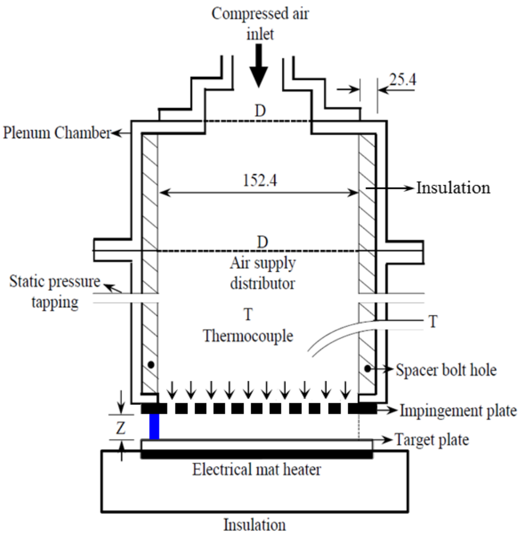

(c) Impingement jet conventional rig

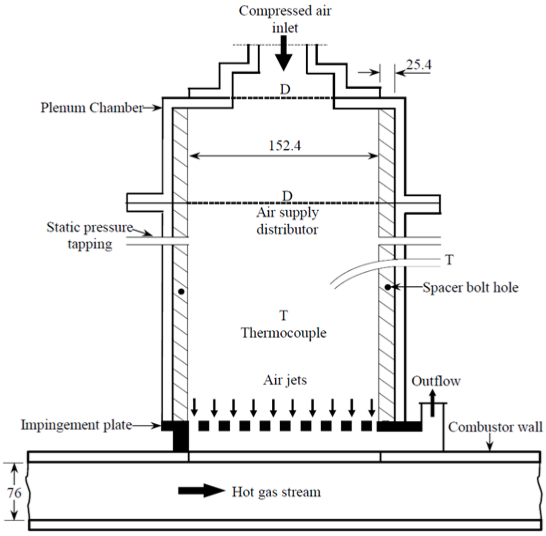

(d) Impingement jet combustion rig

Figure 2.3: Gas turbine cooling range of experiment test rigs [4, 25, 43, 158]

IR measured the temperature with the thermocouples verifying at the same time. Hedlund *et al* [154] measured the infrared radiation contours simultaneously in conjunction with thermocouples, energy balances, digital image processing and in situ calibration analysis. Scherer *et al* [153] used coated sprayed surface on foil and plastic material to know emissivity, between which was adhesive acry-lat-polymer. Surface distribution of temperature was measured and monitored by thermocouples placed between the heater strips. These shows that this method is limited by the influence of radiation and wall is adiabatic temperature [155], which must be corrected to certify CHT computational procedures and thus cannot be apply in this work.

2.4.7 Pressure Sensitive Paint Technique

The pressure sensitive paint technique (PSP) has been employed [159-163], which are used in the determination of film cooling effectiveness. This techniques are based on oxygen-quenched photo luminescent molecules [160, 161] that emits light when exposed, the intensity of which are recorded with charge coupled device (CCD) camera. Using coolant injections of two types normal air and oxygen-free foreign gas [159, 160], where by the displacement of the air molecules on the PSP coated surface that changes the emitted light intensity from the paint, hence partial pressure difference between the two coolant are recorded. This helps in the determination of mass fraction of the tracer or foreign gas for the surface and is related to the adiabatic wall temperature [160], which is shown to be analogous to heat transfer, hence film cooling effectiveness is determined.

2.5 Review of Gas Turbine Cooling Experimental Investigations

Earlier research works carried out are either for jet impingement on curve plate [60, 67, 164-169] that were applicable to turbine blade wall cooling, or jet impingement cooling on flat plate [3, 5, 7, 56, 57, 59, 61, 63, 66, 91, 98, 104, 109, 126, 140-144, 150, 170-173] that are mostly relevant to combustor wall cooling. This flat wall jet impingement cooling experimental investigations have been shown by work of Andrews and Co-investigators as shown in Figure 2.3 (a - d), to be equally applied to turbine blade wall heat transfer cooling [3, 5, 20-22, 25, 43, 45, 46, 62, 81, 99] and they have extended their work to impingement/effusion cooling [4, 19, 23, 44]. Most investigators essentially measure average *h* on impingement target or effusion approach surfaces which is particularly useful for engineering design calculations. This present CHT CFD investigations used similar methods of data averaging for HTC *h* in validating the measured data.

2.5.1 Effusion Cooling Investigations

Effusion cooling or as generally referred to Full-coverage discrete hole wall film cooling is a film cooling phenomena that involves the use of multiples holes as shown in Figure 2.3 (a), which offers considerably simple methods that has been shown to be effective [18, 40, 75, 80, 174-183] in cooling GT components walls. The important variables that have been shown to influence this technique are the hole angle that are either inclined [176, 177, 184, 185] or at right angle to the flow approach [80, 175], the hole density n (m^{-2}) [174], hole pitch to diameter ratio X/D [18, 186] whereby either D or X are varied, hole length to diameter ratio L/D [76] and the mass Flux G [175]. Andrews and Mpadi [83] reported that for a proper selection of effusion hole geometries for combustor wall cooling, the need for the appropriate knowledge of the coolant mass flux G must be a requirements. This CHT CFD work investigates these variables relevant to effusion wall cooling in order to properly know the aerodynamics in the GT combustor and turbine blade walls, which also helps in the design of impingement/effusion cooling geometries.

2.5.2 Impingement/Effusion Cooling Heat Transfer

Impingement/effusion cooling, as shown in Figure 2.3 (b), is one of the most effective cooling system for GT combustor walls and turbine blades that enables lower coolant mass flow to be used [4, 19, 23, 44]. Impingement/effusion arrays of holes are usually designed based on the equal number of holes [4, 23] and unequal number of holes have also been used [6, 7, 44, 172]. A large number of effusion holes is advantageous for effusion cooling effectiveness, whereas a large number of impingement holes may not be necessary [4, 44] and a lower number could reduce manufacturing costs. A very large number of effusion holes approaches the ideal film cooling of transpiration cooling using a porous wall [7, 19, 44, 187]. Al Dabagh *et al* [4] and Andrews *et al* [23], experimentally investigated the wall heat transfer for impingement/effusion cooling for range of square arrays of holes (hole density n - m^{-2}). This present CHT CFD will model their experimental work for a constant isothermal effusion wall with varied coolant mass flux G (kg/sm^2bar). The aim was to develop CHT/CFD design procedures that could be used in combustor wall and turbine blade heat transfer optimisation.

Previous CFD investigation by El-jummah *et al* [32] have investigated the internal wall heat transfer of the impingement cooling only. For both gas turbine combustor and turbine blade wall cooling, backside only impingement cooling is a design option. The backside wall cooling application, is used in combustors to regeneratively cool the combustor and in this case all the combustion air flow is used first to cool the walls. This requires a high G of about 2 kg/sm^2bar and for a low pressures loss this requires a low X/D. The high G low pressure loss is required as the air has to have enough pressure energy for most of the combustor pressure loss to be at the low NOx flame stabiliser. A problem with impingement only backside cooling is that the air has to flow out of the impingement gap and this cross-flow generates complex interactions that lead to the deterioration of the heat transfer in the cross-flow direction [22, 25, 32]. With impingement/effusion cooling for an equal and unequal number of holes, there is no cross-flow as each impingement jet air flow emerges through adjacent effusion holes. This impingement/effusion cooling geometries are investigated in the present CHT CFD work.

2.5.2.1 Impingement/Effusion Design Requirements

Andrews *et al* [19, 23, 61, 174], showed that the combustor design requirements for impingement/effusion system are that ~ 70% of the pressure loss $\Delta P/P$ occurs at the impingement wall, with the effusion wall pressure loss $\Delta P/P$ relatively low as this gives low blowing ratios and a high effusion film cooling effectiveness. For turbine blades, the large static pressure P variations around the blade surfaces makes the relative pressure loss $\Delta P/P$ between the two plates very complex. In the leading edge of the stator vane, due to high static pressure at the hole outlet film cooling system, a low pressure loss is desirable at both the impingement and effusion holes [4, 23]. The requirements for optimum film cooling effectiveness are that the impingement jet size be small or large X/D (or high $\Delta P/P$), while the effusion film cooling hole size is larger or the X/D is small (or low $\Delta P/P$) [4, 44]. Not all investigations of impingement/effusion cooling have used this ratio of the X/D for the two wall, as in the work of Hong *et al* [188]. The number of holes was a key variable as, for the same wall porosity A and pressure loss $\Delta P/P$, the internal hole surface area scales with $n^{0.5}$. Thus the three hole numbers investigated in the experimental work of Al Dabagh *et al* [4] and Andrews *et al* [23], the relative internal surface areas are 1: 1.5: 2.5 or increases in internal hole surface area of 50 and 150 %.

2.5.2.2 Flow Characteristics in Impingement/Effusion Cooling

The design aim in impingement/effusion cooling is to minimise the coolant mass flux used, so as to have the least increase in NOx due to the use of film cooling air [7, 19]. A problem with impingement only backside cooling is that the air has to flow out of the impingement gap and this cross-flow generates complex interactions that lead to the deterioration of the heat transfer in the cross-flow direction [25, 32]. With impingement/effusion cooling and equal number or increased varied number of effusion (unequal) holes, there is no cross-flow as each impingement jet air flow emerges through adjacent effusion holes [4, 19, 23, 44].

For optimum performance of impingement/effusion cooling, the effusion wall should have a low blowing ratio M, which means a low jet velocity hence a low G (kg/sm^2bar) and this in turn requires a low pressure loss ΔP [4, 44]. The design requirement for this is a low X/D with relatively large effusion holes. In contrast, the impingement wall requires a high jet velocity using a low G stated above for best effusion wall backside cooling, which requires a higher X/D. The combination of large/small X/D for the impingement and effusion walls respectively, has been found experimentally to be a practical combination in terms of the overall cooling effectivess [4]. This have been shown to give practical wall pressure loss ΔP at low overall coolant mass flux G (kg/sm^2bar), this need to be verified using CHT CFD which this work is concentrating on.

2.5.3 Impingement Cooling Heat Transfer Systems

The method of heat transfer that effectively resolves the problems of gas turbine combustor wall and turbine blade cooling is impingement jet cooling heat transfer [62], an application that is becoming more common in combustor wall cooling [25, 61]. This method have been shown to be widely and increasingly used [98] for cooling applications of solid surfaces and has long been recognised as an efficient means of cooling or heating [56, 165]. Impingement cooling heat transfer is relevant in the application of drying of textile/paper, tempering of glass, spot cooling of electrical apparatus and cooling of turbojet engine structures [57]. Andrews and Hussain [3] showed that to maintain the acceptable life requirement of the gas turbine combustor or turbine blade walls and to satisfy the NOx regulations, jet impingement cooling heat transfer system is desirable. For ultra-low NOx industrial GT combustors where no film cooling was desirable [36], all the compressor air has been shown to firstly cool the combustor walls before combustion takes effects and this is termed regenerative cooling [5, 25, 43]. The requirements are high mass flow (Table 2.1) rate at a low pressure loss, so that there is adequate pressure loss for flame stabiliser [25].

The desired gas turbine combustor outlet temperatures have been reported to possibly be in the range of 1400 -1700^{o}C [62, 172], It was also reported that the highest firing temperature for the present industrial gas turbines is 1500^{o}C [189] and for jet engine is ~ 2000^{o}C [190]. The availability of high temperature alloys for example: Nimonic-75 and Inconel as combustor wall materials with temperature ranges between 900 - 1200^{o}C [11, 19, 100] showed thermal limitations on the capabilities of such materials to withstand high combustion temperatures T_3 as Appendix A shows. Andrews *et al* [19] cited that materials such as lamilloy and transply, which are generally not available and having complex manufacturing process are meant to overcome structural mechanical strength of the hole-surface wall heat transfer. Generally, there is little hope of improvement in material properties, even though high temperature ceramics are being developed [62]. This limits designers to concentrates on GT cooling systems geometrical considerations based on the types of method employed, whereby HTC *h* can usually be modified with feasible surface heat transfer rate and heat generated.

Livingood and Hrycak [191] reviewed the influences of turbulent air jets flow on GT impingement cooling heat transfer flat wall surfaces for single and multiples jet holes, they showed that the effects of turbulence characteristics requires wider investigations and have been shown to be justifiable argument [192, 193]. This CHT CFD, investigates the influence of turbulence using varied geometrical and flow variables [22, 25, 46] in order to actualised the required heat transfer characteristics. The paper drying work by Chance [56] measured average heat transfer as a function of the system geometries. He reported the effects of plate-to-surface spacing Z (or Z/D), open area on the HTC *h* and the magnitude of the interference caused by spent air flow. He also compared his work with the literature and found good agreement but contrary to the work of Kercher and Tabakoff [57], whose report showed increased *h* with Z/D. Perry [170] reported convection of hot gas jet to plane surface, whereby heat transfer from air jets was measured with temperature differences of up to 400°C at high velocity impinging on various angles. Abdul Hussain and Andrews [43] measurement was for coolant to gas temperature ratio that is typical of gas turbine applications. El-jummah *et al* [22, 25] investigated the influence of varied and fixed X/D, where *n* (m^{-2}) was also fixed and varied accordingly and surface and locally average HTC were found to increase with X/D increment but reduced with increased *n*. The effects of varied mass flux G on impingement jet geometry with fixed X/D and Z/D was also shown by work of El-jummah *et al* [46], higher G showed higher average HTC values and lower G was low average HTC. Consequently the various applications of impingement cooling require G to be varied and X/D to be varied and this is the reason that these two parameters were the dominant variables in the present work [20].

2.6 Impingement Jet Hole Configurations

Applications requiring limited amount of cooling (or heating), a single jet system is preferred, but for surfaces with more area requiring cooling (or heating), it is essential to employ multiple jets structures [104]. The design of the later desires that geometrical and flow parameters are carefully chosen in order to satisfy a sufficiently high average HTC *h*. Since the surface area of gas turbine combustor wall is more than the turbine blade, it is obvious that combustion wall requires higher number of impingement holes than the turbine blade [3, 194]. The larger number of impingement rows array of holes in the combustor wall contributed to numerous experience of self-generated cross-flow along the downstream holes, this was shown in Figure 2.4. This cross-flow deteriorates the heat transfer with distance along the gap and may induce a flow-maldistribution in the rows of impingement holes [5, 32]. Figure 2.4 shows that if P_1 - P_2 (low mass flow rate) < P_1 - P_2 (high mas flow rate) then cross-flow is dominates and if P_3 - P_2 > P_1 - P_2, hole flow-maldistribution is severe [25], this review on cross-flow will be shown in in sub-section 2.5.3.

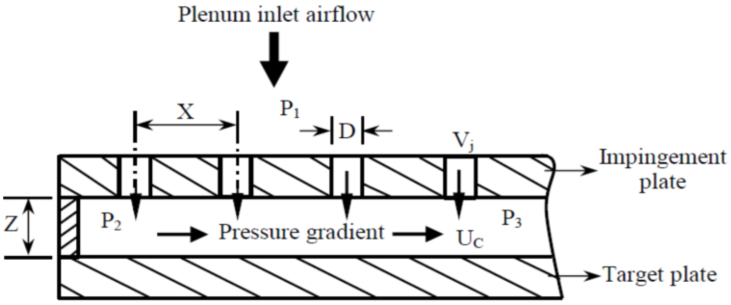

Figure 2.4: Impingement gap geometrical setup with cross-flow pressure gradient [5, 25]

2.6.1 Single Jet Hole Impingement Cooling Heat Transfer

Investigations on a single jet as either circular or slot jet impingement cooling were carried out by a number of researchers [60, 90, 129, 164, 170, 193, 195, 196] and a review was carried out [58, 191]. This will be briefly discuss here as the major investigations of this work is for two dimensional rows of holes. Chupp *et al* [60] investigated ranged of small diameter single circular jet impinging against a highly curved leading edge surface of a turbine aerofoil. Their work looked at variable impingement gap using a tube centred in the leading edge region. They also developed an experimental program to measure the HTC *h* and compare their results with literature. Metzger et al [197] results are for slot jets with fixed Z and slot lengths but varied widths at fixed Re, they only measured average HTC and local values were obtained from this. Janbunatan *et al* [58] compared literature based results on Z/D effects, they showed that heat transfer increases as Z/D decreases to unity. They also reviewed single circular jet impinging orthogonally onto a plane surface for $1.2 < Z/D < 16$ and for range of Reynolds number Re. Their findings showed that the nozzle geometry affects the generation of turbulence in the shear layer, where the influence of nozzle geometry was most significant at stagnation point. The turbulence reduces as radial distance from stagnation point increases. Virtually most investigations on single jet cooling are for either influence of Z or D hence Z/D and some of these are shown in Figure 2.4.

2.6.2 Row of Jet Hole Impingement Cooling Heat Transfer

Single or one dimensional row of impingement jet holes [72, 98, 165, 191, 197-199] (see Figure 2.4) investigations have been shown to be relevant to turbine blade cooling [98] and it helps in regulating the cross-flow [72]. Measurement of a row of jets impingement with constant diameter and variable spacing was compared to slot jets configuration [165]. They showed that a row of circular jets data having larger spacing indicates higher heat transfer than does the slot jet. Hrycak [167] also investigates single row of jets impingement heat transfer on a semi-cylindrical surface and compared his result with single jet impingement on flat plate as well as data of other investigators. His results showed reasonable agreement with that of literature but well below the maximum value found. Metzger *et al* [197] have showed that the heat transfer coefficients for impingements cooling of concave surface using single lines of circular air jets were found to be in good agreement for two-dimensional impingement on plane surfaces. Metzger and Korstad [98] showed that the presence of cross-flow always reduces the average HTC for single lines of circular air jets impinging on plane surfaces. Huang [164] investigated the variation of local HTC *h* for the centre line of round jet, the variation of Z/D to the average HTC and also ranged of X/D and local HTC using empirical equations for single jet impinging on a flat surface were found. Measured data were compared with calculated data generated from the Colburn equation that indicates hardly any change in *h* when Z/D < 6 and local *h* is about 25% higher than average *h* over ranges of X/D of 0 to 20 and Z/D of 1 to 10. They concluded that the results showed the limitations are within the range of interest for industrial air impingement cooling or heating.

2.6.3 Multijet Hole Impingement Cooling Heat transfer

Table 2.2 shows the review for range of geometries as applied to multi or two dimensional jet holes impingement cooling. Koopman and Sparrow [104] showed that surfaces with large area requiring cooling or heating, multijet array impingement heat transfer are more significant. Several investigations have been carried out on different geometrical holes arrangements, either with square (staggered or inline), equilateral triangular or rectangular arrangements [5, 22, 25, 43, 46, 56, 57, 91, 98, 122, 126, 132, 134, 135, 140, 141, 143, 165, 191, 200-202]. Tabakoff and Clevenger [165] compared three configurations of impingement cooling geometries: Single slots jets, row of circular jets and multijet array of round holes. Their results showed that the multijet array of circular holes on the overall have the highest heat transfer than the two other configurations. El-jummah *et al* [22, 25, 46] showed that for the ranged of geometries investigated of an X/D, *n* (m^{-2}) and G (kg/sm2bar) respectively, the square array of 10 number of holes was the optimum

Yamane *et al* [203] showed that increased in the number of arrays of jets increases the strength of wall jets interference, where test geometries for 3 × 3, 5 × 5 and 7 × 7 were carried out. In a similar investigation, measurement of local HTC showed that arrays of two-dimensional air jets, gave an indication of interactions between jets and of the uniformity of heat transfer obtainable with various arrangements [144]. A feature of impingement heat transfer that is rarely investigated, is that the impingement jet on a hot wall is heated by the surface heat transfer with jet interactions [32]. Andrews *et al* [19, 61] and El-jummah *et al* [25, 46] showed that this heated jet reflects in the gap and the reverse flow impinges on the impingement jet surface and heats it. This present CHT CFD, investigates this jets interactions [32] and its effects on GT cooling jet walls by using impingement or impingement/effusion cooling applications.

Investigations were carried out for range of impingement gap (or channel) flow schemes [47, 135, 204, 205]. These are classified as either gap with single flow exit (maximum cross-flow) [25], two-sided exit flow (intermediate cross-flow) [135] or four sided flow exit (minimum cross-flow) [3, 206], the influence of which affects the geometrical design and hence the Reynolds number shown in Table 2.2. The configurations for maximum and minimum cross-flow schemes will be studied here as the earlier relates to the regenerative combustor wall cooling [25], while the latter is typical of turbine blade wall cooling and is equivalent to impingement/effusion heat transfer cooling [19, 91]. Impingement cooling heat transfer of multi-jet holes was shown to be complicated by cross-flow effects from the flow produced by upstream jets [20] as Figure 2.5 shows for varied three G values, which is for smaller X/D or low ΔP/P. But for a fixed low G value shown in Figure 2.6, the high X/D gave high ΔP/P value with insignificant cross-flow and this same G gave low ΔP/P for smaller X/D shown in Figure 2.5, the next sub-section discusses the influence of cross-flow.

2.6.3.1 Cross-Flow on Impingement Heat Transfer

The aerodynamics of impingement heat transfer of gas turbine combustor is a complex phenomenon [3]. It can be influence by the impingement geometries [25, 32, 56, 142] which enhance the cross-flow effects [20, 47, 207]. Experiments on the influence of crossflow on impingement heat transfer have used both a single row [98, 198, 199, 207] and multi-jet arrays [57, 61, 91, 98, 109, 134, 150]. Most investigators found that cross-flow reduced the impingement heat transfer [56], even though the impingement jet velocity was high and the jet deflection by the cross-flow was small [5, 20, 25, 46, 81, 166]. Chance [56] showed that a significant problem with impingement cooling was that the outflow of air in one direction led to a deterioration in the wall heat transfer. The regenerative cooling geometry [5, 22, 25, 46] has a single sided exit from the impingement gap, where the discharge air feeds the low NOx flame stabiliser inlet air plenum chamber.

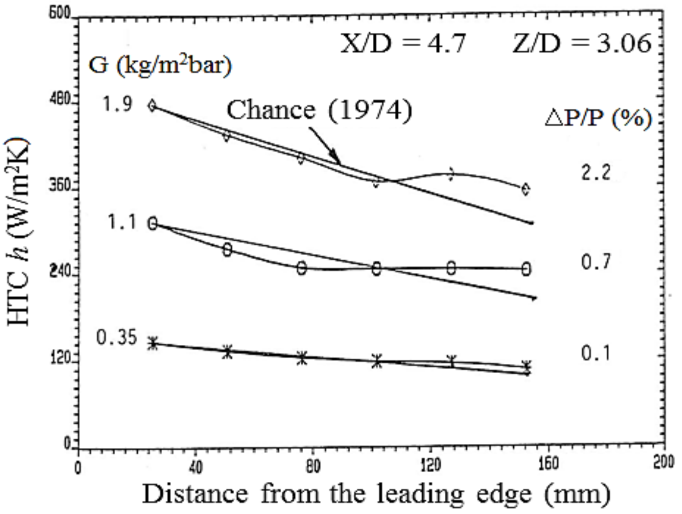

Figure 2.5: Impingement target axial variation of HTC for X/D of 4.7 for three G

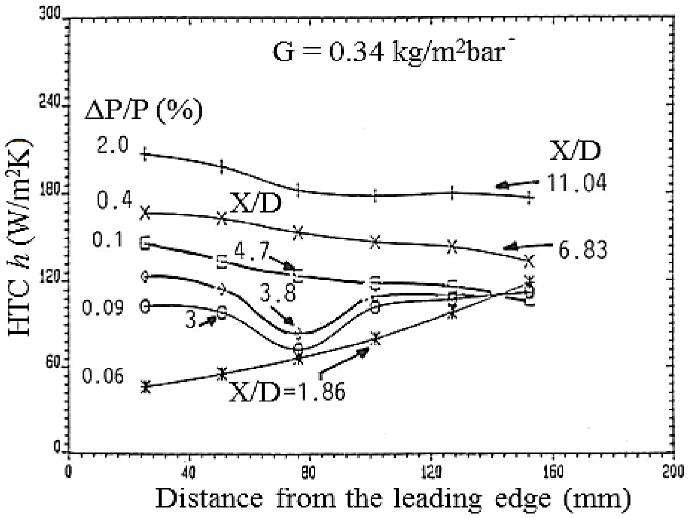

Figure 2.6: Impingement target axial HTC on X/D influence at constant mass flux G

The effects of the cross-flow is strongly influenced by the number of upstream rows of holes N [20, 22, 45]. Cross-flow in the impingement gap contributes to two effects: Firstly, reducing the HTC with number of holes [5, 22, 47, 98] and secondly, causing flow-maldistribution through the holes [22, 25, 46, 122, 208] due to the pressure loss ΔP along the gap being comparable with that through the impingement holes. Both of these effects are reduced if N is small and this leads to a small n (m^{-2}) being preferable [22, 45] which is a problem in cooling design, particularly for combustor walls where the distances to be cooled are greater than in turbine blades [3]. It would be possible to counteract the flow-maldistribution effect by design, this would require the hole size to be non-uniform [22, 45], so that the holes at the leading edge are larger than at the trailing edge of the impingement gap. The design objective would be to achieve the desired equal mass flow rate taking into account the lower pressure loss ΔP across the leading impingement holes. CHT CFD calculations could be used to achieve this redesign, or by using pressure loss ΔP versus hole number of experimental results used to correct the design [22]. This present CHT CFD work could be used in this type of optimum impingement heat transfer design and validate with experimental measurements.

Experimental investigations showed that if X/D is large enough as Figure 2.6 shows, flow-maldistribution between the rows of impingement holes is insignificant in the cross-flow direction. However, at high X/D it shows that impingement heat transfer deteriorates with distance along the gap [25, 43, 46, 56, 57, 63, 67, 98, 123, 142]. This effect was correlated by Chance [56] and Kercher and Tabakoff [57] using the term I_C as in Equation 2.21. Andrews and Hussain [20, 81] converted Equation 2.21 to Equation 2.22 provided the density of the cross-flow and impingement jet is equal or constant. If the deterioration of heat transfer with length of wall to be cooled is to be minimised, Equation 2.22 shows the importance of using a large X or a small number of holes N (small n) for minimum deterioration of h along the gap. How large X and how small n can be made will depend on the thermal gradients in the wall, which this work investigates.

$$\frac{Nu}{Nu_o} = 1 - 0.2361 I_C = 1 - 0.236\left(\frac{G_C}{G}\right)\left(\frac{Z}{D}\right) \tag{2.21}$$

$$\frac{Nu}{Nu_o} = 1 - 0.188\left(\frac{ND}{X}\right) = 1 - 0.188\left(\frac{WD}{X^2}\right) \tag{2.22}$$

Equation 2.22 was shown to be applicable to the data of a wide range of investigators, including the well-known results of Kercher and Tabakoff [57]. It should be noted that the impingement gap size Z, is not a factor in the deterioration of the heat transfer with distance as was shown by Equation 2.22. This was because the impingement jet velocity at the surface decreased with increasing Z (as did the cross-flow velocity), thereby ensuring that there was little change in the surface jet to cross-flow velocity, even though the mean jet to cross-flow velocity increased as Z increased [20]. Equation 2.22 was mainly based on the results of Chance [56] who showed that it was valid for 2 < Z/D < 8 and for X/D values with no flow-maldistribution. The lack of dependence of Equation 2.22 on Z does not mean that there is no effect of Z or Z/D on the heat transfer as there will be the usual dependence of Nu_o on Z/D [33, 56].

Florschuetz *et al.* [142] found for a 10 row impingement array that the trailing edge heat transfer was between 20 and 41% below that of the leading edge for a range of geometries, most of which had flow-maldistribution. Kercher and Tabakoff [57] found the trailing edge heat transfer lower than the leading edge heat transfer by between 5 and 41% depending on the geometry. The greatest effect was for N = 12, X/D = 6.3 and Z/D = 3.9, which is similar to the geometry investigated by El-jummah *et al* [32, 46]. Dyban *et al* [109] varied N from 6 to 20 for 8 geometries without flow-maldistribution. The results showed a reduction of heat transfer from the leading to the trailing edge of between 14 and 59%. The greatest effect was for N = 20 with an X/D of 6. Obot and Trabold [47] investigated the impingement cooling geometry N = 12, X/D = 5.6 and Equation 2.22 predicts a 37% reduction in the heat transfer from the leading to trailing edge. For a Z/D of 6 the measured reduction was 34% in good agreement with Equation 2.22.

Bailey and Bunker [122, 132] presented results for impingement heat transfer with self-induced cross-flow. They used square array jets with most of the their work at X/D of 6 and 9 using only four rows of holes, only the results for X/D of 3 and 9 were presented in detailed. The X/D of 3 configuration was dominated by flow-maldistribution influence, as expected. However, in most of this work for a fixed impingement plate length, X/D was varied at constant D so that the number of rows of holes was decreased as X/D was increased. Any influences of cross-flow on the axial variation of heat transfer are strongly dependent on the number of upstream rows. Only in one geometry was the X/D of 9 tested with a hole size half that of the standard hole size and hence with twice the number of upstream rows of jet holes. They showed very little influence of axial distance on the heat transfer for an X/D of 9 with four rows of holes, but there was a more significant influence for 9 rows of holes. For the highest hole Re tested with 9 rows of holes, the trailing edge had 14% lower heat transfer than the leading edge which showed agreement with geometry of similar results by Florschuetz *et al*. [142] that showed 15% decrease in heat transfer. Their geometry with an X/D of 9 and Z/D of 5.5, Equation 2.22 predicts a 17% decrease in heat transfer and hence is a reasonable predictor of their results.

2.6.3.2 Jet Impingement Without Cross-Flow

Impingement/effusion cooling has no impingement air cross-flow in the gap as all the impingement air flows out of the effusion holes. The nearest impingement cooling geometry to this that is without the effusion jets present, is the four sided flow exit impingement gap cooling system [3, 19, 47, 63, 66, 135] that showed minimum cross-flow effects. This flat surface approximation is also often used in turbine blade cooling for the mid-chord region [91, 126, 209]. The minimum cross-flow effect for the four sided impingement jet flow exit geometry that often used Figure 1.7 (b) setup applied to the rig shown in Figure 2.3 (c or d) [3, 45, 47, 63, 134, 205], has been shown experimentally to be compatable with the impingement heat transfer in impingement/effusion cooling [4, 19, 45].

Previous experimental investigations of these impingement/effusion cooling schemes, for hot wall rigs gives the overall cooling effectiveness [33, 43]. Electrically heated isothermal metal wall impingement experimental rigs [7, 32, 63] shown in Figure 2.3 (c) [3, 5, 22, 25, 210], are the data base on which the present CHT CFD investigations are based. Similar work has been carried out with adiabatic walls [115, 211, 212]. The electrically heated Nimonic-75 metal walls for impingement cooling with a single flow exit have been predicted previously [25, 33]. In this case most applications used high G (Table 2.1), as for combustors the cooling is regenerative and the outlet air feeds either the dilution flow or for the lowest NOx, the lean burning flame stabiliser. For impingement/effusion cooling a low coolant mass flow is required and the optimum geometry will have the main pressure loss ΔP at the impingement wall, as this gives the highest impingement jet velocities [4, 44]. The effusion wall will have a low pressure loss with low jet velocities or low blowing ratio M. This requires for the same n (m^{-2}) or pitch X, larger diameter effusion holes than impingement holes or large X/D for the impingement wall and low X/D for the effusion wall [4, 23]. A constant impingement gap Z of 10mm has been shown as a practical Z for combustor wall impingement cooling [3, 5, 33], at an X/D of 11 this gives a Z/D of 7.25

[25]. Andrews *et al* [19] have shown that for an X/D of 11 the influence of Z/D on the surface averaged heat transfer was small over the range of Z/D 2 - 8.

2.6.4 Effect of Impingement Jet Hole Reynolds Number

The importance of Reynolds number Re (= V_jD/ν) on the design of GT impingement jet and impingement/effusion cooling systems cannot be overlooked, is critically the influenced of geometry as Table 2.2 shows for which the pressure loss ΔP depends. If the impingement jet hole and hole pitch are large, X/D will be small which implies incompresible jet flow but very high Re [132]. This cannot be use for either a regenerative (one exit) cool combustor or impingement/effusion cooling systems [4, 5, 25]. The requirements are low ΔP exit flow and high ΔP during combustion [5, 32] or high ΔP at the jet plate and low ΔP at the effusion plate [4]. The later is only possible with high jet holes X/D hence high pressure, this cannot give too high Re if a low G is used and is applicable to the present work design requirements for impingement/effusion cooling system. Table 2.1 shows the range of GT combustor coolant mass flux G (kg/sm^2bar) as a percentage of combustor air flow that were found by survey carried out by Andrews and Co-workers [41, 83, 99, 100]. These coolant mass flux G together with the air properties shown in Appendix C and jet hole plate geometrical variables, were shown to be significant in the determination of jet velocity V_j (m/s) and the Reynolds number hence the pressure loss on GT cooling systems. The critical Re for turbulent flow limit is > 2300 [49], however the jet turbulence in the impingement hole that has been shown above to be controlled by the jet Re, is largely irrelevant in the heat transfer as it is the impingement on the target surface that creates the intense turbulence that controls the heat transfer [22, 25, 46].

Table 2.1: Gas Turbine Combustor Coolant Mass Flux [99]

Types of Combustor	**Combustor Air Flow (%)** *25*	*50*	*75*	*100*
A	0.56	1.12	1.68	2.24
B	0.35	0.70	1.05	1.40
C	0.59	1.18	1.77	2.36
D	0.51	1.02	1.53	2.04
E	0.58	1.16	1.74	2.32
F	0.82	1.64	2.46	3.28
G	0.25	0.50	0.75	1.00
H	0.75	1.50	2.25	3.00

2.7 Review of Experimental Correlations

Impingement jet cooling heat transfer works are mostly presented along with accompanying experimental correlations, where Re, X/D and Z/D exponents were shown to be the important varied parameters as Table 2.2 shows. Investigators used the correlations to calculate certain measurements characteristics, which are helpful in the determination of some useful experimental quantities [67, 191] that concerns either flow variables or heat transfer related variables. In most cases, presentations are carried out using the dimensionless parameters with only few cases of dimensional ones and are not discuss here. The convenience of using dimensionless parameters are in two fold [56]: Firstly, it allows correlations of results in a more general form and secondly, it reduces the quantity of data that needs to be analysed.

The impingement jet cooling heat transfer experiments were shown to be mostly carried out using electrically heated walls as were discussed above. The steady state heat transfer from arbitrary material surface to an impinging air stream has always been adopted, this was in order to compute for the measurement of the power inputs of the jet system as Table 2.1 referenced. Neglecting the heat losses, the power input to a flat target wall is given by Equation 2.23 and the heat transfer coefficient (HTC) h is calculated from Equation 2.24 [25, 56] for $q'' \neq 0$. This relationship have been used in the determination of surface and locally average HTC for steady state lumped capacitance methods, which is a similar relation that was shown in Equation 2.2 that was earlier shown for the general convection heat transfer. In order to estimate the hole surface HTC for either the impingement or the effusion walls, Equation 2.25 can be applied [64, 158]. Equations 2.26 [91, 123] and 2.27 [196, 200] have been shown to give surface average HTC for $q'' = 0$ where the target surface were adiabatic wall.

$$Q = EI \quad and \left\{ q'' = \frac{Q}{A} \right. \tag{2.23}$$

$$h = \frac{q''}{T_s - T_\infty} \tag{2.24}$$

$$h_X = \frac{\pi h D L}{X^2} \tag{2.25}$$

$$h = \frac{q''}{T_w - T_{aw}} \tag{2.26}$$

$$h = \frac{q''}{T_{aw} - T_w} \tag{2.27}$$

Where Q is the heat transfer rate (W), E is the electric voltage (V), I is the current (A), q" is the heat flux (W/m^2), while T_s, T_∞, T_w and T_{aw} are the target top surface, air coolant, target hot wall and target top adiabatic temperatures (K).

In presenting the heat transfer correlation using dimensionless parameter, the Nusselt number Nu is most often used as the references of Table 2.2 showed. This Nu was shown to be related to Reynolds number Re, Prandtl number Pr, pitch to diameter ratio X/D and gap to diameter ratio Z/D, which is as shown in Equation 2.28 [56, 63, 164]. They showed that this Nu is generally correlated by Equation 2.29, which is similar to the general dimensionless Nu that was shown in Equation 2.5. Mills [49] showed that the Reynolds number Re exponent γ is usually assumed to be 0.8 as most values of Table 2.2 shows or by averaging all of those values. While, the Prandtl number Pr exponent m is usually assumed to be 0.3 for cooling or 0.4 for heating purposes.

$$Nu = f\left(\mathrm{Re}, \mathrm{Pr}, \frac{X}{D}, \frac{Z}{D}\right) \tag{2.28}$$

$$Nu = C\,\mathrm{Re}^{\gamma}\,\mathrm{Pr}^{m} \quad \left\{ where\; C = f\left(\frac{X}{D}, \frac{Z}{D}\right) \right. \tag{2.29}$$

The Colburn analogy shown in Equation 2.30 for a fully developed turbulent flow have been shown as a generally accepted correlation [67, 191] and used by several investigators for the condition where $10^4 \lesssim \mathrm{Re} \lesssim 10^9$ and $0.6 \lesssim \mathrm{Pr} \lesssim 60$. The Pohlhansen analogy of Equation 2.31 is used for Laminar related flows [48, 213].

$$Nu = \frac{hL}{k_f} = 0.0292(\mathrm{Re})^{\frac{4}{5}}(\mathrm{Pr})^{\frac{1}{3}} \tag{2.30}$$

$$Nu = \frac{hL}{k_f} = 0.324(\mathrm{Re})^{\frac{4}{5}}(\mathrm{Pr})^{\frac{1}{3}} \tag{2.31}$$

Where L is the target wall length (m) and k_f is the fluid thermal conductivity (W/m^{2}K). The characteristics length for a non-circular duct is usually replaced by the hydraulic diameter $D_H = 4A_C/\mathscr{P}$, where Ac is the cross-sectional area (m^2) and $\mathscr{P}$ is the perimeter (m) or for a circular pipe (jet orifice or hole) the diameter is used [49].

The effects of impingement cooling for geometrically similar configurations are seen by the arrangement of non-dimensional groups and each one parameter form part of this group for a purpose. For example Pr is included in the correlation to allow calculations for fluids other than air or for the fluid at significantly different temperatures [165]. The Re is the major determining parameter to know the type of fluid flow as either turbulent or laminar flows in any case [48, 49]. Hence, the Reynolds number is used as a criterion for the selection of relevant equation for the calculation of HTC h. Equation 2.32 shows how the Pr can be determined, while Re is found from Equation 2.13. The used of Stanton number (St) of Equation 2.33 has been shown to give analogous relationship between heat and mass transfer [14, 49, 106, 107].

$$\mathrm{Pr} = \frac{\mu C_p}{k_f} \tag{2.32}$$

$$St = \frac{Nu}{\mathrm{Re}\,\mathrm{Pr}} \tag{2.33}$$

The effect of impingement air jet velocity or Reynolds number on heat transfer for a given plate hole number/unit surface area A_f, (or X/D) and at range of fixed Z/D with negligible cross-flow interference was shown to be correlated by Equation 2.34 [56, 63, 172]. Andrews *et al* [61] showed that the generally correlated dimensionless impingement heat transfer relation is given by Equation 2.35 and was based on Equation 2.29 above.

$$Nu\,\mathrm{Pr}^{-\frac{1}{3}} = f\left(\frac{X}{D}, \frac{Z}{D}\right)\mathrm{Re}^{\frac{4}{5}} \tag{2.34}$$

$$Nu = \frac{hD}{k_f} = C\left(\frac{X}{D}\right)^{a}\left(\frac{Z}{D}\right)^{b}\mathrm{Re}^{\gamma}\,\mathrm{Pr}^{\frac{1}{3}} \tag{2.35}$$

They showed that the exponents ‘a’ and ‘γ’ as also shown in Table 2.2 could be determine over a range of impingement gap Z. They also investigated the dependence of the exponent γ on X/D for a range of Z and found that the influence of X/D on impingement heat transfer, is likely to be correlated by Equation 2.36 which represents heat transfer coefficient and Equation 2.37 for a dimensionless Nusselt number. These correlations were mainly for the range Z between 2 to 12 mm.

$$h = 75\left(\frac{X}{D}\right)^{0.64} G^{0.72} \tag{2.36}$$

$$Nu = 0.29\left(\frac{X}{D}\right)^{-1.08}\mathrm{Re}^{0.72} \tag{2.37}$$

Equations 2.38 (for HTC) and 2.39 (for Nu) are the correlations for fixed Z/D = 4.5 at a fixed X = 15.24 mm or $n = 4306/\mathrm{m}^2$ by Andrews and Hussain [21] and Andrews *et al* [61], they showed by this relation that impingement heat transfer is a strong function of both impingement mass flux G and X/D. Andrews and Hussain [20] presented their correlation using Equation 2.40 for which the Nu and Re were based on the impingement hole size D and Z/D < 2. This showed that impingement heat transfer increases due to cross-flow, even with flow-maldistribution.

$$h = 63\left(\frac{GX}{D}\right)^{0.72} \qquad (2.38)$$

$$Nu = 0.28\left(\frac{X}{D}\right)^{-1.0} \mathrm{Re}^{0.72}\,\mathrm{Pr}^{0.33} \qquad (2.39)$$

$$Nu = 0.0185\left(\frac{Z}{D}\right)^{-0.2} \mathrm{Re}^{0.8}\left(\frac{V_c}{V_j}\right)^{0.8} \qquad (2.40)$$

Heat transfer correlation for a range of Z/D > 2 and for a mean value of exponent b evaluated at –0.14 [3, 21] is as shown by Equation 2.41, this was compared with reviewed data and found different exponent b values for Z/D and this is also shown in Table 2.2.

$$Nu = 0.0252\,\mathrm{Re}^{0.72}\,\mathrm{Pr}^{0.33}\left(\frac{Z}{D}\right)^{-0.14} \qquad (2.41)$$

Heat transfer estimates on the effects of cross-flow was shown by Equation 2.21 and has been shown to be based on the work by Chance [56], which is for Z/D between 2 to 8, 0.012 < A_f < 0.07 and I_c < 1.8. This implies that the correlation was a function of the impingement plate design that was independent of Z and the work by Abdul Husain *et al* [43] for an impingement hole diameter of 2.33 mm, where the reduction in heat transfer was due to cross-flow showed reasonable agreement with their measured data.

Overall cooling effectiveness η defined by Equation 2.42, was used to determine the influence of cross-flow along the impingement gap for the axial variation of the centreline wall temperature T_w [43]. This was for the high temperature test facility (combustion rig) cooling effectiveness measurements. Cooling effectiveness of 0.7 was generally considered to be adequate for combustor wall cooling [189]. In a similar work, Abdul Husain and Andrews [5] determined the gas temperature T_g to the cooling air temperature T_∞ ratio T_g/T_∞, the situation where effect of radiation heat transfer was negligible and the hot gas duct walls were air-cooled externally, while the gas flow rate was controlled to attain equilibrium wall temperature as the test section. Appendix B shows how this is theoretically estimated, which shows to be related to the temperature gradient that exists in the cooling air on the target plate. A similar effect was also recently shown using a representation where the gas temperature at the numerator was adiabatic wall temperature and that in the denominator as jet temperature [152] as Equation 2.43 shows. Andrews et al [4, 19, 23] showed that the heating of the impingement jet wall by the reversed flow jet could be related to Equation 2.44, for which this CHT CFD work will be using to predict impingement jet surface heating in the present GT cooling systems.

$$\eta = \frac{T_g - T_w}{T_g - T_\infty} \tag{2.42}$$

$$\eta = \frac{T_{aw} - T_w}{T_j - T_\infty} \tag{2.43}$$

$$T_Z = \frac{(T_I - T_\infty)}{(T_m - T_\infty)} \tag{2.44}$$

2.8 Enhanced Impingement Heat Transfer

The use of obstacles to augment heat transfer in turbine blade cooling channels is common and the typically used obstacles are the ribs wall, rectangular pin, dimples, pin-fins or cylindrical pedestals, bumps and perforated ribs. However, the literature on the addition of various turbulators in the impingement gap shows that enhancing the already high impingement heat transfer is quite difficult and typically a 20% enhancement would be a good performance. Andrews *et al* [194], Abdul Hussain *et al* [214], Trabold and Obot [35], Spring *et al* [133] and Taslim and Fong [215] have experimentally investigated ribs walls 90^o to the impingement jet which flows across the ribs.

Spring *et al* [133] also used CFD predictions (with SST model) that showed near 10% agreement with their experimental average *h* and over 50% local. But their target wall conditions differ from that measured, the experiment was adiabatic and CFD was constant temperature and their argument was based on the small difference between coolant and wall temperature. Also the experiment excludes the obstacle heat transfer in terms of Nu, while CFD includes the obstacle walls. For the in-lined ribs arrangement heat transfer degradation due to increased cross-flow effects, but the staggered arrangement 20 - 50% enhancement downstream from row 5 was recorded.

Trabold and Obot [35] investigated ribbed wall cross-flow for two jet exit flows and found better enhancement for the maximum jet exit flow. They showed that heat transfer downstream degradation due to induced cross-flow and downstream enhancement, which was based on X/D effects. Taslim *et al* [216] combined radial ribs with bumps for combined impingement jet and film cooling. Their enhancement due to the bumps was in the presence of film cooling holes. They showed 65% enhancement *h* in the present of showerhead film cooling holes and 35% enhancement, for only the conical bumps and without film holes. Hoefler *et al* [[137] investigated ribbed surfaces using staggered oblique impingement jets that were inclined with the ribs aligned to the jets. Heat transfer enhancement from 12 - 27% was recorded at 25% surface increment. Impingement heat transfer enhancements have also been used on heated cubes using a numerical approach for a range of Re [217], with the flow aerodynamics predicted.

The used of ribbed walls has been applied by several authors to gas turbine cooling applications [218-227]. Wang *et al* [224] carried out investigation using inclined ribs configuration in a film cooling system and also predicted the flow and thermal fields using 2D CFD. Chung *et al* [221] also investigated inclined ribs that intersected in a duct for internal cooling of GT turbine blades. This zig-zag W configuration geometry was predicted in the present work.

Andrews *et al* [194] investigated ribs parallel to the impingement jet cross flow that gave a small increment in heat transfer, as compared to smooth surface. In the downstream section of the crossflow duct the enhancement at low G was as high as 30% for the best rib geometry, but for surface averaged heat transfer was only a 10 - 20% enhancement at low G and no enhancement at high G. They found that there was improved enhancement if the ribs were slotted and of greater height relative to the duct, this gave a rectangular pin-fin geometry and this is modelled in the present work.

Shizuya and Kawaike [228] investigated a wide range of enhanced impingement cooling configurations and the most effective with a 50% improvement in heat transfer compared with a smooth wall, was the use of cylindrical pin fins in a square array. They investigated X/D of 4 and 8 and found the same 50% enhancement for both geometries. They also investigated combined fins in the crossflow direction with cylindrical pins in the crossflow of each finned passage, These geometries also had a 50% enhancement of the heat transfer. This data was for 20 rows of impingement holes and was the surface average effect. At the X/D of 4 there was a flow maldistribution effect with the heat transfer first decreasing and after row 10 increasing. For an X/D of 8 there was no flow maldistribution and the enhanced heat transfer still showed a deterioration of heat transfer with distance, but with the downstream portion of the passage increasing in heat transfer, whereas for the smooth wall the heat transfer continued to decrease with distance along the gap. For the X/D of 8 they used 6 pins per impingement hole and at an X/D of 4 they used 2 pins per impingement hole. These configurations are the best in the literature for enhanced impingement heat transfer and the use of more obstacles than impingement holes was a key feature of this work. In the present work there was only one obstacle per impingement hole or one row of impingement holes per rib passage.

Azad *et al* [229] also investigated impingement jet cooling heat transfer enhancement using pin-fins for a 4 × 12 holes for three coolant mass flows and with five pins serving each jet flow. This work used the same approach of a rectangular pin as used by Andrews *et al* [210] for one jet flow per one pin and design such pin-fins of Azad *et al* [229]. The use of several pin-fins per impingement hole was first shown to be a good design for enhanced impingement heat transfer by Shizuya and Kawaike [228], as discussed above.

Pin-fins in duct flow have been shown to give a good enhancement factor to the plane duct heat transfer and are used gas turbine blade internal cooling systems [230-233]. Sparrow *et al* [232] compared in-line and staggered pin-fin arrangements and found that the in-line arrangement gives more heat transfer than the staggered one. Metzger *et al* [233] investigated 10 row of staggered arrays of short pin-fins in a rectangular duct that covered the height of the duct. They showed that the heat transfer in the centre of the duct was higher than both upstream and downstream. They also showed that a small number of pins gave the highest heat transfer enhancement. Al-Dabagh and Andrews [230] also studied staggered array of pin-fin with a 50% duct flow blockage. Armstrong and Winstanley [234] reviewed heat transfer enhancement using staggered arrays of pin-fins. They found that duct flow Re and pin height were the most important design variables for heat transfer enhancement.

Lee *et al* [235] showed that heat transfer enhancement was effective using a perforated plate placed at the centre line of the impingement gap. However, this is not very practical for gas turbine applications as it increases the pressure loss and the cooling wall overall thickness. Abdul Hussain and Andrews [214] showed using cross-flow ribs with holes or grid plate type ribs, gave a better impingement heat transfer than plane ribs, for a lower overall pressure loss.

A recent development in enhanced heat transfer is the application of dimples in the target surface [115, 204, 205, 236-239]. Xie *et al* [236] studied three different dimple configurations and found that the optimum heat transfer was for a dimple depth to dimple diameter δ/D_o of 0.3, which was the largest they studied. The present work used this ratio with the impingement geometry of Andrews *et al* [210] to give a prediction using CHT CFD of the potential effectiveness of dimples compared with other enhancement geometries.

Ligrani *et al* [240] and Ligrani [241] reviewed heat transfer enhancement as applied to internal cooling of turbine components. They found that ribbed wall obstacles gave a higher heat transfer enhancement. In the present work on enhanced impingement heat transfer seven different obstacles walls, were modelled with the same impingement jet cooling.

Table 2.2: Review of Impingement Jet Investigation Designs for Range of Reynolds Number

Author	***N***	***X/D***	***Z/D***	***Re × 10^3***	***a***	***b***	***γ***
Huang [164]	1 - 7	0 - 20.0	1.0 - 12.0	1 - 10	-	-	0.85
Andrews *et al* [61]	100 & 625	4.7 - 10.7	0.6 - 13.5	0.2 - 42.4	-1.08	-	0.72
Sparrow *et al* [102]	19	2.0 & 2.5	NA	2 - 20	-	-	0.48
Behbahani & Goldstein[200]	18	4.0 & 8.0	2.0 - 5.0	5 - 15	0.6 - 0.7	-	0.78
Metzger & Korstad [98]	10	2.5 - 5.0	2.0 - 6.7	2 - 6	-	-	-0.34
Andrews & Hussain [3]	100	11.0 & 12.9	0.56 - 36.0	1.2 - 23.6	-	-0.14	0.72
Andrews *et al* [20]	100	7.1	0.5 - 4.3	1 - 13	-	-0.20	0.80
Tabakoff & Clevenger [165]	16	2.5 - 12.5	1.0	5 - 10	-	-	-
Hollworth & Berry [63]	16	10.0 - 25.0	1.0 - 25	3 - 35	-	-0.15	0.80
Chance [56]	36	5.9 - 14.3	2.0 - 8.0	9 - 30	1.02	-0.13	0.74 - 0.88
Koopman & Sparrow [104]	5	4.0 & 6.7	2.0 - 10.0	2.5 - 10	-	-	-
Florschuetz *et al* [142]	15 - 30	5.0 - 15.0	1.0 - 3.0	5 - 50	-	0.09	0.61
Metzger *et al* [140]	15 - 20	5.0 & 10.0	1.0 - 3.0	5 - 20	-	-	-
Perry [170]	1	-	11.0 - 19.0	7 - 30	-	-	0.70/0.80
Hollworth & Cole [64]	20 - 40	4.0 & 8.0	1.0 - 3.0	2 - 25	-	-	0.78
Dyban *et al* [109]	49 - 441	6.0 - 12.0	1.0 - 16.0	1.1 - 17	-	-0.65	0.80
Goldstein & Behbahani [171]	1	3.0 & 6.0	6.0 & 12.0	34 - 121	1.3/1.14	-	0.60
Saad *et al*, [150]	12 - 48	2.0 - 4.0	1.0 - 3.0	3.4 - 21.5	-	-	-
Freidman & Mueller [66]	4 - 17	2.8 - 10.7	4.5 - 9.0	-	-	-	0.72 - 0.83

Table 2.2 (cont'd)

Andrews & Hussain [62]	100	4.7 & 12.9	0.56 &13.5	0.4 - 24.7	-	-	-
Andrews & Hussain [21]	100	2.0 - 21.5	4.5	4 - 20	-1.0	-	0.72
Kercher & Tabakoff [57]	16 - 256	3.1 - 12.5	1.0 - 4.8	0.3 - 30	-	0.09	0.85 - 0.95
Obot & Trabold [47]	16	4.7 - 9.0	2.0 - 16.0	1 - 21	0.6	-0.22	0.77
AbdulHusan & Andrews[5]	100	1.9 - 11.0	1.2 - 7.3	~ 3 - 16	-	-	-
Bailey *et al* [122]	30	4	2.3	170 - 280	-	-	-
Rhee *et al*. [242]	25	6.0	2.0	10	-	-	-
Facchini & Surace [123]	95 - 165	10.0&12.0	3.75 & 5.0	5.9 - 11.5	-	0.44	0.57
Goodro *et al*. [243]	28 - 180	8.0 & 12.0	3.0	8.2 - 30.5	-	-	-
Taslim & Fong [215]	11 & 12	1.0 - 5.0	2.7	10 - 35	-	-	-
Bailey & Bunker [132]	12 & 520	3.0 - 9.0	1.3 - 5.5	14.9-65.1	-	-	0.68
Miller *et al* [244]	45	5.0 & 15.0	6.0 - 10.0	7.5 & 15	-	-	0.80
Andrews *et al* [45]	9 - 625	9.53 - 11.0	0.62 - 20.1	2 - 19	-	-	0.72
Taslim & Khanicheh [145]	9	4.05	2.8	8 - 48	-	-	-
Hrycak [167]	9	1.7 - 8.0	1.5 - 8.0	2.8 - 28	-0.16	-0.22	0.63
Xing and Weigand [134]	81	5.0	1.0 - 5.0	15 - 35	0.09	-	0.80
Xing *et al* [135]	77 & 81	5.0	1.0 - 5.0	15 - 35	0.09	-	0.80
Spring *et al* [245]	45	Irregular	3.0 - 5.0	17 & 34	-	-	0.67
Taslim & Bethka [146]	5	2.8	2.8	8 - 48	-	-	-
Chambers *et al* [127]	19	±1.8 & 4.4	-	10 - 35	-	-	-

Table 2.2 (cont'd)

Van Treuren *et al* [91]	40	8.0	1.0	3.7 - 34.4	-	-	-
Van Treuren *et al* [126]	38 & 40	8.0	1.0 - 4.0	10 - 40	-	-	-
Huber & Viskanta [112]	9	4.0 - 8.0	0.25 - 6.0	3.5 - 20.4	-0.73	-0.12	0.71
El-jummah *et al* [25]	100 - 625	4.7	1.5 - 7.7	3.9 - 19.3	-	-	-
El-jummah *et al* [22]	100	1.9 - 11.0	1.2 - 7.3	3.9 - 22.9	-	-	-
El-jummah *et al* [46]	100	4.7	3.1	1.7 - 9.7	-	-	-
Goldstein *et al* [212]	1		2.0 - 12.0	61 - 124	-	-	0.76
Zimmer *et al* [246]	55	3.0	3.0 & 5.0	1.1 - 8	-	-	-
Yamane *et al* [247]	9	6.0	2.0 - 6.0	~ 5	-	-	-
Trabold & Obot [35]	16	4.7 - 9.0	2.0 - 16.0	1.3 - 21	-	-	-
Sparrow *et al* [102]	1	NA	5 - 15	4 - 25	-	-	0.69/0.77
Gardon and Akfirat [144]	8	16.0 - 64.0	4.0 - 16.0	0.5 - 50	-	-0.62	058/0.62
Gauntner *et al* [67]	334 & 481	6.3 & 7.4	2	1 - 10	-	-	0.63
Parsons *et al* [248]	120	5.0	4.0	5 & 10	-	-	-
Hollworth *et al*, [7]	16	5.0 - 20.0	0.5 - 20.0	3.5 -25	-	-	-
Hilgeroth [65]	9	3.5 - 12.5	2.0 & 6.3	1 - 10	-	-0.20	0.75
Schueren *et al* [131]	28	3.0 - 6.0	2.6 & 4.0	10 - 75	-	-	-
Lee *et al* [151]	21 - 100	5.0 - 12.0	1.5 - 8.0	8 - 50	-	-	-
Kumada and Mabuchi [59]	1	-	2.0 - 40.0	13 - 15	-	-0.62	0.63/0.80

a, b and *γ* are X/D, Z/D and Re exponents, respectively and NA implies not applicable

2.9 Review of Heat Transfer Cooling CFD Investigations

Analytical solutions have been a major tool in evaluating jets impingement design problems. The basis for evaluating jets impingement for paper drying have been provided based on the boundary-layer concept and dimensional considerations, where the heat transfer from a solid surface under air impingement was considered [213]. They looked at the dynamics of air jet impingement heat transfer for both single jet and multiple jets. Myers *et al* [193] developed an analytical heat transfer solution by applying integral techniques to the thermal boundary layer equations for incompressible turbulent jets flow. Their basic heat transfer calculations was for a step wall temperature distribution that was also extended to arbitrary heating conditions, the relation governing energy and continuity equations were here considered.

The influence of turbulence heat transfer enhancement across boundary layer surfaces by impingement jets have been shown to form part, in characterising heat transfer alongside the velocity and position dependent boundary layer thicknesses [192, 249, 250]. Debruge and Han [251] analytically modelled a two-dimensional channel formed by a solid wall (blade surface) and a porous plate (injection source) for cooling turbine blades internally. This model was used to analysed the two dimensional flow and temperature distribution based on the assumptions that a steady incompressible fluid flow and temperature of the porous plate were equal to coolant temperature, where axisymmetric was also assumed. Stoy and Ben-haim [166] developed a one-dimensional simple equation using the basic conservation equations to predict jet trajectory, average jet properties and impingement point for spatially variable cross-flow velocity profiles, their results showed that this analysis gave good predictions. These basic conservations equations have been shown to provide turbulence model CFD equations [250, 252-254] that solves complicated cases of engineering concern.

Recently, the used of CFD in predicting the aerodynamics and heat transfer cases of GT cooling complex geometries have been employed [255-257], which helps to overcome the slowness by analytical model. The CFD solver have been shown to evaluate jets impingement, effusion and impingement/effusion cooling design problems [4, 6, 12, 22, 25, 32, 33, 46, 96, 122, 145, 146, 185, 186, 208, 209, 242, 258-262], whereby the requirement for validation [263, 264] with measured data as an important step in verifying the turbulence models chosen were seen to be achievable. Often, gas turbine cooling CFD investigators uses Reynolds average Navier-Stokes equations (RANS) models [257, 265-272], especially the two equation model [25, 122, 208, 265]. This is because the turbulence in the GT cooling region is considered to be isotropic, typically in the complex stirred flow of the impingement gap. These RANS turbulence models also incorporate solution of problems base on the boundary layer concept where heat transfer and aerodynamics related problems are solve by the wall function or near wall treatment approach [252, 257, 265, 267, 268]. For example, the influence of pressure gradient on boundary layer attachment, showed that an adverse pressure gradient gives rise to flow separation [25, 265] which requires a wall function approach. While locally heat transfer solution near the wall were seen to be predominantly resolved by a low Re near wall treatment approach [122, 266].

Previous CFD investigations of impingement cooling have not been primarily directed at the cross-flow effects and have not used a large number of upstream holes, apart from work on this configuration by El-jummah *et al* [22, 25, 32, 33, 46] and Andrews *et al* [273]. The complex recirculation in the impingement gap and the interaction between adjacent jets on the target surface presents a challenge for CFD predictions. The flow distribution and the HTC *h,* on the liner of gas turbine combustor for jets impingement and cross-flow were predicted by Bailey *et al* [122]. Both structured [12, 22, 25, 217, 219, 262, 274-276] and unstructured [227, 266, 277-280] or hybrid [133, 281] grids have been used depending on the complexity of the geometry. The use of steady state isothermal conditions that were employed experimentally [3, 61, 104, 142] were also applied for the CFD GT cooling analysis [33, 122, 208]. Usually cooling air is at ambient or sea temperatures ~300K, with a range of inlet velocities that determines the hole Reynolds number Re [22, 25, 282]. CFD simulation enables the prediction of the flow fields that characterizes air jet impingement and impingement/effusion cooling [6, 32, 260, 266, 275]. The work of Taslim and Rosso [208] shows particle tracer air flow patterns within the impingement gap, this technique was also used by El-jummah *et al* [32]. Heat transfer characteristics were also shown to be predicted with the aids of conjugate heat transfer (CHT) applied in CFD [22, 25, 32, 33, 46]. The present CFD work, apply the use of CHT to visualize the heated reversed jet flow that experimentalist anticipate effects on the coolant jet and the jet plate, work by El-jummah *et al* [25] showed some of this effects for impingement jet cooling using dimensionless temperature contours.

This work present experimental results and CHT CFD predictions using hot metal walls for classic impingement and impingement/effusion cooling geometries. Most work in the literature on impingement cooling uses adiabatic heat transfer techniques [6, 91, 102, 106, 122, 126, 132, 135, 143, 200, 283]. There is a dearth of experimental data to compare and validate CHT CFD predictions. Some researches on this topic in gas turbines have no experimental validation due to this lack of hot rig metal wall experimental data [284-286]. Sometimes inappropriate wall materials were used, such as Aluminium [287], so that there are no thermal gradients to predict. The use of radiation based wall temperature measures in hot test rigs can result in poor agreement with CHT CFD, possibly due to emissivity calibration problems, as the emissivity is a function of temperature [288, 289]. When imbedded thermocouples are used as in the work by El-jummah *et al* [25] that has shown evidence of agreements, it indicates that for metal turbine blade studies, agreement between CHT CFD predictions and metal temperature measurements [290, 291] are possible. For flat wall effusion cooling that have experimental hot test result for Nimonic-75 walls with imbedded thermocouples, good agreement have been shown [96, 186, 259], which this present CHT CFD will be using applied to impingement and impingement/effusion cooling heat transfer systems.

CHAPTER THREE

CFD METHODOLOGY

Chapter 3

CFD Methodology

3.1 Introduction

Numerous gas turbine (GT) projects on both experimental and numerical investigations have been carried out on jet impingement, effusion and impingement/effusion cooling heat transfer, as Chapter 2 showed. A number of useful techniques have been shown in attempting to fully develop geometries that could be acceptable and feasible in protecting the life of both GT combustor and turbine blade walls. However the problem of these air jets associated cooling heat transfer, is still not completely understood for especially the aerodynamics influence of cross-flow, reversed jets flow and their interaction effects, short holes aerodynamics and the influence of wall conduction as a results of convective effects. The purpose of this work is to use CHT CFD to understand these complex flow aerodynamics as they relates to GT cooling heat transfer solutions, whereby higher grid resolution and a careful choice of turbulence models are required.

3.2 Conjugate Heat Transfer CFD Analysis

Generally, heat transfer coefficient (HTC) h is the influence of convection, which result from fluid motion as shown by Equations 2.4, 2.24, 2.25 or 2.30 of Chapter 2 and is usually a function of temperature gradient dT/dx [49, 264] of Equation 2.1 (also 2.23). The impingement jet, effusion and impingement/effusion heat transfer cooling are typical cases of forced convection heat transfer, as the air flow through the plenum is a compressor airflow [3, 5, 22, 25, 46] hence $h = f(\Delta T)$ and is also related to the heat flux q" and the thermal conductivity $k_s = k_f$ for a solid/fluid interface. In ANSYS Fluent CFD solver [264], a wall and wall-shadow is created automatically (implies coupling) after reading a mesh file and by default energy is balanced between the two sides of the walls, this allow one to specify different thermal conditions on each side. Implying that the heat flux which is strongly dependent on flow velocity and fluid properties is coupled to the fluid flow solution found from the conservation equations, whereby the fluid properties changes with temperature. Therefore for a discrete steady state solution, by defining a specified area (A or X^2) of interest on the coupled wall is determined by using the surface average HTC given by Equation 3.1.

$$\bar{h} = \frac{1}{A}\int h dA \tag{3.1}$$

3.3 CFD Codes

Despite several investigations both experimentally and numerically on GT cooling techniques, the needs to improve on the wall cooling of the GT components with adequate design performance is still necessary [255, 256, 292], especially with the requirement for higher efficiency gas turbine systems [1, 10]. The advents of new meshing tools, typical of the present ICEM CFD code that have variable grid resolution schemes and the coupled usage of CFD solver like the present ANSYS Fluent code [22, 25, 32, 33, 46, 264], computational validations with experimental data are possible [263]. However, the use of CFD simulation software is highly dependent on the choice of turbulence model for high velocity air jets flow that have been characterized by turbulent flow [54, 73, 78, 93, 95, 250, 252, 265]. The better choice and use of these turbulence models give the CFD user final conclusions that are made based on the type of engineering applications [42, 264, 266, 293], implying that a wise selection of turbulence model available in the CFD codes is important. Therefore, in order for the CFD engineer to effectively use these codes, it is necessary to also understand the basic principles of turbulent flow [294, 295].

3.3.1 Turbulent Flow

Turbulence is a flow feature that is described by a chaotic state of motion, by which the velocity and pressure of the flow continuously change with time and is within a bounded region of this flow [292, 294]. Thus, turbulent flow is characterised by velocity fluctuations and highly disordered motion [295] and is generally distinguished by unsteadiness, irregularity, large Reynolds number Re, diffusivity, 3D vorticity fluctuations and dissipation in its nature of flow - generally contains eddying motion over a wide range of scales or sizes. These multiple factors makes the understanding of turbulence for industrial related applications a difficult tasks, as one problem leads to the solution of many other coupled problems of turbulent flow which this work is also concern with. The statistical descriptors of the turbulent flow include [292, 293]: Time average or mean (mean velocities, mean pressures, mean stresses etc.), variance and root mean square (r.m.s) that indicates the spread of fluctuations, turbulence kinetic energy, moment of fluctuating variables, higher order moment, correlation functions (time and space) and probability density function (PDF) - the likelihood for the random variable to take effect. The particle velocity of turbulent flow is decomposed into its steady mean value u with a fluctuating component u' as shown by Equation 3.1 [293] and is called Reynolds decomposition.

$$U(t) = u + u'(t) \tag{3.1}$$

Equation 3.1 shows that the particular properties of turbulent flows includes: The velocity field U (x, t), which is 3D, time dependant and random [292, 293].

The chaotic behaviour of turbulent flow leads to the motion of every eddy - the rotational flow structures that are grouped into large and small scales (or sizes) to be unpredictable. Larger eddies are shown to be **anisotropic** - different fluctuations in different directions, while the smaller eddies at high Re are shown to be **isotropic -** equality in all direction [252, 294, 295]. Hence turbulent flow has an essential feature that the fluid velocity field varies significantly and irregularly, in both position and time and this velocity fields are not repeatable in either a whole or in part of the flow domain. Turbulent flow is shown to be affected by the influence of physical properties such as thermal expansion, acceleration, friction and buoyancy thereby reducing turbulence and impairing heat transfer [296]. This shows that with good engineering judgement of these turbulent flow physics added to available computer resources [293], turbulence modelling that can resolved a projected problem at hand can be achieved. The requirements are accuracy of the project domain, turnaround time and the near-wall treatments of the surface boundary layer, which also relied on the chosen turbulence model [265].

3.3.2 CFD Governing Equations for Steady Flow

The conservative laws that are applied in computational fluid dynamics (CFD) in order to estimate field variables are the Reynolds-averaged mass, momentum and energy equations for steady incompressible flows [54, 249, 257, 264-266, 269-271, 293, 297] and are shown by Equations 3.2, 3.3 and 3.4, respectively and used the summation convention. Usually for a 3D model, these similar equations are also applied in the y and z directions as shown for x and with i and j coordinates.

$$\frac{\partial U_i}{\partial x_j} = 0 \tag{3.2}$$

$$\rho U_j \frac{\partial U_i}{\partial x_j} = -\frac{\partial P}{\partial x_i} + \frac{\partial}{\partial x_j}\left[\mu\left(\frac{\partial U_i}{\partial x_j} + \frac{\partial U_j}{\partial x_i}\right) - \rho\overline{u_i' u_j'}\right] \tag{3.3}$$

$$\rho U_j \frac{\partial T}{\partial x_j} = \frac{\partial}{\partial x_j}\left[\frac{\mu}{\mathrm{Pr}}\frac{\partial T}{\partial x_j} - \rho\overline{T' u_j'}\right] \tag{3.4}$$

The mean components includes; pressure P, temperature T and velocity U, while the fluctuating components are; temperature T' and velocity u'. The fluid density, dynamic viscosity and the Prandtl number are denoted by ρ, μ and Pr, respectively and the Reynolds stresses or turbulent shear stress are shown as $-\rho\overline{u_i' u_j'}$, while the turbulent heat flux is represented by $-\rho\overline{T' u_j'}$. In order to calculate the specific turbulence model for closure, the

Reynolds stresses $-\rho\overline{u_i'u_j'}$ of Equations 3.5 and 3.6, are found from either the Eddy viscosity or Reynolds stress transport models [264-266, 293, 297] and are shown below:

Eddy viscosity model (EVM):
$$-\rho\overline{u_i'u_j'} = \mu_t\left(\frac{\partial U_i}{\partial x_j} + \frac{\partial U_j}{\partial x_i}\right) - \frac{2}{3}\rho k\delta_{ij} \qquad (3.5)$$

Reynolds stress transport model (RSM):
$$-\rho\overline{T'u_j'} = \frac{\mu_t}{\sigma_t}\left(\frac{\partial T}{\partial x_j}\right) \qquad (3.6)$$

In Equation 3.6, $-\rho\overline{u_i'u_j'}$ are solved directly and isotropic turbulence assumption is invalid.

Where μ_t is the turbulent eddy viscosity, δ_{ij} is the Kronecker delta, $k = u_i'u'/2$ is the turbulent kinetic energy (TKE) and σ_t is the turbulent Prandtl number whose value depends on the selected turbulence model. The Eddy viscosity model is obtained from empirical formula as a function of TKE and turbulent length scale (TLS) ℓ, while turbulent heat flux $-\rho\overline{T'u_j'}$ is found based on the simple gradient diffusion hypothesis (SGDH). Generally these models are called the Reynolds-average Navier-Stokes (RANS), which is based on the procedures of the mathematical formulation described above. The applicability of these turbulence models on gas turbine hot surfaces cooling will be investigated in this research work as they are found in ANSYS Fluent commercial CFD solver [264].

3.3.3 Turbulence Models

Flow characteristics in a domain of interest makes turbulence problems difficult and to approach certain solutions seems difficult, for example irregularity results to the use of statistical approach to solve turbulence problems [292, 293]. The ultimate objective in the study of turbulent flows is to obtain a tractable quantitative theory or model that can be used to calculate quantities of interest and practical relevance [252, 295]. This brings to the concern in predicting the mean flow behaviour that have been a major one in the engineering sector, implying that turbulence cannot be ignored. Hence fluctuations that influences extra Reynolds stresses or turbulent shear stresses (shear force/unit area) $R_{ij} = \rho\overline{u_i'u_j'}$ due to eddy motion of fluid particles and the time average of the product of the fluctuating velocity component on the mean flow can be resolved [252].

In a turbulent flow simulation - direct numerical simulation DNS and large eddy simulation LES, equations are solved for time dependent velocity field, which represents the velocity field U (x, t) for one realization of turbulent flow in the Navier-Stokes (N-S) equation [252, 264, 293]. While in turbulence model - simulation and modelling where no distinction is required, equations are solved for some mean quantities (mean velocity, Reynolds stress or turbulent stress, turbulent kinetic energy (TKE), dissipation of TKE, etc.) in the modified Navier-Stokes or the RANS equation. Computations of the vast majority of turbulent flow are supported base on the procedures of the RANS equation described above.

The behaviour, the quantitative description, the fundamental physical processes and the equations for constructing model behaviour of turbulent flows, are the basic principles that requires adequate attention when dealing with problems involving turbulent flow [294]. In order to adequately model any turbulent flow calculations, there must be sufficiently accurate and general description of the turbulence [293]. This shows that the standards used to evaluate a turbulence model in a general-purpose CFD code are [264, 293]: Level of description, completeness, cost and ease of use, range of applicability and accuracy. These listed characteristics indicates that there is no one ‘best’ model [42, 295], but variety of models are available for application in numerous turbulent flow problems. The present impingement air jet and impingement/effusion cooling heat transfer investigations critically follow these basic principles [22, 25, 32, 33, 46] with reasonable strictness.

3.3.4 Types of Turbulence Models

The models used in calculating the properties of turbulence are [264, 295]:

1. The RANS models
- Turbulent Eddy viscosity models (EVMs)
    i. Spalart - Allmaras
    ii. k - ε model (Standard, RNG and Realizable)
    iii. k - ω model (standard and SST)
    iv. Algebraic Models (uniform turbulent viscosity and mixing-length models)
- Reynolds stress transport models (RSM)
2. Large - eddy - simulations (LES) models
3. Models based on the probability density function (PDF) of velocity

Turbulent flow CFD solutions are only as good as the appropriateness and validity of the turbulence model used in the calculations [42, 255, 256, 265]. Assigning adequately the boundary conditions (BC) is also an important aspect of the turbulence properties [42, 293]. Two most important one are the inlet and outlet BCs, properties specified at the outlets are not used unless reverse flow is encountered at the outlet. The ultimate objective of the turbulent flow calculation is to obtain tractable quantities of interest and practical relevance, the increasing power of digital computers are used to achieve this objective [295]. Presently, all commercially known turbulence models have limitations, but with proper attention to the flow physics the accuracy of representation that depends strongly on complexity of the flow is feasible [42].

3.3.4.1 Reynolds-average Navier-Stokes Turbulence Models

In order to compute the turbulent flows with the Reynolds-average Navier-Stokes Turbulence Models (RANS) equations, it is necessary to develop turbulence models that can predict the Reynolds stresses and the scalar transport terms, then close the system of the mean flow equations [252, 265, 298]. The extra terms that appeared in the Reynolds averaged flow equations due to the interactions between various turbulent fluctuations have been shown above to be modelled by the classical turbulence models: EVM and RSM, which were classified based on the additional transport equation that needs to be solved along with the RANS flow equations. The problem of predicting the Reynolds stress R_{ij}, whose presence in the averaged momentum equation prevents closure lies with the kind of manipulations for the RANS models [298]. The most common approach in predicting R_{ij} is the use of the **Boussinesq eddy viscosity relation** shown in Equation 3.7, where C_μ is an empirical constant. It was created based on the analogy between molecular and turbulent motions and it obeys the transport law and assumes isotropic eddy scale [252, 265, 293]. The wide range of this type of models are referred to as EVMs or two - equation models and will be shown here.

$$\mu_t = \frac{\rho C_\mu k^2}{\varepsilon} \tag{3.7}$$

Spalart - Allmaras: Spalart - Allmaras is a one equation model that solves one transport equation for a modified turbulent viscosity $\tilde{\nu}$, as shown in Equation 3.8 and it involves the specification of a length scale by means of an algebraic formula. The model is specifically designed for aerospace applications involving wall - bounded flows on a fine, near-wall mesh, which also permits the use of coarser meshes [264, 293]. It is suitable for mildly complex 2D external/internal flows and boundary layer flows under pressure gradient, but it performs poorly for 3D, free shear and strong separation flows.

$$\mu_t \equiv f\left(\tilde{\nu}\right) \tag{3.8}$$

The k - ε model: This is an EVM classical model, whereby the TKE $k \equiv \overline{u_i' u_j'} / 2$ (L^2/T^2 or m^2/s^2) and dissipation of the TKE $\varepsilon \equiv \nu \overline{\partial u_i' / \partial x_j (\partial u_i' / \partial x_j + \partial u_i' / \partial x_j}$ (L^2/T^3 or m^2/s^3). The μ_t term is equivalent to as shown by Equation 3.9 and employs the Boussinesq eddy viscosity relation which is created by modifying the governing conservative equations [252, 264]. It has two unknown terms that also introduces additional variables for which a turbulence model is required in order to determine these variables in terms of known quantities [293].

The model employed a method that is based on the transport equations of the TKE k and its dissipation rate ε, hence the model solve transport equations for k and ε as shown by Equations 3.10 and 3.11 [264, 293]. It also uses the assumption that the fluid flow is fully turbulent and the effects of molecular viscosity is negligible [252, 293]. In CFD codes, those transported quantities are solved simultaneously with the equations of mass, linear momentum and energy [264].

$$\mu_t \equiv f\left(\frac{\rho k^2}{\varepsilon}\right) \tag{3.9}$$

$$\frac{D}{Dt}(\rho k) = \frac{\partial}{\partial x_j}\left[\left(\mu + \frac{\mu_t}{\sigma_\varepsilon}\right)\frac{\partial k}{\partial x_j}\right] + G_k - \rho\varepsilon \tag{3.10}$$

$$\frac{D}{Dt}(\rho\varepsilon) = \frac{\partial}{\partial x_j}\left[\left(\mu + \frac{\mu_t}{\sigma_\varepsilon}\right)\frac{\partial \varepsilon}{\partial x_j}\right] + C_{\varepsilon 1}\frac{\varepsilon}{k}G_k - \rho C_{\varepsilon 2}\frac{\varepsilon^2}{k} \tag{3.11}$$

Where $C_\mu = 0.09$, $C_{\varepsilon 1} = 1.44$, $C_{\varepsilon 2} = 1.92$, $\sigma_k = 1.0$, $\sigma_\varepsilon = 1.3$ [252]

The k - ε turbulence model is the most popular model that has been widely used and validated [25, 122]: It is robust, economical and reasonably accurate for many flows involving turbulence, but the major drawback is poor performance in a variety of important cases such as fully developed flows in non-circular ducts, swirling flows, rotating flows and unconfined flows [267, 268, 293]. This turbulence models are further grouped into standard, renormalized group (RNG) and realizable k - ε models and are available in most commercial CFD software [264, 265, 293]. To improve upon the standard k - ε model, the RNG was modified using renormalized group theory and the realizable k - ε models statistical techniques. The standard k - ε turbulence model is robust and was shown to be suitable for initial iterations, initial screening of alternative designs and parametric studies. RNG k - ε is suitable for complex shear flows involving rapid strain, moderate swirl, vortices and locally transitional flows for example boundary layer separation [261, 265]. While realizable k - ε model, offers the same benefits with similar applications to RNG and more accurate with an easily converged solutions [185]. It will be shown later that in addition to the choice of turbulence model, accurate grid resolution and correctness in defining the boundary conditions are essential requirements.

The k - ω Model: The k - ω turbulence models with the specific dissipation rate $\omega \equiv \varepsilon/k$ (1/T or 1/s) and the μ_t that is shown by Equation 3.12, solves the transport equations for k and ω as shown by Equations 3.13 and 3.14. This model is categorized into standard and shear stress transport (SST) turbulence models. The standard k - ω model has superior performance for wall bounded boundary layer, free shear and low Reynolds number flows, and is suitable for complex boundary layer flows under adverse pressure gradient and separation [293]. While the SST k - ω model has similar applications to the standard one, but is not suitable for free shear flows because of its dependency on wall distance [258, 266].

$$\mu_t \equiv f\left(\frac{\rho k}{\omega}\right) \tag{3.12}$$

$$\rho\frac{Dk}{Dt} = \tau_{ij}\frac{\partial U_i}{\partial x_j} - \rho\beta^* f_{\beta^*}k\omega + \frac{\partial}{\partial x_j}\left[\left(\mu + \frac{\mu_t}{\sigma_k}\right)\frac{\partial k}{\partial x_j}\right] \tag{3.13}$$

$$\rho\frac{D\omega}{Dt} = \alpha\frac{\omega}{k}\tau_{ij}\frac{\partial U_i}{\partial x_j} - \rho\beta f_\beta k\omega^2 + \frac{\partial}{\partial x_j}\left[\left(\mu + \frac{\mu_t}{\sigma_\omega}\right)\frac{\partial \omega}{\partial x_j}\right] \tag{3.14}$$

3.3.4.2 Reynolds Stress Equation Models

The drawbacks in the k - ε turbulence models led to the development of Reynolds stress transport model (RSM) or second moment closures (SMCs), which account for the directional effects of the Reynolds stress fields [293]. The Eddy viscosity approach is discarded in RSM and Reynolds stresses are directly computed, as was shown above, which implies that individual Reynolds stresses are used to obtain closure of the Reynolds average momentum equation. It has seven unknown terms and can predict flows with complex strain fields or significant body forces [264, 293]. These are the convection, production, rotation, diffusion, dissipation, pressure-strain terms and kinematic Reynolds stress terms. The first three terms are kept in their exact form, while second three group correlation terms needs to be modelled to obtain a solvable term and the kinematic Reynolds stress term incorporates all the other group of six terms.

Reynolds stress model is complex [264, 293], but is generally accepted as the simplest type of turbulence model with the potential to describe all the mean flow properties and Reynolds stresses without necessary adjustments. RSM is physically the soundest RANS model that avoids isotropic eddy viscosity assumption, is suitable for complex 3D flows with strong streamline curvature and strong swirl/rotation typical of swirl combustors with very large inlet swirl. It requires more central processing unit (CPU) time/memory and is also shown to be tougher in convergence [264] due to close coupling of equations that are associated with the mean velocity and turbulent stress fields through source terms. RSM has also shown to be well validated [283] as does the k - ε models, but because of the high cost involved in computation, industrialist limits the use in several types of applications [293].

3.4 CFD User Interfaces

CFD codes are structured around the numerical algorithms which solve fluid flow problems [42, 293]. These codes consist of three basic user interface that defines a problem parameters for which results are examined and are: The pre-processor, solver and post-processor.

1. **Pre-processor**: This is where inputs of flow problems to a CFD program is mainly carried out (also called flow domain) and is dominated by user activities that includes:
    - Defining the computational domain
    - Generating meshes from the domain
    - Selecting the physical and chemical processes to be modelled
    - Defining fluid properties
    - Specifying boundary conditions

2. **Solver**: The solver is the numerical algorithm that incorporate three basic steps that are employed based on the control-volume techniques or finite volume method, which is the method identified for the formulation of most stablished CFD codes, example include: CFX/ANSYS FLUENT, PHOENICS, STAR CD. The following are the major steps:

    - Integrating the governing equations of the fluid flow over the finite control volume,
    - Discretizing the resulting integral equation into sets of algebraic equations,
    - Solving the algebraic equations iteratively.

    The choice of a solver in FLUENT CFD code is limited to pressure - based or density - based and is characterised as either segregated or coupled types [264].

1. **Post-processor**: This displays the domain grid, vector plots, contours, particle tracking, animation of the dynamic results, etc. The increased popularity of engineering workstations has led to the development of large amount of work which has recently taken place in the post - processing field.

3.5 Grid Generation

The grid defines the cells on which flow (velocity vectors, static pressure, shear stress, TKE, etc.) and heat transfer variables (HTC, Nu, heat flux, temperature etc.) are calculated throughout the computational domain. The accuracy of a CFD solution is governed by the number of cells in the grid [42, 293]. It is generally shown that the larger the number of cells the better the solution’s accuracy [42, 263]. Though the number of grid is a significant factor but the accuracy of the solution, costs of running the simulation in terms of computer hardware and the time of carrying out the calculations are all dependent on the fineness of the grid, which also depends on the cell size [42, 264, 293]. Optimal grid are often non - uniform, they are finer in regions of large variations and coarser in regions with relatively insignificant change. Grid generators are incorporated in either the CFD solver (ANSYS workbench) or are operated independently (ICEM CFD meshing tool) and can be read and incorporated to the solver.

3.5.1 Types of Grid

The present work CHT CFD grid generation tool is the ANSYS ICEM CFD code which can be use in generating (or discretizing) either structured, unstructured or hybrid grids.

1. **Structured grid:** A structured grid [42] consists of planar cells with four edges for 2D and are called tetra grid or volumetric cells with six faces for 3D and are referred to as hexahedral (or hex) grid. It is rectangular in shape by which the cells can be distorted to represent another shape, each cell is numbered according to indices (i, j, k) which do not necessary correspond to x, y and z coordinates. In structured grid, fewer cells can be generated and it enables much finer resolution when highly resolved grids are required closed to the wall boundary layer.
2. **Unstructured grid:** Unstructured grid [42] consists of cells of various shapes typically triangles or quadrilaterals for 2D (or tetra) and tetrahedrons or hexahedrons for 3D (or tet) grids. The grid are not uniquely identify by indices i and j, but instead cells are numbered in another way internally in the CFD code. For complex geometries, an unstructured grid is usually much easier to create.
3. **Hybrid grid:** This combines regions or blocks of both structured and unstructured grids [42]. It enables high resolution near wall without requiring high resolution away from it.

3.5.2 Grid Sensitivity

A highly qualitative grid is a requirement for accurate and reliable CFD solution [42]. Grid independence test has been shown to be an important requirement to ascertain the number of cells and quality of a chosen grid size [32, 33, 263, 265, 266] and is grouped into two: Firstly, Adaptive (self) meshing capability incorporated in the simulation software (Fluent CFD solver), it allows for automatic refinement of grid in areas of rapid variations. Secondly, initial refinement of coarse grid until certain key results do not change, which is a systematic search of grid independent results using the meshing software (ICEM CFD). Generally for volume meshing [42, 264, 292], the tetrahedral grid provides a more automatic solution with the ability to add grid controls (based on non-uniformity in edge intervals) to improve the accuracy in critical regions, as calculation are nodes based centre. While, for hexahedral grid it provides a better accurate solution but is more difficult to generate, which is based on uniformity in opposite edge intervals and calculations are on cell centre based.

3.6 Boundary Conditions

Boundary condition (BC) is a mathematical statement or function of the flow field variables (velocity, temperature, density, pressure, etc.) from governing equations that is specified at the surface of the computational domain [42, 264, 265]. The accuracy of CFD solution is also dependent on the imposed BC which is also a determining factor for the type of flow that is being modelled. This is in addition to the dependency of the CFD solution on the equations of motion, the computational domain and the grid. Several types of boundary conditions terminologies are generally available for used in a CFD code which is based on the type of package selected [264]. The available BCs that ANSYS Fluent CFD code employed includes: Wall, inflow/outflow, miscellaneous and internal BCs. These BCs are specified at the face or plane surfaces for 3D flow and or edge or line for 2D flow.

The simplest BC [42] is the Wall at which the velocity is set to zero (no-slip condition), either the wall temperature or heat flux and wall roughness are specified here. The options at the boundaries through which fluid enters (inflow) or leaves (outflow) the computational domain are generally categorized as velocity-specified (e.g. velocity inlet or mass flow BC) or pressure specified (pressure inlet) conditions. The miscellaneous BCs are neither of the two boundaries stated above and are enforced as either periodicity BC - useful when geometry involves repetition or symmetry BC - where force flow field variables are mirror imaged across a plane. Finally, the internal (or interior) BC which are imposed on the faces or edges that do not define the BC of the computational domain, it exists inside the domain.

3.7 Convergence Criteria

Iteration in CFD, is a simulation procedure that is used to determine the smoothness and readiness of a numerical calculation, it also shows the accuracy of CFD predictions [42, 264, 293]. In order to understand that an iteration has yielded the required predicted results, convergence criteria should be satisfied. Judging for convergence requires that residual levels are carefully examined by monitoring the relevant integrated quantities and finally checking for mass and energy balances. The residual plots shows an indication that residual values have reached the specified tolerance. For example by using a pressure-based solver in ANSYS Fluent CFD, the default residuals have to decrease by at least 10^{-3}: The scaled energy residual decreases to 10^{-6} while that of the scaled species residual decreases to 10^{-5}.

Using the k - ε turbulence model for example, the residuals that have been shown for the convergence plots are [22, 25, 33]: The energy, continuity, TKE k, dissipation rate of TKE ε and species velocities. The energy residual define the solution equation for flow of heat for example temperature, continuity residual show the solution for the continuous flow of the fluid used, TKE and dissipation of TKE residuals interprets the solution for the transport equation of k and ε respectively. The velocities residual solve for the individual directional flow velocities of the fluid along the surfaces of the model geometry. These residuals indicates an imbalance left inside a cell and for each residual the specified criteria must be satisfied [42, 264].

Solution Stability: The requirement for a numerical stability is a needed characteristic of numerical algorithms that is necessitated based on the use of elliptic solver in order to get a solution [264, 292]. A converged steady solution may not be stable and can be physically not realisable, as calculation performed on digital computers might damp out or magnify approximation errors that can yield different results [292]. In order to confirm the accuracy of the algorithm used that will stabilized the converged solution, a transient state solution incorporated in most commercial CFD codes is used and stability is monitored based on calculated flow time and when data (example HTC) no longer changes with flow.

3.8 Near Wall Turbulence Modelling

The boundary layer (BL) velocity and temperature profiles have been divided as either laminar or low Re sub-layer, buffer region and log-law region or turbulence layer [264, 299, 300]. The methods used in describing the BL velocity and temperature profiles are usually by dimensionless parameters that include: dimensionless distance from the wall y^+, dimensionless velocity along the wall u^+ and wall dimensionless temperature T^+ and all are interrelated as Equation 3.15 - 3.21 show and as $u^+ = y^+$ [264, 292].

$$y^+ \equiv \frac{\xi u^*}{\nu} \tag{3.15}$$

$$u^* \equiv \sqrt{\frac{\tau_w}{\rho}} \tag{3.16}$$

$$\tau_w \equiv \mu \left. \frac{\partial U}{\partial \xi} \right|_{\xi=0} \tag{3.17}$$

$$u^+ \equiv \frac{U}{u^*} \tag{3.18}$$

$$T^+ \equiv \frac{T_w - T_\infty}{T^*} \tag{3.19}$$

$$T^{*} \equiv \frac{\alpha q''}{k_s u^{*}} \tag{3.20}$$

$$T^{+} = \Pr y^{+} \tag{3.21}$$

Where ξ is the normal distance of first cell from the wall (m), ν is the kinematic viscosity (m^2/s), u^* is the frictional velocity (m/s), τ_w is the wall shear stress (kg/s^2m), ρ is the fluid density (kg/m^3), U is the fluid velocity along the wall (m/s), μ is the dynamic viscosity (kg/ms) and α is the thermal diffusivity (m^2/s).

The near wall modelling approaches are grouped into [299] either a low Re or wall function types and are characterised based on their dependency of mesh (or grids) refinement close to the BL. If the first cells are near the laminar region, the approach used is the low Re modelling and the y^+ value < 5, but for region above this, specifically the log-law layer the $y^+ > 30$ and within the limit 30 to 300. In the range of $5 < y^+ < 30$ is the buffer region and is usually not advisable to have grids lying in this region [42, 292, 299]. These two approaches are applied to the GT cooling of this present investigation, in order to determine the turbulence model that give better estimate and also fits in the available experimental data. Once a better approach is selected, this will be use as a validation approach throughout this investigations.

Generally, the flow physics in gas turbine components wall cooling of this CHT CFD geometries, critically depends on the choice of turbulence models and the types of grid. It involves the use of short holes with entrance effects and duct (or gap) with jet flow interactions [25, 46, 73, 80]. The aerodynamics, involve flow through short holes, being turned through large angles with high degree of swirl and turbulence due to separated, reattached and developed flow. The heat transfer part involves low Reynolds number, laminar flow in the BL and this leads to the crux of the problem in CHT CFD. In order to model the main aerodynamic flow features one particular turbulence model is require and a completely different one for the near BL flow. Ideally this should be implement using more than one turbulence model, but it requires that a high performance computer (HPC) is used in addition to needed lengthy time frame as the work involves parametric analysis. It is therefore easier to make some compromises, coupled with the available experimental data for validation purpose, to choose only one turbulence model and a type of grid that can estimate all the variables involved in the GT cooling computational domains.

CHAPTER FOUR

VALIDATION OF CHT CFD METHODOLOGY WITH MEASURED RESULTS

Chapter 4

Validation of CHT CFD Methodology with Measured Results

4.1 Introduction

This Chapter discusses the CHT CFD procedures and the predicted validations with the relevant measured results. The experimental data that were used for this validation are: the hole outlet pressure loss $\Delta P/P$, surface and locally X^2 average heat transfer coefficients (HTCs) *h* (W/m^2K) or Nusselt number Nu (or $NuPr^{-0.33}$) and are for geometries that include:

- The impingement air jet single sided flow exit geometry - where two types of grid (hexahedron and tetrahedron) and four types of turbulence models using wall function were computed,
- The effusion cooling geometry - whereby, low and high Reynold number Re turbulence models were computed for varied near wall treatment y^+ values.

These selected cooling systems, were based on the understanding that the impingement gap and effusion short holes aerodynamics, influences the pressure loss ΔP and are the essential parts of the hole and target (or approach) surfaces heat transfers. Low Re turbulence models are not applied on impingement cooling system, because of the need for a higher performance computer (HPC) and difficulties in convergence for prolonged period of time hence only effusion wall were used for this.

4.2 Experimental Test Walls and the Measured Variables

Figure 4.1 (a - d) show the schematic diagram of the test plates for impingement jet and impingement/effusion cooling rig (Chapter 2) [4, 5, 19, 22, 23, 25, 44, 46, 83], with the location of the imbedded grounded junction mineral insulated thermocouples shown. The thermocouples are at 25.4mm intervals placed on the centreline between the impingement surface jets and thus at the most remote places, relative to the high local convective cooling of the impingement points. Conductive heat transfer within the wall smoothed out the strong gradients in surface convective heat transfer, as the Biot numbers for all conditions were < 0.2. The thermocouples thus measured a surface averaged temperature and were located at the lowest local convective heat transfer position and hence would give slightly higher temperatures than the mean and thus result in conservative heat transfer measurements. In addition to the central thermocouples, Figure 4.1 (b) show that on the target wall there were six thermocouples located 25.4 mm either side of the centre line. These were used to determine the transverse variation of the surface averaged heat transfer *h*. The variation in the thermocouple response between the three and five transverse thermocouples in Figure 4.1 (b) was 5 % and this was used as the accuracy of the measurements of *h*.

The target wall thermocouples were used to determine the locally surface averaged heat transfer coefficient using the lumped capacitance method. The thermally insulated wall was electrically heated in the absence of any impingement coolant flow to about 80^{o}C and then the electrical heating was switched off, after which the impingement flow was established. The transient cooling of the target wall by the impingement flow enabled the surface averaged HTC to be determined using Equation 2.24. Abdul-Husain and Andrews [5] have shown that this method gave good agreement with steady state methods of heat transfer measurements. In the CHT CFD, the wall temperature on the heated side of the wall is held at a constant 80^{o}C as it would be on a steady state heat transfer test rig.

The only aerodynamic experimental measurement was that of the pressure loss $\Delta P/P$ from the plenum chamber air feed to the external ambient air after the discharge from the impingement gap [4, 19, 22, 23, 25, 44, 46, 83]. The key component of the pressure loss is the flow separation and reattachment inside the impingement holes. Also, this impingement gap pressure loss is affected by flow-maldistribution influenced by hole pitch to diameter ratio X/D and the number of upstream rows of holes N, larger X/D (or smaller N) implies higher pressure loss and lower X/D (or larger N) gives low $\Delta P/P$ [22, 25]. The objective of this part of the work is to identify the turbulence model and grid combination that best reproduces the experimental results. If the predicted pressure loss is in agreement with the measurements, then this is a strong indicator that the key features of the aerodynamics are correctly predicted.

4.3 The Model Geometries

The experimental test rigs that were earlier shown in Figure 2.3 (a - d) of Chapter 2 are used here to setup the symmetrical elements of the computational domains. These setups were also used to generate 3D grid model geometries. The setups and the grid models are all based on either one of the schematic flow schemes that were shown in Figure 1.7 (a - c) of Chapter 1. Throughout the remaining Chapters of this work, these similar grid model geometrical procedures will also be used for the computation of either impingement air jet single sided flow exit, impingement air jet four sided flow exits or impingement/effusion cooling systems and are only refer to this Chapter. These computational geometries were varied, as Z/D, X/D, L/D or G (kg/sm^{2}bar) changes, only one representative setup with an accompanied grid model geometry for each of the cooling systems and their respective part descriptions are shown here. For clarity of the pictorial view of the grid geometries only the surface parts are shown, while the interior zones that include the solid and fluid are left out.

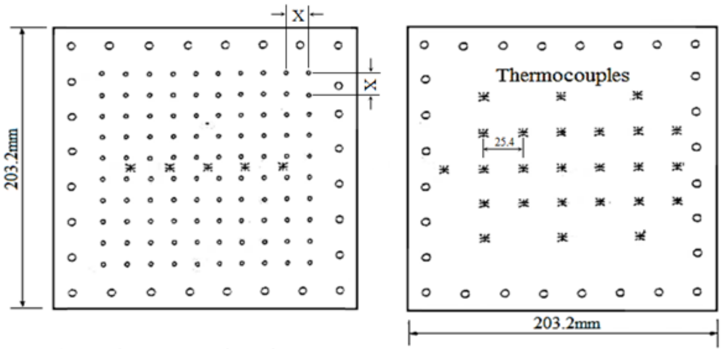

a) Impingement jet plate

b) Target plate

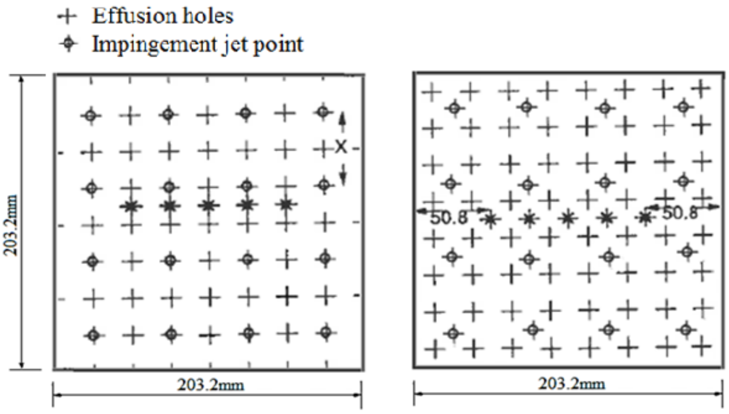

c) Inline effusion holes

d) Off-set effusion holes

Figure 4.1: Gas turbine cooling experimental test walls with thermocouple locations [25, 41]

4.3.1 Assumption of Symmetric Conditions

The used of symmetric boundary conditions as employed by El-Jummah *et al* [22, 25, 32, 33, 46] is used to carry out the present impingement jet single exit flow (ISEF) CHT CFD investigations. This similar approach using quarter (5 × 5) of a square array of 10 × 10 impingement jet geometry is also used for impingement jet four exit flow (IFEF) investigations. While, for square arrays of 10 × 10 impingement jet holes of an impingement/effusion system, only quarter hole is required with equal quarter hole for effusion if their n (m^{-2}) is also equal, but for unequal n (m^{-2}) values only the effusion symmetrical approach varied. Figure 4.2 and Figure 4.3 show these symmetrical elements that were used to model the grid model geometries shown in Figure 4.4Figure 4.5Figure 4.6, respectively, whereby for Figure 4.5 (i) the grid is accompanied by its representative symmetries. For Figure 4.5 (i a), the symmetrical approach as applied to effusion cooling was X^2 half hole as the flow through the effusion holes for the 10 × 10 square array of holes is symmetrical [80, 86]. This show that for all symmetrical representation shown, even if the values of geometrical or flow conditions are varied, they still remain the same and are only varied by their dimensions.

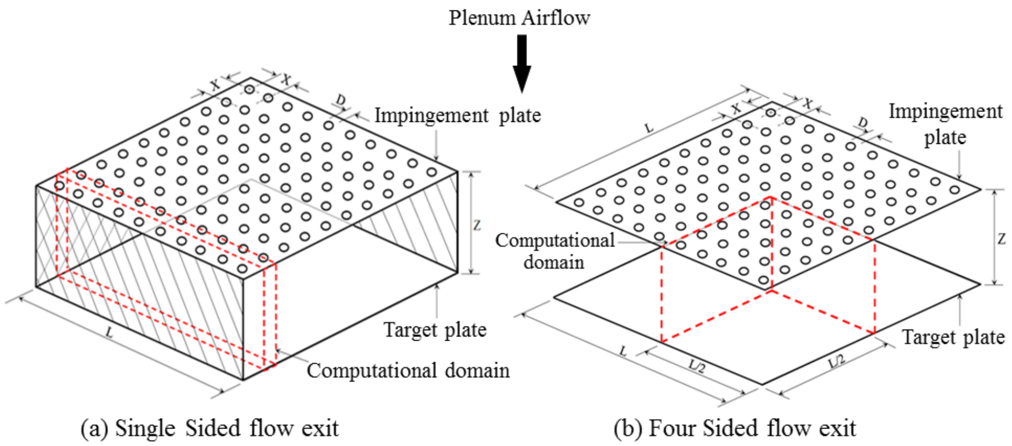

Figure 4.2: Symmetrical elements for impingement jet cooling geometries

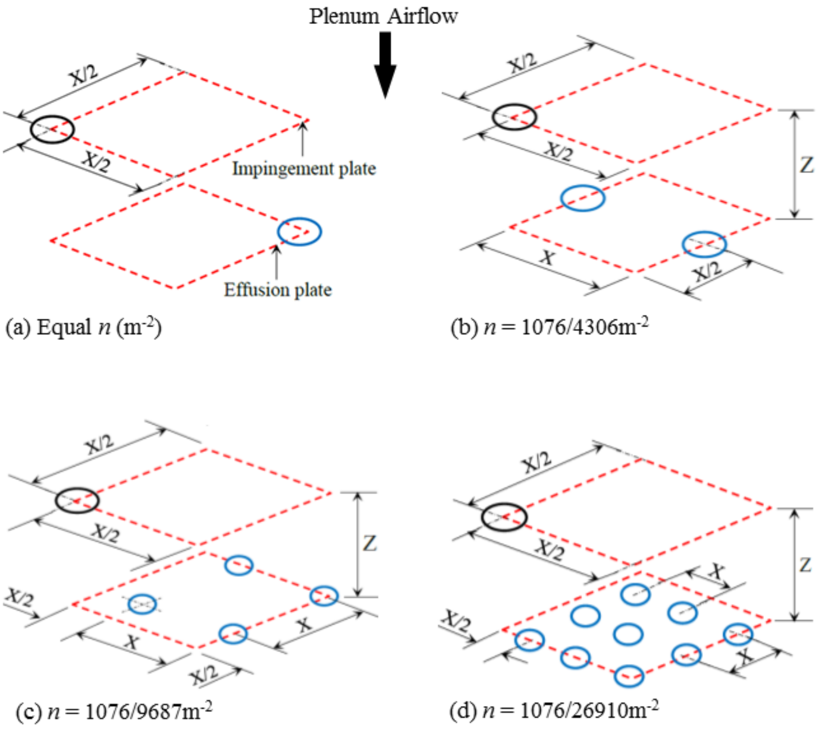

Figure 4.3: Symmetrical elements for impingement/effusion cooling geometries

4.3.2 Computational Grid Models

Table 4.1 - 4.5 show the geometrical parameters that were used in modelling the grid geometries shown in Figure 4.4, 4.5 and 4.6 using the ANSYS ICEM CFD meshing tool. These model grids employed the computational domain described above and are shown by the highlighted red dashed regions in Figure 4.2, 4.3 and 4.5 (i a), which are used for the prediction of the GT cooling systems that have been experimentally investigated [3-5, 19, 22, 23, 25, 32, 33, 43-46, 76, 82, 83, 194, 214, 230]. Figure 4.4 (a and b) are the model geometries for the two grid types: hexahedral (hex) and tetrahedral (tet) grids and each show

the representative parts that formed part of the modelling. For each of the grid types, the cell size in the holes (or number of cells/plane) and the impingement gap were varied based on the differences in hole sizes D, gap and Reynolds number Re. Similarly, from Figure 4.5 (ii)Figure 4.6, the cell size are also varied as the hole size increased or the jet Re increased as in both cases Z is fixed. The effusion cell size shown in Figure 4.5 (i a - e) were only varied in the hole and was based on types of turbulence model used or the size of the jet hole. In all these geometries, any increase in X/D, Z/D, *n* (m-^{2}) or G (kg/sm^{2}bar) or the Re also increased the total computational grid size and the coupled effects of any two also affects it, while the plenum cell sizes are fixed for all the models. By varying the cell distance ξ close to the hole and target (or effusion approach) surfaces, the y^+ value is also varied and fixed as shown in as Table 4.6 - 4.10, which is a useful tool in determining the accuracy of the data required.

Table 4.11 is the flow variables that was used to compute the geometries shown in Figure 4.4 (a and b) in order to determine the grid (hex and tet) that better predict the aerodynamics and heat transfer data, in the impingement jet holes and gap. Once a reasonable grid type is selected, this grid will be use all through the present CHT CFD work. To be conservative, the grid cell dimensions were for both types were fixed at the same values, even though the tet grid generation, this are likely altered as the grid was automatically generated. Table 4.6 show that both the grid target surface averaged y^+ values were fixed at ~ 35 and the tet grid having close to trice the total grid size of the hex grid. Using the wall function approach,

Table 4.1: Geometrical Parameters (ISEF)

Variables	Dimensions
D (mm)	3.27
X (mm)	15.24
Z (mm)	10.0
L (mm)	6.35
L/D	1.94
X/D	4.66
Z/D	3.06
X/Z	1.52
n	4306 m^{-2}
Array	10 × 10

Table 4.2: Effusion Hole Geometrical Parameters

X/D	**11.04**	**6.54**	**4.66**	**3.78**	**3.06**	**1.86**
X (mm)	15.24	15.24	15.24	15.24	15.24	15.24
D (mm)	1.38	2.33	3.27	4.03	4.98	8.18
L (mm)	6.35	6.35	6.35	6.35	6.35	6.35
L/D	4.60	2.73	1.94	1.58	1.28	0.78
A (%)	0.64	1.84	3.62	5.50	8.39	22.7
***n* (m^{-2})**	4306	4306	4306	4306	4306	4306
Array	10 × 10	10 × 10	10 × 10	10 × 10	10 × 10	10 × 10

Table 4.3: Geometrical Parameters (IFEF)

D (mm)	1.38
X (mm)	15.24
Z (mm)	10.00
L (mm)	6.35
L/D	4.60
X/D	11.04
Z/D	7.25
X/Z	1.52
A%	0.64
n (m^{-2})	4306
Array	10 × 10

Table 4.4: Geometrical Parameters of Equal Hole Plates

Variables	*Impingement*			*Effusion*		
***n* (m^{-2})**	**4306**	**9688**	**26910**	**4306**	**9688**	**26910**
Array	10×10	15×15	25×25	10×10	15×15	25×25
D (mm)	1.41	0.93	0.63	3.27	2.23	1.30
X (mm)	15.24	10.10	6.10	15.24	10.10	6.10
L/D	4.50	6.83	10.08	1.94	2.85	4.89
X/D	10.80	10.83	9.54	4.7	4.7	4.7
Z/D	5.67	8.53	12.51	2.40	3.57	6.12
A (%)	0.67	0.66	0.83	3.61	3.80	3.60

Table 4.5: Geometrical Parameters of Unequal Hole plates

Variables	*Impingement*	*Effusion*		
***n* (m^{-2})**	**1076**	**4306**	**9688**	**26910**
Array	5 × 5	10 × 10	15 × 15	25 × 25
D (mm)	2.88	3.27	2.23	1.30
X (mm)	30.48	15.24	10.10	6.10
L/D	2.21	1.94	2.85	4.89
X/D	10.58	4.7	4.7	4.7
Z/D	2.70	2.40	3.57	6.12
A (%)	0.70	3.61	3.80	3.60

these grids were computed for four different types of turbulences models that include: k - ε (standard, RNG, Realizable) and RSM turbulence models and were all run at fixed G of 1.93 kg/sm^{2}bar, X/D of 4.66 and Z/D of 3.06 [22, 25, 46]. This computations were also run for varied G from 1.08 - 1.93 kg/sm^{2}bar using the standard k - ε turbulence model.

Computations were also carried out using the flow variables of Table 4.12 at a fixed X/D of 4.66 and G of 1.93 kg/sm^{2}bar for two low Re (SST and standard k - ω) and wall function (RSM and three k - ε) turbulence models. This was in order to determine the model that better estimate the flow aerodynamics and heat transfer data in the effusion cooling short hole, as this is critical to the prediction of $\Delta P/P$. Therefore, the model that better predict this hole aerodynamics will be anticipated to be a step choice for this Ph. D. work. Also computed are varied G from 1.08 - 1.93 kg/sm^{2}bar at fixed X/D of 4.66 using the SST k - ω, enhanced wall function (EWF) standard $k - \varepsilon$ and standard $k - \varepsilon$ (WF) turbulence models. The computations for a varied X/D from 1.86 - 11.04 as Table 4.12 show at a fixed G of 1.93 kg/sm^{2}bar, using the standard $k - \varepsilon$ turbulence models were also carried out, this was in order to determine the effect of L/D with varied D. **Table 4.8** show the variation of y^+ values for the types of turbulence models used and for varied X/D, all the y^+ values were varied between 30 - 35. These computations were carried out using hex grid and for a fixed number of plane, for the upper and bottom plenum and were characterised by BL growth close to the jet plate. This was because the flow from the inlet plenum through the jet holes converges, this boundary layer growth was also applied in the hole for $y^+ < 5$ as in Figure 4.5 (ib and d).

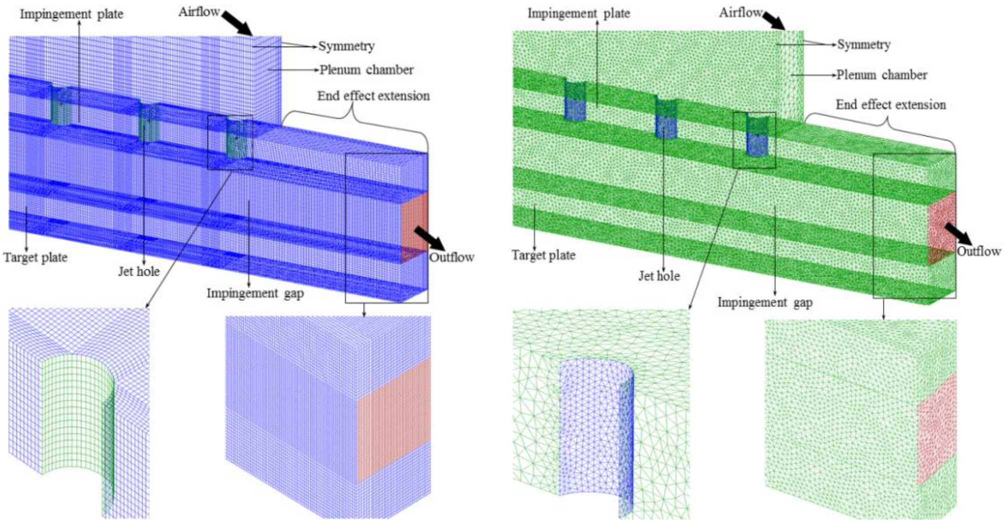

(a) Hexahedral grids (b) Tetrahedral grids

Figure 4.4: Impingement jet single exit flow grid model geometries

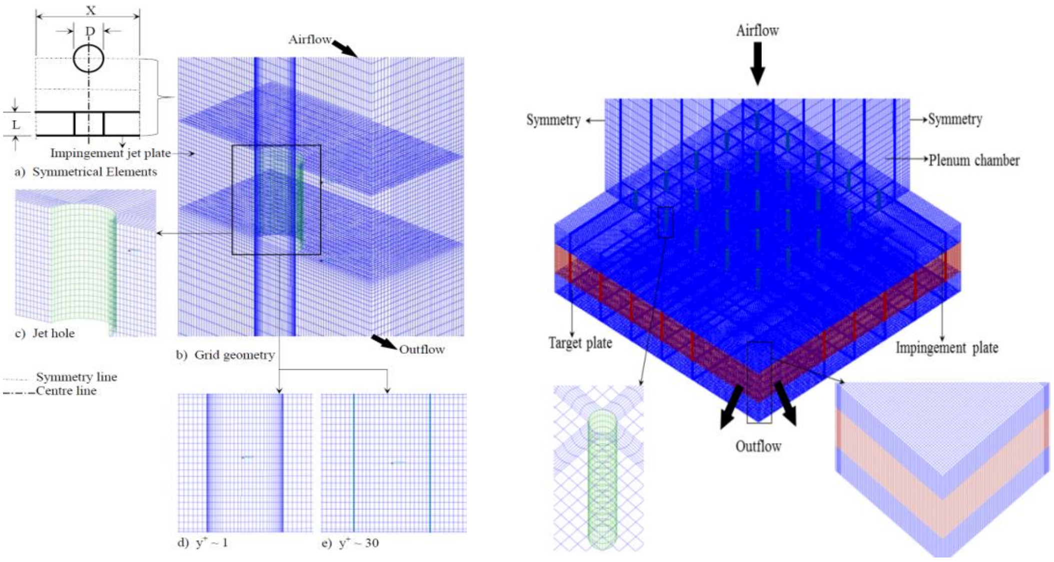

(i) Effusion X^2 system (ii) Impingement jet four exits flow

Figure 4.5: Gas turbine cooling grid model geometries

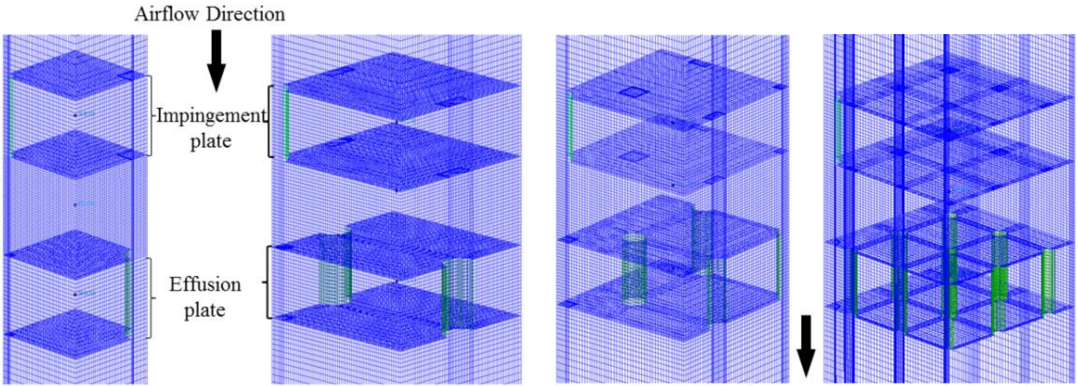

(a) Equal n (m^{-2}) (b) $n = 1076/4306m^{-2}$ (c) $n = 1076/9687m^{-2}$ (d) $n = 1076/26910m^{-2}$

Figure 4.6: Impingement/effusion cooling grid model geometries

Table 4.6: Percentage of Parts Grid Cell Sizes for $y^+ \sim 35$

ISEF **Parts**	**Hexa grid** 1.27×10^6	**Tetra grid** 3.36×10^6
Plenum (%)	37.6	36.0
Test plates (%)	28.5	21.7
Gap (%)	26.8	31.8
Hole (%)	7.1	10.5

Table 4.7: Grid Size (IFEF)

Parts	**Size/(%)**
Total cells	3.94×10^6
Total nodes	3.73×10^6
Plenum	38.2
Test plates	15.7
Gap	37.2
Hole	08.9

Table 4.8: Grids Size and Turbulence Models y^+ Values for X/D of 4.66

Models	**Grid Size**	**Plenum (%)**	**Jet Plate(%)**	**Hole (%)**	y^+
SST k- ω	0.37×10^6	70.3	11.5	18.2	1.04
Std. k- ω	0.37×10^6	70.3	11.5	18.2	2.03
Std. k - ε (EWF)	0.37×10^6	70.3	11.5	18.2	1.98
Std. k - ε (WF)	0.29×10^6	75.9	12.9	11.2	31.5
Real k- ε	0.28×10^6	76.5	12.6	10.9	32.5
RNG k-ε	0.28×10^6	76.5	12.6	10.9	35.4

Table 4.9: Grid Size for G of 0.94 kg/sm^2bar at $y^+ \sim 35$

Parts	**4306/4306**	**9687/9687**	**26910/26910**
Total cells	0.28×10^6	0.16×10^6	0.15×10^6
Plenum (%)	28.7	30.3	33.1
Gap (%)	40.6	38.7	36.8
Jet hole (%)	07.5	07.9	08.2
Eff. hole (%)	06.4	06.8	07.2
Plates (%)	16.8	16.3	14.7

Table 4.10: Grid Size for G of 0.94 kg/sm^{2}bar at $y^+ \sim 35$

Parts	1076/4306	1076/9687	1076/26910
Total cells	0.73×10^6	0.50×10^6	0.84×10^6
Plenum (%)	29.8	32.4	37.3
Gap (%)	27.3	24.7	19.8
Jet hole (%)	07.6	07.6	07.6
Eff. hole (%)	10.2	13.8	18.2
Plates (%)	25.1	21.5	17.1

Table 4.11: Impingement Flow Conditions

G (kg/s.m^{2}bar)	1.93	1.48	1.08
V_j (m/s)	43.41	33.5	24.3
V_c (m/s)	24.0	18.4	13.4
V_j/V_c	1.8	1.8	1.8
Re_h ($= \rho V_j D/\mu$)	9680	7440	5400
T_∞(K)	288	288	288
T_w (K)	353	353	353
ρ (kg/m^3)	1.225	1.225	1.225

Table 4.12: Flow Conditions at Fixed G of 1.93kg/sm^{2}bar

X/D	11.04	6.54	4.66	3.78	3.06	1.86
V_j (m/s)	243.60	85.49	43.41	28.56	18.72	6.92
Re_h	22870	13550	9660	7830	6340	3850
T_∞ (K)	288	288	288	288	288	288
T_w (K)	353	353	353	353	353	353
ρ (kg/m^3)	1.225	1.225	1.225	1.225	1.225	1.225

4.3.3 Grid Independence Test

To estimate how many cells would be required to obtain a grid-independent solution, a grid independence test was conducted [32, 33]. This influence of cell size on computational accuracy was carried out using hexahedral grid with wall function standard k - ε turbulence model and the results is as shown in Figure 4.7. El-Jummah *et al* [32, 33] tested for the impingement jet cooling heat transfer using number of cells from 10^5 to $\sim 1.5 \times 10^6$ by the symmetrical and model grid procedures that was shown above. This was based on a 10 × 11 row of jet holes, whereby the extra one row of holes was used as an end effect. An imposed hot side heat flux of 100kW/m^2 was also used, a value with coolant to hot gas temperature difference of 400^{o}C and corresponding to a global hot gas side convective heat transfer of 250 W/m^{2}K.

A representative Nusselt number Nu for the square area of the target wall was computed to investigate the influence of the number of computational cells on heat transfer. This was for impingement jet conditions of an X/D, Z/D, *n* and G of 5.0, 3.3, 4444 m^{-2} and 1.93 kg/sm^{2}bar (where jet Re = 9200), respectively. The results showed that at least 10^6 cells are

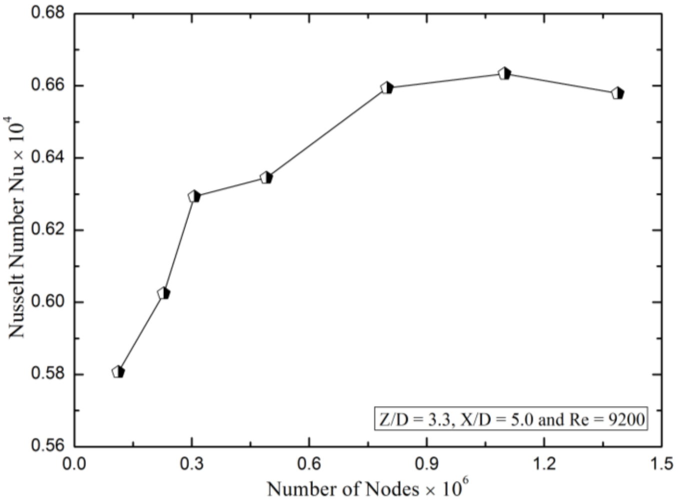

Figure 4.7: Grid Independence test for range of grid cells [32, 33]

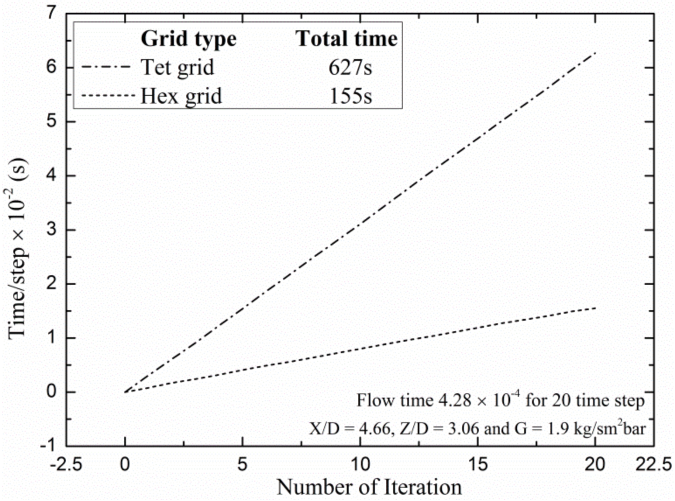

Figure 4.8: Comparison of computational time using standard k - ε turbulence model (WF)

required to reduce grid sensitivity effects and the values tested that gave insignificant change in the results, was for cells between 0.8 to 1.45 million. Therefore, the grid cells of 1.3×10^6 with ~1120 nodes (~ 60 nodes/plane with 0.04 - 0.5 mm cell size) in each air hole was chosen for the CFD investigations. This was considered to be sufficient to resolve any influence of cross-flow on the velocity profile of the impingement jet discharge, as well as to compute the flow separation at the air hole inlet, reattachment at the central region and exit flow development. Figure 4.8 show the computational time for a 20 time step of the impingement jet single exit flow, which compared iteration time/each time step for the hex and tet grids. The computation was carried out using a wall function standard k - ε turbulence model. It shows that the hex grid took ~ 8 s/time step and the tet grid took approx. 31 s/time step, indicating that the tet grid takes longer time to give a converged solution and is equally in the same range for any other wall function turbulence model.

4.4 Validation of Turbulence Models With Model Grid Types

The only available experimental data that are used to validate the comparison of the grid types on impingement jet single exit flow [5, 22, 25, 32, 33, 46, 132] and effusion [80, 83] cooling CHT CFD predictions, are the pressure loss ΔP/P and the locally surface-averaged heat transfer coefficient (HTC) *h* data. A feature of impingement cooling with a single sided exit is that the outlet flow after the jet impinges on the cooled wall, can only flow in one direction. This produces a cross-flow in the impingement gap [56] that has an associated pressure loss along the gap. The pressure loss results in a lower mass flow to the first hole, whilst the last air hole has a higher mass flow. The magnitude of this difference (or flow-maldistribution) depends on the X/D and gap size Z of the impingement air hole array. This also affects the axial variation of heat transfer in the cross-flow direction. If the flow-maldistribution is predicted correctly the pressure loss and the heat transfer will be correctly predicted [25, 33].

For the effusion geometries, the short hole inlets aerodynamics involve hole inlet entry effects that generates inlet flow separation and reattachment in the hole [80, 83]. This also affect the key experimental parameter ‘pressure loss ΔP/P’ which can only be successfully predicted, if these inlet flow effects are correctly predicted [73]. An effusion wall has active heat transfer within the wall thickness due to short hole heat transfer influenced by the turbulence, which is in addition to the film cooling effectiveness of the effusion cooling. Thus the overall cooling is the wall heat transfer plus the adiabatic effusion cooling, to give an overall cooling effectiveness. Gas turbine combustor and turbine blade cooling jet walls are typical of the situation where short holes in metal walls act as a heat exchanger, to cool the walls. Therefore, any of the turbulence models with the associated near-wall approach that successfully predicts these coupled effects, should be a valid model for the present work and will be use in carrying out all the CHT CFD parametric investigations.

4.4.1 Pressure Loss Predictions

The predicted static pressure loss across the impingement wall as a function of hole number is shown in Figure 4.9 (a and b) for the hex and tet grids. This was determined as the pressure difference between the air supply plenum chamber and the static pressure on the impingement gap side of the impingement plate at the centre of two impingement jet holes. El-jummah *et al* [32] predicted that the lower flow through the leading holes gave a lower pressure loss ΔP/P. They showed that the difference in static pressure between the first hole pressure loss and the last is the pressure loss of the cross-flow down the gap, which was added to a 0.45% pressure loss to that across the first hole and was the influenced of the flow-maldistribution. They also showed that this cross-flow velocity ΔP/P was the source of energy for generation of turbulence by the cross-flow as it interacts with the impingement

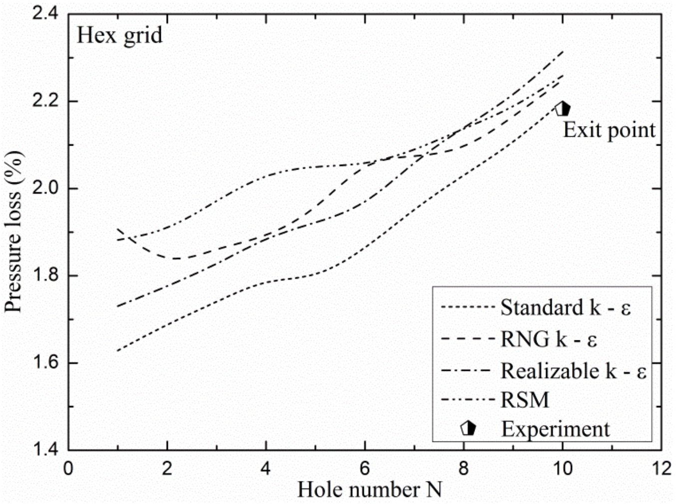

(a) Hex grid

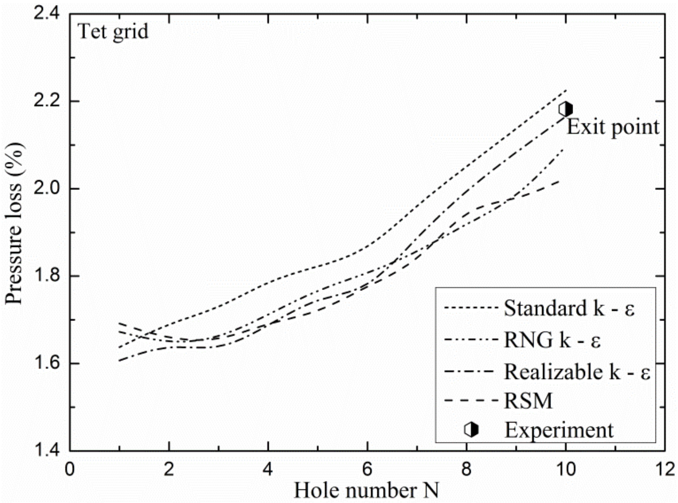

(b) Tet grid

Figure 4.9: Predicted impingement hole outlet pressure loss ΔP for the types of wall function RANS turbulence models at fixed X/D = 4.66, Z/D = 3.06 and G of 1.93 kg/sm^{2}bar

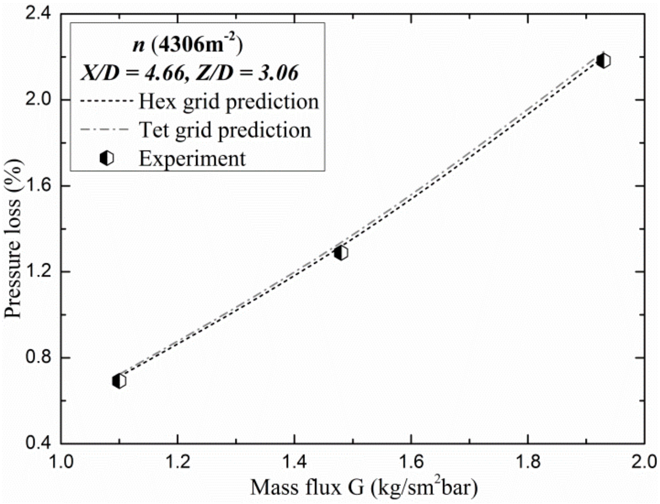

Figure 4.10: Comparisons of two grid types predicted and experimental pressure loss hole exit impingement gap using wall function standard k - ε turbulence model for three G values

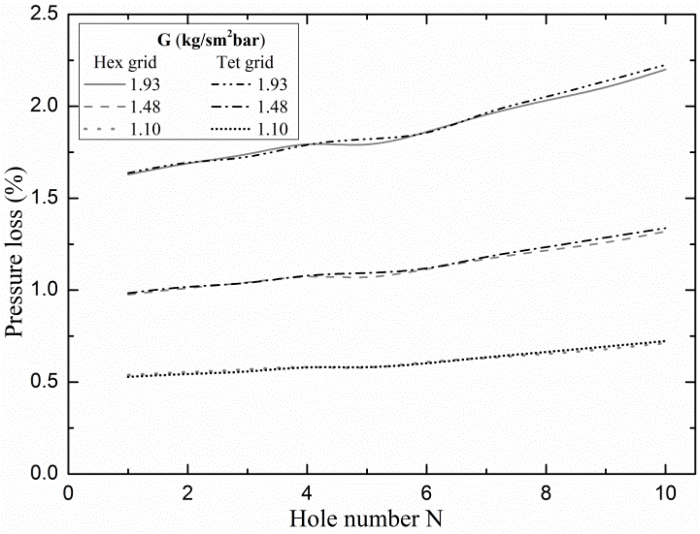

Figure 4.11: Predicted impingement hole outlet pressure loss ΔP of two grid types wall function standard k - ε turbulence model for three G values at X/D of 4.66 and Z/D of 3.06

jets. El-jummah *et al* [46] showed that the pressure loss at the exit to the impingement holes was between one and two dynamics heads, depending on the velocity profiles and this is similar to that due to a sharp 90^o bend. Thus the presence of the target plate does not change the pressure loss ΔP/P from that of a free discharge. The second major aspect of the pressure loss was that due to the flow along the duct and the interaction of the cross-flow with the impingement jets. They also showed that around three quarters of the ΔP/P was across the wall and one quarter due to cross-flow along the impingement gap.

The pressure loss of Figure 4.9 (a and b) show that the predictions given by the standard k - ε and Realizable k - ε turbulence models of the hex and tet grids, respectively, better agreed with the experimental exit data. In addition to this, the standard k - ε turbulence models of the tet grid shown in Figure 4.9 (b), also show close agreement with measured data.

The other turbulence models of the hex grid over predicted the pressure loss, while that of the tet grid under predicts it. Although only one measured data point was used and this may not be adequate to a reasonable conclusion, hence the prediction for other G values were compared to the measured data in Figure 4.10, for both grids using WF standard k - ε model. This was based on the fact that both the grids are in agreement with measurement using this model, as Figure 4.9 (a and b) show, whereby Figure 4.10 indicated excellent agreement with measurement for the two grids. These exit pressure loss predictions were based on predicted ΔP/P across the hole number of Figure 4.11. Both the results agreed to each other, this could be based on the predictions of the hole flow-maldistribution.

4.4.2 Heat Transfer Predictions

The influence of cross-flow on the average surface heat transfer per hole, using the surface area X^2 for each hole is shown in Figure 4.12 (a and b). These are the average of the surface distributions of heat transfer shown in Figure 4.15. The experimental results are the heat transfer based on the six thermocouples in the target wall on the centreline between the holes. These are in the minimum heat transfer position and hence should underestimate slightly the locally surface averaged HTC h if there are any significant thermal gradients [46]. All the models using tet grid and the RNG model with hex grid poorly under predict the measured results. This should be based on the grids uniformity in the impingement gap, hence refinement close to the target wall could be a solution if low Re model is to be applied and this requires a HPC and more iteration time as Table 4.6 and Figure 4.8 show.

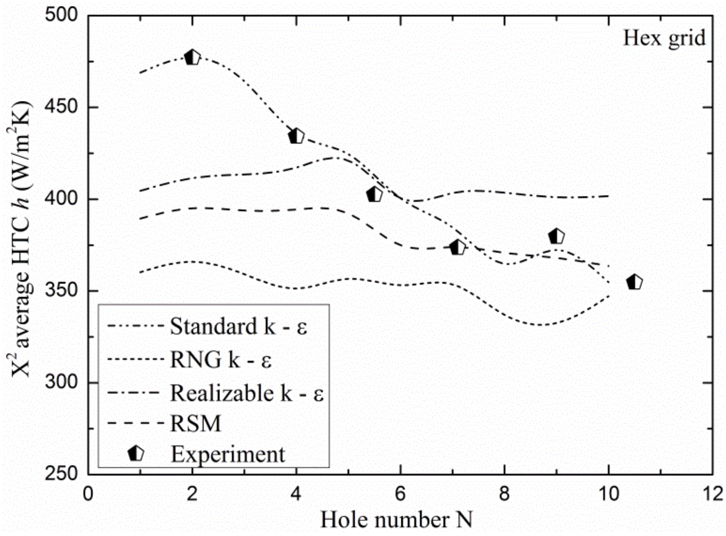

(a) Hex grid comparison

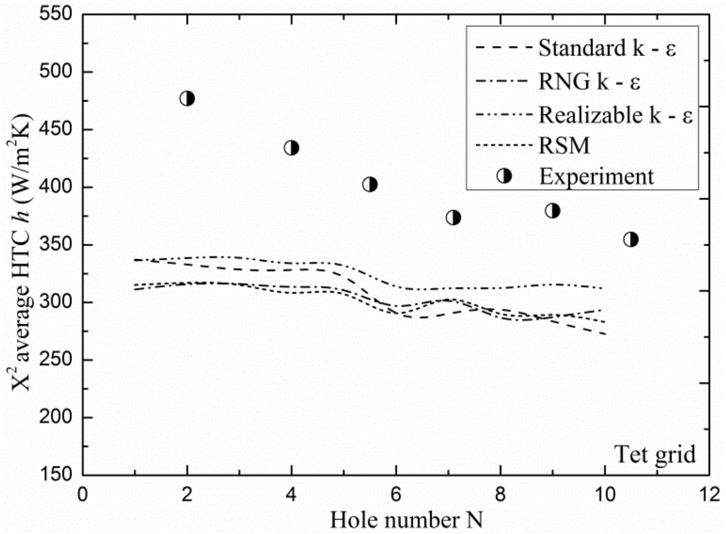

(b) Tet grid comparison

Figure 4.12: Comparisons of predicted and experimental impingement jet target surface locally X^2 average HTC h for the types of wall function RANS turbulence models

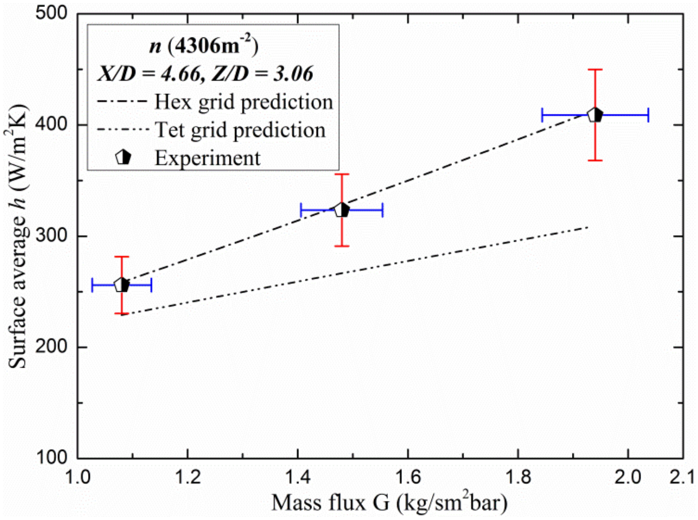

Figure 4.13: Comparisons of the two grid types predicted and experimental impingement jet target wall surface average HTC *h* using wall function standard k - ε turbulence model

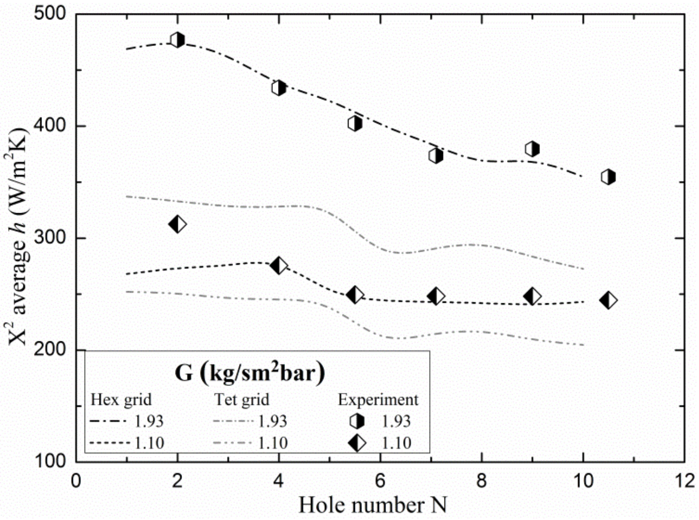

Figure 4.14: Comparisons of two grid types predicted and experimental impingement jet target surface locally X^2 average HTC *h* using wall function standard k - ε turbulence model

Figure 4.13 compares this complete 10 row impingement wall predicted surface averaged HTC *h* with the averaged of the locally X^2 averaged HTC *h* over the six thermocouples at 25.4 mm spacing for three G (1.08 - 1.93 kg/sm^{2}bar) values. This was caried out using only the standard k - ε turbulence model (based on Figure 4.12) for both hex and tet grids, it shows that there is perfect agreement with the measured surfaced average *h* for the hex grid, while the tet grid poorly predict the this measured data. The results confirmed the justification that standard k - ε turbulence model gave better agreement possibly because this model linked the turbulence region with the BL. This is contrary to the pressure loss prediction of Figure 4.10 that show good predicted data, indicating that is the grid in the gap that requires refinement, especially the tet grid close to the wall. Table 4.6 and Figure 4.8 show that the present total cell size for the tet grid is large enough and so could be more, this can take longer time to give a converged solution, if low Re model is used as the number of cells will significantly increase. Figure 4.14 compares the predicted and measured locally X^2 averaged HTC *h*, over the 10 impingement jet holes and for two G of 1.08 and 1.93 kg/sm^{2}bar values that were based on surface distribution shown in Figure 4.15 and Figure 4.16. These are for the two grid types and with standard k - ε turbulence model, only the hex grid gave very good agreement with the measured data.

Figure 4.15 (i a - d and ii a - d) show the surface distribution of Nusselt number Nu on the target wall, which compares the wall function RANS and RSM turbulence models and are for the two grid types, at fixed X/D of 4.66, Z/D of 3.06 and mass flux G of 1.93 kg/sm^{2}bar. This show that the standard k - ε model predict the experimental deterioration of heat transfer with axial distance correctly [5, 22, 25]. By comparing the target surface distribution of the Nusselt number for the two grids using standard k - ε turbulence model as Figure 4.16 (a and b) show, the hex grid of Figure 4.16 (a) gave better and agreeable distribution. This is based on the comparison shown in Figure 4.17 of the surface Nu measured distribution found using liquid crystals [115, 132], by which the hex grid gave near perfect agreement.

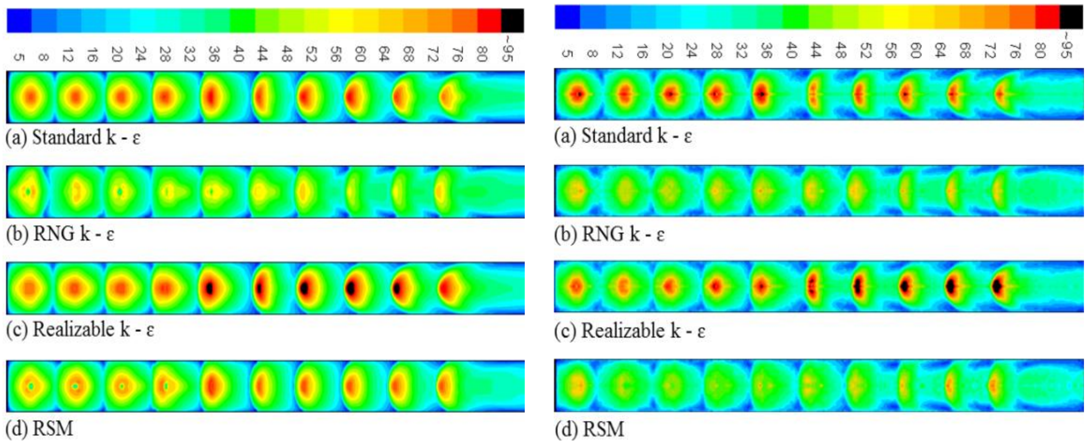

(i) Hex grid

(ii) Tet grid

Figure 4.15: Comparisons of two grid types predicted impingement jet target surface distribution of Nusselt number Nu for the types of wall function RANS turbulence models

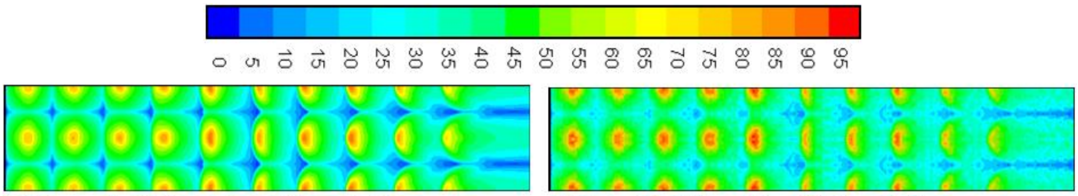

(a) Hex grid: X/D = 4.7 and Z/D = 3.06

(b) Tet grid: X/D = 4.7 and Z/D = 3.06

Figure 4.16: Comparisons of two grid types predicted impingement target surface distribution of Nusselt number Nu using wall function standard k - ε turbulence model

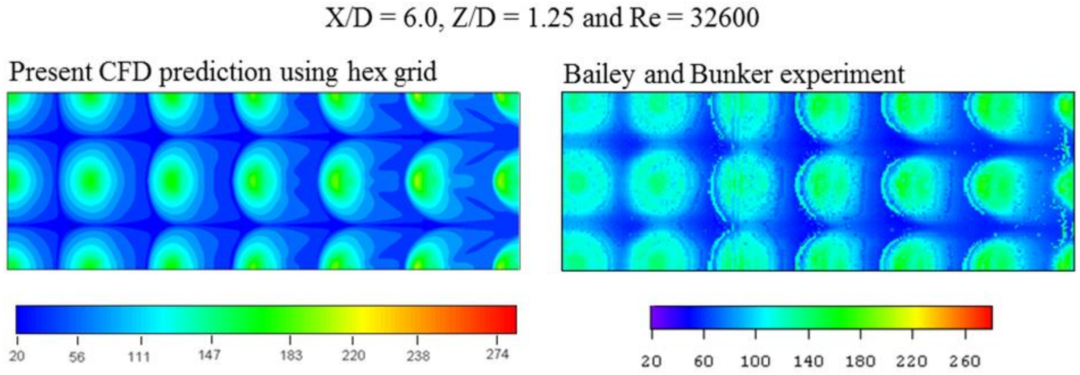

Figure 4.17: Comparisons of predicted impingement target surface distribution of Nusselt number using wall function standard k - ε turbulence model for hex grid and experiment

Comparison of the hex grid predicted and measured data of Bailey and Bunker [132] Nusselt number target surface distribution of Figure 4.17 are for fixed X/D, Z/D and Re of 6.0, 1.25 and 32600, respectively. These range of agreements, indicates that not only is the aerodynamics that the hex grid using wall function standard k - ε turbulence model are adequately predicted, but also the heat transfer data.

4.4.3 Prediction of Flow-Maldistribution

El-jummah *et al* [32] showed that the flow-maldistribution with the leading holes receiving 7% less air, while the trailing holes receiving 9% more air was in excellent agreement with a simple 1D computation, whereby 16% total flow-maldistribution was predicted. This strongly supports the view that the flow-maldistribution was driven by the static pressure difference along the duct. Figure 4.18 (a and b) are the predicted flow-maldistribution for the hex and tet grids of the impingement jet single exit flow. The predicted impingement hole velocity enables the mean velocity of each hole to be determined, which was calculated in the middle of the hole to avoid any inlet and outlet flow recirculation zones. This predicted mean velocity for each hole as shown in Figure 4.18 (a and b) have been normalised to the mean velocity for all the holes and is the flow-maldistribution that was set by the total mass flux G of Table 4.11 for which this computation was carried out. This show that both the hex and tet grids of all the WF turbulence models predicted the holes flow-maldistribution correctly, but with haphazard central holes distributed flow for the tet grid which could affect heat transfer. This should be based on the fact that the tet grid calculations was at centre of tetrahedral nodes, while the hex grid that gave smooth and continuous maldistribution was because the calculation was based on the cell centre. The only way to pick out the data from the tet grid was to tilt the hole centre plane along the length or the nodes, or the surface central plane will be seen as zero since velocity on the wall is zero (no-slip condition) [42].

The CFD predictions of the flow-maldistribution for range of G from 1.08 - 1.93 kg/sm^{2}bar using standard k - ε turbulence model for hex and tet grid, are shown in Figure 4.19. This predicted velocity profile across the impingement holes at a position upstream of the exit used the same approach as found in Figure 4.18 and was based on Table 4.11 calculated mean. Figure 4.19 show that the flow mal-distribution increases from ~ 11 to 18 % for hex grid and from 7 to 22 % for tet grid as the total mass flux G increases. By approximation both predictions are satisfactory, even though the differences in the tet grid prediction was high and can influence the heat transfer prediction. Figure 4.18 (b) and Figure **4.19** both for the tet grid, show some unexpected variations in the flow-maldistribution, which should have been a smooth variation with the number of holes as for the hex grid of Figure 4.18 (a) and Figure **4.19**.

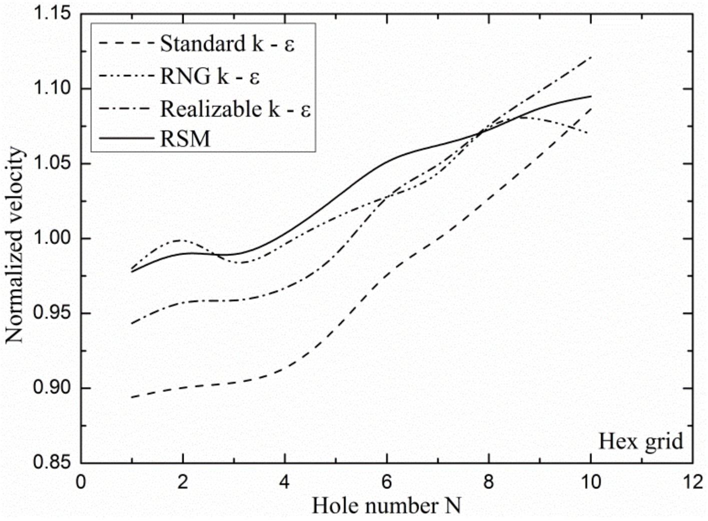

(a) Hex grid

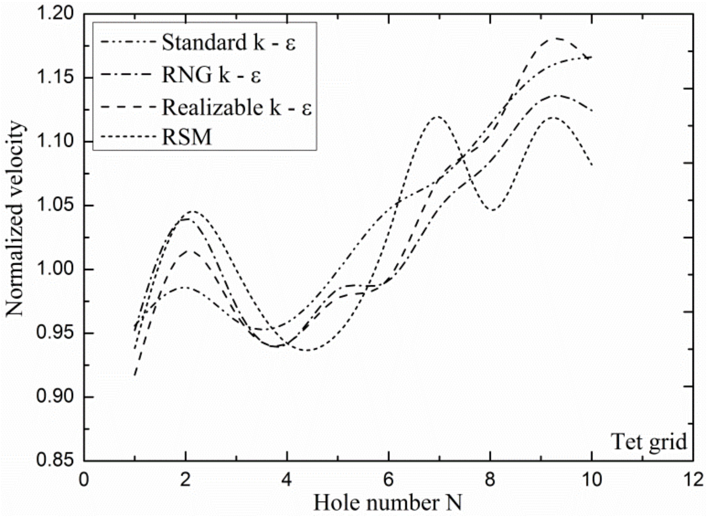

(b) Tet grid

Figure 4.18: Predicted impingement hole flow-maldistribution for the types of wall function turbulence models at fixed X/D of 4.66, Z/D of 3.06 and G of 1.93 kg/sm^{2}bar

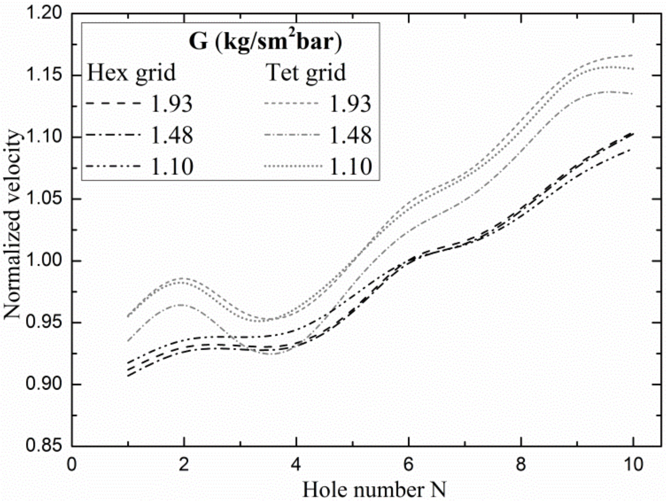

Figure 4.19: Predicted impingement hole flow-maldistribution of two grid types wall function standard k - ε turbulence model for three G values at X/D of 4.66 and Z/D of 3.06

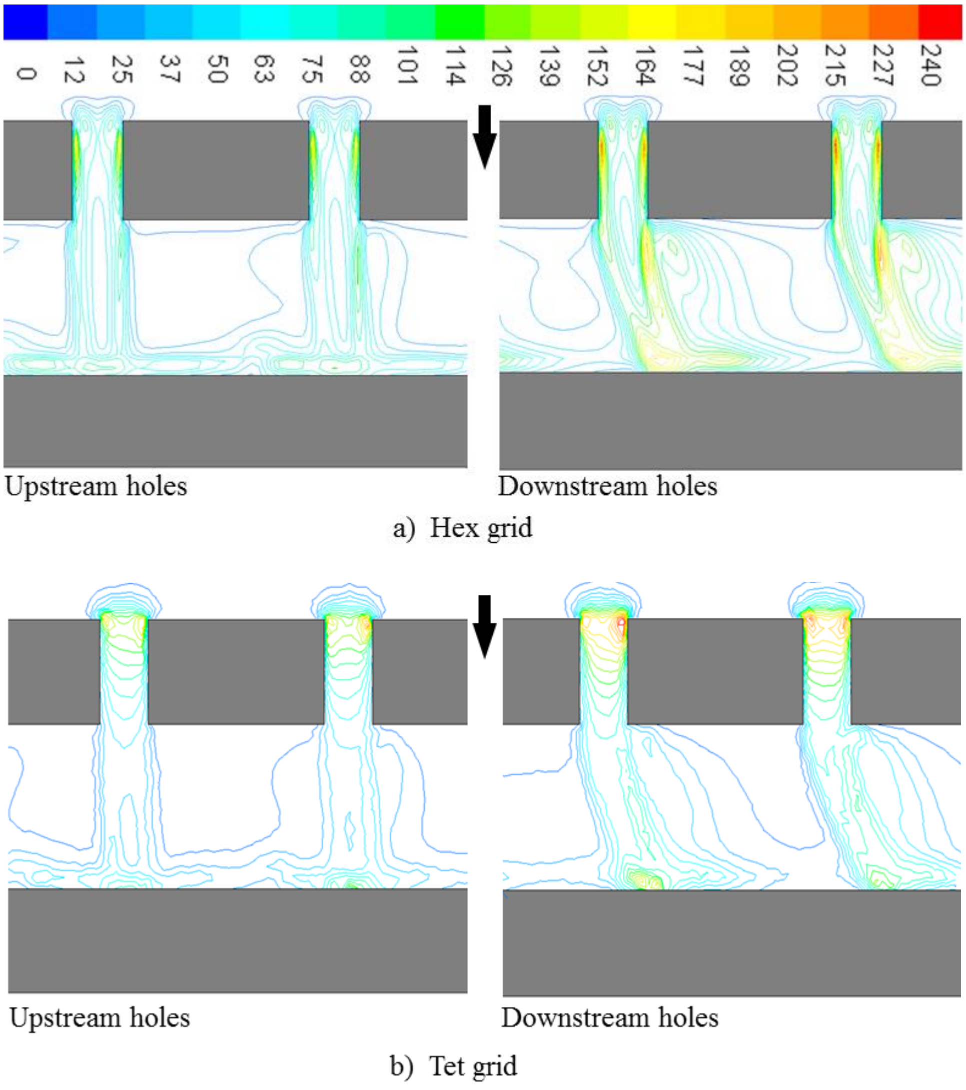

Figure 4.20: Contours of TKE (m^2/s^2) for the hole centre line symmetric plane using wall function standard k - ε model for fixed X/D of 4.66, Z/D of 3.06 and G of 1.93 kg/sm^{2}bar

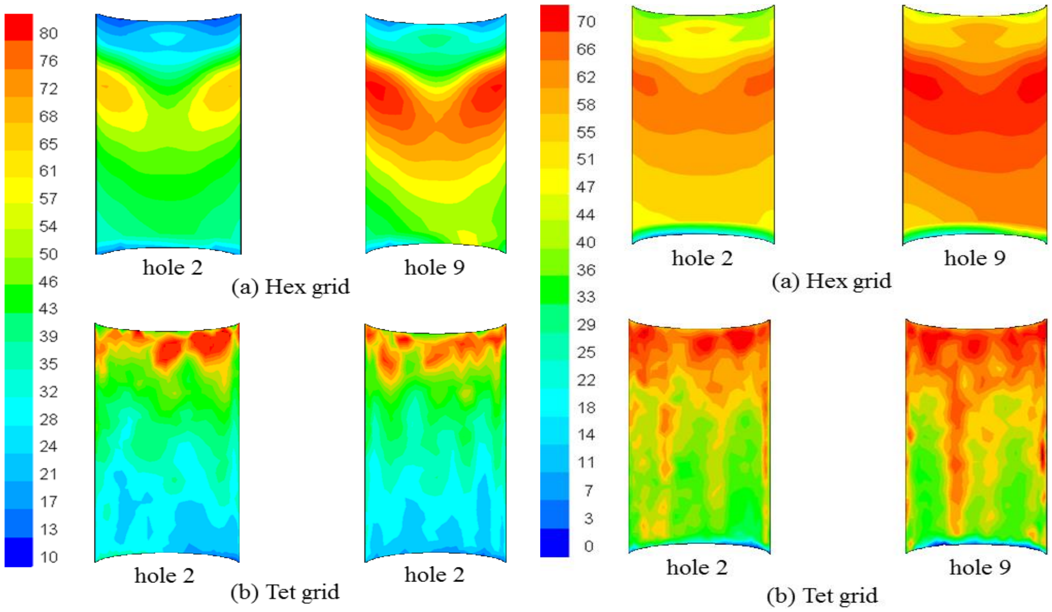

(i) TKE (m^2/s^2) contours (ii) Nusselt number contours

Figure 4.21: Impingement Jet holes surfaces aerodynamics and heat transfer using wall function standard k - ε model for fixed X/D of 4.66, Z/D of 3.06 and G of 1.93 kg/sm^{2}bar

4.4.4 Influence of Aerodynamics on Impingement Hole Surface

The aerodynamics of the impingement jet short hole, typically the turbulence has been shown to influence wall heat transfer [25, 46, 73, 80, 83]. The influence of the turbulent kinetic energy (TKE) inside the impingement jet upstream and downstream holes that was predicted using the hex and tet grids with a wall function standard k - ε turbulence model, is shown in Figure 4.20 (a and b). The hex grid predictions of Figure 4.20 (a) show that the short hole flow separation, reattachment and development [80] were all correctly predicted, this also influenced the surface TKE of Figure 4.21 (i a) [25, 46]. Figure 4.20 (b) predicted TKE show that the short hole flow characteristics are absent on the tet grid, which also predicted poorly the hole surface TKE of Figure 4.21 (i b). These TKE predictions of the hole wall surfaces also influenced the Nusselt number predictions of Figure 4.21 (ii a and b), whereby both the grids predicted Nu show the same pattern with the hole surface TKE. Figure 4.21 (ii a) show that all the aerodynamics features that influenced the surface heat transfer are also shown, while Figure 4.21 (ii b) show that these, do not exists.

4.5 Validation of Turbulence Models y^+ values

The empirical velocity profiles for turbulent pipe flow termed the power-law [42] and defined by Equation 4.1, was also applied to an effusion short pipe flow. The result is as shown in Figure 4.22 and is the profile for low Re and wall function turbulence models using hexa grid. Table 4.12 show the flow condition for a fixed X/D of 4.66 and at constant G of 1.93 kg/sm^{2}bar, from which Figure 4.22 was predicted and 1/7 power-law velocity profile calculated which are compared. The region that show normalized velocity in the range of unity indicates laminar flow and above unity is turbulence. The velocity profile for the standard k - ε turbulence model show smooth trend axially at the hole exit with averagely the highest turbulence level and SST k - ω has the poorest predicted profile.

$$\frac{V}{V_j} = \left(1 - \frac{r}{R}\right)^{1/\vartheta} \tag{4.1}$$

Where the exponent ϑ is a constant whose value depends on the Reynolds number Re, it increases with increased in Re. For $\vartheta = 7$, generally approximates many flows in practically application, which also give rise to the one-seventh power-law velocity profile. V is the velocity in the core region of the pipe (m/s), R is the pipe radius (m) and r is the axial variation along the radius (m).

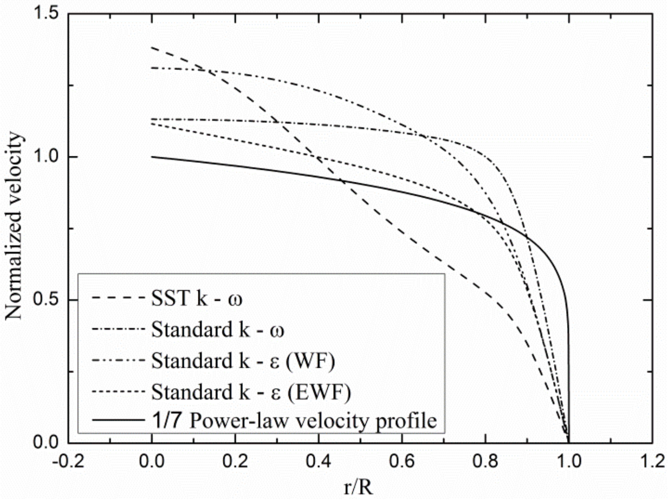

Figure 4.22: Comparison of predicted low and high Re turbulence models for varied y^+ values and power-law normalized hole outlet velocity profiles for G of 1.93 kg/sm^{2}bar

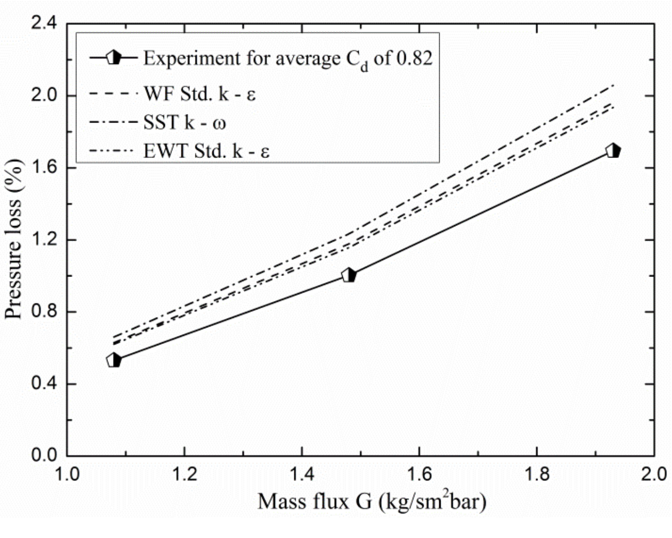

Figure 4.23: Comparison of predicted low and high Re turbulence models of varied y^+ values and experimental hole exit impingement gap pressure loss for fixed X/D = 4.66

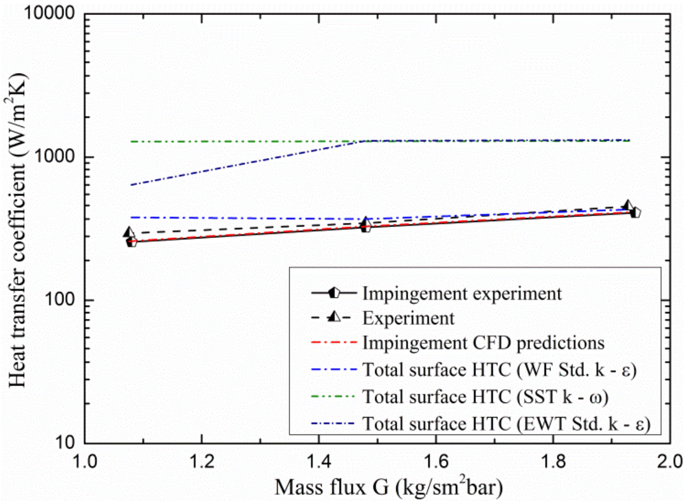

Figure 4.24: Comparison of predicted low and high Re turbulence models of varied y^+ values and experimental impingement and hole surfaces average HTC for X/D of 4.66

The geometry with X/D of 4.66 and L/D of 1.94 in Table 4.12, the discharge coefficient C_d was determined as 0.82 [83] and the pressure loss based on this C_d, is shown as a function of the mass flux G in Figure 4.23. Only the three CFD turbulence models that predicted the inlet flow separation and reattachment are shown and will be shown later, as the other models did not predict the correct flow or pressure loss correctly. The standard k - ε model with standard wall function and enhanced wall function were very similar, with the enhanced wall function slightly closer to the experimental measurements for the C_d of 0.82.

The SST k - ω turbulence model gave a higher predicted pressure loss than either of the other two turbulence models. However, even the best agreement with the k - ε model was a higher predicted pressure loss than the measurements. This indicates that the inlet flow separation and reattachment had not adequately been predicted. The most likely cause of the disagreement would be over prediction of the skewness of the outlet velocity profile so that the hole outlet pressure loss was over predicted. The exit pressure loss, if the velocity profile across the outlet area was uniform is one dynamic head and if the flow was laminar with a parabolic velocity profile the exit pressure loss would be 2 dynamic heads. This illustrates that the prediction of the hole outlet velocity profile has to be correct if the pressure loss is to be adequately predicted.

Figure 4.24 show the predicted total surface average HTC *h* as a function G and was the combination of hole approach *h* + its surface h_x found from Equation 2.24 and 2.25. These predictions are for the standard k - ε (WF and EWF) and the two k - ω turbulence models. Also compared in Figure 4.24 are the CFD prediction and experiments by El-jummah *et al* [46] and the Experiment by Andrews and Mpadi [83]. The standard k - ε turbulence model (WF) predicted closely the total surface average HTC of the experiment [83] for G of 1.48

and 1.93 kg/sm^{2}bar with a slight over prediction for the 1.08 kg/sm^{2}bar. While the SST k - ω and the standard k - ε (EWF) turbulence models over predicted the total surface HTC. This is unexpected as the grid in the hole has been adequately refined, which means that is the aerodynamics in the hole that is important here. This prediction also show that the total surface HTC is slightly above the surface average HTC of the impingement target wall that was shown in Figure 4.13. This indicates that the impingement jet wall heat transfer that has been shown to be affected by reversed heated jets which heats up the impingement jet plate [25, 46] should not be overlooked.

4.5.1 Aerodynamics Inside Short Hole

The predicted velocity vectors are shown in Figure 4.25 (i) for an X/D of 4.66 and L/D of 1.94 and for a range of turbulence models. All the turbulence models predicted flow separation at the hole inlet. Reattached flow inside the hole was only predicted by the k - ε turbulence model, in both standard WF and EWF and by the SST k - ω model but the flow

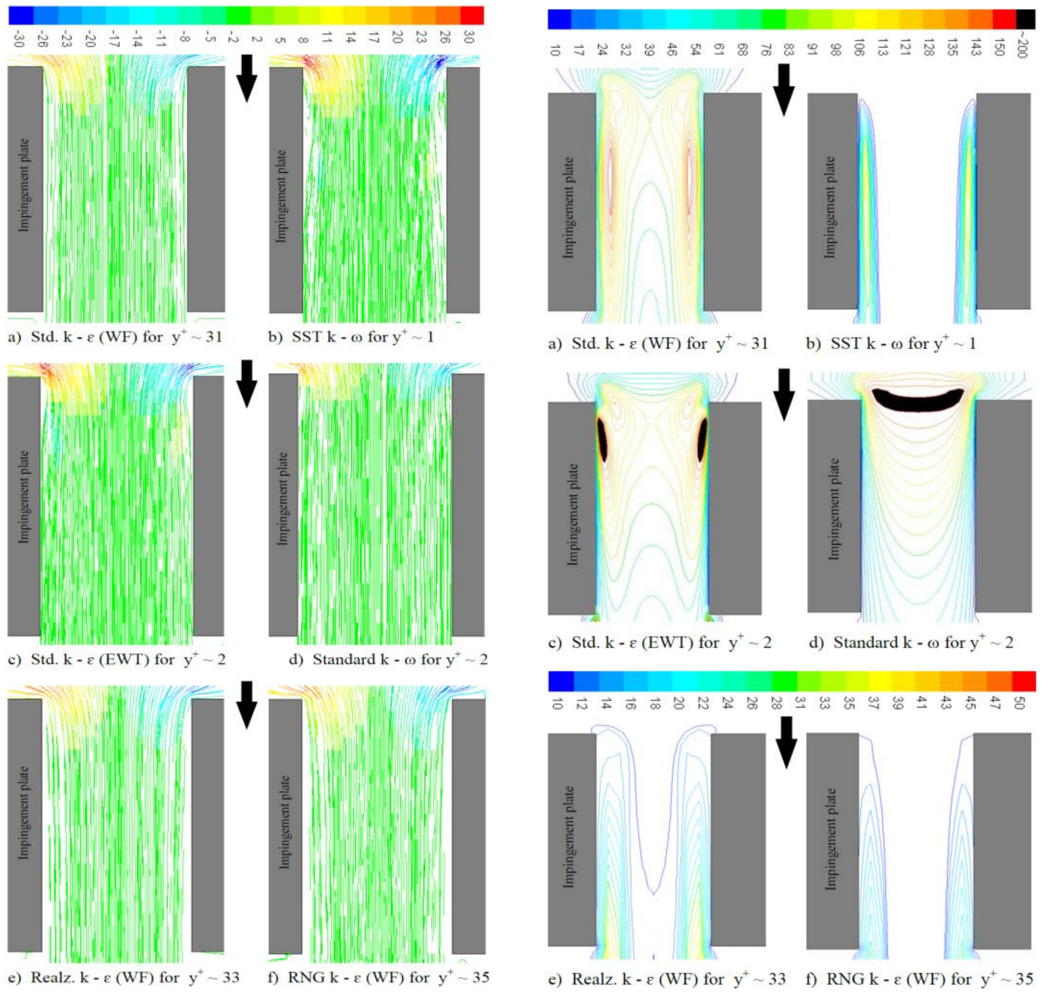

(i) Pathlines of x-velocity vector (m/s) (ii) Contours of TKE (m^2/s^2)

Figure 4.25: Predicted low and high Re turbulence models of varied y^+ values holes aerodynamics for fixed X/D of 4.66 and G of 1.93kg/sm^{2}bar

here interacts within gap of the wall and separated flow. The realizable k - ε and RNG k - ε turbulence models with standard wall functions did not predict flow reattachment within the length of the hole. In terms of predicting the inlet flow separation and reattachment there was no advantage of the more advanced models and advanced wall functions compared with the standard k - ε and standard wall function model.

The predicted turbulence kinetic energy (TKE) for an X/D of 4.7 and L/D of 1.94 is shown in Figure 4.25 (ii). With flow separation, the recirculation zone is a region of high TKE which occurs within an L/D of 1 and is normally centred at 0.4 - 0.5 hole diameters from the inlet [73, 83]. The standard k - ε with standard wall functions predicts the inlet flow separation and high TKE in the inlet recirculation zone. The k - ε with enhanced wall functions also predicts the turbulence in the expected location and the standard wall functions have the region of high turbulence over a larger proportion of the hole length than would be expected. However, this is an area where there are no good turbulence measurements due to the presence of the walls that make laser Doppler anemometry (LDA) measurements difficult. However, it is clear that all the other models either predict the turbulence in the wall region is extended over too long a distance or is predicted to be at the hole inlet away from the walls, as for the k - ω turbulence model with $y^+ \sim 2$. This poor predictions of the TKE should be the reason for the disagreement of the predicted total surface HTC shown in Figure 4.24 using EWF and SST with measured data.

4.5.2 Short Hole Heat Transfer

The surface distribution of the predicted HTC inside the hole is shown in Figure 4.26 for an X/D of 4.66 and for six turbulence models. Only the k - ε turbulence model with standard wall functions predicted the enhanced heat transfer at the separated inlet flow reattachment point. The k - ε with enhanced wall functions predicted the flow reattachment with high heat transfer much too far downstream of the hole, as did the SST k - ω turbulence model. The realizable k - ε and RNG k - ε, both with standard wall functions, had a prediction that there is no enhancement of the hole surface heat transfer due to the short hole inlet flow, which is incorrect. This must be the reason for the very good agreement with the measured surface averaged heat transfer for the standard k - ε and poor agreement for the other low Re models of Figure 4.24.

Part of the wall heat transfer due to an array of holes is due to the acceleration of the flow into the hole. This creates high radial inward flow velocities around the perimeter of the hole inlet. This is predicted in Figure 4.27 for the k - ε turbulence model with standard wall functions. Figure 4.27 also compares these predicted hole inlet surface distribution of

Nusselt number predictions with those measured by Cho *et al* [79, 80], for the closest Re to the present work. This show a very similar distribution and value of surface heat transfer close to the hole inlet as predicted in Figure 4.27 (b) - top. Also shown in Figure 4.27 (b) - bottom, is the enhanced heat transfer due to entrained flow into the hole outlet free jet flow. This is lower than for the enhanced inlet surface heat transfer but never the less is significant. It is debatable whether this discharge surface heat transfer is part of the overall wall heat transfer in the presence of a cross-flow, when the wall is an effusion wall, or when there is cross-flow in impingement jet cooling. However, in the experimental measurements this discharge jet heat transfer was present and hence is part of the validation of the computational procedures. Cho *et al* [79] have pointed out that this outlet jet entrained flow surface heat transfer might not be present in effusion cooling, due to the outlet cross-flow. The present computations would enable the heat transfer of the flow through effusion type walls to be computed without the external entrained flow. The experimental results could also be corrected for this effect using these CFD results.

The hole inlet and outlet surface predicted Nu distributions for X/D from 1.86 to 11.06 are shown in Figure 4.28 (a). The effect of decreasing X/D at constant X is for constant mass flux G to increase the velocity in the hole. This increases the velocity approaching the hole

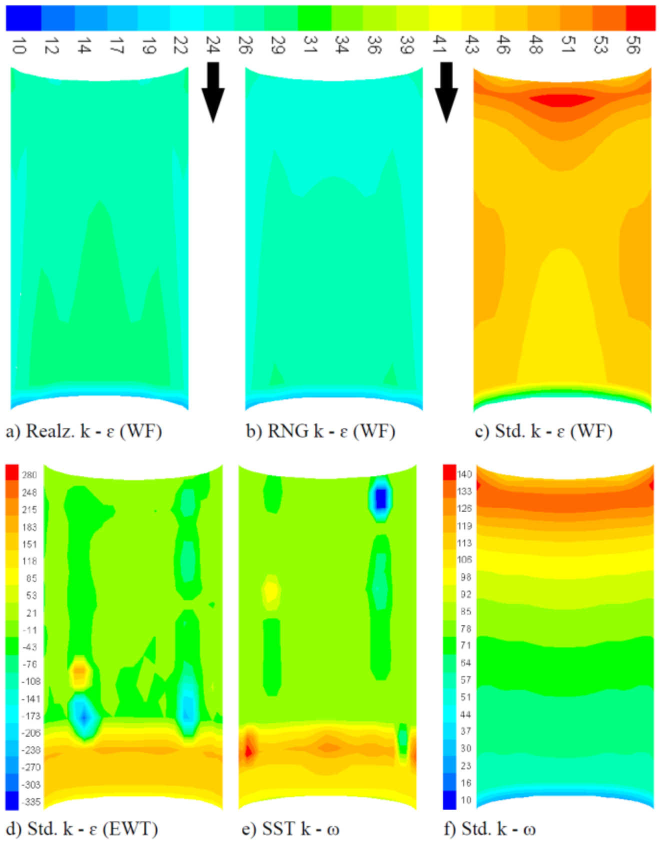

Figure 4.26: Predicted contours of Nusselt number on hole surfaces for the types of low and high Re turbulence models for a fixed X/D of 4.66 and G of 1.93kg/sm^{2}bar

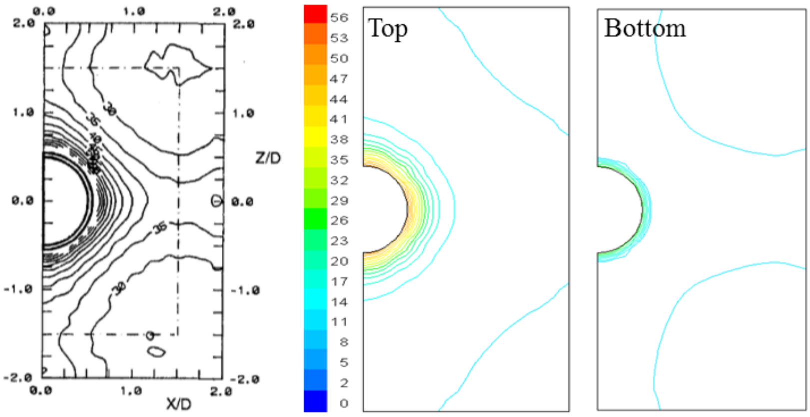

a) Re = 11800

b) Re = 9660 for X/D = 4.66

Figure 4.27: Comparison of experimental (on the left) and standard k - ε model (WF) predicted Nusselt number surface distribution on the jet hole approach (or inlet) surface

and hence increases the Nu on the hole approach surface, the same happens on the hole discharge surface. These predicted effects are the influence of high TKE inside the holes as Figure 4.28 (b) for the range of X/D from 3.06 - 11.04. For low X/D the heat transfer is less concentrated inside the hole due to lower turbulence. These distributions are unexpected and show a different pattern with increase in X/D. If there was a uniform flow separation and reattachment at the inlet, then there would be a uniform high heat transfer at the reattachment position. This would be a zone of high heat transfer around the circumference of the hole about half a hole diameter from the inlet, where the peak turbulence occurs. The predictions show this for X/D = 1.86 and 4.66, but for the other X/D there is clear evidence of a predicted 3D effect with two concentrated high heat transfer regions in the half of the surface shown. This would give four high Nu zones for the complete hole. This implies that the inlet flow separation did not result in a uniform rolling 2D vortex, but was split into four separate vortices with high heat transfer at the centre of these vortices. This is most clearly seen in the predictions for an X/D of 11.04.

4.5.3 Short Hole Thermal Entry Length Effects

The predicted pressure loss as a function of X/D for the standard k - ε turbulence model with standard wall function is shown in Figure 4.29 compared with the experimental results for a constant G of 1.93 kg/sm^{2}bar. Comparison at constant mass flux is more relevant than at constant Re, as the Re varies due to the hole diameter difference at each X/D [83]. The results show that for X/D < 6.5 the predictions were slightly higher than the measurements and for X/D > 6.5 were slightly lower than the measurements and at X/D of 6.5 were in exact agreement. Overall these good pressure loss predictions indicated that this turbulence model with standard wall functions adequately resolved the internal aerodynamics inside the hole, which controlled the relative pressure loss ΔP/P.

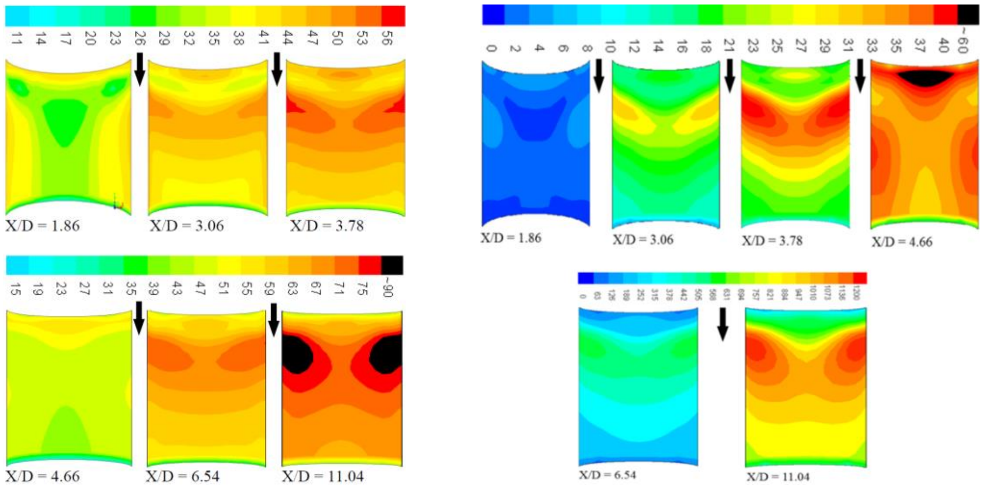

(a) Nusselt Number (b) TKE (m^2/s^2)

Figure 4.28: Contours of plots on hole wall surface for range of X/D at G = 1.93kg/sm^{2}bar

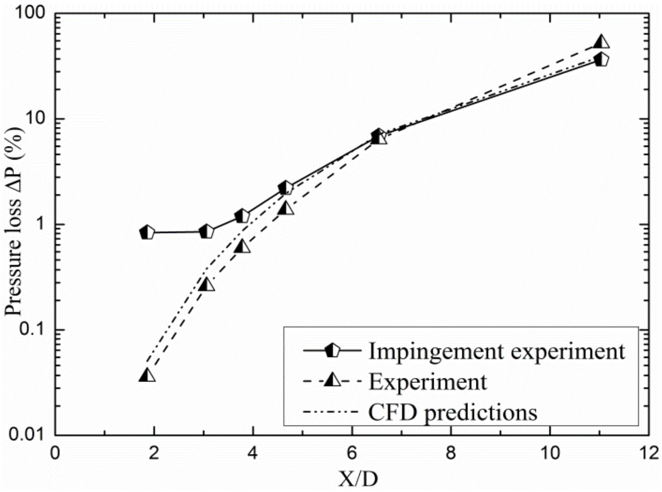

Figure 4.29: Comparison of standard k - ε turbulence model (WF) predicted and experimental ($C_d = 0.82$) pressure loss for a fixed G of 1.93kg/sm^{2}bar using hex grid

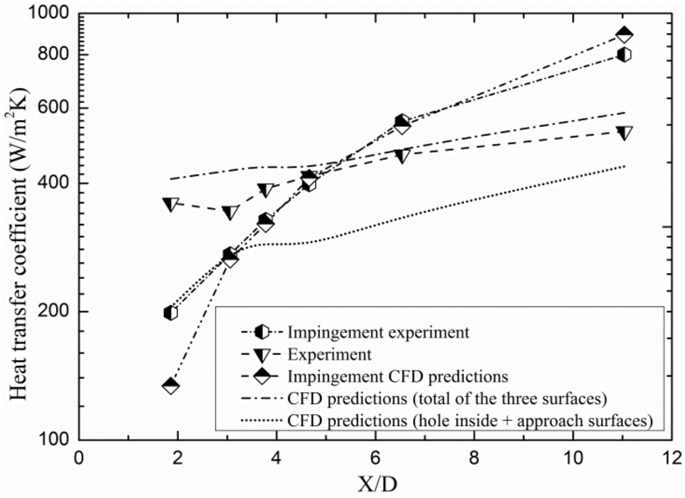

Figure 4.30: Comparison of standard k - ε turbulence model (WF) predicted and experimental hole approach and inlet surfaces average HTC for a fixed G of 1.93kg/sm^{2}bar

The surface variation of the short hole heat transfer shown in Figure 4.28 (a) combined with the approach surface were predicted and are shown in Figure 4.30, also predicted was the addition of the discharge wall to this. These were compared with single exit flow impingement jet CFD predictions and experimental results, also compared was with similar geometrical measured data and are as a function of X/D. The results show that the combination of the predicted three surfaces agreed with the measured data. Figure 4.30 also show that the heat transfer data of smaller X/D of 1.86 and 3.06 values perfectly agreed with impingement single exit flow measured data, which show the significance of L/D. In both cases, the trend of the results are similar, which indicate that the predictions are correct.

4.6 Conclusions

The CFD predicted aerodynamics for a 10 row impingement square array with single sided cross-flow had a predicted pressure loss in reasonable agreement with the experimental measurements. The complexity of the aerodynamics of impingement flow with large numbers of holes and flow exit in one direction has been clearly demonstrated. This is an indication that the flow separation in the impingement holes and the subsequent generation of turbulence from the pressure loss energy were correctly predicted. The comparison of the predictions with experimental results shows that hex grid using standard k - ε turbulence model with standard wall functions better resolves the aerodynamics inside the holes.

The action of the cross-flow in impingement square array with single sided exit flow was to deflect the reverse jets in the gap and to decrease its effectiveness. The cross-flow also convected the surface turbulence downstream of the impingement point and thus reduced the average turbulence on the surface. The net result was a reduction in the mean local surface average heat transfer with distance on the impingement gap target wall. The CFD predictions of this heat transfer reduction using hex grid and standard k - ε turbulence model (WF) were in good agreement with the experimental measurements. But the use of tet grid requires that some refinements are employ, for which low Re turbulence models could be use.

These results led to the conclusion that the standard k - ε turbulence model with standard wall functions could estimate, the combination of the short holes and impingement gap aerodynamics, as well as the known variation of surface heat transfer in the holes and on the impingement target plate. The range of y^+ value from 30 - 35 have been used, which have shown very good predictions of the measured heat transfer data.

CHAPTER FIVE

SINGLE SIDED FLOW EXIT IMPINGEMENT HEAT TRANSFER COOLING RESULTS

Chapter 5

Single Sided Flow Exit Impingement Heat Transfer Cooling Results

5.1 Introduction

Impingement jet heat transfer of gas turbine (GT) combustor and turbine blade walls has been shown in Chapter 2, to employed the regenerative cooling application that are essential to ultra-low NOx industrial GT combustors [301-303]. The number of holes in the array has received little study in the literature, which has concentrated on the dimensionless groups pitch to impingement hole diameter ratio X/D and impingement gap to hole diameter ratio Z/D. These dimensionless parameters do not enable an impingement array to be defined unless X or D is known, and this immediately specifies the number of holes. Essentially a given surface area could be cooled by 100, 1000 or 10,000 jets holes [22], by which X/D and Z/D could be constant and all would fit the requirements of existing correlations. In the square array of N^2 holes, the hole density *n* is $1/X^2$. So even if X/D is fixed, hole density is not defined until X is fixed. The objective of the present study was to demonstrate that CHT CFD could identify the optimum *n* by fixing or varying X/D, Z/D and G based on the increase in thermal gradients in the metal wall as *n* is reduced.

Conductive heat transfer in the metal wall occurs in practical engines, but most experimental and CFD investigations of impingement heat transfer are for adiabatic wall conditions [5, 25]. The issue of the design of impingement systems in terms of the number of holes and the optimum X/D are not amenable to design from current correlations [22, 45]. Essentially the optimum impingement cooling design for a fixed Z, is for the lowest number of rows of holes N and the largest X/D that can be tolerated without excessive thermal gradients in the metal wall. This cannot be determined from experiments with adiabatic walls. Basically the thermal gradients, will determine the number of holes and the maximum pitch X allowable and this will determine the optimum number of holes. The present work investigates the influence of X/D at fixed and varied *n*, whereby CHT CFD will be use to enable the optimum impingement cooling designs and predict the wall metal temperatures and thermal gradients.

Experimental investigations showed that impingement gap generated cross-flow increases as the number of impingement jets increase or the surface area to be cooled increases [45]. This cross-flow is particularly significant problem for regenerative cooling of the large surface area of combustor walls. It has also been shown to reduce heat transfer at the trailing edge [304-307], which also has associated complex aerodynamic jets interaction [308, 309].

The literature on impingement cooling is mainly for turbine airfoil cooling applications with low coolant mass flux and high pressure loss. The low pressure loss requirement necessitates relatively low X/D along the air hole geometry and a strong influence of impingement gap cross-flow pressure loss on the impingement hole flow-maldistribution [310, 311]. As turbine entry temperatures increase in modern low NOx high thermal efficiency GTs for power generation, the regenerative cooling requirements for impingement system become more difficult and this work investigates to show that CHT CFD could be reliably used in the design process.

5.2 Experimental Test Geometries and Flow Conditions

Chapters 2 and 4 showed the detailed descriptions, of the impingement jets experimental test rigs (Figure 2.3c) and associated test walls with embedded thermocouples locations (Figure 4.1 a and b) that were used for the present model computations. The thermocouples have been shown to measure a surface averaged temperature that were located at the lowest local convective heat transfer position, hence would give slightly higher temperatures than the mean and thus result in conservative heat transfer measurements and is the method used here. Therefore, the details experimental techniques are not shown, hence only the geometrical and flow variables will be discuss in this section. In addition to this is the hexahedral model grid computations, whereby Chapter 4 discussed the details procedures, using wall function standard k - ε turbulence model.

Table 5.1 -Table 5.4 shows the impingement square array geometries that were investigated experimentally [5, 22, 25, 43, 46, 99] and computationally. These are actual size practical combustor wall cooling geometries [25, 33, 45]. Experimentally, each air hole diameter was measured using a calibrated conical insert micrometre and the air hole size was the average of all the holes. The influence of varying G (for fixed Z/D) and Z/D (for fixed G) are shown in Table 5.1 and are for constant *n* and X/D. Table 5.2 is for a fixed *n* and G with varied X/D (at fixed X) and Z/D (not significant as Z is fixed), Table 5.3 is for a fixed X/D (of varied X and D) and G for varied *n* and Z/D (also not significant), Whilst Table 5.4 is for a fixed Z/D and G with varied X/D (of varied X only) and *n*. The discharge coefficients in Table 5.3 were determined on an airflow rig as in Figure 2.3 (a), with a free discharge that had no influence of the impingement gap on the flow. Table 5.5 - 5.6, shows the flow variables that have been calculated based on the impingement geometries and G.

The coolant mass flux G were measured using calibrated variable area flow meters with corrections for the air temperature and pressure, the accuracy relative to a calibrated orifice plate flow meter was 2%. The accuracy of the heat transfer coefficient HTC *h* measurements relied on the calibration of the thermocouples, which was minimised in the transient method

Table 5.1: Geometries for a Constant *n* of 4306 m^{-2} With Fixed X and D

Z/D	**6.42**	**4.89**	**3.67**	**3.06**	**2.14**	**1.22**	**0.76**
Z (mm)	21.0	16.0	12.0	10.0	7.0	4.0	2.5
D (mm)	3.27	3.27	3.27	3.27	3.27	3.27	3.27
X (mm)	15.24	15.24	15.24	15.24	15.24	15.24	15.24
***n* (m^{-2})**	4306	4306	4306	4306	4306	4306	4306
Array	10 × 10	10 × 10	10 × 10	10 × 10	10 × 10	10 × 10	10 × 10

Table 5.2: Geometries for Constant *n* of 4306 m^{-2} and X With Varied D

X/D	**11.04**	**6.54**	**4.66**	**3.78**	**3.06**	**1.86**
D (mm)	1.38	2.33	3.27	4.03	4.98	8.18
X (mm)	15.24	15.24	15.24	15.24	15.24	15.24
Z (mm)	10.0	10.0	10.0	10.0	10.0	10.0
L (mm)	6.35	6.35	6.35	6.35	6.35	6.35
L/D	4.60	2.73	1.94	1.58	1.28	0.78
Z/D	7.25	4.29	3.06	2.48	2.01	1.22
X/Z	1.52	1.52	1.52	1.52	1.52	1.52
A (%)	0.64	1.84	3.62	5.50	8.39	22.7

Table 5.3: Geometries for a Fixed X/D ~ 4.66

***n* (m^{-2})**	**1076**	**4306**	**9688**	**26910**
Array	5 × 5	10 × 10	15 × 15	25 × 25
N	5	10	15	25
D (mm)	6.54	3.27	2.20	1.31
X (mm)	30.48	15.24	10.16	6.10
Z (mm)	10.0	10.0	10.0	10.0
L (mm)	6.35	6.35	6.35	6.35
L/D	0.97	1.94	2.91	4.85
Z/D	1.53	3.06	4.55	7.65
X/Z	3.05	1.52	1.02	0.61
C_d		0.91	0.89	0.81

Table 5.4: Geometrical Parameters for Constant Z/D of ~ 7.0

X/D	**21.02**	**15.11**	**11.04**	**7.15**	**5.32**	**4.66**
D (mm)	1.45	1.44	1.38	1.42	1.43	1.31
X (mm)	30.48	21.77	15.24	10.16	7.62	6.10
Z (mm)	10.0	10.0	10.0	10.0	10.0	10.0
A%	0.18	0.34	0.64	1.54	2.78	3.62
***n* (m^{-2})**	1706	2110	4306	9688	17222	26910
Array	5 × 5	7 × 7	10 × 10	15 × 15	20 × 20	25 × 25

Table 5.5: Flow Conditions at a Fixed X/D and Z/D

G (kg/sm^{2}bar)	**0.35**	**0.71**	**1.08**	**1.48**	**1.93**
V_j (m/s)	7.7	16.0	24.3	33.5	43.4
V_c (m/s)	4.3	8.8	13.4	18.4	24.0
V_j/V_c	1.8	1.8	1.8	1.8	1.8
***n* (m^{-2})**	4306	4306	4306	4306	4306
Re_j (=V_jD/ν)	1650	3560	5400	7440	9680
T_∞ (K)	288	288	288	288	288
T_w (K)	353	353	353	353	353
ρ (kg/m^3)	1.225	1.225	1.225	1.225	1.225

Table 5.6: Flow Conditions for a Fixed G of 1.93 kg/sm^{2}bar

Z/D	**6.42**	**4.89**	**3.67**	**3.06**	**2.14**	**1.22**	**0.76**
V_j (m/s)	43.41	43.41	43.41	43.41	43.41	43.41	43.41
V_c (m/s)	95.68	59.80	34.17	23.92	19.93	14.95	11.39
V_j/V_c	0.45	0.73	1.27	1.82	2.18	2.90	3.81
$Re_g(=V_cD_H/\nu)$	28602	29452	30164	30540	31114	31712	32020
T_∞ (K)	288	288	288	288	288	288	288
T_w (K)	353	353	353	353	353	353	353
ρ (kg/m^3)	1.225	1.225	1.225	1.225	1.225	1.225	1.225

Table 5.7: Flow Conditions for a Fixed G of 1.93 kg/sm^{2}bar

n (m^{-2})	**1076**	**4306**	**9688**	**26910**
V_j (m/s)	43.41	43.41	43.41	43.41
V_c (m/s)	23.92	23.92	23.92	23.92
V_j/V_c	1.82	1.82	1.82	1.82
Re_j (=V_jD/ν)	19310	9660	6440	3860
T_∞ (K)	288	288	288	288
T_w (K)	353	353	353	353
ρ (kg/m^3)	1.225	1.225	1.225	1.225

Table 5.8: Flow Conditions at a Constant Z/D of ~ 7.0

	G = 0.35 kg/sm^{2}bar			**G = 1.08 kg/sm^{2}bar**		
X/D	**21.02**	**15.11**	**11.04**	**7.15**	**5.32**	**4.66**
V_j (m/s)	163.71	84.59	45.16	57.41	31.78	24.39
V_c (m/s)	4.44	4.43	4.43	13.42	13.40	13.47
V_j/V_c	36.87	19.10	10.19	4.28	2.37	1.81
Re_j (=V_jD/ν)	16148	8286	4240	5546	3092	2174
T_∞ (K)	288	288	288	288	288	288
T_w (K)	353	353	353	353	353	353
ρ (kg/m^3)	1.225	1.225	1.225	1.225	1.225	1.225

as temperature differences were the key measurement not the absolute temperature [5, 22, 25, 46]. The test wall had other thermocouples 25.4 mm away from the centreline. This enabled the variability in the transverse direction of the heat transfer to be determined. This variability could occur due to non-uniform flow distribution between the impingement holes that was due to hole manufacturing tolerances. These thermocouples showed a transverse variation of h of < 4%. The error in the least squared fit of the transient cooling data for temperature difference was < 1% and so the total error for h was < 5% and for coolant mass flux G, the error was 2%. These flow errors are roughly the size of the symbols for the experimental results in the plots of h, but the 5% error in h will be mark by a vertical bar on the experimental results.

The other experimentally measured variable was the impingement flow relative pressure loss $\Delta P/P$. It was measured as the static pressure difference from the plenum chamber to the external ambient air. This pressure loss was corrected for the one dynamic head pressure loss of the cross-flow that occurs at the exit from the gap using Equation 2.16, to compute the mean cross-flow duct exit velocity. The pressure loss was measured using a digital micro-manometer accurate to 0.01 mm wg and calibrated against a certified inclined water manometer. The pressure losses measured in the present work were around 2% of the plenum chamber absolute pressure and this was a pressure loss of about 200 mm wg. The pressure difference could be measured to better than 1% accuracy. The CHT CFD computes the pressure loss from the plenum chamber air supply to the static pressure on the impingement jet wall 25.4 mm downstream of the last row of impingement holes on the centreline between the holes.

5.3 Influence of Aerodynamics in Impingement Gap

The 3D particle paths of Figure 5.1 show the reverse jet flowing between the impingement jets, Figure 5.1 (a) is between the first two rows of holes and Figure 5.1 (b) is between the last two rows of holes. The reverse flow jet Figure 5.1a) is already deflecting towards the exit plane and this trend increases along the gap to the exit plane. Figure 5.1 (b) shows that this centreline reverse flow jet is deflected by 45° and is intensified by the cross-flow [32]. This jet has a strong impingement on the impingement air hole wall, well downstream of the jets that started the interaction. However, this impingement is at a lower velocity than at the leading edge and the distribution of turbulence around the jet is adverted downstream, as will be shown below.

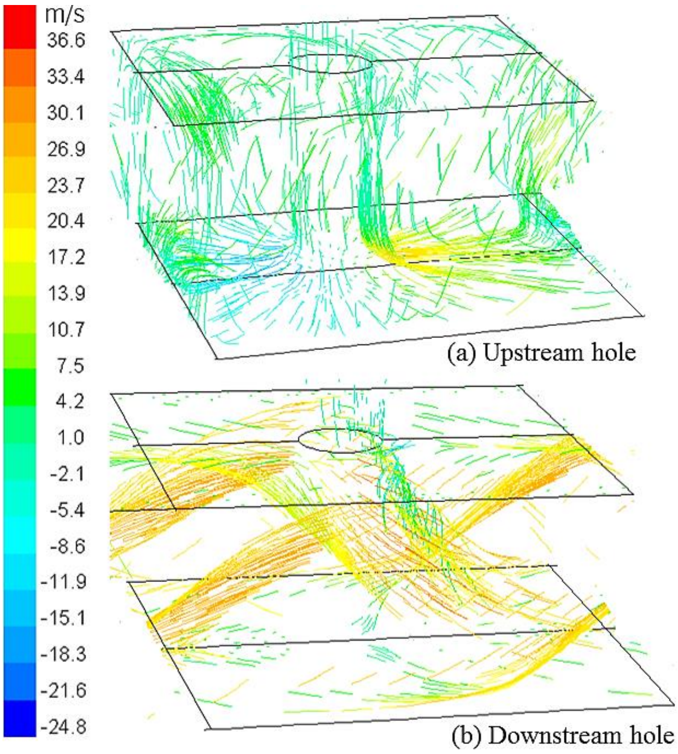

Figure 5.1: Impingement gap predicted velocity pathlines for X/D of 4.66 and Z/D of 3.06

5.3.1 Flow-Maldistribution

A feature of impingement cooling with single sided exit from the gap, is that the pressure loss generated by the cross-flow generates a flow-maldistribution for low impingement wall pressure loss. Equations 2.11 and 2.12 show that at constant G, the impingement wall pressure loss reduces as X/D reduces or A increases. Thus, at low X/D the pressure loss along the cross-flow direction is significant relative to the impingement wall pressure loss and flow-maldistribution occurs with the downstream impingement holes receiving more air [25]. Andrews and Hussain [81], showed using Equation 2.20 that flow-maldistribution could be predicted for incompressible jet flow by the ratio G_N/G_1, derived from the ratio y (Equation 2.19) of jet to cross-flow pressure loss. El-jummah *et al* [25] showed that the flow-maldistribution predictions were made based on the mean velocity in each hole at the midpoint of the hole length, which is shown as a ratio to the mean hole velocity based on equal mass flow distribution between the holes, given as V_j.

The mean velocity in a central plane within the impingment holes was evaluated from the CFD computations, which predicted the ratio of the flow through hole row 10 and row 1 as the flow-maldistribution [33]. Figure 5.2 shows the predicted influence of Z/D (Table 5.1) on the flow-maldistribution between the impingment holes created by the cross-flow. This shows that flow-maldistribution is of major importance for $Z/D < 3.06$ and of little significance for $Z/D > 3.06$. For Z/D of 3.06 the total maldistribution of coolant mass between the last hole and the first is 16%, which is in good agreement with the 1D flow predictions [33].

The predicted flow-maldistribution between the 10 rows of impingement holes for the ranged of X/D given by Table 5.2 is shown in Figure 5.3. Flow-maldistribution was predicted to be large for $X/D > 4.7$. The X/D of 4.66 is at the limit of the condition where flow-maldistribution between the holes starts to become a significant problem [308-311]. In Table 5.1, the Z/D ratio changes with reduced X/D as Z was held constant. For an X/D of 4.66, the predicted influence of Z/D [33] showed that the impact on the flow-maldistribution shows a very small difference of Z/D at this X/D. Thus, the big change in flow-maldistribution for an X/D of 1.86 at a Z/D of 1.22 predicted Figure 5.3 was due to the X/D effect and not the Z/D effect. This is because, a Z/D of 1.3 and X/D of 4.66 were shown to have the same flow-maldistribution difference, as for Z/D of 3.06 and X/D of 4.66. For an $N = 10$, X/D of 4.66 and Z/X of 0.656, Equation 2.17 gives a flow ratio of 1.15 (or 11.5%) flow difference between the first and last hole [46]. This is relatively small and shows that an X/D of 4.66 is just at the limit of where flow mal-distribution starts to become significant for lower X/D. Figure 5.4 shows that the flow-maldistribution is about 15% and increases from 12% to 20% as the total G increases from 0.35 - 1.93 kg/sm^2bar at this X/D.

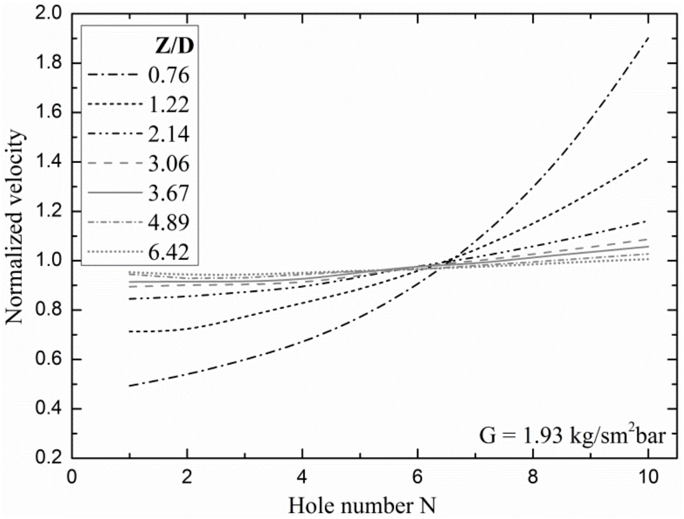

Figure 5.2: Impingement holes predicted flow-maldistribution for varied Z/D at constant G

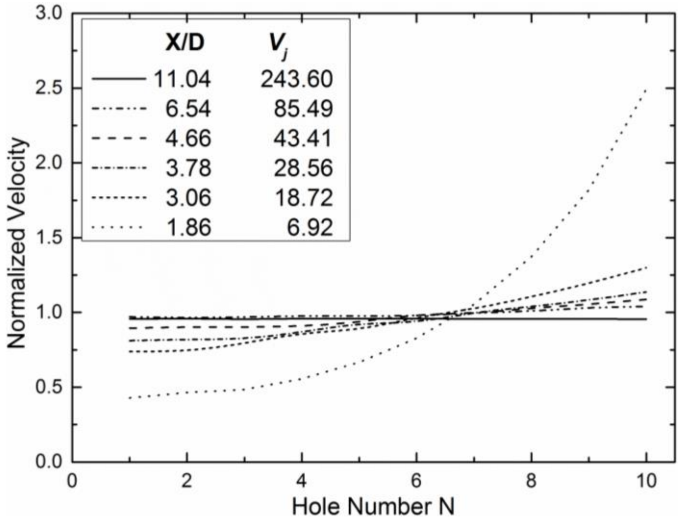

Figure 5.3: Impingement holes flow-maldistribution for varied X/D at G of 1.93 kg/sm^{2}bar

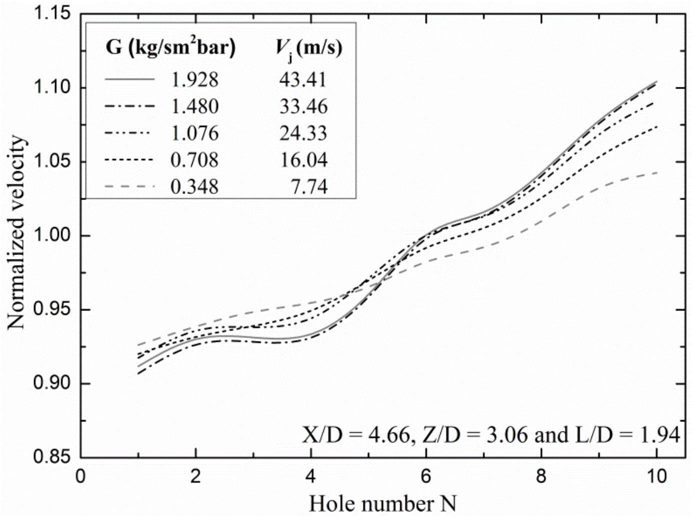

Figure 5.4: Impingement holes predicted flow-maldistribution for varied G at X/D and Z/D

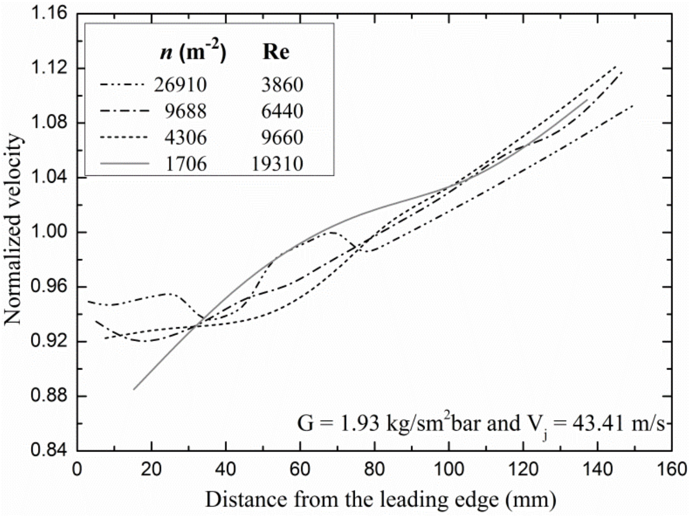

Figure 5.5: Impingement holes predicted flow-maldistribution for fixed G and X/D of 4.66

The prediction of the flow-maldistribution for varied *n* (or N) is shown in Figure 5.5, this indicates that there was a similar flow-maldistribution for all *n* and the differences in the shapes of the lines was due to the difference in the number of holes. The cross-flow alters the velocity profile (4, 5, 22) on the hole outlet and this effect varies with rows of N holes, which is far from uniform with the cross-flow. The predicted flow-maldistribution in Figure 5.5 is approximately 18% between the last and first hole. This is a greater influence of cross-flow on the flow-maldistribution than the 11% flow-maldistribution predicted by the simple 1D theory of Equations 2.19 and 2.20, which assumes a uniform V_c over the gap area. This is significant but relatively low and will not be a dominant feature of the impingement heat transfer, but it will reduce the deterioration in local surface average *h* with axial distance along the impingement wall surface [22].

The simple 1D flow-maldistribution theory of Equations 2.19 and 2.20 is increasingly in error with excessive flow-maldistribution predicted, as X/D was reduced compared with the CFD predictions [25]. The reason for this is that it has been assumed in the simple theory that the outlet velocity profile of each hole was not influenced by the cross-flow and that the impingement gap has its full area available for cross-flow. But the impingement jets block the cross-flow and this blockage gets greater as X/D reduces or D increases. This increases the pressure loss of the cross-flow as well as causing more jet deflection, however the main effect is that of the hole outlet cross-flow velocity profile [32] that produces a peak in the hole to its downward edge. Hence it increases the hole pressure loss for the downstream holes, which reduces the mass flow through that hole and thus reduces the flow-maldistribution given by 1D theory that ignores these effects. Thus the flow-maldistribution is lower at low X/D in the CFD predictions compared with the 1D predictions. This flow-maldistribution theory is based on a simple incompressible flow analysis.

5.3.1 Turbulence Kinetic Energy

The turbulent kinetic energy (TKE) on the impingement target wall is a key aerodynamic parameter as the surface turbulence levels controls the convective heat transfer [22, 25, 32, 33, 46]. The predicted spatial distribution of TKE for the geometries in Table 5.1Table 5.2 are shown in Figure 5.6 and are for G of 1.93 kg/sm^{2}bar. Varied Z/D and X/D are the only chosen geometries, as these are the major varied parameters that the influence of TKE is more significant, which are based on their varied D and Z. The contours in the plane of the impingement jets in Figure 5.6 (left) show high turbulence inside the impingement holes and peak turbulence in the shear layer at the edge of the impingement jets, which varies with geometries. In the downstream portion of the impingement gap the turbulence is deflected downstream and peak turbulence varies on the target wall (right). This leads to the reduction or increased in heat transfer as Z/D and X/D are varied as will be shown later. The impingement jets flow along the surface with high turbulence and then impinge against each other. This gives another generation of turbulence between the impingement jets as shown in Figure 5.6 and can results in a similar Nu distribution that was found using Equation 2.35.

The predicted TKE distributions for the various Z/D are shown in Figure 5.6 (i) on the centreline of the impingement jets (left) and on the impingement target wall surface (right). Figure 5.6 shows another important influence of flow-maldistribution at low Z/D, which moves the zone of highest turbulence to the downstream region of the impingement cooled wall. For larger Z/D it indicates in Figure 5.6 that the action of the cross-flow is to convect turbulence away from the impingement target wall surface. Turbulence is predicted to be distributed across the cross-flow instead of being concentrated on the target surface. This results in the deterioration in impingement heat transfer with distance, as found experimentally in Figure 2.5 of Chapter 2.

The predicted TKE in the gap in-line with the jets (left) and the target wall (right) for the range of X/D is shown in Figure 5.6 (ii). This shows that a major action of the cross-flow is to convect the high turbulence shear layer downstream around the jet and this effect increases as X/D is reduced. The action of the cross-flow prevents the impingement jets from flowing upstream on the surface and thus there is no surface flow impingement between the surface jet flows, which reduces the creation of turbulence on the surface. On the target surface, the peak turbulence lies below the impingement point of the jet and there is low turbulence at the reverse flow jet position on the wall. The peak turbulence decreases as X/D is decreased due to the associated reduction in peak impingement jet velocities for the same mass flux. Figure 5.6 (ii) also shows the impact of the cross-flow on the target surface turbulence distribution, this is negligible at an X/D of 11.04, but becomes increasingly significant as X/D is reduced. Figure 5.6 (ii) shows that at an X/D of 4.66 or below the convection of the turbulence downstream of the impingement point is an increasing feature of the effect of cross-flow. Also, the flow-maldistribution starts to increase the peak turbulence in the downstream portion of the cross-flow at low X/D.

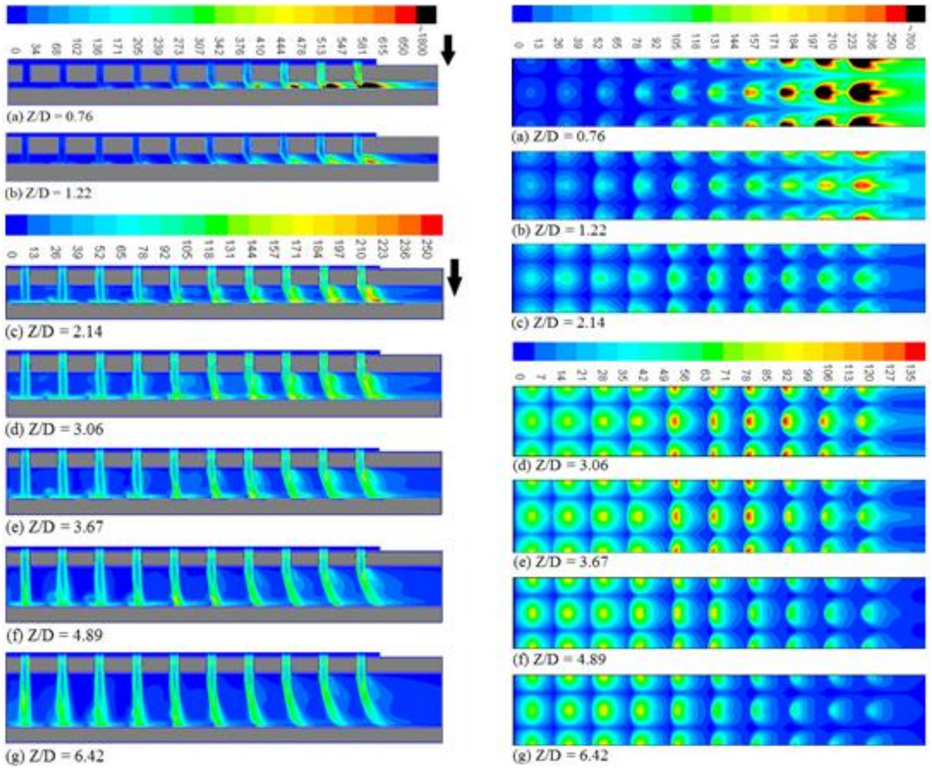

(i) Range of Z/D for a fixed X and D

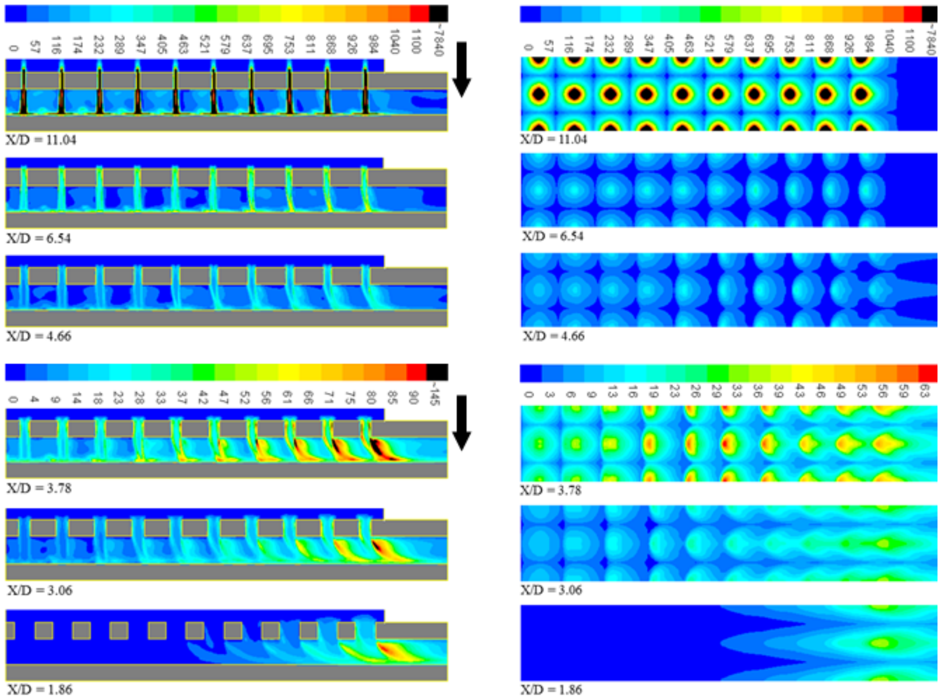

(ii) Range of X/D for a fixed X and Z

Figure 5.6: Predicted contours of TKE (m^2/s^2) for G of 1.93 kg/sm^2bar

5.4 Predicted and Measured Pressure Loss

The pressure loss was the only aerodynamic parameter measured in the experimental work. The size of the holes and the X and D values were too small for aerodynamic measurements to be made in the impingement gap. The bulk of the pressure loss occurs in the flow through the impingement holes and is controlled by the flow separation at the sharp edged air hole inlet and its subsequent reattachment to the air hole wall at around an L/D of 1 [22, 76]. Therefore, the holes with L/D ~ 1 are sufficiently long to ensure that this occurred.

The impingement jet velocity and the aerodynamics of the flow inside the holes, controls the pressure loss [80, 83]. Total pressure loss is a key aerodynamic parameter as it is controlled by the flow of air through the impingement holes, where inlet flow separation and flow reattachment occur. The interaction of the cross-flow with the impingement jets must also be correctly predicted, if the increase in pressure loss due to cross-flow is to be adequately predicted. The CFD predictions enable the pressure loss through the impingement jet wall and that along the impingement gap due to the cross-flow to be determined. The predicted pressure loss is the static pressure in the air supply plenum chamber minus the static pressure at the impingement jet wall on the centre point between the holes.

5.4.1 Hole Exit Pressure Loss

Figure 5.7 shows the predicted change in the impingement wall pressure loss as a function of the hole number along the gap for Z/D from 0.76 to 6.42. Figure 5.7 shows that there was a significant increase in the pressure loss for Z/D < 3.06. At very low Z/D there was a major component of the pressure loss due to the flow along the gap. At Z/D = 0.76 the pressure loss through the wall at the first hole was 0.7% and increased to nearly 6% by the tenth hole. For Z/D > 3.06 the pressure loss across the impingement wall dominated the pressure loss. These results show that any increase in the impingement heat transfer at low Z/D occurs with an increase in pressure loss. If comparison was made at the same pressure loss the impingement wall at Z/D > 3.06 should have a smaller hole size to increase the pressure loss to that of the low Z/D impingement geometry. This has not been done in any experimental work on the influence of Z/D on impingement heat transfer. Thus the apparently significant influence of low Z/D on impingement heat transfer is mainly due to the increased pressure loss and hence increased turbulence levels that occurs at low Z/D.

This predicted pressure loss for varied X/D from 1.86 - 11.04 is shown in Figure 5.8, as a function of the axial distance along the impingement gap in terms of the number of holes. Equations 2.11 and 2.12 show the strong link between the pressure loss and X/D and the impingement wall porosity A. Thus at high X/D of 11.04, the pressure loss at the high coolant mass flux of 1.93 kg/sm^{2}bar was predicted to be very high which is at an unrealistic

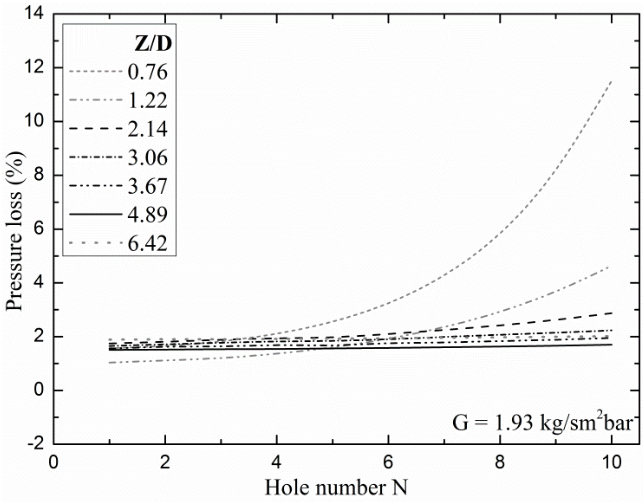

Figure 5.7: Impingement jet holes predicted pressure loss for varied Z/D at constant G

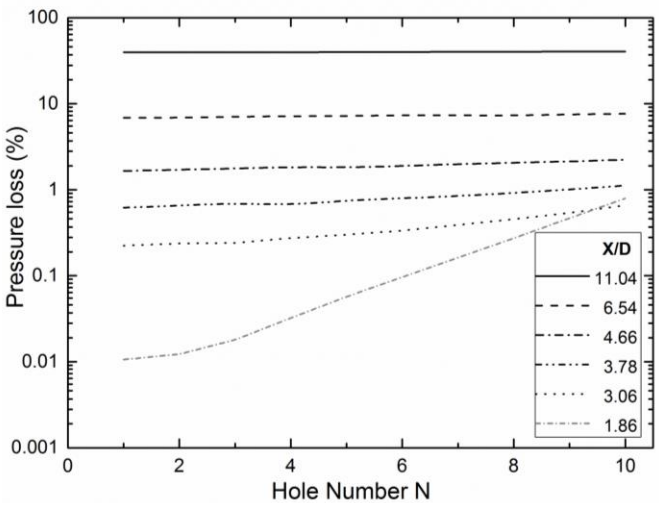

Figure 5.8: Impingement holes predicted pressure loss for varied X/D at constant G

level for gas turbine applications. This is because an X/D of 11.04 would not be used with all the compressor flow. It is the design choice for local hot spot cooling of combustor or turbine blade walls, where a small proportion of the total compressor air flow is used but at a low local G with a 3 - 4% pressure loss. However, the variation of X/D at constant G was the objective of the present CFD investigation.

Figure 5.8 show that the pressure loss along the cross-flow gap was predicted to be small relative to the impingement jet wall pressure loss at high X/D. However, as X/D is reduced and the pressure loss reduces, the cross-flow pressure loss becomes more significant, especially for X/D < 3.78. It is in this region that the flow-maldistribution becomes significant as shown in Figure 5.3. The pressure loss was experimentally measured as the static pressure difference between the plenum chamber and the external ambient air. This was then corrected for the small pressure loss of the cross-flow discharge from the impingement gap. This was computed as one dynamic head pressure loss, based on the mean impingement gap flow V_c of 23.92 [25]. This correction was 0.34% and was the same for all X/D. The CFD predictions did not predict the pressure loss of the dump expansion from the gap and predicted the pressure loss to the upstream wall static pressure 25.4 mm downstream of the last row of impingement holes.

The predicted pressure losses as a function of the air hole number are shown in Figure 5.9 for five coolant mass flux G. This shows the increase in pressure loss along the duct due to the interaction of impingement jets with the cross-flow. Figure 5.9 shows that the major part of the pressure loss is that through the impingement wall and that the pressure loss due to flow along the impingement gap is much smaller, but still significant. At the highest G, 73% of the total pressure loss occurs across the impingement jet wall. At the next highest G, 77% of the pressure loss was across the impingement wall. Thus around three quarters of the pressure loss is across the wall and one quarter due to cross-flow along the gap.

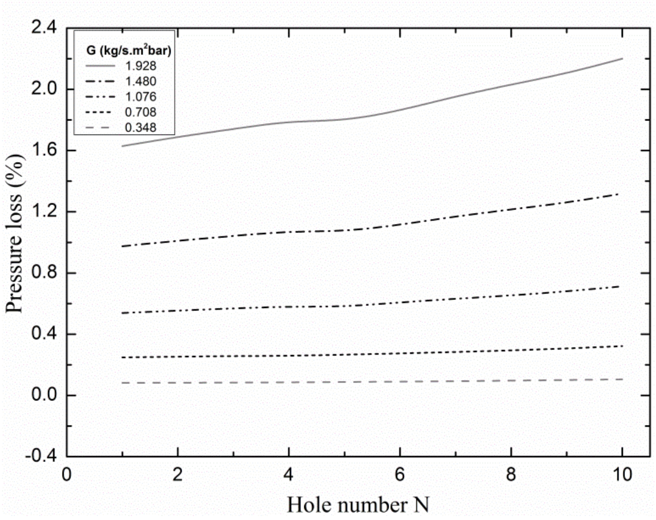

Figure 5.9: Impingement holes predicted pressure loss for varied G at fixed X/D and Z/D

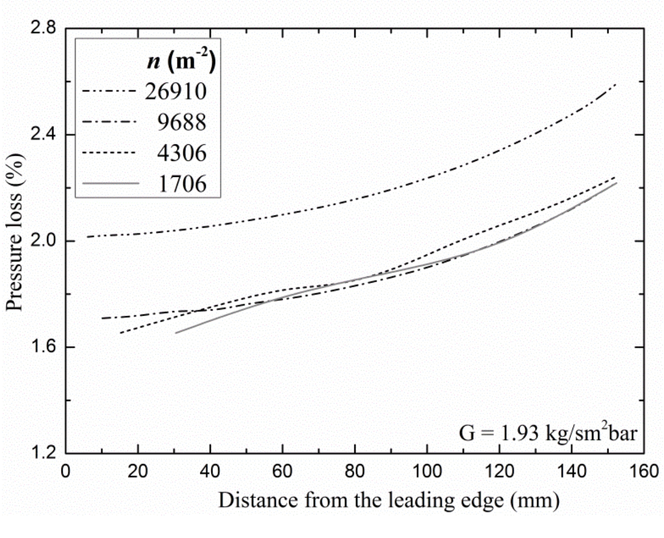

Figure 5.10: Impingement holes predicted pressure loss for varied *n* at constant G and X/D

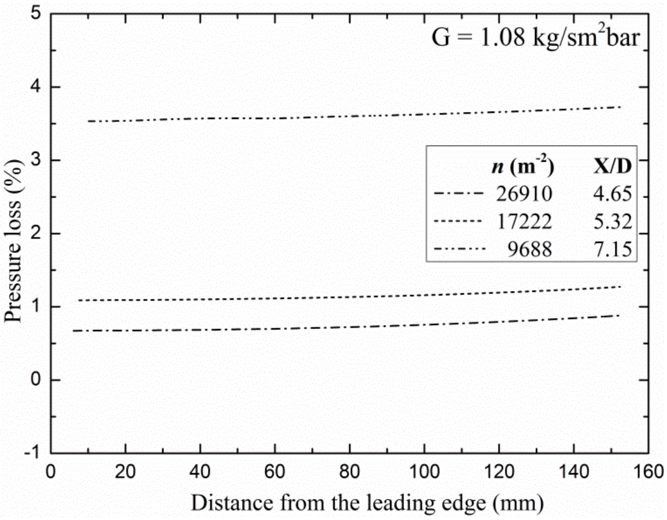

Figure 5.11: Impingement holes predicted pressure loss for varied *n* and X/D at constant G

The predicted pressure loss results are shown as a function of the distance along the impingement gap in Figure 5.10 Figure 5.11, which are the predictions for G of 1.93 and 1.08 kg/sm^{2}bar, respectively. Figure 5.10 show that the difference in pressure loss was nearly constant along the impingement gap, hence the difference in the overall pressure loss was due to that pressure loss in the holes, not due to any effect of the cross-flow. Equations 2.11 and 2.12 only give the same pressure loss of Figure 5.10, if the hole C_d is constant. With the largest number of holes, Table 5.3 shows that C_d decreased from 0.91 for N = 10 to 0.81 for N = 25 and this is an 11% reduction in C_d, which will give a 23% increase in the pressure loss for the same air mass flux and wall porosity. Figure 5.10 shows that at the start of the impingement gap, the impingement walls with N = 10 and 15 had a predicted pressure loss of about 1.67% and this increased to 2% for the N = 25 wall. This is a 20% increase in the predicted pressure loss, which is close to that measured experimental data [22]. This shows that the flow inside the holes and the cross-flow aerodynamics along the impingement gap flow were adequately predicted. But for a reduced G of 1.08 kg/sm^{2}bar and varied large *n* from 9688 - 26910 m^{-2} as shown in Figure 5.11, the pressure loss increases from 0.9% for N = 25 to 1.27% for N = 20 and finally to 3.72% for N =15. This should be based on the differences in increased X/D as Table 5.4 show, which also show that the reduced hole size with N influences the increased in pressure loss, which is contrary to Figure 5.10.

The reason for the higher pressure loss for N = 25 in Figure 5.10 and for all N in Figure 5.11 walls, was the increase in hole L/D ~ 4.5 and the differences in the method of manufacture of the wall. Spark erosion for the N = 25 wall and is the same for all *n* of Figure 5.11, while drilling was used for the larger holes [45], which gave a different wall surface finish. The CFD predictions do not specifically include any effect of the wall roughness on the predictions. However, as the wall function approach was used for the boundary layer, this occupied more of the flow when the hole diameter was small and this acts as a pseudo wall roughness effect and gives a good prediction of the increased pressure loss.

5.4.2 Impingement Gap Exit Pressure Loss

The measured pressure loss was based on the static pressure difference between the impingement air plenum chamber and the atmospheric discharge from the impingement gap, which is equivalent to the static pressure at the last hole. This measurement includes the dump pressure loss as the flow expands from the gap. If the mean velocity in the gap is used and a free discharge one dynamic head pressure loss is assumed, then the extra pressure loss in the experiments can be estimated.

Figure 5.12 compares the predicted pressure loss as a function of Z/D for the tenth hole in the array. For the impingement mass flux of 1.93 kg/sm^{2}bar, the velocity in the impingment gap after the tenth hole varied from 95.7 m/s for Z/D = 0.76 to 11.4 m/s for Z/D = 6.42. The corresponding dynamic head pressure loss at the free discharge from the impingment gap was 5.53, 2.16, 0.71, 0.35, 0.24, 0.14 and 0.08%, respectively for the range of Z/D (0.76, 1.22, 2.14, 3.06, 3.67, 4.89 and 6.42). Figure 5.12 shows that at low Z/D (0.76 - 2.14), the measured pressure loss were slightly higher than that predicteded, but that the above free discharge pressure loss in the experiments was the main part of the difference. For higher Z/D in Figure 5.12 shows that there was good agreement between the measured and predicted pressure loss. This indicates that the predicted aerodynamics in the impingement gap and impingement holes were reliable.

The predicted pressure loss for varied X/D of Table 5.2 is compared with the measured pressure loss in Figure 5.13, this shows very good agreement. This predicted pressure loss agreement with the measurements shows that the predicted aerodynamics in the impingement hole and gap are likely to be reliable. Table 5.2 geometries were computed at a constant impingement gap Z, so that the cross-flow velocity was the same irrespective of the X/D. However, this did involve a change in Z/D as D was increased at constant X in this work. El-Jummah *et al* [46] compares the predicted pressure loss for this varied Z/D and that at a constant X/D of 4.66, they showed that at similar Z/D of 1.2 - 1.3 the influence of increased X/D at near constant Z/D was to increase the pressure loss substantially, as shown by Equations 2.11 and 2.12. The predicted final total pressure loss for the range of G values shown in Table 5.5 and for the X/D of 4.66 shown above, is compared with the measured pressure loss in Figure 5.14, which also shows perfect agreement with the measured results.

The measured and predicted overall pressure losses from the plenum chamber to the impingement gap outlet wall for varied *n* of Table 5.3 are shown in Figure 5.15. There was excellent agreement and this indicates that the main features of the impingement flow aerodynamics were correctly predicted. The pressure loss is dominated by the flow through the impingement holes as the impingement wall has no influence on the hole pressure loss provided that the Z/D > 1 and thus did not restrict the hole outlet flow (30). The pressure loss was in the range 2.2 - 2.6% depending on *n*. However, this is too high for regenerative cooling with a G close to 2 kg/sm^{2}bar. A minimum pressure loss of 2% is required for low NOx combustors with higher pressure loss or 3 - 4% common. This results in overall pressure losses of 4 - 6%, which are too high and reduce cycle thermal efficiencies. As a consequence, this investigations is for the impact of *n* at a lower X/D with lower pressure loss at the same G. Equations 2.11 and 2.12 show that as G, A and X/D are held constant, there should be no influence of *n* on the pressure loss. Figure 5.15 shows that there was a small increase in the overall pressure loss with increased *n* and this was due to differences in the hole discharge coefficients C_d shown in Table 5.3. However, the agreement of the CFD results in predicting this increased pressure loss with *n* shows that the CFD resolved the

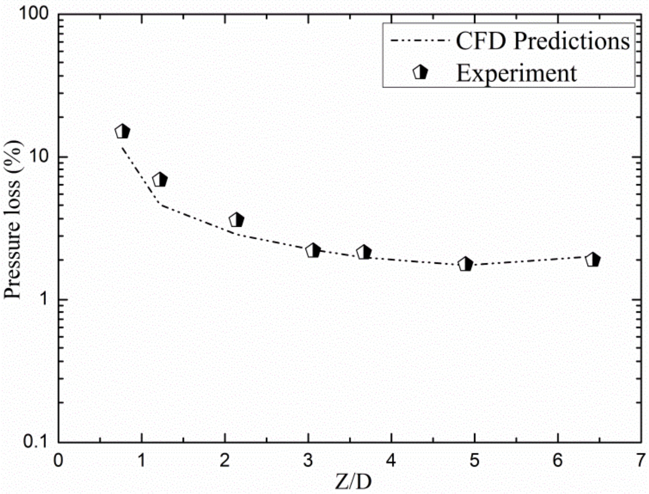

Figure 5.12: Predicted pressure loss versus experiment for varied Z/D of G = 1.93kg/sm^{2}bar

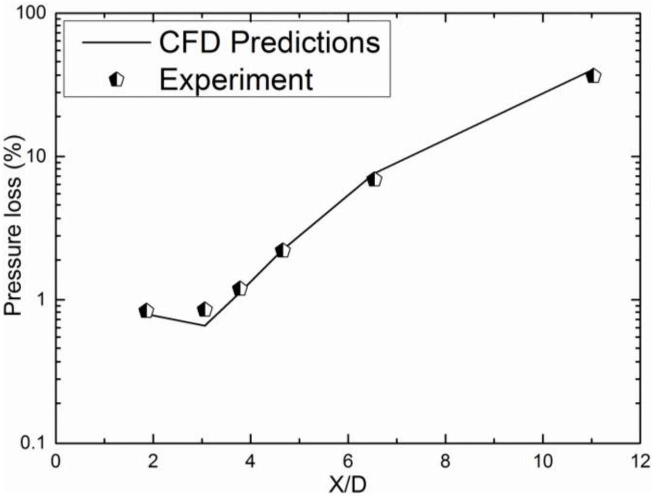

Figure 5.13: Predicted pressure loss versus experiment for varied X/D at G = 1.93kg/sm^{2}bar

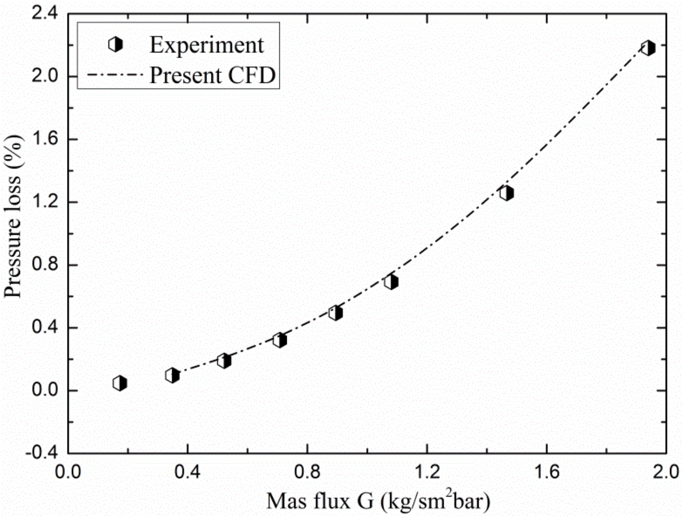

Figure 5.14: Predicted pressure loss versus experiment for range of G at fixed X/D and Z/D

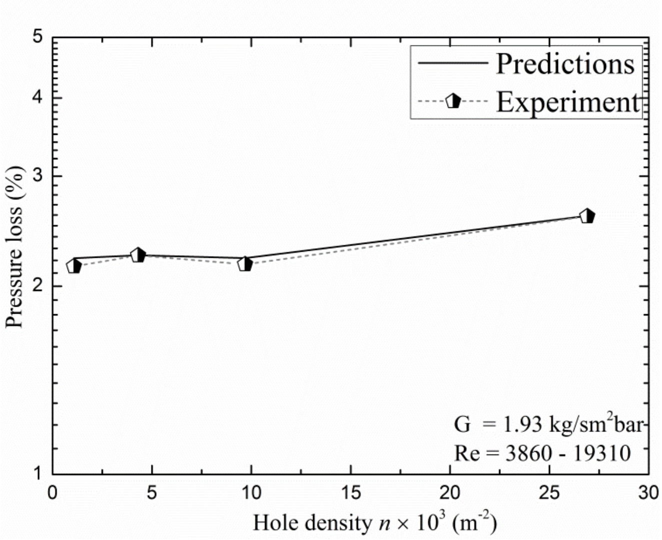

Figure 5.15: Predicted pressure loss versus experiment for varied *n* at constant X/D and G

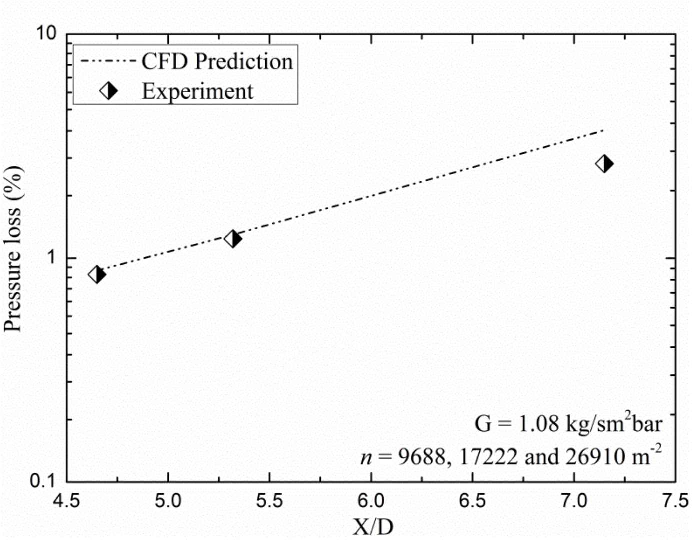

Figure 5.16: Predicted pressure loss versus experiment for varied *n* and X/D at constant G

flow inside the holes adequately. The predicted pressure loss as X/D is varied with *n* in Table 5.4 is compared with the measured data in Figure 5.16, this show perfect agreement for *n* of 1076 and 26910 m^{-2}. But for *n* of 9688 m^{-2}, the agreement was predicted poorly for which the CFD over predict the measured results. This disagreement is not well understood as similar *n* of X/D = 4.66 in Figure 5.15 showed good agreement with the experiment.

5.5 Predicted and Measured Heat Transfer

The measured and predicted heat transfer coefficients (HTC), as defined in Equation 2.24, were converted into Nusselt number Nu by Equation 2.35. El-jummah *et al* [25, 32, 33] showed that comparison of the Nu distribution on the target surface with TKE distribution on the target surface, indicates that Nu is controlled by the surface distribution of TKE. The Nu profiles are very similar to those for TKE, which obviously controls the convective heat transfer. It has been shown in Chapter 2 that the experimental deterioration in HTC on the target wall is control by the impingement gap cross-flow. This has been clearly shown by the Nu surface distribution and by averaging the regions of the X^2 jets impingement, gives the locally averaged HTC [25] as will be shown here.

5.5.1 Surface Distribution of Nusselt Number

Nusselt number contour plots are shown in Figure 5.17 (right), 5.18 and 5.19 on the target surface and also on the impingement jet wall in Figure 5.17 (left). Figure 5.17 (i) shows the Nu for varied Z/D whilst 5.17 (ii) shows that of varied X/D, the target surfaces Nu are as were shown for the TKE in Figure 5.6. As previously explained, the impingement Z/D and X/D shows the important of varying Z and D, which also shows the significance of TKE in the hole and its influence in the gap on the target wall.

The predicted target surface Nu distribution of Figure 5.17 shows that for Z/D > 2 and X/D > 3.06, the peak heat transfer coefficient deteriorates in the downstream portion of the impingement wall, as found in the experimental work in Figure 2.5. The predicted surface distribution of the target surface Nusselt number in Figure 5.17 (i) - right, for the range of Z/D shows the well-known influence of flow-maldistribution caused by the cross-flow. With flow-maldistribution, low Z/D < 3.06, the heat transfer is greater at the trailing edge and the reverse is the case for large Z/D. For a Z/D of 2.14 - 3.06 the wall is more uniformly cooled. The experimentally observed (Figure 2.5) deterioration in heat transfer with distance along the gap on the target wall when there is no flow-maldistribution (large Z/D), is predicted in Figure 5.17 (i). This is accompanied by an increase in heat transfer to the impingement jet wall surface (Figure 5.17 - left), but at lower levels of Nu than the impingement target surface. The reason for this decrease in Nu on the target surface with axial distance was shown in Figure 5.6, where the reduction in turbulence at the surface with axial distance was demonstrated. Turbulence at the surface gives the enhanced heat transfer so that lower turbulence and lower heat transfer go together.

Figure 5.17 (ii - right) shows that at a high X/D of 11.04, the 10 rows of jets produced nearly identical heat transfer. After the fifth hole the Nu distribution starts to distort in the downstream direction due to the action of the cross-flow. This distortion gets worse as X/D decreases and the porosity A increases. At the lowest X/D (1.86) the individual impingement jets are seen to be too low as local regions of high heat transfer and the cross-flow smears the region of high heat transfer in the downstream portion of the test wall. The predicted Nusselt number on the impingement jet surface (Figure 5.17ii - left), shows the heat transfer caused by the reverse flow jets as shown in Figure 5.1. The heat transfer was lower than on the target wall, but the reverse flow impingement jet can be seen to give a local enhancement of the jet wall heat transfer. This reverse flow heating of the impingement jet wall raises the temperature of that wall, which then heats up the impingement cooling air. There are regions of low heat transfer between the jets. On the impingement jet surface the heat transfer was much smaller, but peaked in line with the reverse jets that flow in the centre of each four air hole impingement group. More heat transfer to this surface occurs with downstream distance.

The predicted surface distribution of the Nusselt number Nu, on the impingement jet target surface for range hole density *n* is shown in Figure 5.18. Figure 5.18 (i) is the predictions for larger *n* using G of 1.08 kg/sm^{2}bar and 5.18 (ii) is for smaller *n* at G of 1.08 kg/sm^{2}bar, choosing in order to avoid compressibility effects. This follows a very similar pattern to that of the surface turbulent kinetic energy distribution in work by El-jummah *et al* [4]. For the 5 rows of holes, Figure 5.18 (ii) shows that there was a very high Nu at the impingement point of the jet and a very low Nu in between the jet impingement points (2, 3). This will be shown later to be the cause of high surface thermal gradients on the target surface. As the number of rows of holes is increased, the Nu number distribution becomes more even, although the high heat transfer at the impingement point can still be seen. For 25 rows of holes the destruction of the impingement jet flow by the cross-flow as Figure 5.18 (i) shows, leads to low Nu over the downstream half of the target wall. This effects for the larger *n* reduces with reduced N as shown by N = 20 and 15 in Figure 5.18 (i) and for N of 15 with X/D = 7.15 that has peak Nu, the downstream reduction is near the last four holes.

Comparison of similar *n* of different X/D are shown in Figure 5.18, whereby 5.19 (i) is for *n* of 9688 m^{-2} at G of 1.93 kg/sm^{2}bar and X/D of 7.15 (ia) and 4.63 (ib) and 5.19 (ii and iii)

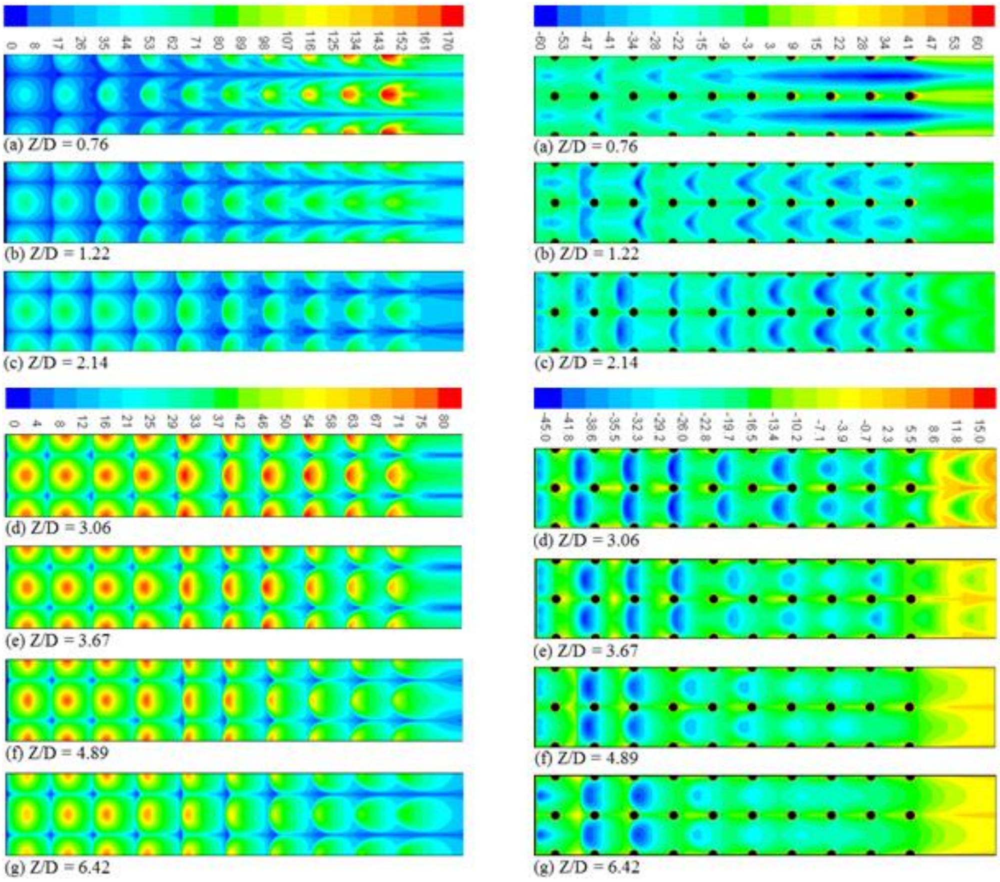

(a) Z/D = 0.76 (a) Z/D = 0.76

(b) Z/D = 1.22 (b) Z/D = 1.22

(c) Z/D = 2.14 (c) Z/D = 2.14

(d) Z/D = 3.06 (d) Z/D = 3.06

(e) Z/D = 3.67 (e) Z/D = 3.67

(f) Z/D = 4.89 (f) Z/D = 4.89

(g) Z/D = 6.42 (g) Z/D = 6.42

(i) Range of Z/D for a fixed X and D

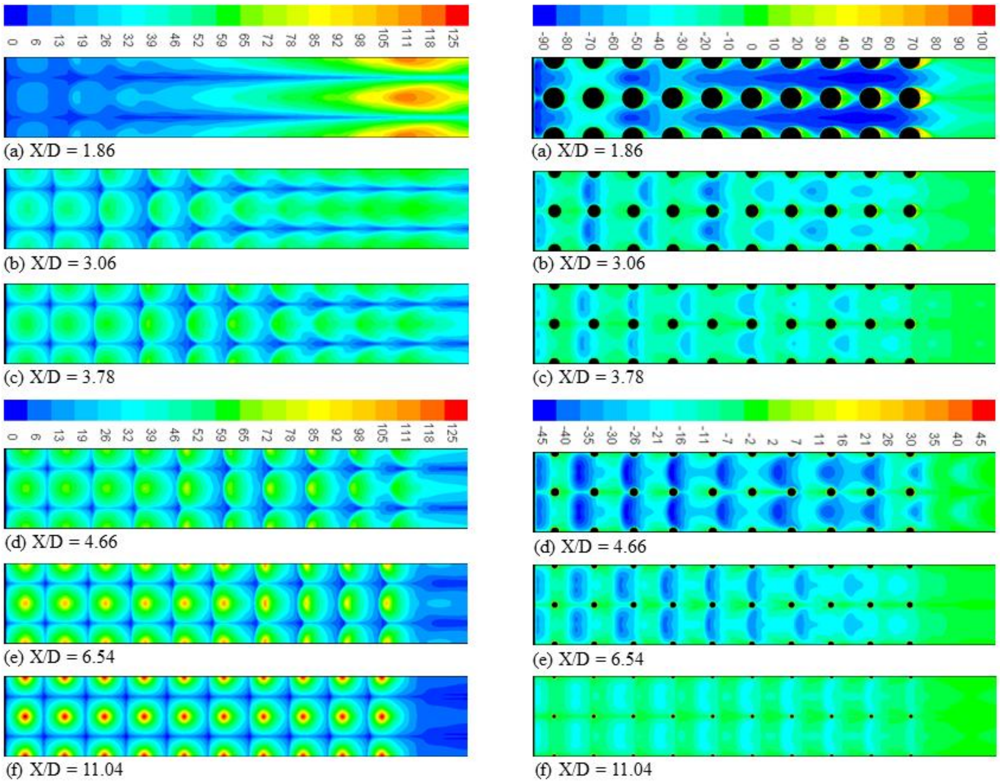

(a) X/D = 1.86 (a) X/D = 1.86

(b) X/D = 3.06 (b) X/D = 3.06

(c) X/D = 3.78 (c) X/D = 3.78

(d) X/D = 4.66 (d) X/D = 4.66

(e) X/D = 6.54 (e) X/D = 6.54

(f) X/D = 11.04 (f) X/D = 11.04

(ii) Range of X/D for a fixed X and Z

Figure 5.17: Predicted contours of Nusselt number for G of 1.93 kg/sm^{2}bar

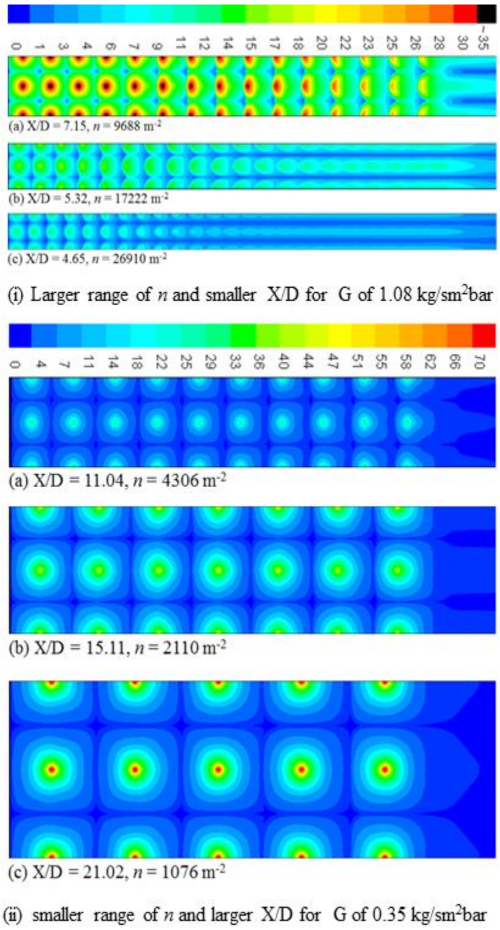
(a) X/D = 7.15, n = 9688 m^{-2}
(b) X/D = 5.32, n = 17222 m^{-2}
(c) X/D = 4.65, n = 26910 m^{-2}
(i) Larger range of n and smaller X/D for G of 1.08 kg/sm^{2}bar
(a) X/D = 11.04, n = 4306 m^{-2}
(b) X/D = 15.11, n = 2110 m^{-2}
(c) X/D = 21.02, n = 1076 m^{-2}
(ii) smaller range of n and larger X/D for G of 0.35 kg/sm^{2}bar

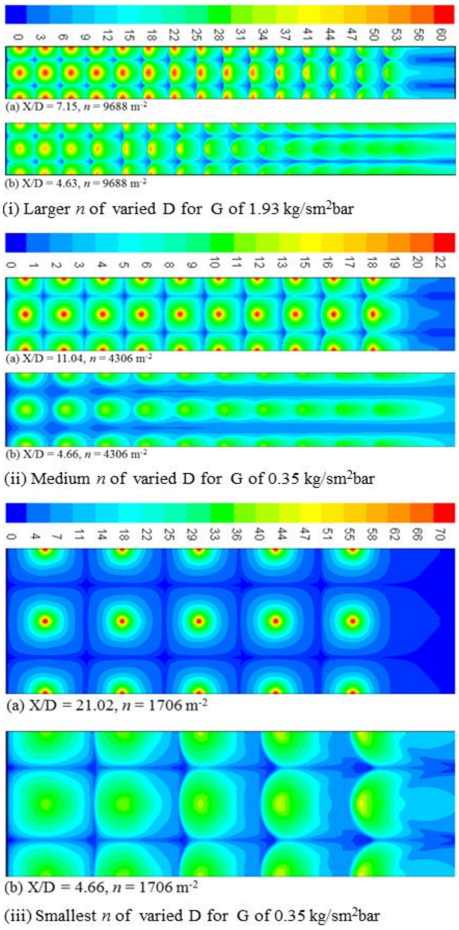
(a) X/D = 7.15, n = 9688 m^{-2}
(b) X/D = 4.63, n = 9688 m^{-2}
(i) Larger n of varied D for G of 1.93 kg/sm^{2}bar
(a) X/D = 11.04, n = 4306 m^{-2}
(b) X/D = 4.66, n = 4306 m^{-2}
(ii) Medium n of varied D for G of 0.35 kg/sm^{2}bar
(a) X/D = 21.02, n = 1706 m^{-2}
(b) X/D = 4.66, n = 1706 m^{-2}
(iii) Smallest n of varied D for G of 0.35 kg/sm^{2}bar

Figure 5.18: Contours of Nu for varied *n*

Figure 5.19: Comparison of Nu for varied *n*

are for *n* of 4306 and 1076 m^{-2} computed at G of 0.35 kg/sm^{2}bar in order to avoid influence of compressibility based on large X/D. Figure 5.189 (iia and iiib) are for X/D of 11.04 and 21.02 and each are compared at a fixed X/D of 4.66 [22]. In all, the larger X/D shows peak Nu at the impingement point, while the smaller fixed X/D shows that cross-flow dominates downstream the target surface and is worse for the largest *n*, as was shown above. Figure 5.189 (iii) show that the X/D of 4.66 surface Nu coverage is much more fully with each X^2, but for X/D of 21.02 the Nu is lowest between the rows of jets and on average could give lower temperature gradient.

The target surface average predicted and measured results for varied Reynold number, are compared in Figure 5.20 with other experimental results [5, 46, 47, 56, 140] for similar impingement geometries, by which data point were digitized using software digitizer. The results of Obot and Trabolt [47] and El-jummah *et al* [46], are very close to the predicted results for a very similar hole geometry. Other measurement disagree slightly because they have significant hole geometry differences, but in all cases the trend are the same. Though the results of Xing *et. al* [135] is not included in this based on the differences in Re (greater than 15,000), but the results has similar trend to this work.

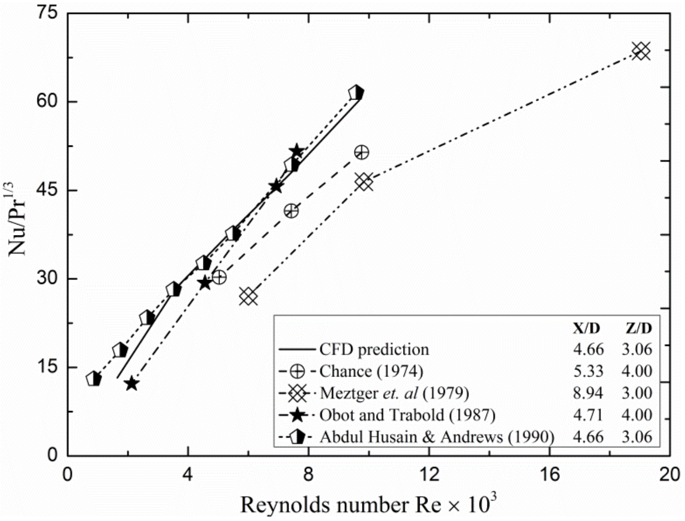

Figure 5.20: Target surface comparison of predicted versus literature experimental Nu

5.5.2 Surface Average Heat Transfer Coefficient

The X^2 surface average *h* were computed for each impingement jet and the mean surface average *h* over all rows of holes as a function of Z/D, X/D, G and *n* are shown in Figure 5.21Figure 5.25. The predictions are compared with the equivalent surface averaged experimental measurements and the agreement for all geometries are very good and within the experimental error bars, apart from X/D of 1.86, G of 0.35 kg/sm^{2}bar and *n* of 1076 m^{-2}. The reason for this is related to the treatment of laminar flow in the impingement hole at low X/D and G. At this lowest G, there was a significant underprediction of the surface averaged heat transfer by 1/3. Flow separation is not predicted at the hole inlet and this influences the magnitude of TKE predictions in the impingement gap [46]. These results show that the present CFD procedures are only reliable for impingement hole Re that are turbulent. It is concluded that the k - ε turbulence model is not appropriate when portions of the flow are under laminar flow conditions. Only the predictions of Z/D and *n* shows decreasing surface average HTC as their values were increased, which shows that there are limits at which impingement gap and number of holes could be acceptable.

The under prediction of *h* for X/D = 1.86 was greater than expected as the Biot number was lowest (J) and the wall would be at a more uniform temperature. This under prediction was possibly influenced by the very low hole Re of 3850, shown in Table 4.12, which was the mean hole Re. The flow-maldistribution discussed above, would result in the leading edge hole having a laminar flow of about 1500 Re and hole 10 would be at a Re of about 8500. This is also confirmed by the hole turbulence predictions with zero turbulence predicted at the leading edge holes in Figure 5.6. A slightly higher surface averaged heat transfer compared with the measurement was expected, as the measurements used thermocouples located midway between the impingement holes and hence were located in the hottest part of the wall, which would result in lower *h* if the wall temperature gradients were significant. This is shown in Figure 5.22 for all X/D apart from X/D of 11.04. The ability of the thermocouples to measure the surface averaged *h* depends on the Biot number being low. The Biot number decreased with decrease in X/D due to the decrease in *h* [25, 33]. These effects are shown below in terms of the wall surface temperature gradients.

The over prediction at the lowest number of impingement jet holes in Figure 5.25 was probably due to an experimental error. The test wall was instrumented with thermocouples at 25.4mm spacing with the hole pitch at 30.4mm. It is likely that at this condition the non-uniformity in the surface heat transfer, which was shown to be very large [22], is too great for the thermocouple to represent a surface averaged measurement. The experimental thermocouples were placed in the worst position for impingement heat transfer. This was done so as to be conservative in the measurements. However, in the case of the five upstream holes the measurements are not reflecting the surface averaged heat transfer due to the large thermal gradients.

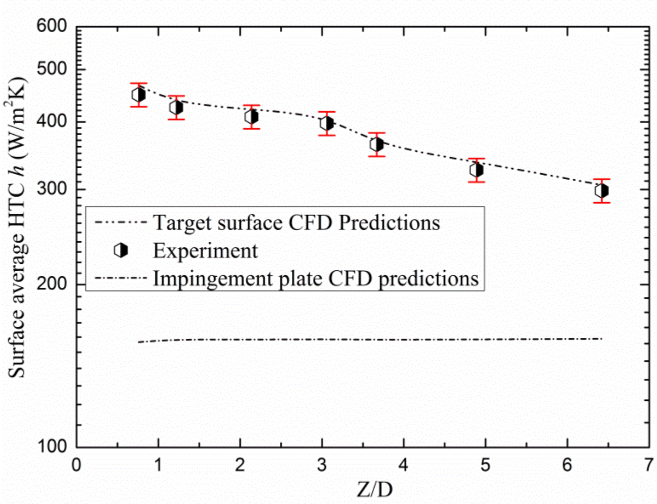

Figure 5.21: Comparison of Z/D predicted and experimental target surface average HTC *h*

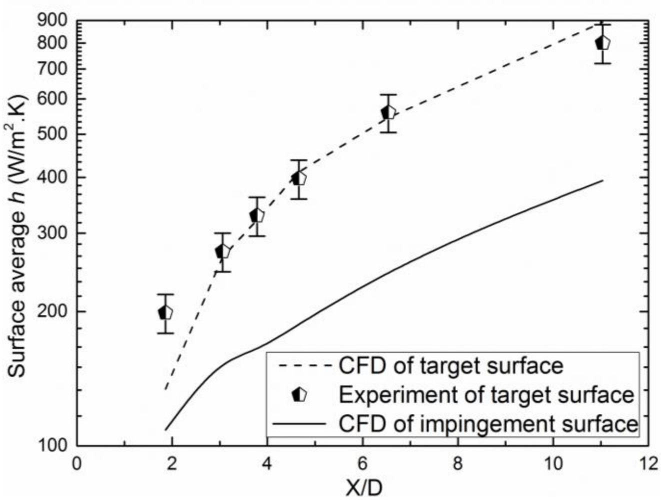

Figure 5.22: Comparison of X/D predicted and experimental target surface average HTC *h*

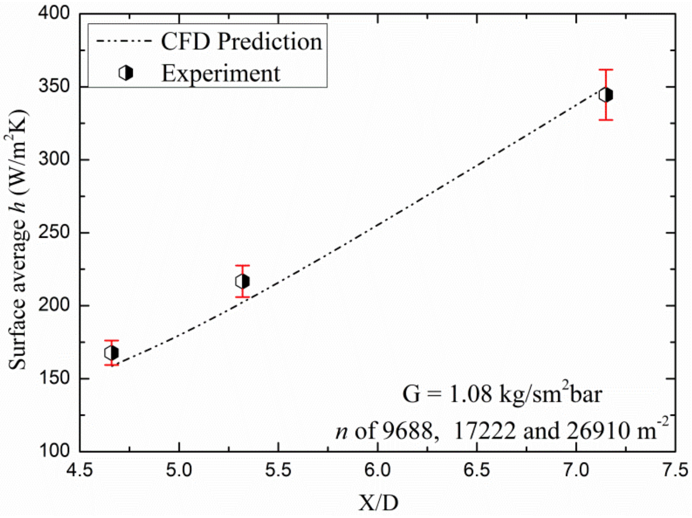

Figure 5. 23: Comparison of varied *n* and X/D predicted and experimental target surface *h*

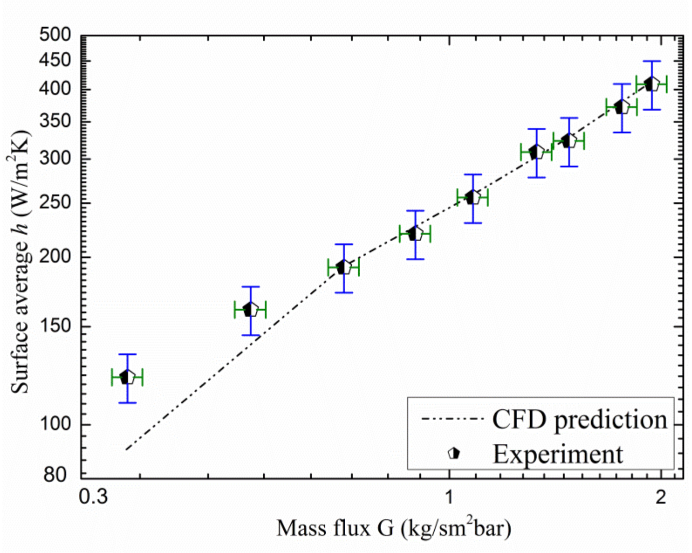

Figure 5.24: Comparison of range of G predicted and experimental target surface average *h*

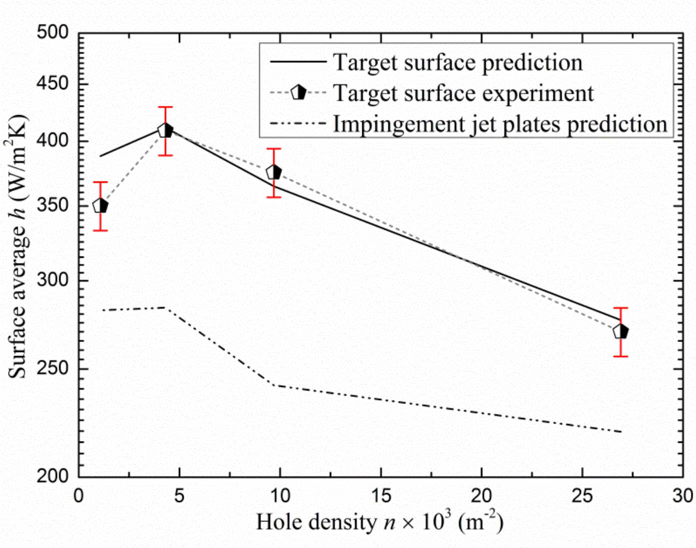

Figure 5.25: Comparison of varied *n* predicted and experimental target surface average *h*

Figure 5.25 shows that increasing the number of rows of impingement jets for the same impingement jet wall porosity and X/D at constant Z results in deterioration in the wall averaged heat transfer. This was due to the impact of the cross-flow and is clearly seen in the surface distribution of Nu plots in Figure 5.18. Figure 5.25 indicates that 10 rows of holes or *n* = 4306 m^{-2} was the optimum number of holes to use for this application at X/D = 4.66 and a Z = 10 mm. However, the current predictions indicate only a small loss of *h* for 1076 m^{-2}, but the associated thermal gradients discussed below might be unacceptable.

There were no measurements made on the impingement jet surface, but it is considered that the predicted heat transfer to this surface will be reliable as the target surface results agreed with the experiments. Figure 5.21Figure 5.22Figure 5.25 shows the computed surface average heat transfer coefficient *h* for the impingement jet wall for the varied Z/D, X/D and *n*. These are selected mainly to show the impact of reversed jets and jets interactions with cross-flow on geometries as Figure 5.1 shows based on changes in the impingement gap Z, holes size D, pitch and number of holes N. Figure 5.21 shows the predicted surface averaged *h* for the impingement jet walls for range of Z/D from 0.76 - 6.42. This impingement jet wall heat transfer shows that there is insignificant changes as Z was increased and almost a flat trend was shown, with slightly higher value for Z/D of 0.76. This impingement jet wall *h* is about 35% of that for the target walls on average for all Z/D.

Figure 5.22 compares the predicted impingement jet surface averaged *h* and that for the target wall at all X/D, this jet wall *h* indicates about 40 - 60% predicted *h* of the target wall. However, there were significant variations in this ratio with X/D and between the first few holes and the last few holes. Obviously the heating of the impingement jet wall by the recirculating impingement jets from the hot surface is a significant part of the overall complex heat transfer in impingement cooling. For the varied *n*, Figure 5.25 shows that these heat transfer to the impingement jet surface predictions has a maximum at the lowest number of holes. The ratio of the impingement jet wall to target wall surface averaged *h* varied between 0.65 for 9688 m^{-2} to 0.76 for the 26910 m^{-2}. For the highest *h* on the impingement cooled surface that ratio was 0.68 at 4306 m^{-2}. Overall it would be reasonable to take the impingement jet wall recirculated flow surface averaged heat transfer coefficient at 70% of that of the target surface. This high ratio indicates that it is an important part of the overall wall cooling heat transfer.

5.5.3 Axial Variation of X^2 Locally Average Heat Transfer Coefficient

The locally X^2 surface average HTC *h* results for the geometries varying Z/D, X/D, G and *n* are shown in Figure 5.26 - Figure 5.29 and were computed at G = 1.93 kg/sm^2bar. These predicted results were averaged over the X^2 surface area cooled by each hole and the experimental results only surface average by conduction in the metal wall. The thermocouple position in the lowest heat transfer region will underestimate the true local surface averaged *h* due to the residual temperature gradients in the wall, as the Biot number was low but not 0, as Figure 5.30 shows for varied Z/D. The extent of these temperature gradients was also computed and will be shown later.

Figure 5.26 (a and b) shows the prediction of the surface averaged *h* (over X^2) as a function of the number of holes in the cross-flow direction for the range of Z/D values. The predictions are shown to agree well with the experimental results at Z/D from 1.22 - 6.42, which are all within 5% error as shown above. But for Z/D of 0.76 in Figure 5.26 (a), the agreement was poor and this is because of the pressure loss disagreement, shown in Figure 5.12 caused by highly reduced grid in the impingement gap.

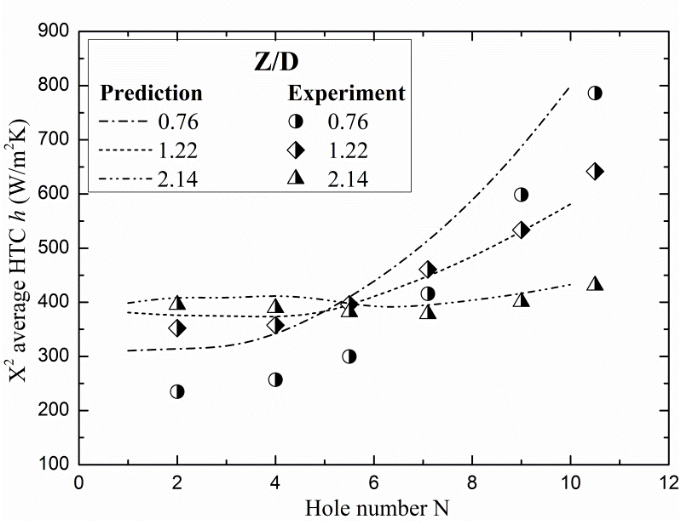

(a) Smaller range of Z/D at fixed G of 1.93 kg/sm^{2}bar

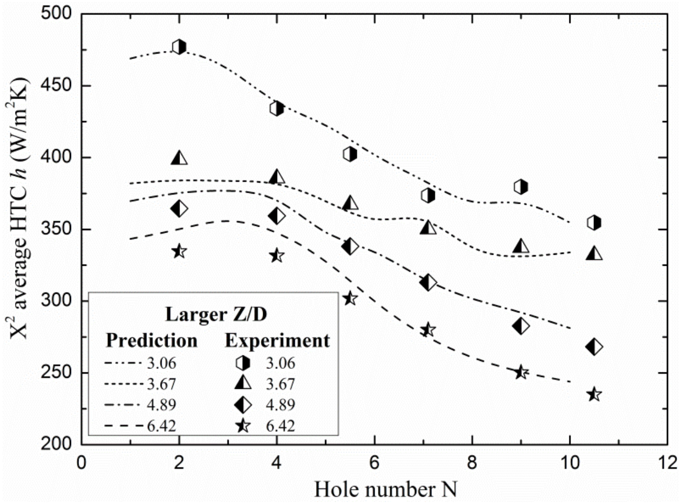

(b) Larger range of Z/D at fixed G of 1.93 kg/sm^{2}bar

Figure 5.26: Comparison of Z/D target wall predicted and experimental X^2 average HTC *h*

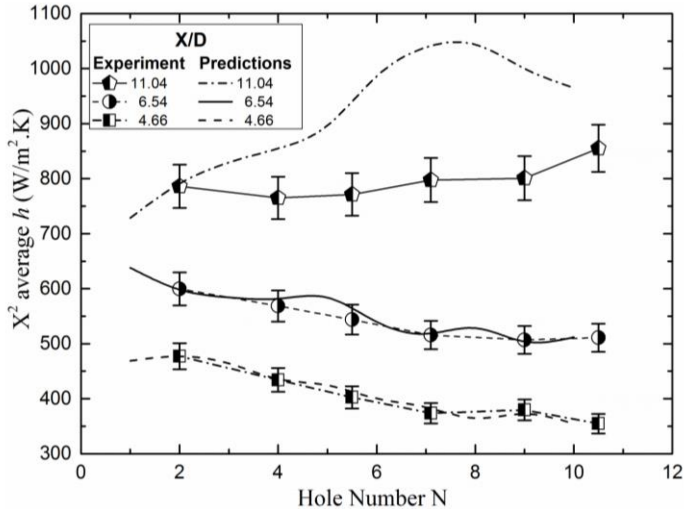

(a) Higher X/D at fixed *n*

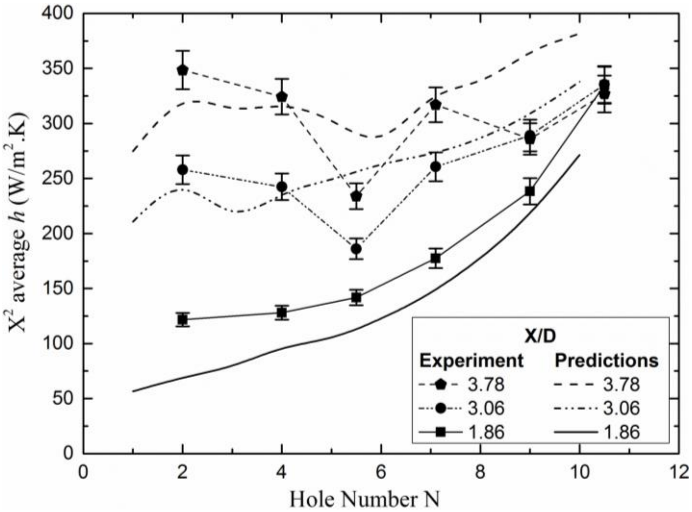

(b) Lower X/D at fixed *n*

Figure 5.27: Comparison of X/D target X^2 average HTC *h* for constant G of 1.93kg/sm^{2}bar

Figure 5.27 (a) shows the locally X^2 surface average HTC *h* predicted and experimental results for the range of higher X/D of Table 4.12. The experimental results shows that for X/D of 11.04, the heat transfer was fairly uniform with a slight increase in the trailing edge region, possible due to the duct flow additional heat transfer of the cross-flow. These results indicate that at an X/D of 11.04 the deterioration of heat transfer with distance, as correlated by Equation 2.22, does not occur. This supports the prediction of the aerodynamics shown by El-jummah *et al* [25], where there was minimal movement of the jets by the cross-flow. The agreement of the CFD results with the experiments was rather poor for X/D of 11.04, apart from in the leading edge region. The reason for this might be associated with the use of incompressible flow CFD, when at this X/D the jet velocities are very high at 244 m/s, as Table 4.12 shows, where compressible flow CFD should be used.

For X/D of 6.54 and 4.66, Figure 5.27 (a) shows that there was very good agreement between the experimental and the CHT CFD results. Both the experiments and predictions showed the deterioration of *h* with the cross-flow, due to the downstream convection of the turbulence on the surface, as shown above and correlated in Equation 2.22. This is in a region of X/D where flow-maldistribution was not significant. However, at lower X/D of Figure 5.27 (b), the experimental results showed first a decrease in *h* with distance along the impingement gap, due to the cross-flow effect correlated by Equation 2.22 and then an increase due to the influence of flow-maldistribution. This effect was reasonably well predicted using CHT CFD for an X/D of 3.76, although the leading and trailing edges were under predicted and the central section over predicted. Figure 5.27 (b) shows that the difference in the predictions and measurement were highest at the leading edge.

Finally, at the lowest X/D of 1.86 the experimental and predicted results were in agreement over a continuous increase in *h* from the start to end of the gap, due to the strong flow-maldistribution at this X/D with a very low impingement jet pressure loss. However, the predictions under predicted the experimental results at all axial positions. The difference was 50% at the start of the gap and 18% by hole 10. As discussed above in relation to the surface averaged *h* results, these results are difficult to explain as predicted *h* is higher than that measured would be expected, due to the location of the thermocouples on the centreline between the impingement holes. The prediction of the X/D of 1.86 in Figure 5.6 showed very low TKE over the first few rows of holes, which was due to the very low predicted proportion of flow in these holes as shown in the very low predicted velocities by El-jummah *et al* [25]. The resultant predicted flow-maldistribution in Figure 5.3 was severe with > 5 times the flow in row 10 to that in row 1. Table 4.12 gives the hole Re as 3850, based on the assumption of equal distribution of the air flow. However, the Re in the first row of holes with the predicted flow-maldistribution was 1540 and the applicability of the turbulent flow modelling under very low jet Re conditions is probably the main cause of the prediction errors for the X/D = 1.86 impingement geometry.

The influence of cross-flow on the average surface heat transfer per hole, using the surface area X^2 for each hole is shown in Figure 5.28 for range of G from 10.35 - 1.93 kg/sm^{2}bar. These are the average of the surface distributions of heat transfer shown in Figure 5.17 (id and iid) for G = 1.93 kg/sm^{2}bar and the equivalent for other decreased G [46]. Figure 5.28 shows very good agreement between the experiments and the predictions at the highest G values of 1.93kg/sm^{2}bar, with a trend similar to the highest G prediction for G = 1.48kg/sm^{2}bar. The agreement is also good at G of 1.08kg/s.m^{2}bar, except at the leading edge two holes where the predictions were significantly below the measurements. El-jummah *et al* [46] showed this should be based on lower Nu for the three leading holes and the absence of a cool spot in the predicted temperatures. A possible reason for this could be an over prediction of the flow-maldistribution, so that the leading edge holes were predicted to have a lower velocity than actually occurred. Figure 5.4 shows some unexpected variations in the flow mal-distribution, which should have been a smooth variation with the number of holes.

Figure 5.29 shows the predicted X^2 surface average HTC for varied *n* at fixed X/D of 4.66, as a function of the distance along the impingement cross-flow gap. The predictions are expected to be slightly higher than the measurements as the thermocouples on which the measurements were based were located at the lowest local heat transfer position and relied on the metal wall thermal conduction to produce the surface averaging. This was done so that the experimental results, which were used directly in combustor wall cooling designs, would be conservative.

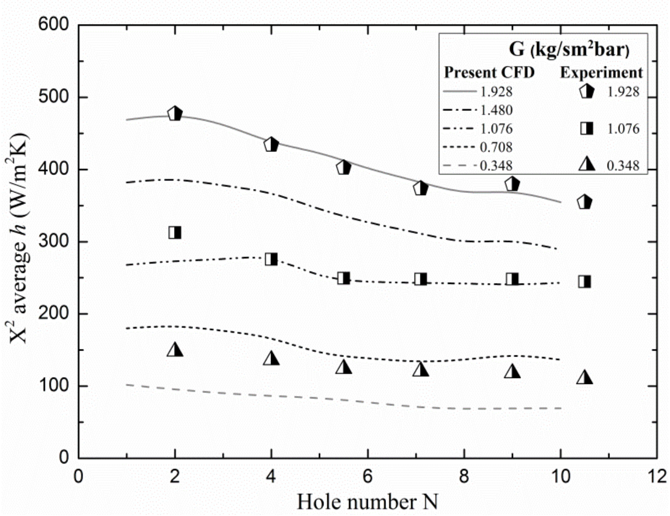

Figure 5.28: Comparison of target X^2 average HTC *h* for range of G at fixed X/D and Z/D

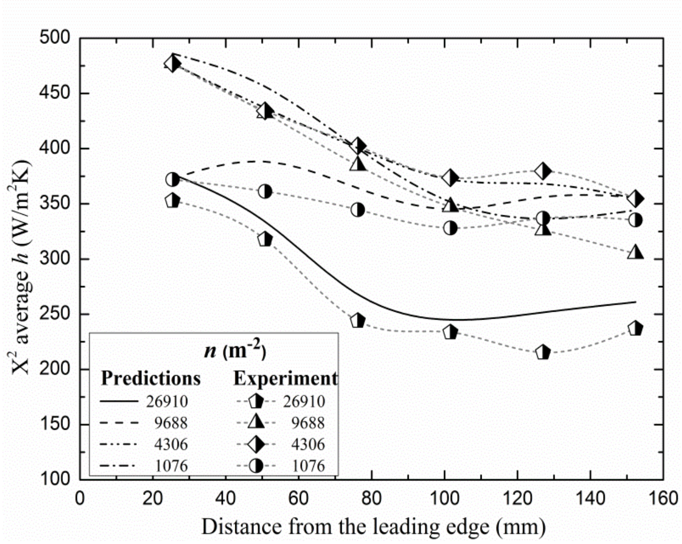

Figure 5.29: Comparison of target X^2 average HTC *h* for varied *n* at fixed X/D and G

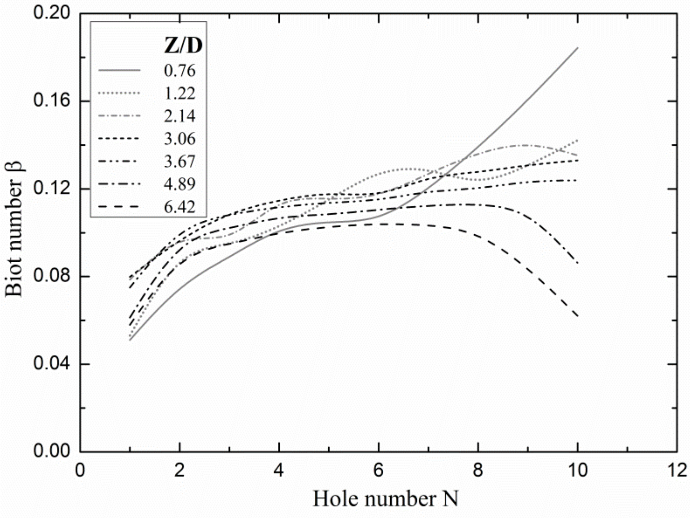

Figure 5.30: Target wall X^2 average Biot number for range of Z/D at fixed X/D and G

For *n* = 26910 m^{-2} the predicted local *h* were all slightly higher than the measurements, as expected, as the thermocouple was averaging the heat transfer of more than one impingement jet. The predictions for *n* = 1076 m^{-2} were higher than the measurements, this was because the thermal gradients were highest at this wide jet spacing and the thermocouple was furthest from the impingement point. The agreement of the predictions and measurements was very good for *n* = 4306m^{-2}. For *n* = 9688m^{-2} (15 × 15) the predictions were quite different from the measurements as the predictions were significantly below the measurements at the leading edge of the impingement gap and higher at the trailing edge. This resulted in good agreement for the mean surface average *h* predictions and measurements, as shown in Figure 5.25.

5.6 Target Wall and Impingement Gap Predicted Temperatures

An obvious feature of the heat transfer is that the longer the impingement air jets are in contact with the hot wall, the greater the temperature rise of the air jets will be. Thus the reflected jets are hotter than the impingement jets and the temperature of the cross-flow increases with axial distance. El-jummah *et al* [22, 25, 46] showed that this could be predicted using the dimensionless temperature T^* of Equation 2.6 for an imposed hot wall temperature and Equation 2.7 for an imposed hot wall heat flux [32, 33].

An interesting feature of the heat transfer is well modelled by CHT CFD, namely where the hot wall heats the impingement jets, so that the reflected jets are hotter than the incoming cold impingement jets. The present experimental results were undertaken with active electrical heating of the target wall. The CHT CFD predictions enabled the surface distribution of metal temperature in the presence of the impingement cooling to be predicted. The use of T^* enables the present results to be applied to other higher temperature operations, the predicted results in terms of the T^* are shown Figure 5.31 for varied Z/D. The dimensionless air temperatures T^* in the impingement gap were predicted using Equations 2.6 and 2.7 as in Figure 5.31 (i and ii), together with the predicted temperature contours in the wall thickness.

The range of Z/D [33] T^* predictions, are shown for the plane in-line with the impingement jets and for the plane between the jets. The Z/D geometries are chosen to show the effects of Z and hot side heated walls (all). Figure 5.31 (i) was computed using Equation 2.6 at an imposed T_w of 353K and Figure 5.31 (ii) was using Equation 2.7 at an imposed q" of 100 kW/m^2. The differences between the two as Figure 5.31 shows are with the cooling of the hot metal wall. Figure 5.31 shows that at large Z/D a further reason for the deterioration in heat transfer with distance is that the impinging jets are heated by the cross-flow before the jet impinges on the wall. In between the jets the central reverse flow jet is clearly seen as it is hotter than its in-lined counterpart. This is an important reason for the deterioration in heat transfer with distance along the gap in the absence of flow-maldistribution for large Z/D. Figure 5.31 clearly shows the direction of the cold jets penetrating though the hotter cross-flow air.

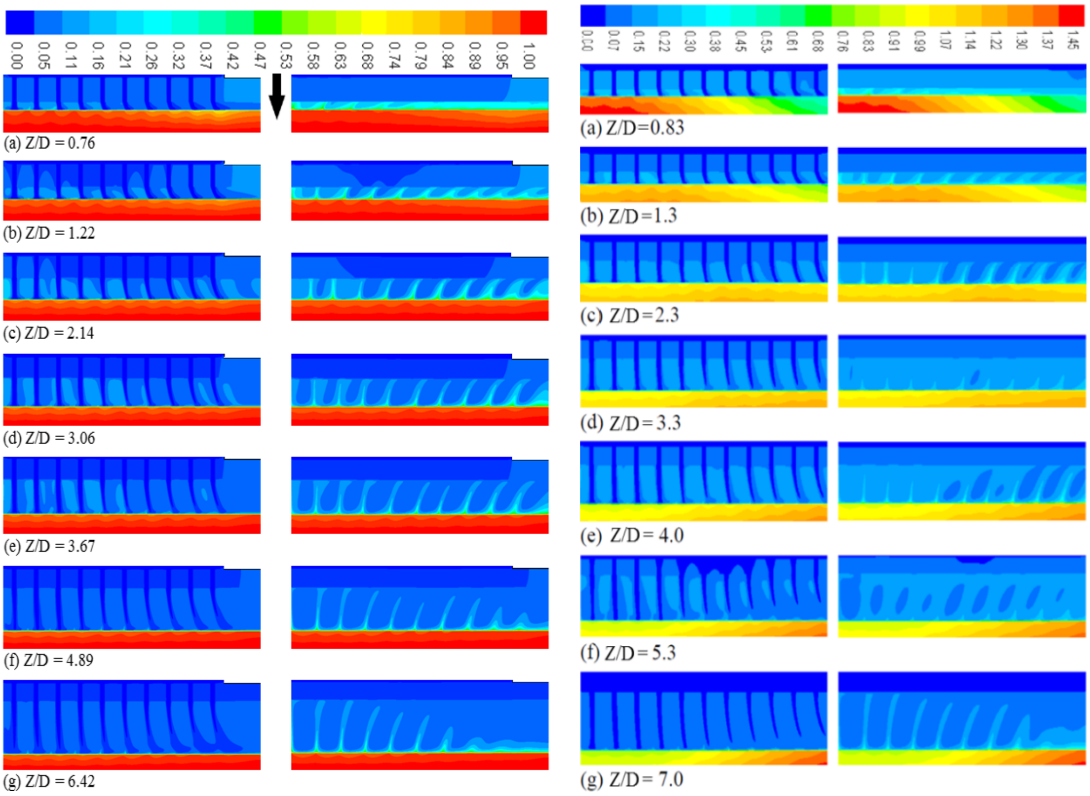

In-line with and between* N *rows of holes

(i) Imposed T_w for G of 1.93 kg/sm^{2}bar (ii) Imposed q" for G of 1.84 kg/sm^{2}bar

Figure 5.31: Contours of normalized temperature in the impingement gap for varied Z/D

5.6.1 Effects of Imposed Hot Side Wall Conditions

Figure 5.31 (i) is the computations for a fixed temperature of 353 K [22, 25, 46] that was imposed at the hot side of the target wall, while for Figure 5.31 (ii) the thermal conditions that were assigned are a fixed heat flux of 100 kW/m^2 [32, 33] similar to those used by Abdul Husain *et al* [43]. Both are with adiabatic Nimonic-75 metal target walls at the sides and no conditions are imposed on the impingement cooled surface as this is part of the conjugate analyses.

For the hot side imposed temperature, T_w of 353 k was applied directly in Equation 2.6 and the target wall thermal gradients, are seen to be uniformly varying with the 6.35 mm wall thickness as Figure 5.31 (i) shows. But for the hot side imposed q" of 100 kW/m^2, the temperature across the thickness varies as Figure 5.31 (ii) shows, hence $T_w = T_m$ of the hot side in Equation 2.7. This could be the reason for the lack of significant cool spots in Figure 5.32 (a) with the application of Equation 2.7, but in Figure 5.32 (b and c), Figure 5.33 and Figure 5.33, the cool spots dominates and are the region of higher HTC *h* shown in Figure 5.17, Figure 5.18 and 5.19, respectively.

El-Jummah *et al* [32] have shown that the thermal conductivity k_s of the wall was an important parameter in the conjugate heat transfer, the Nimonic-75 low k_s of 11.7 W/mK compared to Aluminium high k_s of 202.4 W/mK was shown to have an important influence on the axial variation of temperature and HTC *h*. Coolant air of 288 K used, as in the experimental work of Andrews and Husain [3] with the same measured wall heat flux of 100 kW/m^2 from a flame side cross-flow of 27 m/s at 750 K. The value of heat flux with a coolant to hot gas temperature difference of 400^{o}C, corresponds to a global hot gas side convective heat transfer of 250 W/m^{2}K.

5.6.2 Surface Distribution of Temperature

The present predicted surface distribution of T^* for the varied Z/D and X/D are as shown in Figure 5.32 (b and c), Figure 5.33 and Figure 5.334. These plots are very similar in distribution to those for the distribution of Nu in Figure 5.17, Figure 5.18 and 5.19, respectively as expected. These shows the existence of significant thermal gradients, in spite of the internal heat conduction within the wall. The impingement target wall predictions of the surface T^* contours for the range of Z/D are shown in Figure 5.32 (a and b). Figure 5.32 (a and b) shows major axial temperature gradients with high leading edge temperatures at low Z/D and high trailing edge temperatures at high Z/D. This is more clearly shown in Figure 5.35 (a and b) for the X^2 surface average normalized temperature axial distribution. In both cases the temperature normalization are by Equations 2.6 and 2.7, respectively.

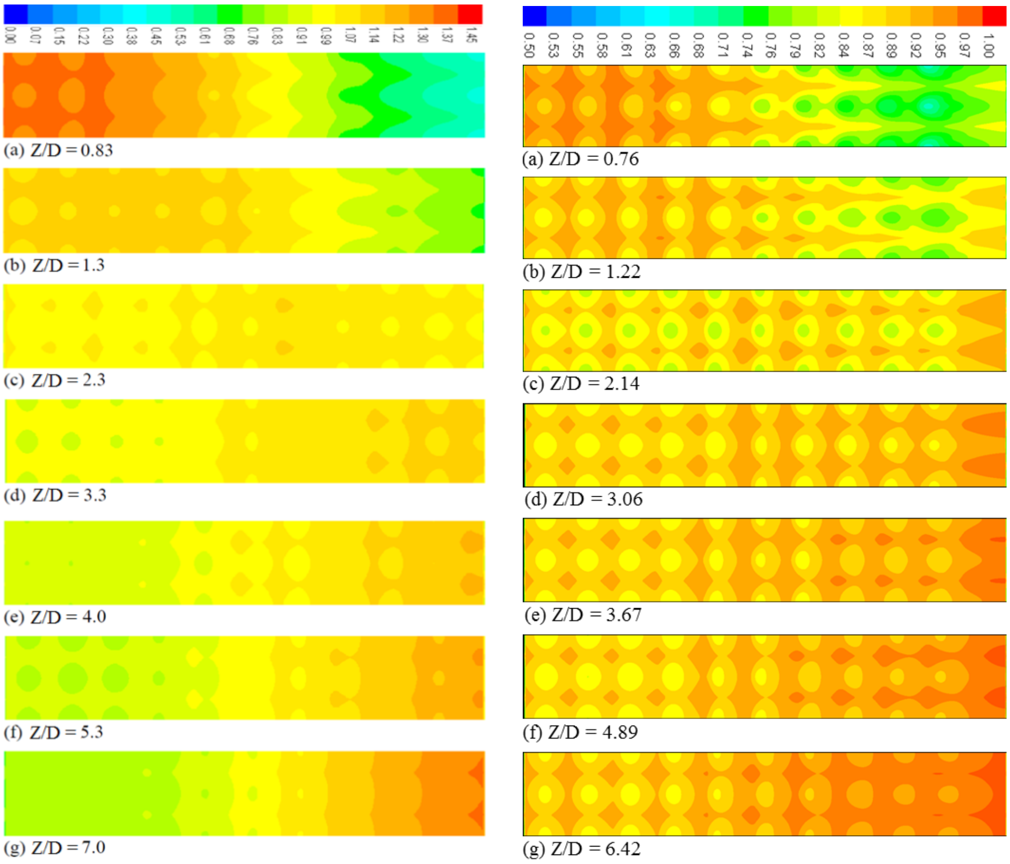

(a) Varied Z/D for G of 1.84 kg/sm^{2}bar (b) Varied Z/D for G of 1.93 kg/sm^{2}bar

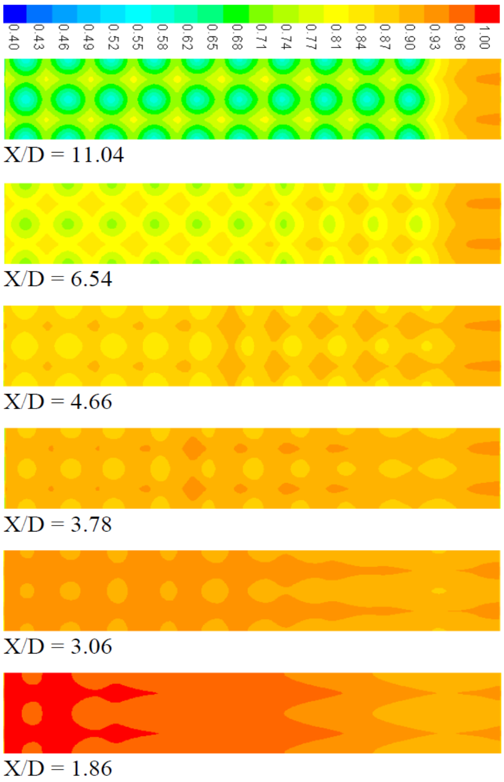

(c) Varied X/D for G of 1.93 kg/sm^{2}bar

Figure 5.32: Target surface distribution of normalized temperature

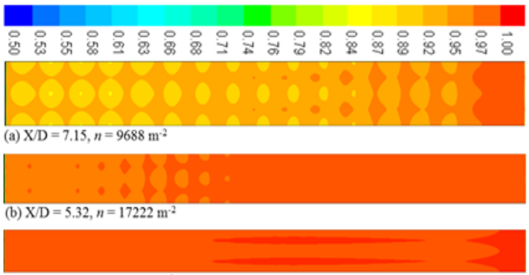

(a) X/D = 7.15, n = 9688 m^{-2}

(b) X/D = 5.32, n = 17222 m^{-2}

(c) X/D = 4.65, n = 26910 m^{-2}

(i) Larger range of n and smaller X/D for G of 1.08 kg/sm^2bar

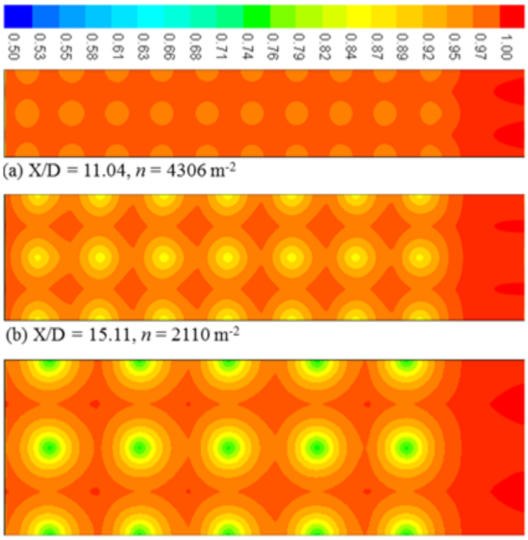

(a) X/D = 11.04, n = 4306 m^{-2}

(b) X/D = 15.11, n = 2110 m^{-2}

(c) X/D = 21.02, n = 1076 m^{-2}

(ii) smaller range of n and larger X/D for G of 0.35 kg/sm^2bar

Figure 5.33: Contours of T^* for varied n

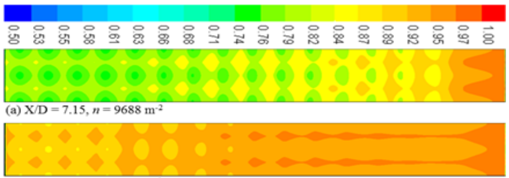

(a) X/D = 7.15, n = 9688 m^{-2}

(b) X/D = 4.63, n = 9688 m^{-2}

(i) Larger n of varied D for G of 1.93 kg/sm^2bar

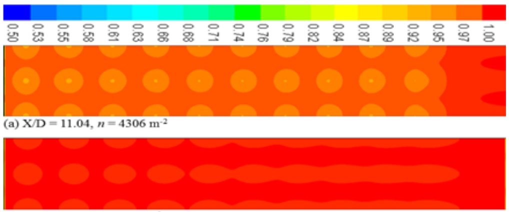

(a) X/D = 11.04, n = 4306 m^{-2}

(b) X/D = 4.66, n = 4306 m^{-2}

(ii) Medium n of varied D for G of 0.35 kg/sm^2bar

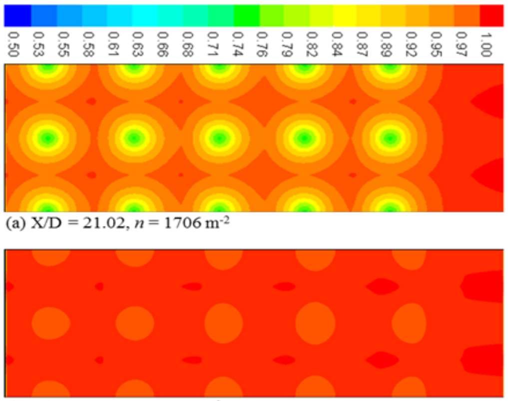

(a) X/D = 21.02, n = 1706 m^{-2}

(b) X/D = 4.66, n = 1706 m^{-2}

(iii) Smallest n of varied D for G of 0.35 kg/sm^2bar

Figure 5.34: Comparison of T^* for varied n

Figure 5.32 (c) shows the predicted T^* for the range of X/D geometries shown in Table 5.2, this shows that as the X/D decreases with increased in jet hole size, the cold spot with axial distance downstream the impingement gap gradually disappears. Hence the X/D of 1.86 has the highest T^* and the cold spot is shown to be almost absent, this further confirmed that this X/D has the lowest HTC as was shown above. However, the predicted temperature gradients are much lower than those for the local Nu gradients predicted in Figure 5.17 (ii). For example, for X/D = 11.04, the Nu variation between the impingement point and the mid-distance between the impingement points is a factor of 10/1, but the same T^* gradient is only about 1.5. This is the reason why in Figure 5.36, the X/D is shown to have the highest X^2 average T^* and decreases as X/D was decreased. Figure 5.36 also shows that upstream the impingement gap and up to the central rows of holes, the X/D of 1.86 - 4.66 are in the range of similar X^2 average T^* and increases downstream, with only X/D of 1.86 decreasing. This indicates that the X/D of 4.66 (n = 4306 m^{-2}) and based on the Nu predictions shown in Figure 5.17 (i and ii), balanced out between the cooling heat transfer and the wall thermal gradients. In Figure 5.18, for n = 1076 m^{-2} the min to max Nu was about a factor of 5, but in Figure 5.33 the min to max temperature is about a factor of 1.25.

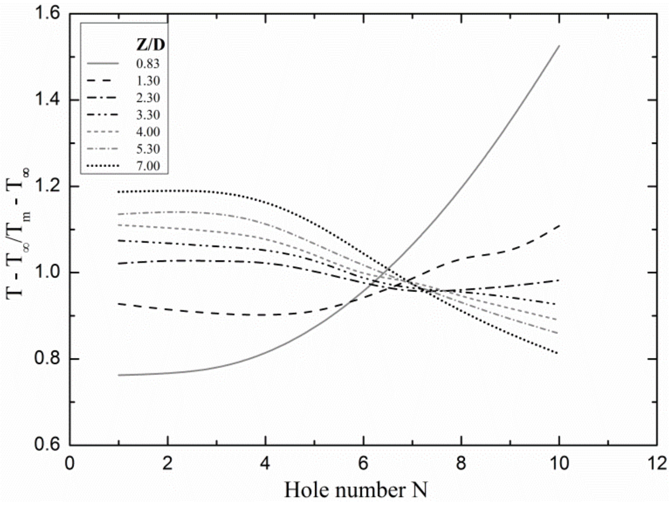

(a) Imposed q'' for G of 1.84 kg/sm^{2}bar

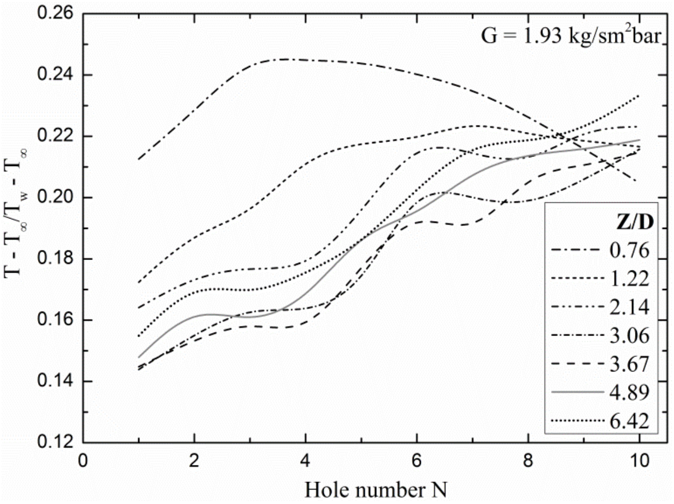

(b) Imposed T_w for G of 1.93 kg/sm^{2}bar

Figure 5.35: Predicted target surface average T^* for varied Z/D at fixed X/D

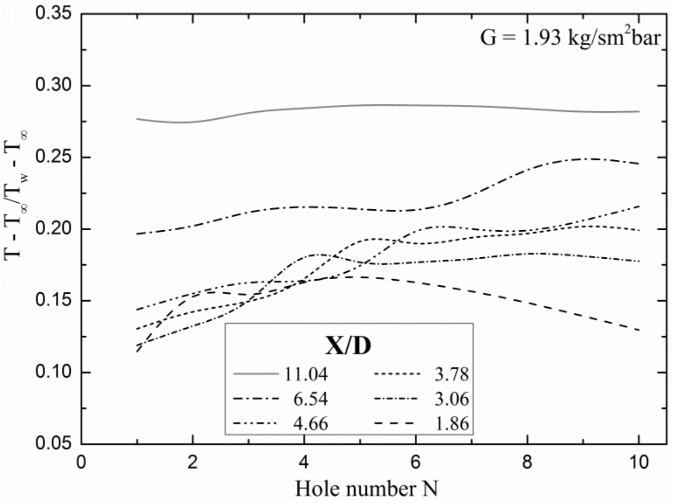

Figure 5.36: Predicted target surface average T^* for varied X/D at fixed *n* and G

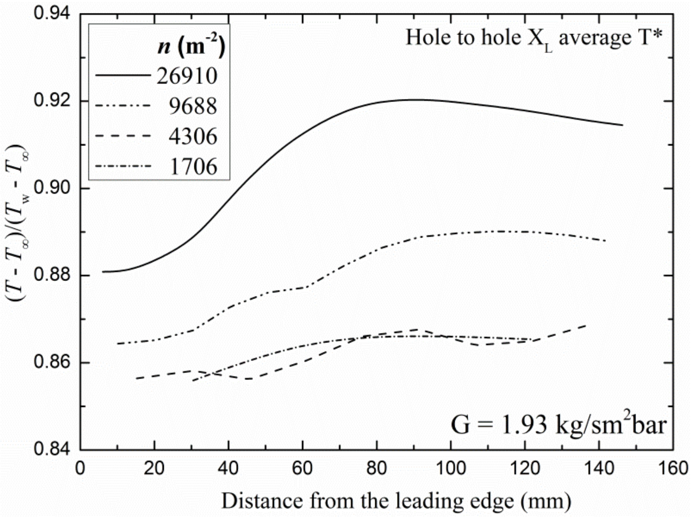

Figure 5.37: Predicted hole-to-hole target surface average T^* of varied *n* at fixed X/D and G

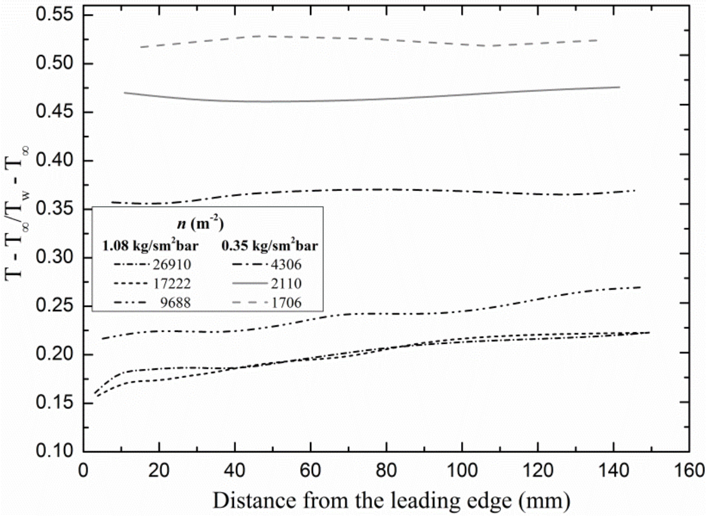

Figure 5.38: Predicted target X^2 average T^* for varied *n* and X/D of two G values

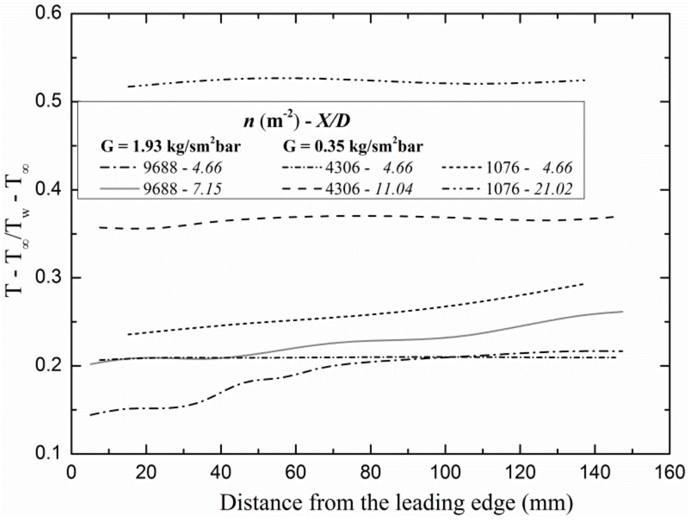

Figure 5.39: Comparison of target X^2 average T^* for varied *n* and X/D of two G values

Figure 5.33 shows that as *n* is decreased and X/D is increased (as X is also increased), the region of the hottest spot on the target wall is increased, but for a fixed X/D with increased in jet hole size this hottest spot vanished gradually. By comparing between these two X/D geometries with changes in *n*, Figure 5.33 shows that the varied X/D indicates better cooling as it has higher cool spot. But Figure 5.37Figure 5.38Figure 5.39 shows that the X^2 average T^* contradict what have been shown in Figure 5.33, as Figure 5.37 and 5.39 shows that X^2 average T^* increases with increased *n* at fixed X/D, while Figure 5.38 and 5.39 shows that T^* increases with decreased *n* for increased X/D. Figure 5.39 compares surface X^2 average T^* that was shown in Figure 5.33, this shows that for similar *n* but different X/D, the smaller X/D of 4.66 of all *n* indicates better surface temperature gradients even though they show the worse in Figure 5.33.

5.7 Conclusions

Experimental results for impingement cooling were presented for ranged of geometries, where Z/D, X/D, *n* (or N) and G were varied. The impingement jet and target metal walls were Nimonic-75 of 6.35 mm metal thickness. Square array impingement jets were investigated using CHT CFD for these range of geometries and mass flux. At a constant mass flux G typical of the total compressor exit regeneratively cool combustor wall: the geometries Z/D was varied by changing only Z, X/D was varied by changing the hole diameter D at constant pitch X and Z, X/D was also varied (where *n* or N were varied) for smaller fixed D and Z at varied X and finally *n* was varied at fixed X/D for varied X and D at fixed Z. The mass flux G was also varied for a fixed geometry of $n = 4306\ m^{-2}$ at X/D = 4.66 and Z/D = 3.06, a similar variable for varied Z/D. These conditions were appropriate for an application of impingement cooling to regenerative combustor wall cooling for low NOx combustor applications.

For all these impingement cooling geometries, the measured locally surfaced averaged heat transfer coefficient (HTC) *h* and the impingement flow relative pressure loss $\Delta P/P$ were predicted. These results were compared for geometries with the same G and geometries with varied G, which have been shown give excellent agreement with the experimental surface and X^2 averaged HTCs and with the measured pressure loss, whereby only few expception could not agree and the reasons for this were given. The CHT CFD computations employed the standard k - ε turbulence model using standard wall function, this showed that the aerodynmics of the impingement cooling were correctly predicted by this model based on the agreement given.

The experimental results showed that there was a strong influence of *n* on the surface averaged heat transfer *h*. The greater number of jets in the cross-flow direction as *n* was increased for fixed X/D resulted in a reduction of heat transfer with distance along the impingement wall. This reduced the surface average heat transfer, but as X/D was varied and increased it increases it. For smaller *n* the distribution of the heat transfer across the surface was poor and gave rise to the highest thermal gradients. There were hot spots between the jets that reduced the overall surface averaged heat transfer to below that for 4306 m^{-2}.

For an X/D of 1.86 and G of 0.35 kg/sm^2bar (X/D = 4.66 and $n = 4306$ m^{-2}), the predictions were low for pressure loss and low for *h*, although the axial variation of *h* was predicted to be similar to that measured. The reason for this was considered to be due to the laminar flow in the impingement holes for the lower G and the under prediction of turbulence generated by these flows. Similarly for the smaller X/D laminar flow occurred in the first few rows of holes, which was not taken into account in the predictions.

The CFD predictions that were influenced by the cross-flow for range of geometries and for varied rows of holes, showed that for the first few holes with low cross-flow, there was interaction between the jets on the surface that produced a reverse jet on the centre-point of the square array. This reverse jet was shown to carry heated air from the surface to the impingement jet surface which was subsequently heated.

The action of the cross-flow was to deflect this reverse jet and to decrease its effectiveness. The cross-flow also convected the surface turbulence downstream of the impingement point and thus reduced the average turbulence on the surface. The net result was a reduction in the mean local surface average heat transfer with distance. The predictions of this heat transfer reduction were in good agreement with the experimental measurements.

The CHT CFD predictions enabled the heat transfer to the impingement jet wall to be predicted. On average this *h* was about 50% of that for the impingement target wall at all X/D and an average of 70% of the target wall HTC for varied *n* at fixed X/D, for Z/D with varied gap this was about 30% and shows insignificant change with reduced Z/D. This should be a significant feature of the overall impingement heat transfer process. However, there were significant variations in this ratio with X/D and between the first few holes and the last few holes.

The conjugate heat transfer CFD was able to predict the surface distribution of temperature and the temperature gradients through the thickness of the Nimonic-75 wall. The axial gradients in surface temperature were much lower than the impingement jet side gradients in heat transfer coefficient, due to the internal conduction of heat within the metal wall. These gradients increased as the HTC increased and were greatest at the highest X/D. Thermal gradients increased as *n* decreased but were considered acceptable for the optimum *n* of

4306m^{-2} for maximum h and unacceptable for the lower n of 1076m^{-2}. The conjugate heat transfer CFD gave very good agreement with the metal temperatures measured experimentally in the Nimonic-75 wall and showed that thermal gradients were relatively low. This indicates that CHT CFD is adequate for the prediction of metal temperatures in gas turbine cooling systems such as impingement cooling and should be used in optimization studies for optimum cooling configurations.

Conjugate heat transfer CFD has been shown to give good predictions of impingement cooling and is a viable design tool for combustor and turbine blade cooling design.

CHAPTER SIX

FOUR SIDED EXIT FLOW IMPINGEMENT COOLING

RESULTS

Chapter 6

Four Sided Exit Flow Impingement Cooling Results

6.1 Introduction

This work investigate impingement conditions relevant to impingement/effusion cooling which has zero cross-flow and hence the minimum impingement cross-flow scheme with four sided exit is appropriate. This application also uses low G as the air is taken from the combustor air flow and needs to be minimised if NOx is to be minimised [36]. In this application the impingement wall has the bulk of the combustor pressure, which combined with the low G requires a high X/D with smaller jet size at fixed X or fixed n (m^{-2}). Impingement/effusion cooling has no impingement air cross-flow in the gap as all the impingement air flows out of the effusion holes. The nearest impingement geometry to this, without the effusion jets present, is for the impingement gap to have four sided exit [3, 19, 21, 47, 63, 66], so that cross-flow is minimised. From the centre hole to the edge the number of upstream rows of holes N in this work is 5, compared with 10 for the equivalent single sided exit case. This automatically reduces the influence of cross-flow in the impingement gap.

The minimum cross-flow effect for the four sided impingement jet flow exit geometry shown in Figure 1.7 (b) [3, 45, 47, 63, 134, 205] has been shown experimentally to be compatable with the impingement heat transfer in impingement/effusion cooling [4, 19, 45]. Previous experimental investigations of these impingement/effusion cooling schemes, for hot wall rigs gives the overall cooling effectiveness [33, 43]. Electrically heated isothermal metal wall impingement experimental rigs [7, 32, 63], as shown in Figure 2.3 (c) [3, 5, 22, 210, 312], are the data base on which this CHT CFD are based. Similar work has been carried out with adiabatic walls [115, 211, 212], a four sided exit geometry with a flat surface heat transfer that approximates to a large diameter combustor surface with low curvature was used [56, 57, 66, 126, 195]. This flat surface approximation is also often used in turbine blade cooling for the mid-chord region [126, 209].

This CHT CFD investigates, the influence of mass flux G for a fixed X/D of 11.04 and Z/D of 7.25 four sided impingement jet flow exit that has been investigated experimentally [3, 19, 45], using the test rig shown in Figure 2.3 (c). For single sided impingement flow exit the optimum number of impingement holes was shown to be $n = 4306\ m^{-2}$, which is 10 rows of square array holes. For impingement/effusion cooling a low coolant mass flow is required, as explained above, and the optimum geometry will have the main pressure loss at the impingement wall, as this gives the highest impingement jet velocities. The effusion wall will have a low pressure loss with low jet velocities or low blowing ratio M. This requires, for the same *n* or pitch X, larger diameter effusion holes than impingement holes or large X/D for the impingement wall and low X/D for the effusion wall. The impingement wall X/D of 11.04 and for a design G of 0.4 kg/sm^{2}bar gives a 3% pressure loss ΔP/P, which is typical of combustor wall pressure loss. El-jummah *et al* [25] have previously predicted the effect of the impingement X/D for single sided exit for a high G of 1.9 kg/sm^{2}bar. This showed the large increased in impingement heat transfer that occurred as X/D was increased for the same G. The range of G in the present work was varied from 0.2 - 1.1 kg/sm^{2}bar, which also varied the hole Reynolds number from 2.1×10^3 - 13.1×10^3, this corresponded to the range of G in the experimental data base used for comparison [3, 5, 19, 21].

6.2 Experimental Geometries Modelled

The specific impingement geometry modelled in the present work was the same as that used experimentally [19, 61] and is given in Table 4.3. This geometry is a practical actual size combustor cooling geometry and is not a scaled up model of the geometry as is often used. The holes were manufactured using spark erosion and thus had a practical internal surface roughness. The flow conditions modelled were also the same as those used experimentally, but with no specific surface roughness procedure other than the use of wall functions. The flow conditions are summarised in Table 6.1, which also gives the experimentally measured pressure loss Δ/P/P. The ranges of jet Re are all higher than the critical Re for turbulent flow limit > 2300. However, the jet turbulence in the impingement hole, which is controlled by the jet Re is largely irrelevant in the heat transfer as it is the impingement on the target surface that creates the intense turbulence that controls the heat transfer [83, 195].

The use of realistic hole sizes in the present work ensures that the length scale of turbulence is correctly modelled, as this is set by the hole diameter [17, 18, 82, 83]. The common practice of investigating impingement heat transfer is of the order of 10 times the hole size [45], so that spatial resolution of the heat transfer can be achieved. This has a problem that the length scale of turbulence is increased, which may influence the heat transfer. In engines impingement Re are higher than in the present work due to the high pressure which increases the flow density, but does not change the jet velocity. The turbulence on the impingement plate is considered to be more realistically generated using actual scale impingement geometries than in scaled up geometries. However, it does mean that experimental spatial resolution of heat transfer is lost and for metal surfaces gives only the locally surface averaged heat transfer, which was the data used to validate this computations.

Table 6.1: Impingement Four Sided Exit Flow Conditions

G kg/sm^{2}bar	V_i (m/s)	Re_h ($\rho V_j D/\mu$)	$\Delta P/P$ (%) Predicted	Measured
0.20	25.34	2380	0.74	0.63
0.30	38.02	3570	1.62	1.42
0.50	63.32	5940	4.30	3.94
0.63	79.77	7490	6.58	6.23
0.77	97.61	9160	11.71	9.35
1.10	139.36	13080	17.62	19.08

The experimental results for four sided exit impingement heat transfer that are modelled here [5, 312], used the lumped capacitance method for determining the surface averaged heat transfer coefficient (HTC) *h*. The target wall was 6.3 mm thick and was heated to about 80°C. The heat was removed and the impingement flow established. There was an array of imbedded thermocouples in the target wall (Figure 4.1 b) and the transient cooling of the target wall by the impingement flow was recorded [3, 19, 21, 45, 61]. The time constant of the cooling was determined and from this the local surface averaged HTC *h*, was determined from Equation 2.24, for each thermocouple location. From this, the Nusselt number Nu in Equation 2.35 could be determined. An additional experimental technique was also used and this was to operate the test rig at steady state with insulated heated target plate. A steady state heat balance then determined the locally averaged target surface temperature from which *h* could be determined. This was the technique used to measure the surface averaged temperature of the impingement jet wall, which are directly used in this work.

The computational domain and grid model geometry are those shown in Figures 4.2 (b) and 4.5 (ii), which were designed using representative parameters shown in Table 4.1. The total number of cells in all the grid geometries for the ranged of G (0.2 - 1.1 kg/sm^{2}bar) geometries modelled, varied from 3.64 - 3.94 million cells (Table 4.7), whereby the hole cell size 'ξ' were kept constant with 21 planes/hole (120 cells/plane). Using the standard k - ε turbulence model (WF), the first cell size near the target wall was kept at $y^+ \sim 35$ for all G.

The CHT CFD predictions of these results used the steady state approach in determining the heat transfer and imposed a constant temperature of 80°C on the hot side of the wall. This technique for determining *h* and Nu has been shown previously to agree with experimental data for single sided exit impingement heat transfer [32, 46, 312]. The hole surface HTC h_x given by Equation 2.25, was also predicted as there are established short hole heat transfer data [76, 79, 80, 83] that this can be compared with. Xing and Weigand [134] used the liquid crystals techniques to measure the surface distribution of HTC *h*. Obot and Trabold [47] used a segmented copper target plate to determine the locally averaged HTC *h*. Hollworth and Berry [63] used a continuous copper plate, similar to the experiments that are modelled in the present work, apart from the difference in thermal conductivity of the walls.

6.3 Computational Results

The key predicted aerodynamics data are the pressure loss ΔP/P (%), impingement hole/gap velocity profiles and the distribution of turbulent kinetic energy (TKE) [32, 46]. While, the heat transfer data are the HTC *h*, Nusselt number Nu and normalised temperature T^*. These computational procedures were shown to give good prediction of measured impingement pressure loss ΔP/P (%) and HTC *h* with single sided exit [3, 19, 47].

6.3.1 Influence of Mass Flux G on Aerodynamics

The predicted and measured influence of G on ΔP/P are shown in Table 6.1 and these results are shown as a function of G in Figure 6.1 (a) and as a function of Reynolds number Re in Figure 6.1 (b). Figure 6.1 (b) also show a comparison of the pressure loss for single sided flow exit [25] for the same impingement wall geometry, which show that the change from four sided exit to single sided exit has little effect on the pressure loss. This is because the main pressure loss, is due to the flow through the holes and is not a major pressure loss along the impingement gap caused by the cross-flow [32]. Also shown in Figure 6.1 (b) are predictions found by El-jummah *et al* [25] at very high G, where the Re is varied by varying the hole diameter at constant coolant flow rate. The same computational procedures as in the present work were used and good agreement with the experimental results was shown. The present work also has reasonable agreement with the experimental results as Table 6.1 and Figure 6.1 show.

The difference between prediction and measurements varied between 5 and 27%, with the best agreement for G = 0.6 - 1. The measurements in Table 6.1 are based on the assumption of constant C_d in Equation 2.11. However, the actual experimental results [83] show a dependence of C_d on Re and at low Re of 4000 was 0.77 and at 2000 was 0.76. For high mass flows at Re > 10,000 compressibility effects are significant and the C_d falls to 0.76. These changes in C_d account for most of the differences in the predictions and measurement for low and high G in Figure 6.1 (a) as a C_d difference of 0.76 from 0.8 is a 10% difference in pressure loss. When this is taken into account the agreement between measurement and predictions is all better than 10%. This shows that the predictions of the aerodynamics were reasonable.

Figure 6.2 (a and b) show the present CFD three-dimensional (3D) predicted for a G of 0.5 kg/sm^{2}bar and two-dimensional (2D) experimental [7] velocity pathlines. The interactions of the jets on the target surface which creates a flow reversal jet flow on the centreline between the impingement holes is shown in Figure 6.2. This reverse flow takes away heat from the target wall [32] and recirculates it to heat up the impingement jet wall.

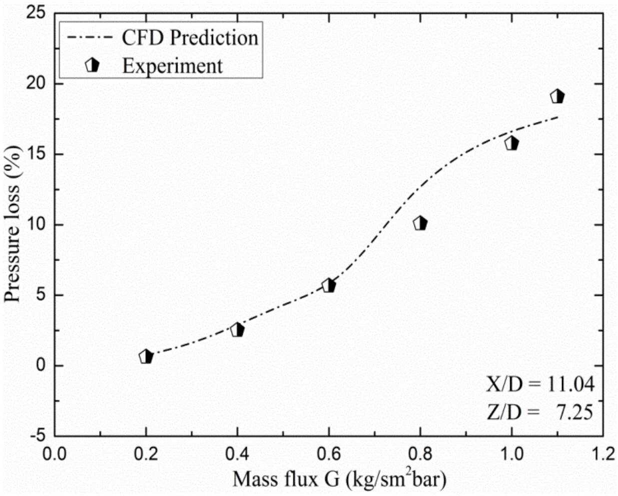

(a) Four sided exit flow

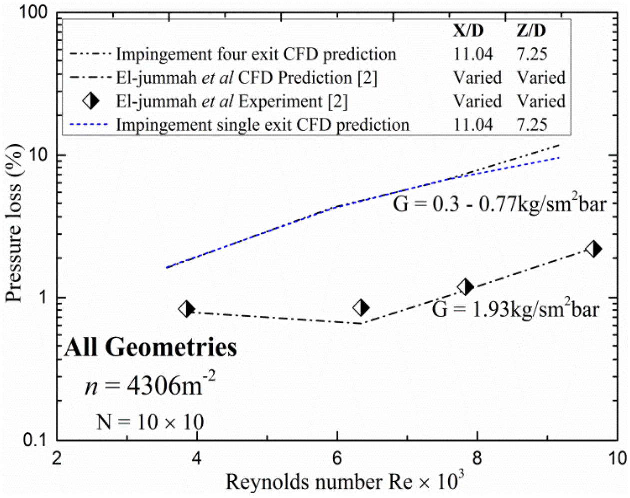

(b) Comparison with El-jummah *et al* [25] predictions

Figure 6.1: Comparison of predicted and measured pressure loss as a function of G and Re

The surface distribution of turbulent kinetic energy (TKE) for a G of 0.5 kg/sm^{2}bar for the square arrays of 100 holes is shown in Figure 6.3. The peak TKE distribution is centred around the impingement point with low turbulence elsewhere on the surface. Figure 6.3 show that as the flow moves to the outer regions, there is some evidence of convection of the turbulence in the cross-flow direction, but this is much lower than for single exit cross-flow. The central region is unaffected by the cross-flow for the central 16 holes, which is two rows of holes in the cross-flow direction. The central four holes are compared with the leading edge four holes for single sided exit in Figure 6.4, for the same G of 0.5 kg/sm^{2}bar and the same X/D and Z/D. Figure 6.4 (a) for the present four sided exits has lower TKE between the impingement points. This indicates that with single sided exit the flow for the first row of holes is affected in a way that increased the turbulence between the impingement points, as the flow has to turn in one direction. This will be shown later to results in better heat transfer for the single sided exit.

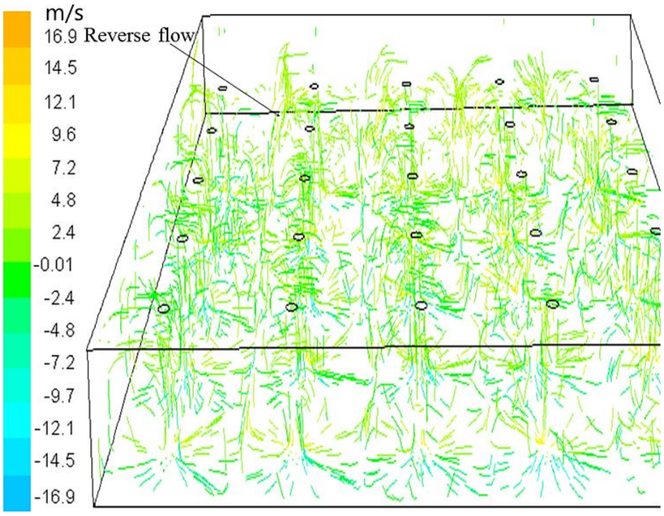

(a) CFD predictions: 3D for G of 0.5 kg/sm^{2}bar

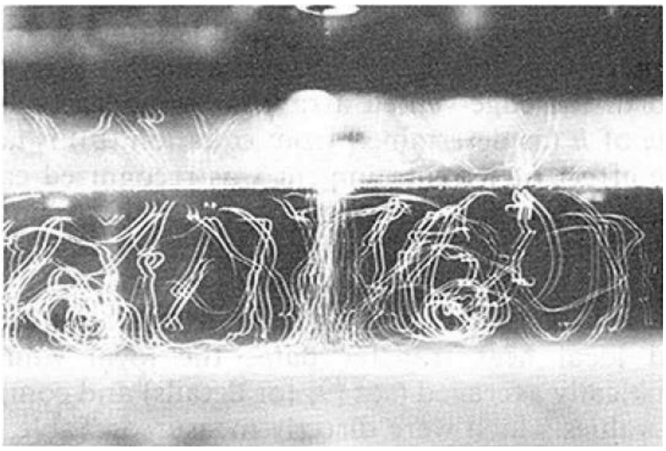

(b) Experiment [7]: 2D

Figure 6.2: Impingement gap jet flow pathlines velocity (m/s)

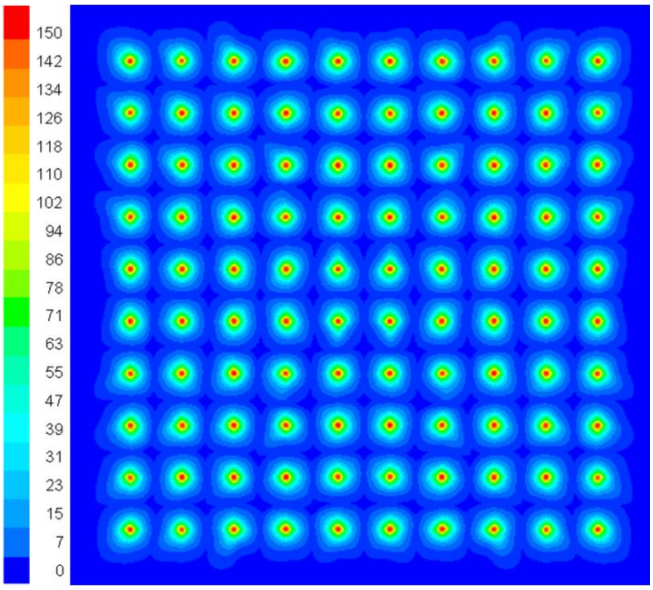

Figure 6.3: Contour of TKE (m^2/s^2) on target surface for G of 0.5 kg/sm^{2}bar

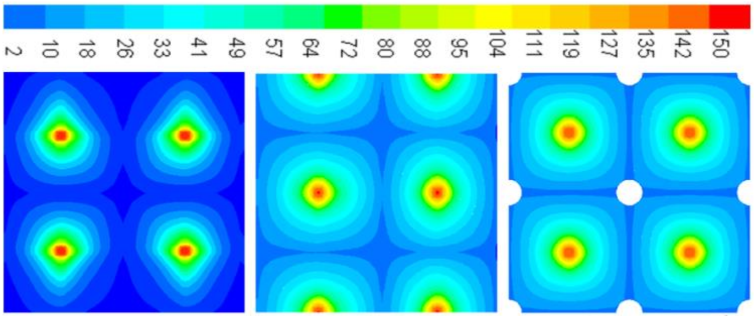

(a) Imp. 4 side exit ($4306m^{-2}$) (b) Imp. single exit ($4306m^{-2}$) (c) Imp/eff. ($4306/4306m^{-2}$)

Figure 6.4: Comparison of target surface contours of TKE (m^2/s^2) for G of 0.5 kg/sm^2bar

Figure 6.4 (c) compares the impingement only predictions in Figure 6.4 (a and b) with the equivalent turbulence for impingement/effusion cooling. This predicts that the surface distribution of turbulence in the inter impingement jet region is enhanced with very little of the surface having the lowest turbulence level. With impingement only flow there is a reverse jet flow, shown in Figure 6.2, but this flow is reduced with impingement/effusion cooling due to the extraction of the effusion flow at the location of the reverse flow jet. This forces the impingement surface flow to remain attached to the surface with a consequence in the better surface distribution of turbulence, relative to the impingement only cases.

6.3.2 Surface Distribution of Nusselt Number

The pattern of the predicted surface TKE distribution of Figure 6.3 is shown in Figure 6.5 to be similar for the target surface Nusselt number Nu distribution, for 0.5 kg/sm^2bar. Similar predicted comparisons of Figure 6.4 are also shown for the Nu surface distribution on the target surface in Figure 6.6 (a, b and c). Figure 6.5 show that the impact of the cross-flow for four sided exit is relatively small and is only apparent in the outer regions. For the central region Figure 6.6 (a) show there is still some distortion of the Nu profiles in the outflow direction in a similar way that the TKE profiles were distorted in Figure 6.4 (a). For single sided exits the Nu profiles for the second row of holes in Figure 6.6 (b) show a more uniform distribution and a reduced area of the lowest Nu. For the impingement/effusion flow, Figure 6.6 (c) show a much better surface coverage of high Nu, which is due to the flow acceleration into the effusion holes, which locally enhances the cooling in the hole entry region. In all three cases in Figure 6.6, the peak impingement Nu is the same.

Figure 6.7 shows the comparison of the surface averaged Nu predictions with the surface averaged experimental measurement of Andrews and Hussain [3], for the same geometry that was modelled with an X/D of 11.04. This shows reasonable agreement that are within the measured error bar of 11%. There was exact agreement between prediction and measurement for Re = 2500 and 7500. There was an under prediction of the measurements by 17% at Re = 3500, 14% at Re = 6000, and 12% at an Re of 900. At the highest Re there was an over prediction of 4%. On average the predictions were 6.5% lower than the measurements.

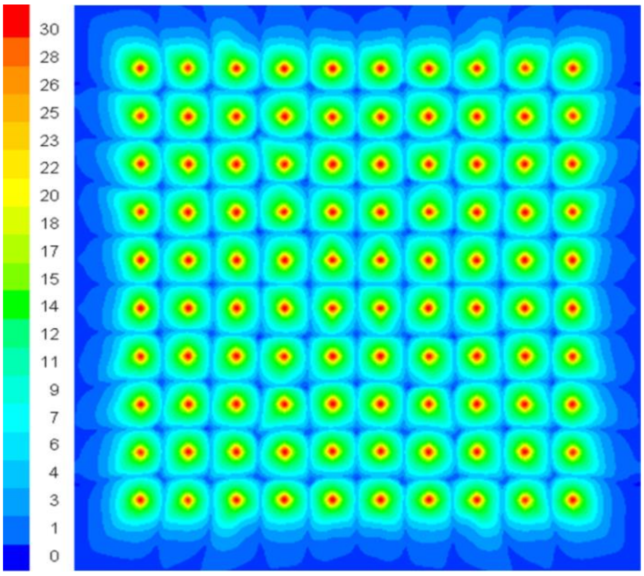

Figure 6.5: Contour of Nusselt number on target surface for G of 0.5 kg/sm^{2}bar

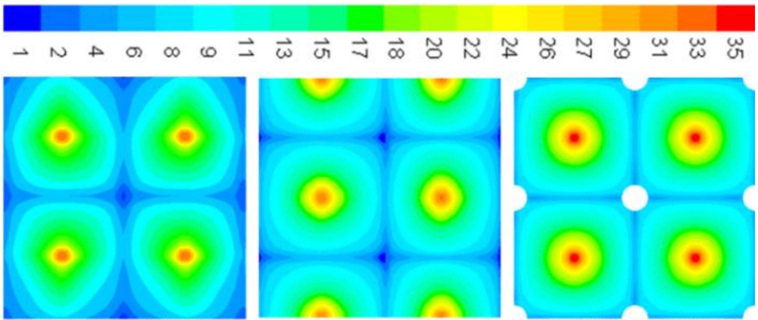

(a) Imp. 4 side exit (4306m^{-2}) (b) Imp. single exit (4306m^{-2}) (c) Imp/eff. (4306/4306m^{-2})

Figure 6.6: Target surface comparison of Nusselt number contours for G of 0.5 kg/sm^{2}bar

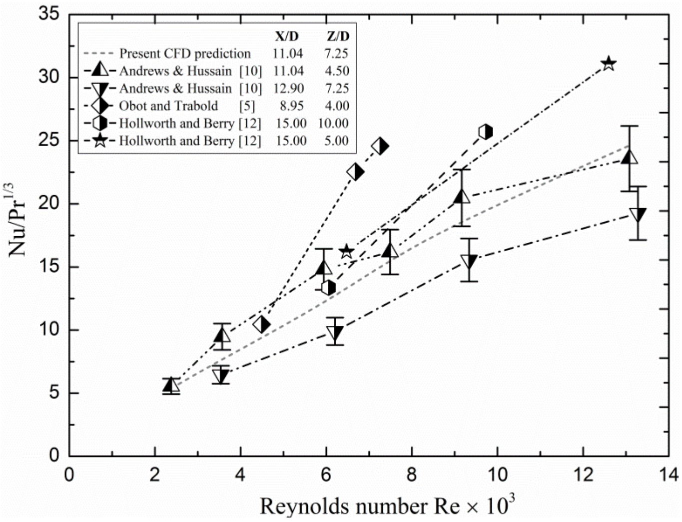

Figure 6.7: Comparison of predicted and literature measured Nusselt number variation

Figure 6.7 also compares the present predictions for four sided exit impingement heat transfer with other measurements for similar X/D. The differences are significant and mainly due to the differences in X/D. However, the results of Andrews and Hussain [3] showed a decrease in Nu with increase in X/D. Hollworth and Berry's [63] results for an X/D of 15 were similar to the present for a Re of 6500, but their Re exponent was higher. Obot and Trabold [47] for an X/D of 9 had a similar Nu for Re = 5000 but a larger increase in Nu with increase in Re.

6.3.3 Influence of Mass Flux G on Surface Average Heat Transfer

Figure 6.8 shows the surface distribution of *h* on the target and impingement jet surfaces for three G values. This is the first time that heat transfer to the impingement jet surface has been predicted and measured. Figure 6.8 (ia) show that at low G there was little surface coverage of the enhanced impingement heat transfer and Figure 6.8 (iia) show that there were no reflected jets giving heat transfer on the impingement surface between the impingement jets. However, at higher G the high heat transfer due to the reflected jets were predicted to occur at the midpoint of the four impingement jets. This heat transfer was convected in the direction of the exit flow as the flow moved to the exit and a cross-flow was experienced.

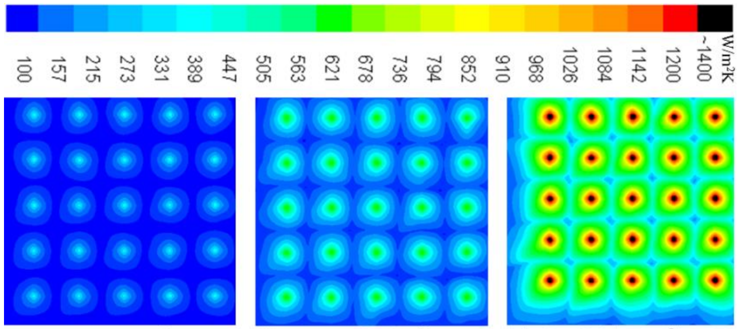

(a) G = 0.2 kg/sm^{2}bar (b) G = 0.2 kg/sm^{2}bar (a) G = 1.1 kg/sm^{2}bar

(i) Target surface

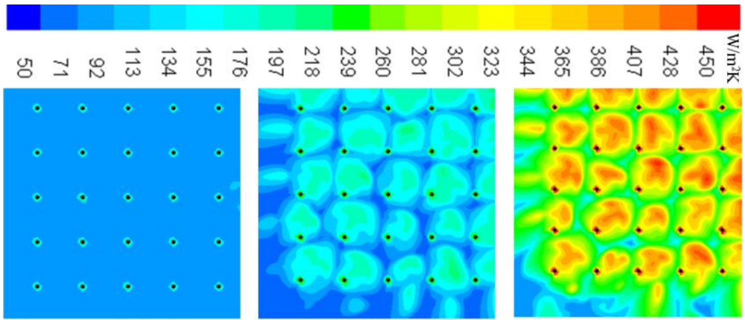

(a) G = 0.2 kg/sm^{2}bar (b) G = 0.5 kg/sm^{2}bar (c) G = 1.1 kg/sm^{2}bar

(ii) Impingement plate

Figure 6.8: Surface distribution of HTC *h* for varied G at constant unit pressure

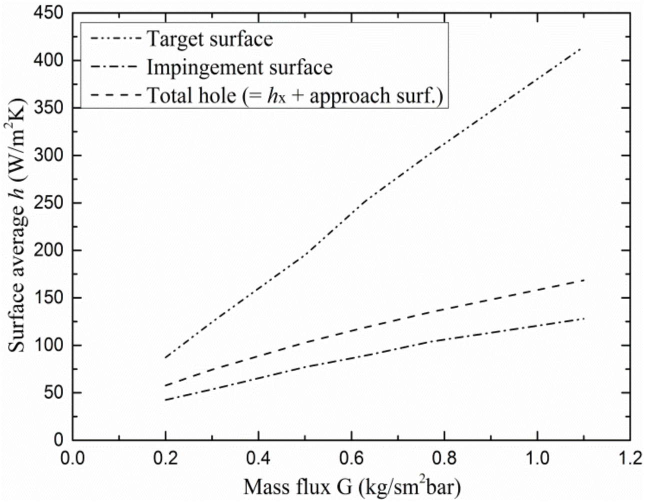

Figure 6.9: Comparison of predicted surface average HTC as a function of mass flux G

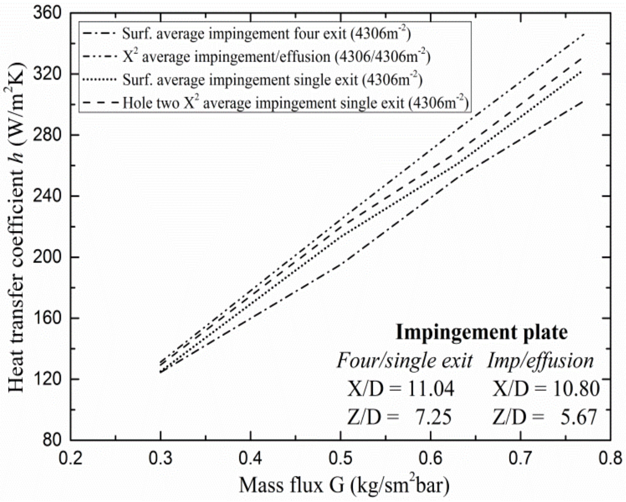

Figure 6.10: Comparison of the present work with impingement single flow exit and impingement/effusion predicted surface average and X^2 average HTC h on the target wall

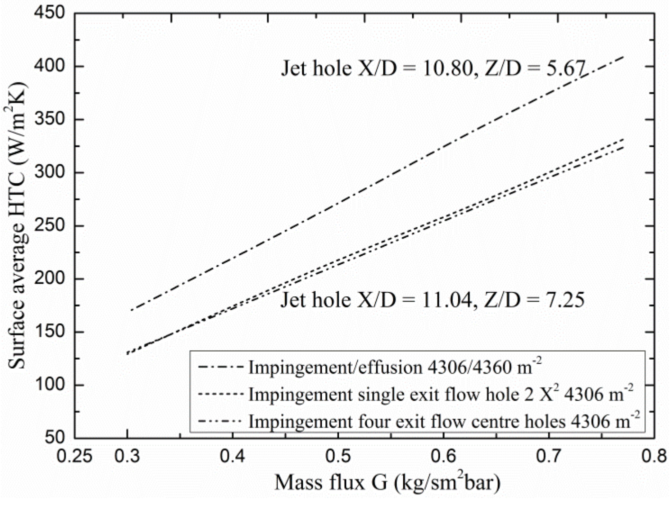

Figure 6.11: Comparison of predicted cooling heat transfer on target or effusion approach surfaces for three different type of cooling with similar n (m^{-2}) of varied mass flux G

The predicted surface average heat transfer as a function of G is shown in Figure 6.9. There are three components to the heat transfer that were predicted Figure 6.9: Firstly the impingement target wall heat transfer, secondly the heat transfer due to the reverse flow jets to the impingement jet wall and thirdly the heat transfer to the coolant as it passes through the heated impingement wall. At low G of 0.2 kg/sm^{2}bar all three heat transfer modes are of similar magnitude, although the target wall heat transfer is the highest, followed by the impingement jet wall and finally the heat transfer in the jet holes. However, the increase in the heat transfer coefficients with G is much greater for the impingement target wall. The reverse jet heat transfer to the impingement wall was 53% of the impingement target wall heat transfer at the lowest G, but 31% at the highest G. The heating of this surface by the reverse jet was predicted to be recycled as heat transfer to the impingement air as it flowed through the wall. This occurred on the hole approach surface and inside the holes.

6.3.3.1 Surface Averaged HTC for Different Cross-flow Schemes

Figure 6.10 compares the predicted surface averaged *h* for different impingement wall configurations. The present predictions for the four sided exit are compared with those for a single sided exit flow. The single sided exit predictions for the first two hole, where cross-flow is at a minimum is also shown in Figure 6.10. Finally these three geometries are compared with predictions for impingement/effusion cooling for a very similar geometry. Figure 6.10 shows that all four of these configurations were predicted to be simlar with only small differences. The highest *h* was for the impingement/effusion configuration and the lowest was the present predictions for four sided exit impingement heat transfer. The difference in these two was due to the suction effect of the effusion hole flow on the wall impingement jet flow. This leads to more surface TKE and higher surface heat transfer. In between these two was the surface average heat transfer for the second row of impingement holes, where the cross-flow effect was not significant. This was obviously higher than the total surface area average heat transfer for the same single sided impingement flow exit. The lower total impingement target surface heat transfer was due to the deflection of the jets and associated turbulence by the cross-flow [32, 33, 46]. Figure 6.11 show the quantitative predicted HTC *h* comparison between the three configurations, shown in Figure 6.6 for the range of G values, which further confirmed the above conclusion that the central region of Figure 6.6 (a) has the same heat transfer data with region of minimum cross-flow of Figure 6.6 (b). Figure 6.11 also show that the predicted HTC of the impingement/effusion configuration gave higher values than does the other two geometries.

6.3.3.2 Heating of the Impingement Jet Plate

Andrews *et al* [19], experimentally measured the impingement jet plate heating using the dimensionless temperature T_Z of Equation 2.44. In the present work the dimensionless temperature T^* in Equation 2.6 was also predicted, which allows the surface distribution of the impingement jet metal temperature to be shown in a dimensionless form. The predicted values of T_z for the mean impingement wall temperature are shown in Figure 6.12 where they are compared with the experimental measurements [19]. The results for lower G of 0.2 and 0.45 kg/sm^{2}bar show very good agreement with the experiments, but for G of 0.77 and 1.1 kg/sm^{2}bar the prediction disagrees with the measurement. For impingement/effusion cooling it is the lower G that is of interest. It is possible that the experimental test rig was not as adiabatic as intended, but this would influence all the measurements. The aerodynamics should be correct as the predicted and measured pressure loss agreed at all G. The implication of these results is that the peak heat transfer on the impingement surface in Figure 6.8 (iic) are over predicted. It is possible that the disagreement is due to the five thermocouples in the impingement jet wall that are not representative of the mean surface averaged HTC. However, the agreement with low G values would suggest that this is not the problem. Therefore, no explanation for the lack of agreement at high G values.

Figure 6.13 shows the equivalent predictions for the impingement jet wall as were given in Figure 6.10 for the target wall. The present predictions for the mean HTC to the impingement jet wall are shown in Figure 6.13 for the four side exit and compared with those for a single sided exit. The single sided exit predictions for the first two hole, where cross-flow is at a minimum is also shown in Figure 6.10. Finally these three geometries are

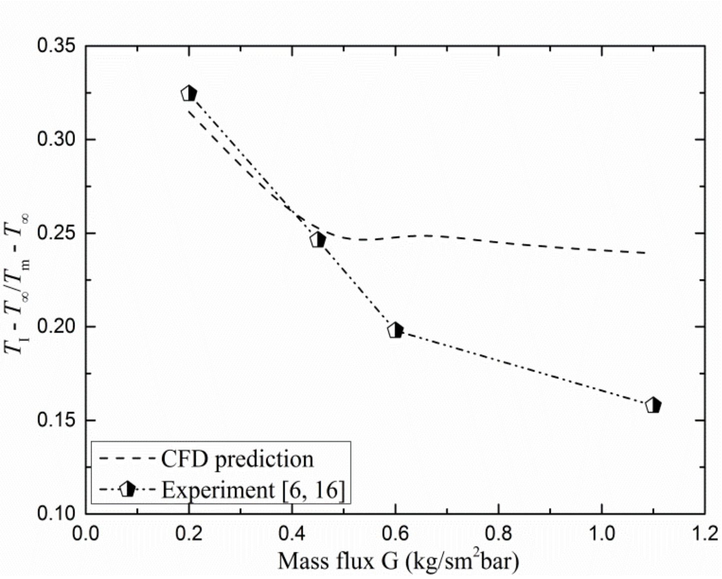

Figure 6.12: Comparison of surface Tz on impingement jet plate for varied mass flux G

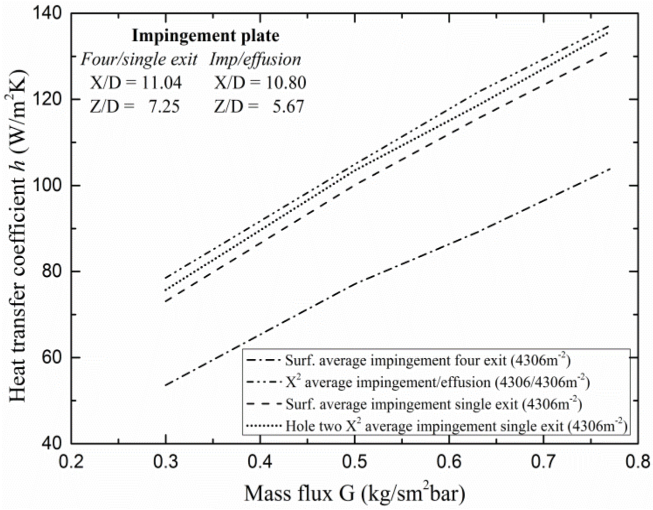

Figure 6.13: Comparison of the present work with impingement single flow exit and impingement/effusion predicted surface and X^2 average HTC *h* on impingement jet plate

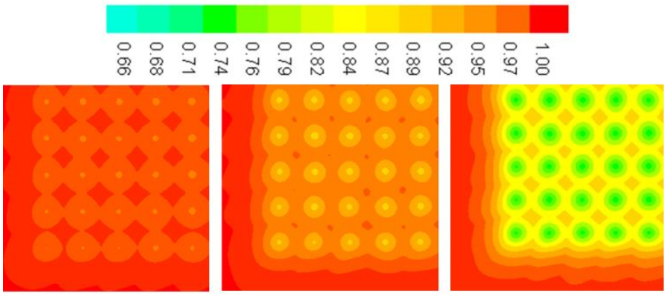

(a) G = 0.2 kg/sm²bar (b) G = 0.5 kg/sm²bar (c) G = 1.1 kg/sm²bar

(i) Target surface

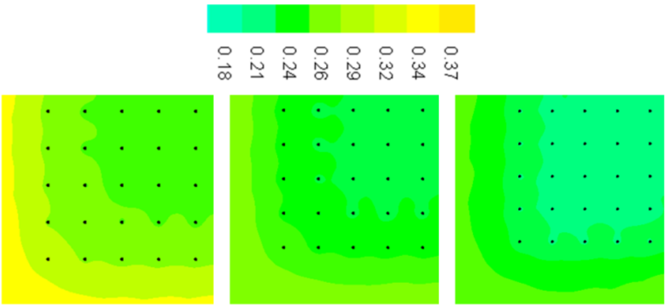

(a) G = 0.2 kg/sm²bar (b) G = 0.5 kg/sm²bar (c) G = 1.1 kg/sm²bar

(ii) Impingement plate

Figure 6.14: Contours of normalised temperature T^* for varied G at constant unit pressure

compared with predictions for impingement/effusion cooling for a very similar geometry. Figure 6.13 shows that the predicted surface averaged HTC *h* for the impingement jet wall was significantly lower for the present four sided exit predictions. The highest heat transfer was for the impingement/effusion geometry, even though the recirculation in the gap was reduced by the effusion hole outflow. However, this was only marginally higher than the impingement jet wall heat transfer for single sided exit in the leading edge region, which was only slightly higher than for the impingement jet wall surface averaged heat transfer.

The big difference for the four sided exit is the cross-flow number of holes is reduced by a half, but also the cross-flow area is increased by a factor of 4. It is clear that it is this lower cross-flow effect that is reducing the heat transfer to the impingement wall compared with the singe sided exit results. El-jummah *et al* [22, 25, 32] have shown that for single sided exit the aerodynamics of the cross-flow displace the flow towards the impingement jet wall and increase the heat transfer there. The surprising predictions in Figure 6.13 were the highest heat transfer for the impingement/effusion geometry, where there is no cross-flow. However, the impingement jet outlet velocity is the same and the entrainment of this jet is the main driving force for the recirculation of the flow from the effusion wall. With no cross-flow to destroy this flow it appears to result in the greatest heat transfer to the impingement jet wall.

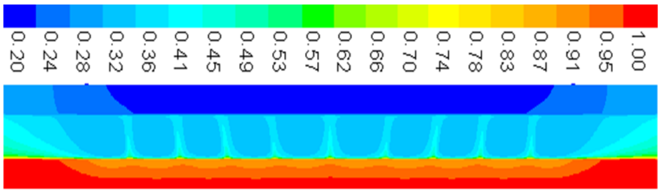

(a) Impingement four sided flow exits (4306m^{-2})

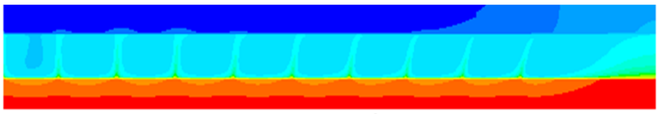

(b) Impingement single sided flow exit (4306m^{-2})

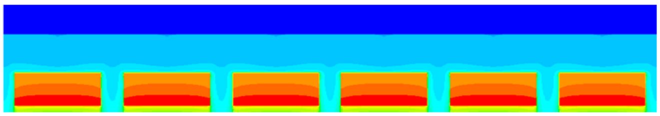

(c) Impingement/effusion (4306/4306m^{-2})

Figure 6.15: Comparison of jet hole centre line contours of normalised temperature T* for G of 0.5 kg/sm^{2}bar with impingement and impingement/effusion cooling geometries. View on the centreline between impingement jets, which is in-line with the effusion holes.

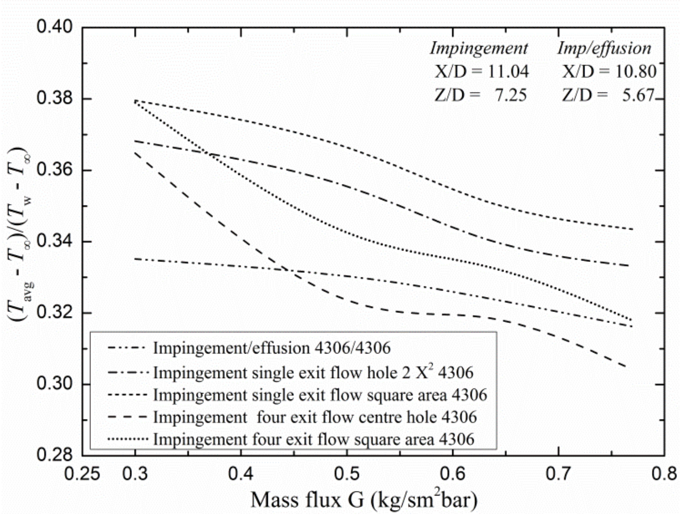

Figure 6.16: Comparison of predicted normalized temperature on target or effusion approach surfaces of three different types of cooling with similar *n* (m^{-2}) for varied G

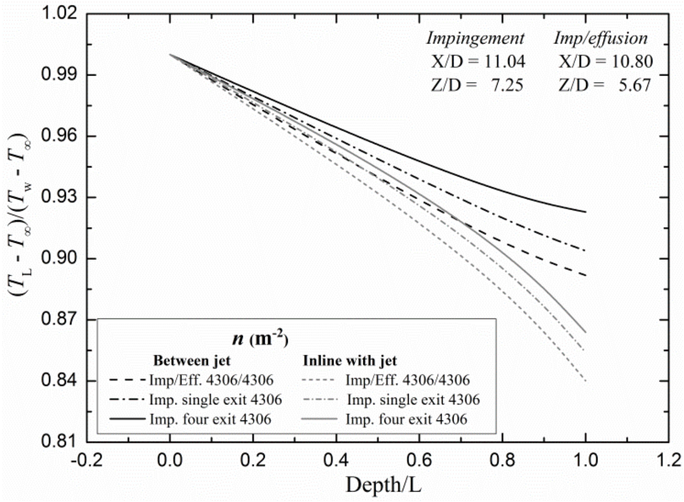

Figure 6.17: Comparison of predicted normalized temperature T^* on target or effusion approach walls for three types of cooling system with similar *n* (m^{-2}) for G of 0.5 kg/sm^{2}bar

Figure 6.14 show for three values of G the predicted surface distributions of the dimensionless temperature T^* for the target wall. In Equation 2.6 for T^*, the hot wall side temperature T_w is the imposed 80^{o}C and T is the predicted temperature on either the cooled target wall or the impingement jet wall. On the target wall of Figure 6.14 (ia, b and c), the distribution showing the lower T^* implies higher *h*. These dimensionless temperature plots include the uncooled flange area of the test section, which can be ignored. Figure 6.14 (i) show that the target wall temperature gradients were significant at high G, but at low G the wall was a fairly uniform temperature. The extra cooling as G is increased comes with increased thermal gradients. In contrast the thermal gradients predicted on the impingement jet wall are shown in Figure 6.14 (ii) to be much more uniform for all G. The cross-flow effect in the exit region can be seen with cooler walls, especially at low G. Equation 2.6 was also used to show the heating of the air jets and the thermal gradients in the metal walls as shown in Figure 6.15. This clearly show the heated reverse jets flow that causes the heat transfer to the impingement jet wall. The deflection of the reverse flow jet by the cross-flow is also clear. Figure 6.15 show that impingement/effusion cooling gave better cooling of the impingement wall. As there was no cross-flow to increase this wall heating, the mean temperature was lower. This is the reason for the surface averaged *h* in Figure 6.13 being highest for the impingement/effusion configuration.

6.3.4 Thermal gradients in the metal wall

Figure 6.16 show the deviation of the surface average normalized temperature T^* on the target wall as a function of mass flux G (0.3 - 0.77 kg/sm^{2}bar), which is for the different impingement wall configurations similar to Figure 6.10. Figure 6.16 compares the present predicted surface averaged T^* of Figure 6.14 for the four sided exit with those for a single sided exit flow. Also compared are the present work predicted locally averaged X^2 T^* for the central region, with the single sided exit for hole two where cross-flow is at a minimum. Finally these geometries are compared with the predictions for impingement/effusion cooling for a very similar geometry. Figure 6.16 show that for all these geometries, T^* decreases with increasing G [46] and on the average, the four exit central region impingement T^* could be in the range of the impingement/effusion T^* that has smaller decrease linearly with G. At high G values, the four exit surface averaged T^* was predicted to be the same to the impingement/effusion one and for smaller G, this gave higher averaged T^* data that are the same with the impingement single exit flow data. The impingement single exit flow have the highest surface averaged T^*, while impingement/effusion and four exit central region having the lowest T^*, with the four exit surface and single exit average X^2 T^* in between the two. This indicates that the four exit central region could give similar cooling performance to the impingement effusion one that has the best cooling as was also shown in Figure 6.10.

The predicted thermal gradient through the depth of the target wall as Figure 6.15 show for a G of 0.5 kg/sm^{2}bar, is quantitatively shown in Figure 6.17 for the three geometries discussed above and are at the region of minimum cross-flow impingement only geometries. The gradients in-line with the impingement jet and between the jets are shown in Figure 6.17 and were greatest in-lined with the jets, due to the higher HTC there. For all the cooling configurations, the thermal gradients were greatest at the target top surface due to the greater heat removal with cooler surface temperature and highest at the hottest side imposed temperature. In both the in-line with and between jets, the thermal gradients of the present geometry were predicted to have the highest, with impingement/effusion having the lowest and impingement single exit in between the two. This further justify that the impingement/effusion cooling have the highest heat transfer.

6.4 Conclusions

The CHT CFD predictions for four sided exit impingement heat transfer for G from 0.2 to 1.1 kg/sm^{2}bar at X/D of 11.04 and Z/D of 7.25 showed excellent agreement with the experimental surface averaged Nusselt number. The average difference of the predictions for the surface average Nu from the measurements was 6.5% lower.

The predictions of the pressure loss were in very good agreement with the measurements, indicating that the aerodynamics were correctly predicted.

The predictions showed that there was a reverse flow from the target wall to the impingement jet wall that results in heat transfer and heating of that wall. The predictions of this heating showed good agreement with measured T_Z at lower G, but not at higher G.

The predictions of the impingement jet wall heat transfer coefficient was 70% of the target wall heat transfer coefficient and hence a significant feature of the overall impingement heat transfer process.

The locally X^2 averaged normalized temperature T^* for the central region of the four exit flow impingement jet geometry were shown to have the same T^* data to an impingement/effusion cooling one.

CHAPTER SEVEN

IMPINGEMENT COOLING HEAT TRANSFER ENHANCEMENT RESULTS

Chapter 7

Impingement Cooling Heat Transfer Enhancement Results

7.1 Introduction

This Chapter is concerned with the maximisation of the blade cooling using impingement cooling with heat transfer enhancement using obstacles in the impingement gap. The advantage of maximising the internal wall cooling is that less film cooling air flow will be required, as film cooling air flow deteriorates the thermal efficiency of the compression work of the air, which is not fully recovered in the expansion process. The turbine blade efficiency is also deteriorated by the increased aerodynamic losses caused by the presence of the film cooling air. For impingement cooling without effusion cooling there is a cross-flow in the impingement gap as the impingement air from the first rows of jets flows along the gap to the trailing edge exit and this has been found to reduce the surface heat transfer in the downstream portion of the cooled surface [20].

El-Jummah *et al* [25, 32, 33, 46] have predicted the downstream surface heat transfer deterioration using 3D CHT CFD, which showed that a greater problem in wall cooling design for GT combustor walls, as the distances to be cooled are greater than in turbine blades [3, 194]. However, the reasons for this deterioration in heat transfer are not well understood and are often simply ascribed to the deflection of the impingement jet by the cross-flow. CFD investigations of the aerodynamics in the impingement gap, showed that the effect of cross-flow is more compact and is linked to the movement of impingement jet turbulence to cover only the downstream portion of the jets as well as deflection of the reverse flow jets that reduces the efficient removal of heat, from the cooled surface and increases the transfer of heat to the impingement jet surface. Experimental investigations showed that for high X/D [25] with very high air jet velocities and relatively low impingement gap cross-flow velocities, this deterioration of heat transfer with axial distance still occurred. As the flow in a duct has a significant heat transfer on its own if the impingement and duct flow heat transfer were additive then the heat transfer would increase in the downstream direction, which does not occur in any single sided exit impingement heat transfer experiments. To overcome this disadvantage of the impingement air jets, enhanced heat transfer is used by the addition of obstacles on the target walls, which have been shown to reduce or eliminate the deterioration of heat transfer along the gap with distance [194, 210, 214]. This Chapter shows the enhanced walls procedures as applied to impingement single exit geometries that offered improvement in the overall surface HTC *h*.

7.2 Obstacle Walls Design Considerations

The present CHT CFD investigations are in two phase: firstly, the experimental results of Andrews *et al* [194, 210, 214], using the test rig in Figure 2.3 (c) for the types of target plates shown in Figure 7.1 are predicted and secondly, round pin fins, zig-zag ribs, and dimpled surfaces were predicted for the same geometries. Andrews *et al* [194, 210, 214] investigated two types of obstacles (ribs and rectangular pins), which were investigated with two cross-flow alignments of co- and cross-flow, as Figure 7.1 shows. These were used as validation cases for the current CHT CFD investigations. The rib heights for co-flow were higher than for cross-flow due to pressure loss considerations. Four separate test walls were investigated with the ribs machined from a solid block of stainless steel. The rectangular pins or slotted ribs were intended to generate more turbulence in channel flow (co-flow) and large scale recirculation and enhanced turbulence in cross-flow.

Other impingement cooling enhancement designs were also predicted based on designs shown in the literature to be effective. These are: dimpled surface [115, 204, 205, 236-239], round pin-fins [229, 313] the angled ribs forming a zig-zag geometry [35, 133, 215-217, 224], these are shown in Figure 7.2. The geometries modelled were the same as that used for the smooth target wall impingement cooling with a 10 × 10 array of impingement jet holes [22, 25, 46] for a fixed X/D of 4.66, Z/D of 3.06 and n of 4306 m^{-2}, as summarised in Table 4.1. The range of mass flux G was 1.08 - 1.93 kg/sm^2bar as undertaken by El-jummah *et al* [46] for the smooth walls and as Table 4.11 shows. Each coolant G that was predicted using a new computation, only the number of cells in the gap were varied and the overall changes in each grid geometry was small, which decreases as G was decreased. This will imply that for each heat transfer enhancement geometry, a new grid geometry will be required, which requires three grid geometries for each obstacle computations. The present work on the effect of obstacles in the impingement gap was compared with predictions for impingement smooth wall cooling, so that the enhancement of heat transfer could be predicted.

7.2.1 Model Grid Geometry

The impingement cooling geometry was the same as that modelled in the work of El-jummah *et al* [46] for smooth target walls, as shown in Table 4.1. This work investigates the potential improvement in the heat transfer using obstacles in the impingement gap, as summarised in Figure 7.2 with dimensions in Table 7.2. The first two obstacles in Figure 7.2 were those investigated by Andrews *et al* [194, 210] and Abdul Hussain and Andrews [214] with a rib thickness t of 3mm. The ribs consisted of a continuous rib of height H, 45% of Z or rectangular pin with H 80% of Z with equal pin width W and pin gap. These two obstacles were investigated for two cross-flow direction relative to the ribs: co-flow parallel

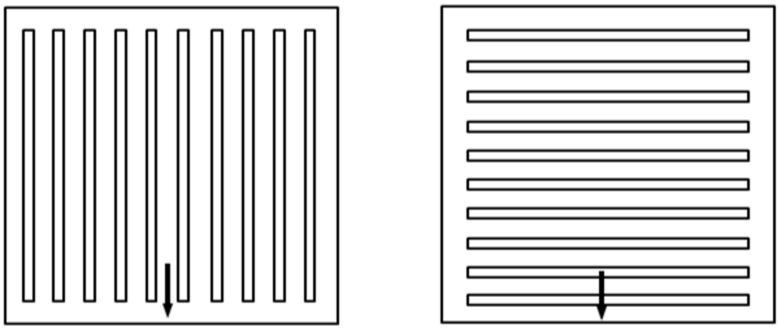

(a) Ribs wall: Co-flow (b) Ribs wall: Cross-flow

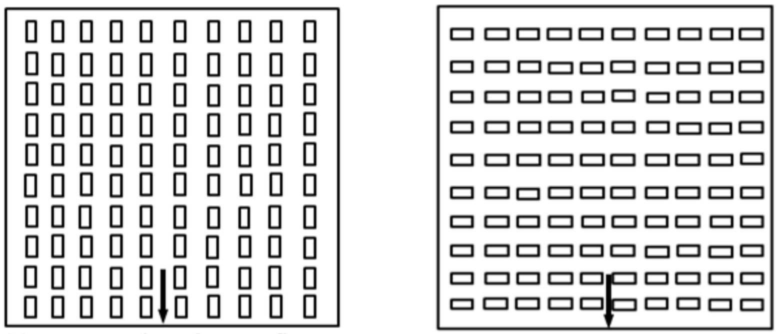

(c) Rectangular pin: Co-flow (d) Rectangular pin: Cross-flow

Figure 7.1: Experimental obstacles target plates [194, 210, 214]

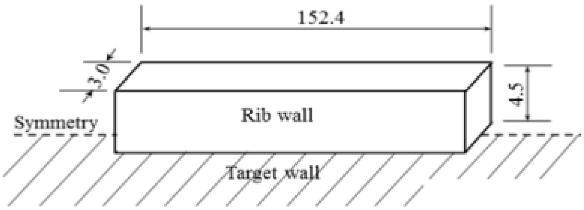

(a) Ribs Wall

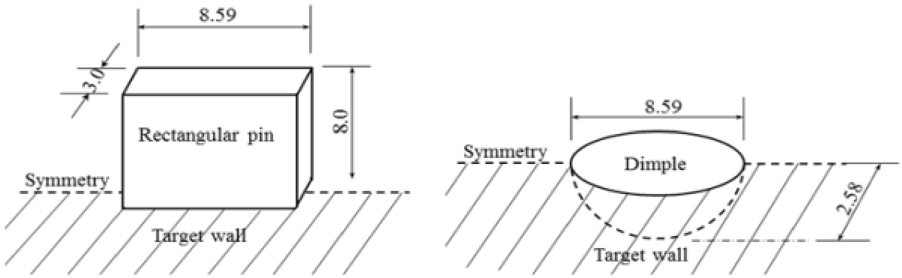

(b) Rectangular pin (c) Dimpled slot

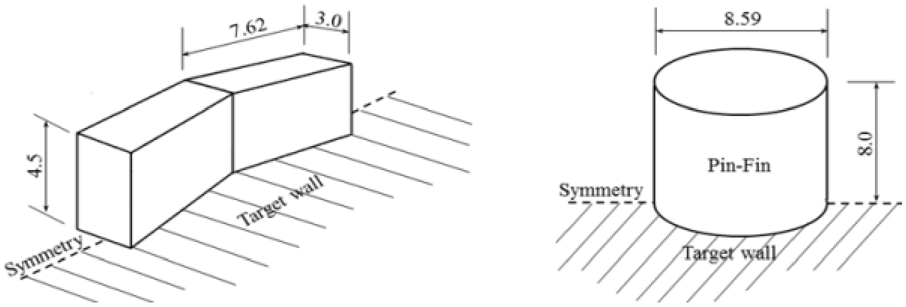

(d) Zig-Zig ribs wall (e) Pin-Fin

Figure 7.2: Cross-sectional dimensions of the obstacles walls

Table 7.1: Obstacle Walls Parameters

Types	W or D_o (mm)	H or δ (mm)	t (mm)	H/W δ/D_o
RP: Cross-flow	Continuous	4.50	3.0	
RP: Co-flow	Continuous	4.50	3.0	
RW: Cross-flow	8.59	8.00	3.0	0.93
RW: Co-flow	8.59	8.00	3.0	0.93
ZR: Cross-flow	Continuous	4.50	3.0	
PF: Cross-flow	8.59	8.00	-	0.93
DS: Dimple	8.59	2.58	-	0.30

to the ribs and cross-flow. The blockage of the ribs was greater in the cross-flow direction and so the pressure loss increased was higher. The gap between the top of the rectangular pins is necessary to allow for thermal expansion as the wall and rib are hotter than the impingement wall. If there was a solid connection, differential thermal expansion would create thermal stresses and cracking. In addition three alternative heat transfer enhancements were investigated for the same impingement configuration: cylindrical pin-fins; zig-zag fins in cross-flow and dimples of depth δ and diameter D_o.

The computational grids modelled using ANSYS ICEM with the addition of obstacles on the target wall are shown in Figure 7.3 for the rectangular pin cross-flow, Figure 7.4 (a - d) and Figure 7.5 (a -c) show the grids. The dimpled obstacle of Figure 7.5 (c) formed part of the target wall depth which resulted in the impingement gap fluid grids replacing part of the target solid wall grids. This increases the impingement gap cell size and reduced the target wall cells as a proportion of the total computational cells, as shown in Table 7.2. For the grid geometries for all obstacles, the number of cells in the plenum was fixed at 35.3 % of the total grids. The dimpled target surface was modelled with the dimples in-line with the impingement jet. The other obstacles grids were in the impingement gap, hence the obstacle solid walls replaced part of the impingement gap fluid grids as shown in Table 7.2. Obstacles in co-flow were modelled on the symmetry plane between holes, which involved half the obstacle and the cross-flow obstacles were by using the whole obstacle width.

The approach that was used to model the zig-zig obstacle of Figure 7.2 (a) or 7.5 (d) was similar to that used experimentally for an inclined ribs by Wang *et al* [224]. The geometrical dimensions were those used by Andrews *et al* [194] and Abdul Hussain *et al* [214] and are correlated with the dimensional idea of Wang *et al* [224]. The zig-zag ribs were essentially a modification of the straight ribs [210], but were only used with cross-flow. The used of inclined ribs to the cross-flow is common in enhanced heat transfer for duct flow and this was applied to impingement cooling ducts. The half circular pin-fin obstacle of Figure 7.2 (e) or 7.5 (b), has all its variables the same as the rectangular pin: cross-flow obstacle of Andrews *et al* [210], whereby the width is the pin-fin diameter D_o at fixed height H.

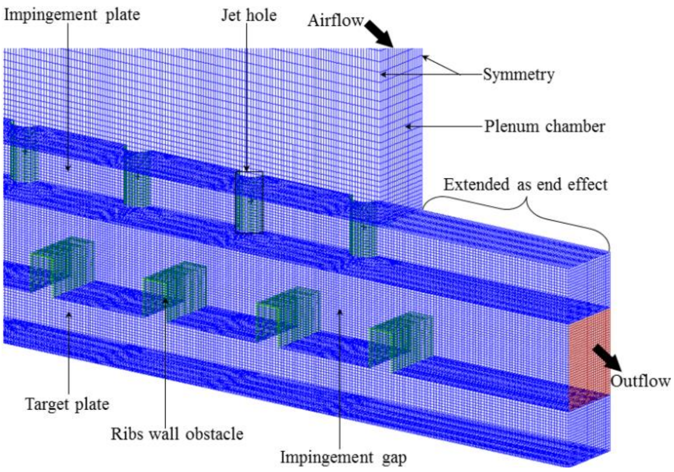

Figure 7.3: Model grid geometry with enhanced target wall

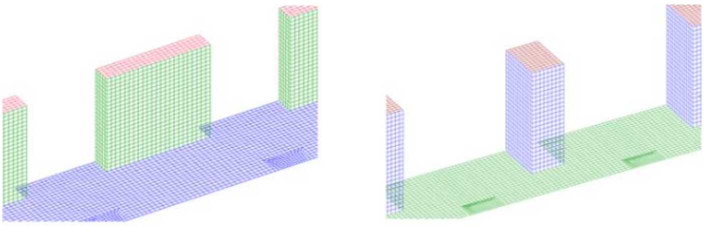

(a) Rectangular pin: Co-flow

(b) Rectangular pin: Cross-flow

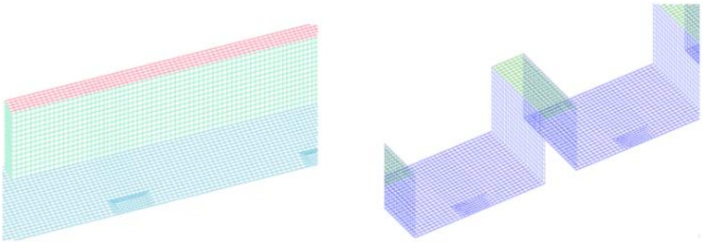

(c) Ribs wall: Co-flow

(d) Ribs wall: Cross-flow

Figure 7.4: Modelled grids for rectangular pin-fin and ribs obstacles

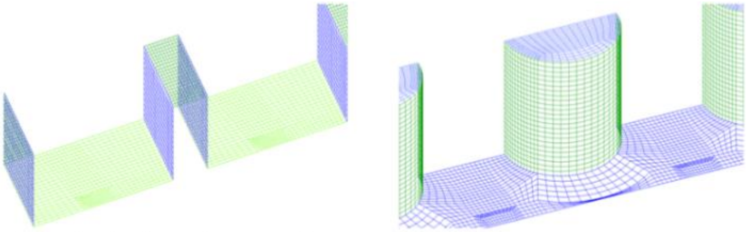

(a) Zig-Zig (inclined) ribs: Cross-flow

(b) Pin-Fin: Cross-flow

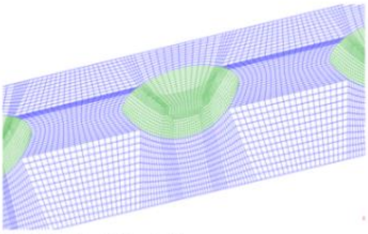

(c) Dimple: Direct-flow

Figure 7.5: Model grids for zig-zag, circular pin-fin and dimples

Table 7.2: Percentage of parts grids for y^+ ~35

Types	Parts (%)			
	Test walls	**Obstacles**	**Gap**	**Holes**
RP: Cross-flow	28.5	7.2	20.6	8.4
RP: Co-flow	28.5	7.2	20.6	8.4
RW: Cross-flow	28.5	8.1	19.7	8.4
RW: Co-flow	28.5	8.1	19.7	8.4
ZR: Cross-flow	28.5	8.3	19.5	8.4
PF: Cross-flow	26.5	6.7	23.4	8.1
DS: Direct-flow	22.8	5.7	27.4	8.8

7.2.2 Computational Procedures

The present CHT CFD investigations for the various types of obstacles were computed for varied G of 1.08, 1.48 and 1.98 kg/sm^{2}bar, respectively. The standard k - ε turbulence model in ANSYS Fluent was used with a wall function y^+ value ~ 35, as shown in Table 7.2 and as discussed in Chapter 4. The y^+ values have been reported [25, 46] to be in the range of the near wall using the law of the wall - $30 < y^+ < 300$. The flow aerodynamics in the impingement gap of this present work are critical to the solution, for example the hole flow separation and recirculation have been adequately predicted by the k - ε model, so this model is also selected here. Table 4.11 shows the computational flow boundary conditions that have been used and are the same to that employed by El-jummah *et al* [46]. The convergence criteria were set at 10^{-5} for continuity, 10^{-11} for energy and 10^{-6} for k, ε and momentum (x, y and z velocities), respectively.

7.3 Predictions of the Aerodynamics

The aerodynamics in the impingement gap is complex, as shown by El-jummah *et al* [32] using CHT CFD modelling. The additions of obstacles to the target wall was aimed at increasing the heat transfer by inserting a rib at the location of the reverse flow between each impingement jet. This increases the complexities of the aerodynamics as the cross-flow builds up with succesive rows of impingement jets. This flow complexity is shown in the velocty pathlines of Figure 7.6 (a - e) and Figure 7.7 (a - c). Comparing Figure 7.6 (e) for a smooth wall to the other aerodynamics with obstacles, shows that for co-flow the aerodynamics are similar, with the cross-flow giving additional convective heat transfer due to the flow along the ribs which does not greatly change the aerodynamics. However, for cross-flow over the ribs there is a significant change in the aerodynamics, as shown in Figure 7.6 (a and c). For the continuous rib, the reverse flow jet is deflected over the rib by the cross-flow giving a complex interaction with the next impingement jet. By the downstream rib after 10 holes, there is little flow in the wall region and the cross-flow is all across the impingement target wall. This is not conducive to good heat transfer on the target surface and it will be shown later that there is little benefit of the continuous ribs in cross-flow. With the rectangular pin-fins in cross-flow, the cross-flow at the downstream end of the gap is strong and the flow between the ribs recirculates behind the ribs and this is a potential additional surface heat transfer mode. It will be shown later that this does cause the heat transfer to increase in the downstream portion of the wall.

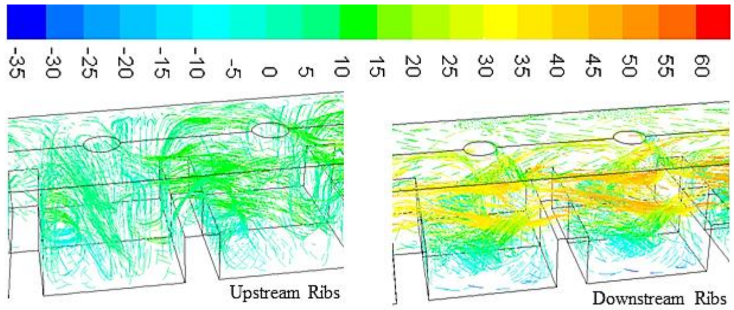

(a) Ribs wall: Cross-flow

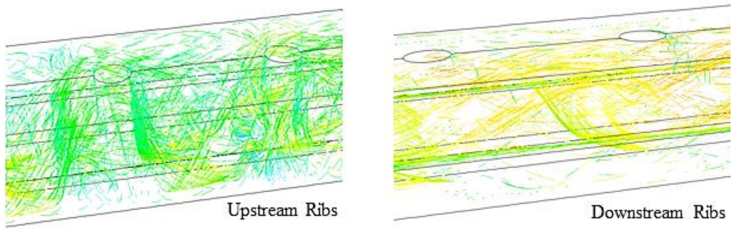

(b) Ribs wall: Co-flow

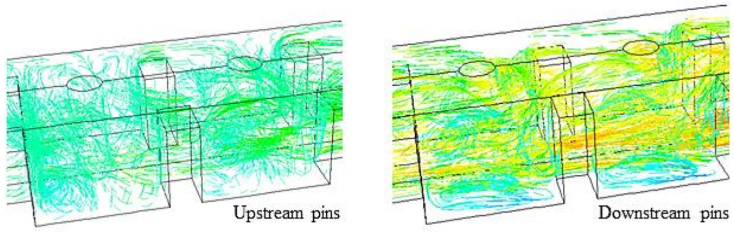

(c) Rectangular pin: Cross-flow

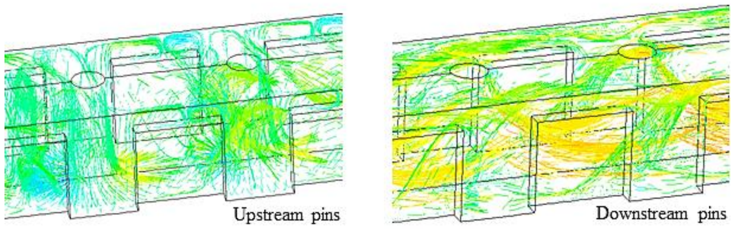

(d) Rectangular pin: Co-flow

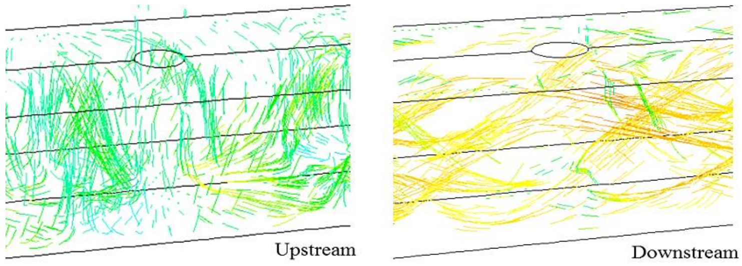

(e) Smooth target Surface

Figure 7.6: Impingement gap velocity pathlines (m/s) for the experimental obstacles

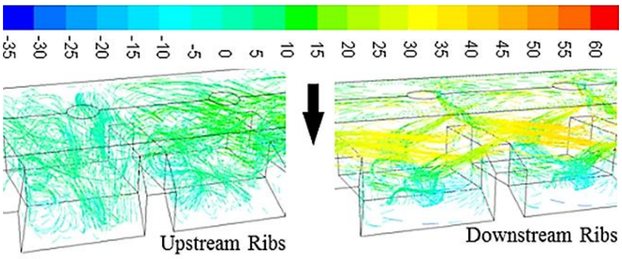

(a) Zig-zag (Inclined): Cross-flow

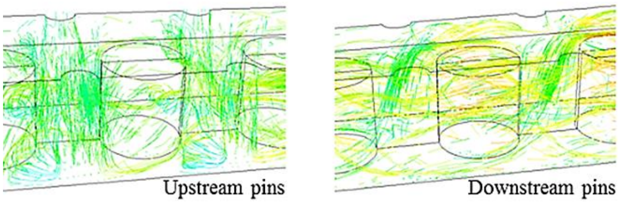

(b) Pin-fin: Cross-flow

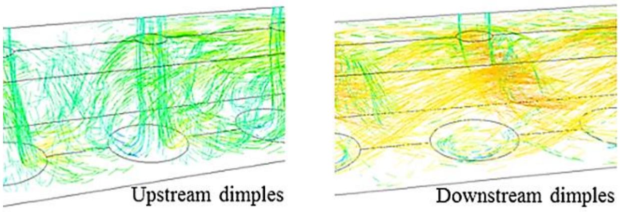

(c) Dimpled: Direct-flow

Figure 7.7: Velocity pathlines (m/s) in the impingement gap for the new obstacle walls

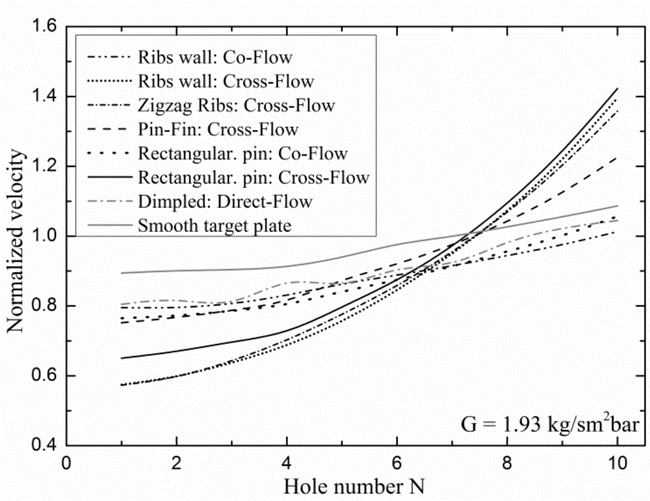

Figure 7.8: Flow-maldistribution in impingement jet holes

For the new enhanced heat transfer devices in Figure 7.7 (a - c) the dimple results show a stronger reverse flow of the impingement jet and potentially a greater resistance to cross-flow deflection of the flow on the surface. Some evidence for this will be presented later. The cylindrical pin-fins has the edge of the impingement jet close to the surface of the cyinders and potentially this should enhance the heat transfer. However, in the downstream part of the flow the aerodynamics are dominated by the flow between the pin-fin cylinders. The zig-zag rib has similar aerodynamics to the flat rib in cross-flow, but there is evidence of a differences downstream vortex structure that may be beneficial.

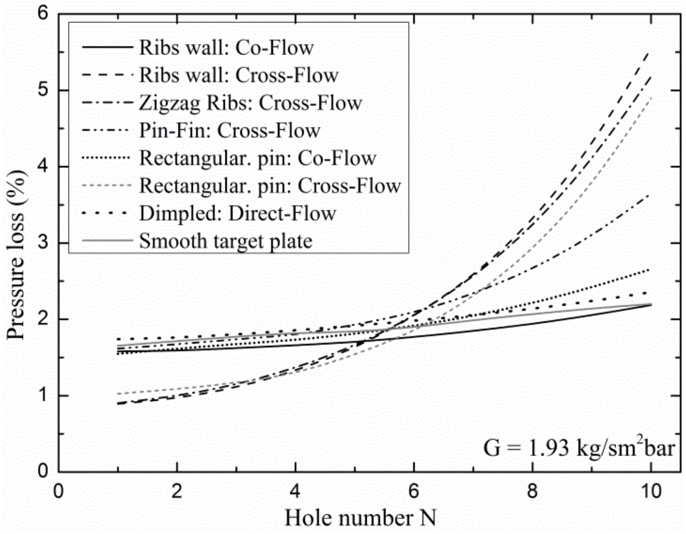

Figure 7.9: Impingement gap holes outlet pressure loss for the obstacles

7.4 Predictions of the Axial Pressure Loss Profiles

The cross-flow obstacles create a blockage to the cross-flow, which increases the pressure loss due to the cross-flow and this is shown in Figure 7.8 to lead to an increased flow-maldistribution between the impingement holes for all the cross-flow configurations which block the cross-flow. Figure 7.8 also shows that the co-flow ribs and the dimpled obstacles which have the minimum blockage to the cross-flow have a flow-maldistribution similar to the smooth wall.

The cross-flow over the obstalces leads to higher pressure loss as shown in Figure 7.9. The increased flow-maldistribution with obstacles also creates a lower pressure loss across the leading holes in the gap, which is the effect that gives rise to the increased flow-maldistributoin in Figure 7.8. Figure 7.9 shows that the cross-flow obstacle geometries are predicted to have higher pressure loss than the smooth wall, while the dimpled wall was predicted to have a very similar pressure loss to the smooth wall, which was expected as there is no increased blockage to the cross-flow. However, the reduced pressure loss for co-flow with ribs was unexpected. It appears that as the rib prevents the impingement of adjacent impingement jets in the transverse direction this changes the reverse flow jet in a way that reduces its impact on the cross-flow pressure loss.

7.5 Velocity Profiles

Figure 7.10 (i) and 7.11 (i), shows the flow velocity profiles in the symmetry planes of the jet half holes and that between the holes, for the geometries in Table 4.1. Figure 7.10 (i) and 7.11 (i) shows the reason why the flow-maldistribution of Figure 7.8, were predicted high for the cross-flow configurations, as all their last holes velocities are the peak. Comparison of the predictions of obstacles with the smooth wall results, shows that the influence of the cross-flow configurations was greater as the mean cross-flow velocities are also the peak, which is the same in the plane of the obstacles. For the continuous ribs: cross-flow the deflection of the jet by the higher cross-flow velocity over the ribs was also high, but in the downstream region these deflected jets impinges on the upstream face of the ribs and this could produce better cooling in that zone.

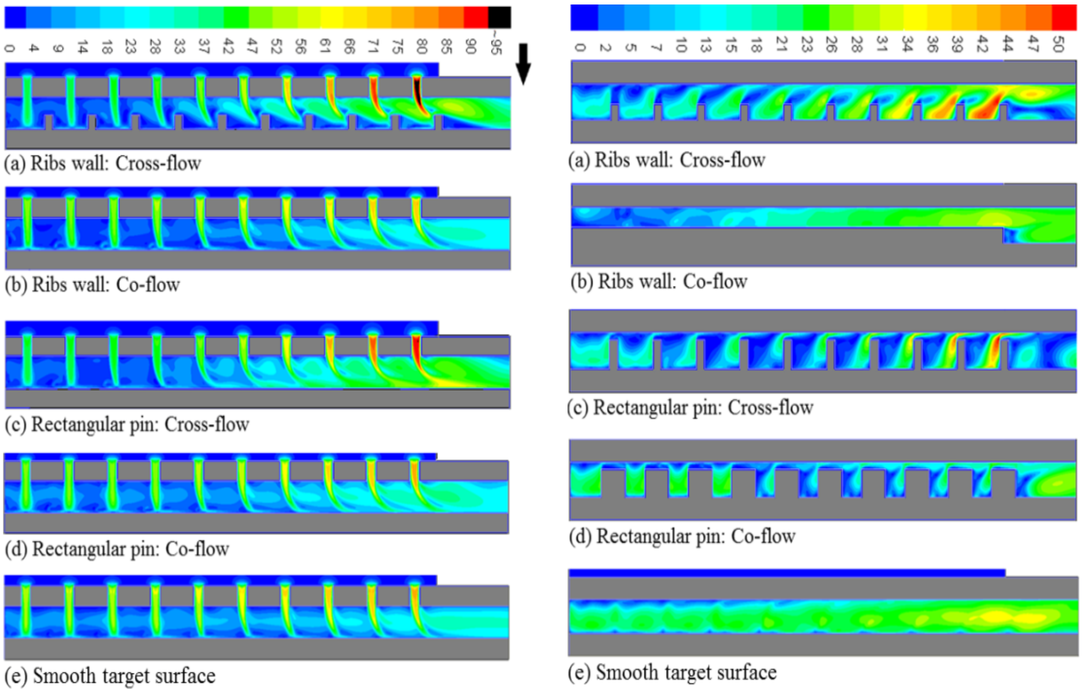

(a) Ribs wall: Cross-flow

(b) Ribs wall: Co-flow

(c) Rectangular pin: Cross-flow

(d) Rectangular pin: Co-flow

(e) Smooth target surface

(a) Ribs wall: Cross-flow

(b) Ribs wall: Co-flow

(c) Rectangular pin: Cross-flow

(d) Rectangular pin: Co-flow

(e) Smooth target surface

(i) Rows of half holes symmetry plane

(ii) Symmetry plane between rows of holes

Figure 7.10: Impingement gap contours of flow velocity (m/s) for the experimental geometries modelled with a comparison with the smooth wall at G of 1.93 kg/sm^{2}bar

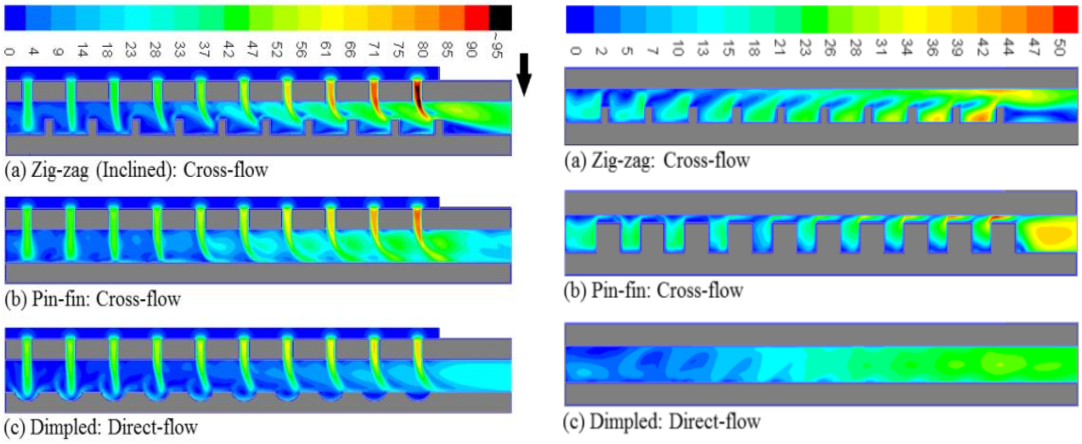

(a) Zig-zag (Inclined): Cross-flow

(b) Pin-fin: Cross-flow

(c) Dimpled: Direct-flow

(a) Zig-zag: Cross-flow

(b) Pin-fin: Cross-flow

(c) Dimpled: Direct-flow

(i) Rows of half holes symmetry plane

(ii) Symmetry plane between rows of holes

Figure 7.11: Impingement gap contours of flow velocity (m/s) for the new obstacles geometries modelled at G of 1.93 kg/sm^{2}bar

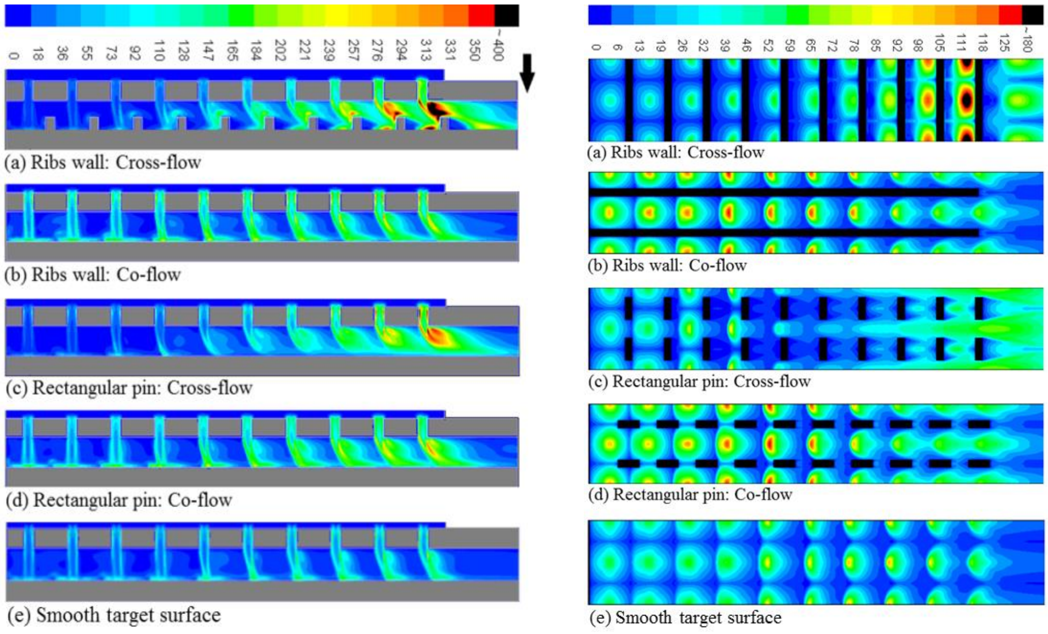

(i) Rows of half holes symmetry plane

(i) Rib, rectangular pin and smooth walls

Figure 7.12: Contours of TKE for the experimental geometries at G of 1.93 kg/sm^{2}bar

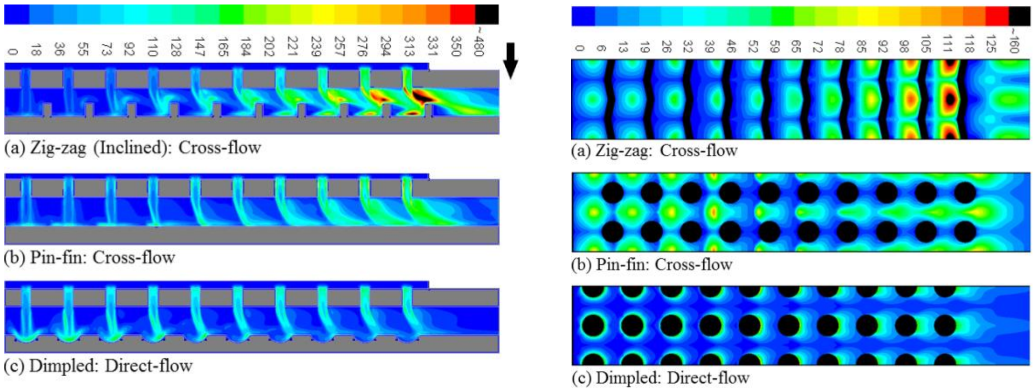

(i) Symmetry plane between rows of holes

(ii) Zig-zag rib, pin-fin and dimpled walls

Figure 7.13: Contours of TKE for the new obstacles geometries at G of 1.93 kg/sm^{2}bar

The zig-zig obstacle in Figure 7.11 (ia) with cross-flow had similar velocity profiles to the straight rib, as in Figure 7.10 (i), with the deflected downstream jets impinging on the ribs instead of the cooled surface. The dimpled surface showed strong upstream flow recirculation out of the dimple as shown in Figure 7.11 (ic). As the cross-flow from the upstream impingement jets increased, the flow recirculation increased. However, in the downstream part of the test wall the impingement jet deflection by the cross-flow carried the impingement jet out of the dimple and all the advantage of the dimple was lost. The cylindrical pin-fins have many of the same features as the rectangular pins with a high jet deflection by the locally high cross-flow velocity between the pins.

7.6 Turbulent Kinetic Energy Profiles

The turbulent kinetic energy (TKE) on the wall surface controls the wall heat transfer [25, 32, 46]. Figure 7.12 (i) show the predicted TKE, in the symmetrical plane in-lined with the impingement jets, for the rib and rectangular pin-fins obstacles and are compared with the smooth wall TKE. Figure 7.13 (i) shows the predicted TKE for the zig-zag, cylindrical pin-fin and dimpled roughness. These predictions show that the action of the obstacle is often to reduce the turbulence on the surface and to move the peak turbulence to the obstacle surface. This is most clearly shown for the rib and zig-zag rib: cross-flow in Figure 7.13. The only surface roughness that increases turbulence on the wall is the dimpled surface, but this is greatest at the leading edge and the advantage disappears once the impingement jet is deflected out of the dimple by the cross-flow.

The distributions of TKE on the target wall are shown in Figure 7.12 (ii) for the experimentally modelled and Figure 7.13 (ii) for the newly modelled geometries. Clearly the enhanced flow-maldistribution with cross-flow ribs and zig-zag ribs results in very high surface TKE for the downstream jets, with correspondingly lower upstream surface turbulence. The rectangular and circular pin-fins in cross-flow were predicted to have low turbulence in the central region of the wall, but increased turbulence at the leading and trailing edge. This was due to the greater deflection of the impingement jet by the higher local cross-flow velocity between the pins. The co-flow rib and pin-fin ribs were predicted to have similar TKE for the smooth wall and this is expected as the turbulence generation by the obstacles is at a minimum in the cross-flow configuration. These geometries are only likely to show an enhanced heat transfer if the flow along the ribs is a significant cooling mechanism, it will not be due to enhanced turbulence.

7.7 Validation of Predicted Pressure Loss

Figure 7.14 compares the measured [194, 210, 214] and predicted pressure loss from the air feed plenum chamber static pressure to the impingement gap exit static pressure, well downstream of the last obstacle, which is the overall wall pressure loss. The predicted ΔP for the co-flow obstacles gave excellent agreement with the measurements, while that of the cross-flow shows slightly higher predicted pressure loss. The reason for this was that in cross-flow, the distance downstream of the last obstacle, the flow that should have recovered the dynamic pressure due to flow acceleration was longer than the computational domain. This can be seen in Figure 7.13, where the gradients in the wall turbulence at the last computational plane are greater for the cross-flow obstacles than for the smooth wall. The agreement of predictions and measurement of the pressure loss, indicates that the flow aerodynamics were adequately modelled.

Figure 7.15 compares the predicted ΔP/P for all the obstacle geometries and the smooth target wall. The key prediction is that none of the obstacles has a great increase in the pressure loss, in spite of the increased blockage to the cross-flow by some of the obstacles. The reason for this, is that the pressure loss is dominated by the flow through the impingement holes and this is common to all the geometries. Figure 7.15 shows that only the dimpled wall, the straight rib and zig-zag rib in cross-flow have a significant increased in the pressure loss. The two continuous rib designs would be expected to increase the pressure loss as they have a 45% blockage of the cross-flow and both force the cross-flow to deflect towards the impingement jet wall. The increase in pressure loss for the dimpled wall was unexpected as this has no blockage of the cross-flow. However, the aerodynamics discussed above show that the dimple produces a stronger reverse flow of the jet in the upstream impingement jets and this will give a greater aerodynamic blockage of the cross-flow which then increases the pressure loss.

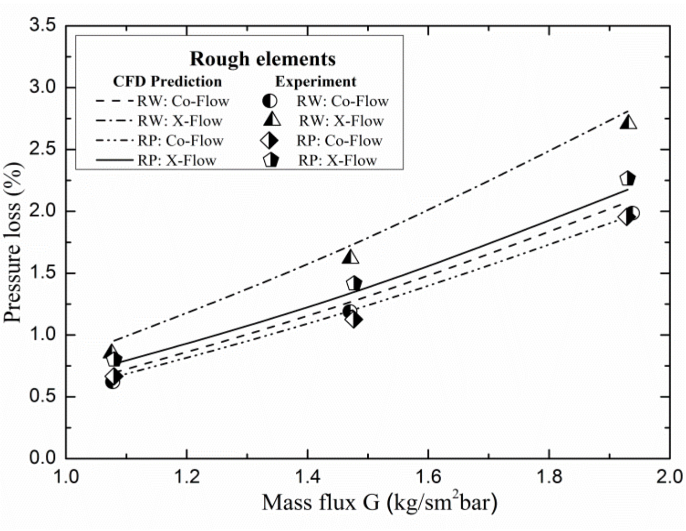

Figure 7.14: Comparisons of predicted and measured pressure loss as a function of G

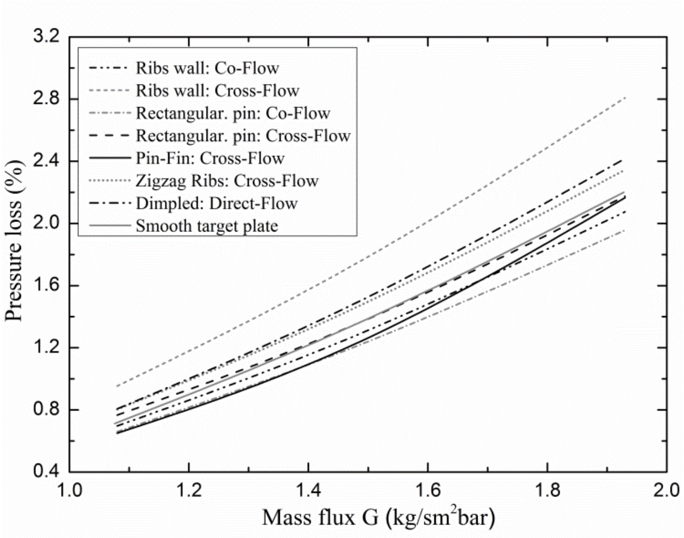

Figure 7.15: Range of G comparisons of predicted impingement gap exit ΔP/P for obstacles

The fins with co-flow and the rectangular pin in co-flow both were predicted to have a similar pressure loss to the smooth wall. This was unexpected as there would be additional flow friction losses by the cross-flow against the finned surfaces. However, these fins prevented surface interaction between the impinging jets in the transverse direction and the turbulence generated in this interaction would put up the pressure loss. These two effects appear to have cancelled out with a pressure loss similar to the smooth wall.

The rectangular and circular pin-fins in cross-flow were both predicted to have a lower or the same pressure loss as the smooth wall. These were unexpected results as the pins block the cross-flow by about 40% of the cross-flow area. However, this blockage is low compared with the blockage to the flow of the impingement wall of 96.4%. The full height of the impingement gap is available for cross-flow in these designs, whereas the continuous ribs force the cross-flow to separate from the surface and this appears to be the key reason for the increase in pressure loss for the continuous ribs in cross-flow.

7.8 Validation of the Surface Averaged HTC

It has previously been shown that the present CFD procedures give good predictions of the smooth wall impingement heat transfer [25, 32, 33, 46]. The present predictions for the influence of obstacles on the average heat transfer coefficients HTCs h are compared with the measured HTCs [194, 210, 214] in Figure 7.16 and Figure 7.17 using Equation 2.24.

All the predictions for the surface averaged HTC are within 12% of the measurements at all G, generally any error is an under prediction. For the continuous rib with co-flow the agreement was perfect with no significant error at any G. For the rib in cross-flow the predictions were 6% low at low G and 3% low at high G. For the rectangular pin-fin in co-flow the predictions were in good agreement at all G. For the rectangular pin-fins in cross-flow the predictions were 8% low at high G and 12% low at low G. The more complex is the interactions of cross-flow with the obstacle, the higher the error that was found. However, these predictions for most of the geometries are sufficiently close to the measurement to have confidence that surface averaged heat transfer can be reliably predicted for geometries for which no measurements have been made.

Figure 7.17 compares the predicted X^2 locally surface averaged HTC compared with the experimental measurements of the axial dependence of the surface average HTC. There is now a more significant disagreement between predictions and measurements than there was for the whole surfaced averaged HTC. The best agreement on the axial variation of locally surfaced average HTC was for the continuous rib in co-flow and the rectangular pin-fin in co-flow. The prediction was 3% low at hole 2 and 3% high at hole 10 for the continuous rib with co-flow and for the rectangular pin-fin in co-flow the predictions were 2% high at hole

2 and in agreement at hole 10. In contrast the cross-flow predictions had a much larger error with the continuous rib being 7% low at hole 2 and 12% high at hole 10. The highest error was in the central region with a 13% low prediction at hole 5. The situation was worse for the rectangular pin-fins in cross-flow with all the predictions being well below the measurements. At hole 2 the under prediction was 7%, at hole 5 it was a 35% under prediction and at hole 10 only a 4% under prediction. The trend of local surface averaged HTC with distance was not correctly predicted in this case. Thus the predictions are good with co-flow geometries but not as good for the more complex cross-flow aerodynamics. Thus comparison of the predictions and measurements on a complete 10 hole surface averages masks some disagreement in the axial variation of locally surface averaged HTC.

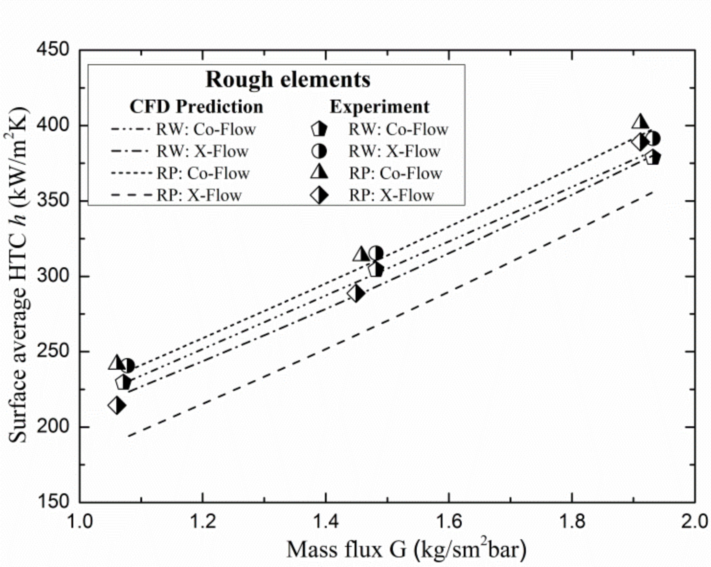

Figure 7.16: Comparison of predicted and experimental target surface *h* for obstacles walls

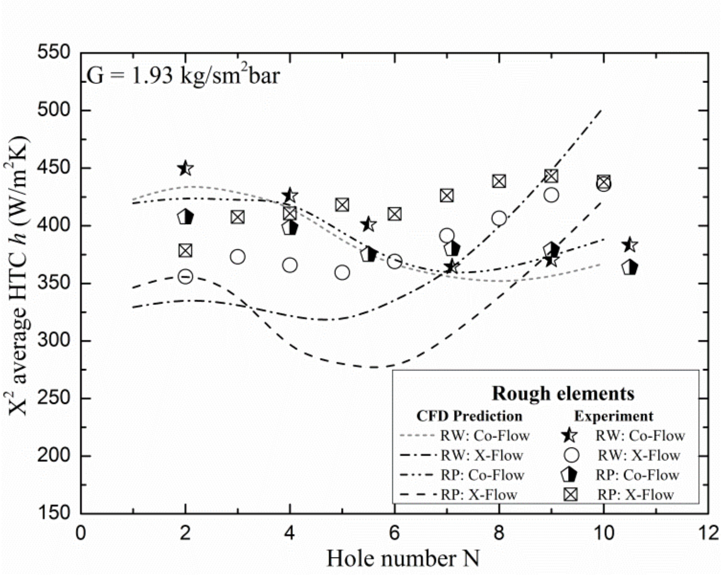

Figure 7.17: Comparison of predicted and measured target locally X^2 average *h* at fixed G

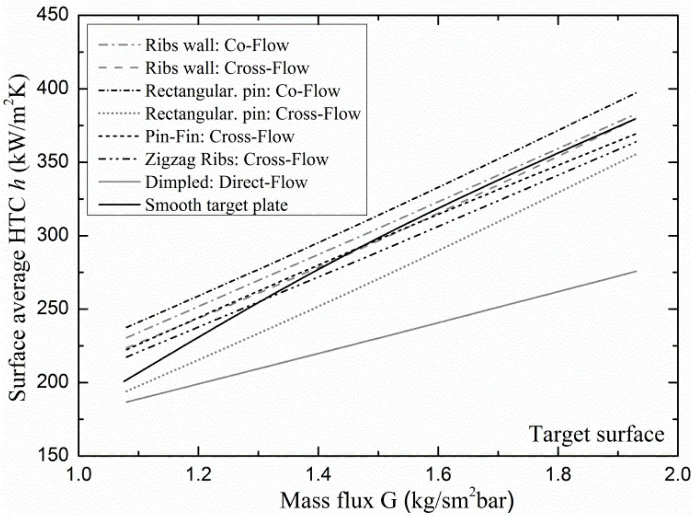

Figure 7.18: Comparison of predicted target surface HTC for the obstacle walls at varied G

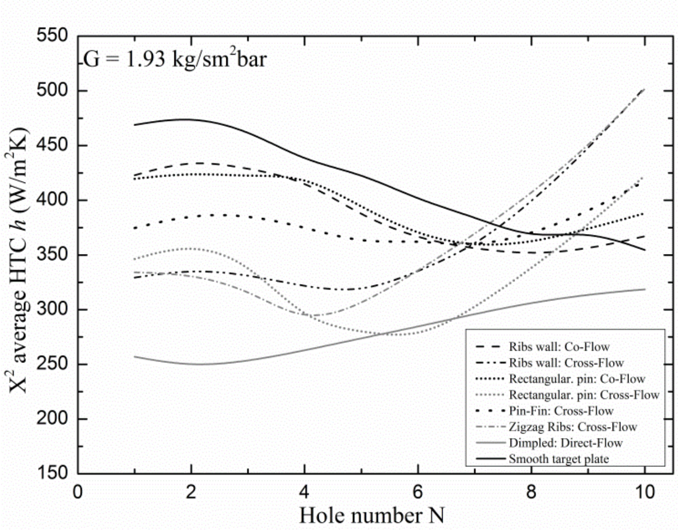

Figure 7.19: Comparison of predicted target wall locally X^2 average *h* for fixed G

A feature of the experimental results that is reproduced in the predictions is that for the co-flow results with the cross-flow having a clear channel flow between the obstacles, the trend of the local surface averaged results is for the HTC to decline with distance, as for the smooth wall results. However, with the cross-flow configuration there is no clear passage for the cross-flow and this changes the axial variation of local surface average HTC with distance. Now the HTC increases in the trailing edge region instead of decreasing. This effect is shown in Figure 7.17 to be greatest for the continuous rib in cross-flow. Thus the main effect of the obstacles is to remove the feature of the smooth wall geometry that led to the local surface averaged HTC deteriorating with distance along the impingement target surface.

Figure 7.18 compares the predicted surface averaged HTC for all the obstacles investigated and compares them with the smooth wall HTC predictions. Figure 7.18 shows that the rectangular pin in co-flow had the greatest improvement on the smooth wall surface averaged heat transfer. However, this improvement was only 20% at low G and 5% at high G. Two of the obstacle surfaces were predicted to have lower surface averaged HTC than a smooth wall and these were the rectangular pin-fin in cross-flow and the worst case was the dimpled surface. The rectangular pin-fin results are unexpected as this creates the greatest turbulence and increased pressure loss. However, the predicted TKE in Figure 7.12 and 7.13 was not created on the target surface but on the rib tip and towards the jet wall surface. This is an ineffective turbulence generation by the cross-flow obstacle interaction. For the dimple surface the action is to create a stronger recirculating flow in the gap and to remove the wall jet interaction on the target surface, so that there is less turbulence on the surface and less heat transfer. However, other investigators have shown a benefit of dimpled surfaces experimentally, but this is not predicted for the X/D = 4.7 and 10 mm impingement gap that is modelled in the present work.

Figure 7.19 shows the predicted X^2 average HTC as a function of distance along the target wall and compares the effect of the obstacles with the trend for the smooth wall. Figure 7.19 shows that the predicted influence of obstacles in the gap is predominantly on the axial variation of the locally surface average heat transfer. Part of this effect is related to the flow-maldistribution increase discussed above. The action of cross-flow over obstacles was to increase the pressure loss in the gap, which makes the flow-maldistribution worse. The increased flow in the downstream jets is part of the reason why the ribs with cross-flow geometries have the highest HTC in the downstream part of the target wall, compared with the opposite trend for the smooth wall. All the co-flow geometries showed a similar trend to that of the smooth wall with a decrease in HTC with distance and the highest HTC at the leading section of the target wall.

7.9 Distribution of Target Surface Nusselt Number

Figure 7.20 shows the CHT CFD predicted surface distribution of Nusselt number Nu on the target wall using Equation 2.35, for the various obstacles and compares these with the smooth wall predictions. The Nu surface distribution is very similar to that of the TKE in Figure 7.13. Figure 7.20 - left shows that the smooth wall results are difficult to improve on and all the obstacle Nu surface distributions show lower values than for the smooth wall. Any enhancement of heat transfer has to come from the heat transfer to the rib or pin-fin surfaces, which is not shown in Figure 7.20. The quite poor Nu distribution for the rectangular pin-fins on the target surface is partially compensated for by the heat transfer on the pin-fin surface, which extract heat from the target surface by conduction.

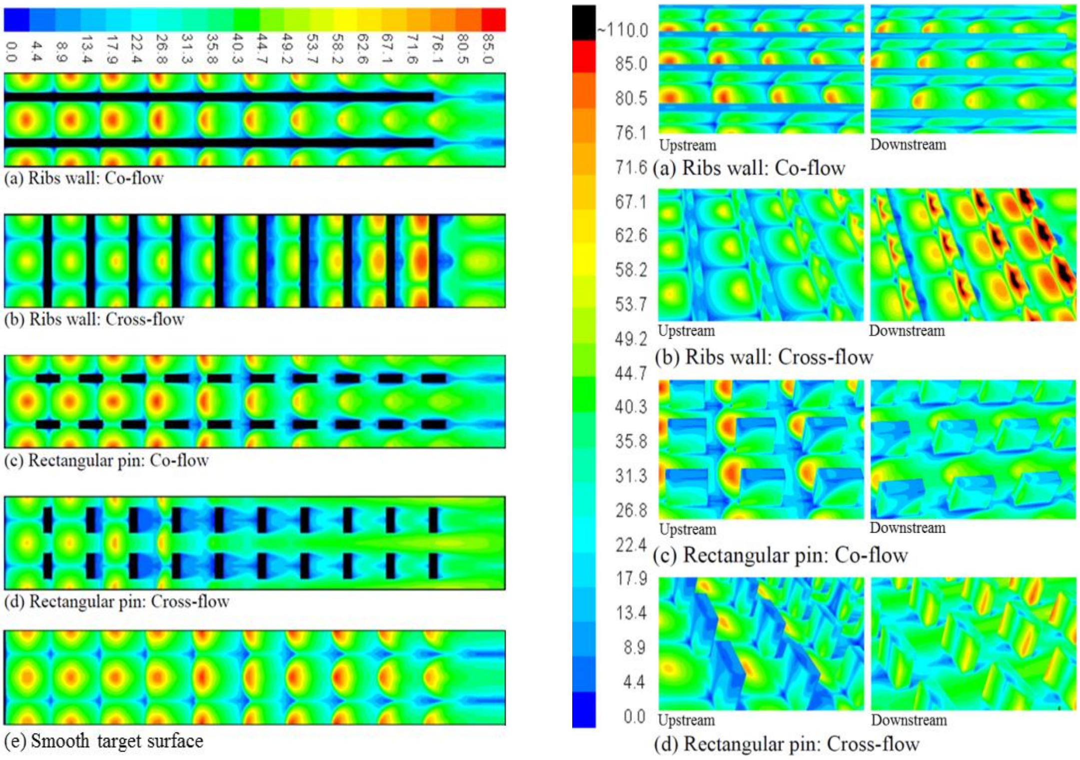

(i) Ribs and rectangular pin in co and cross-flow compared with the smooth wall predictions

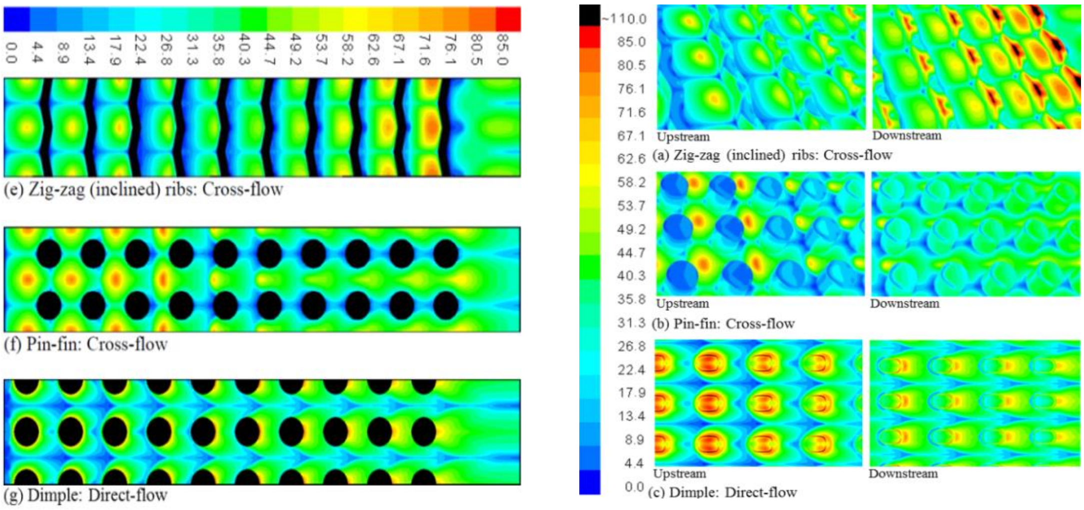

(ii) Zig-zag, cylindrical pin-fins and dimpled surfaces

Figure 7.20: Contours of Nu on the obstacles target surfaces for G of 1.93 kg/sm^{2}bar

The heat transfer to the obstacle surfaces is shown in Figure 7.20 - right which shows the high heat transfer on the rib and rectangular pin-fin surfaces in the downstream part of the flow, where the cross-flow deflects the jets strongly onto the rib surface. For the dimpled surface the movement of the jet outside the dimple in the downstream dimples, is shown to lead to a deterioration in heat transfer.

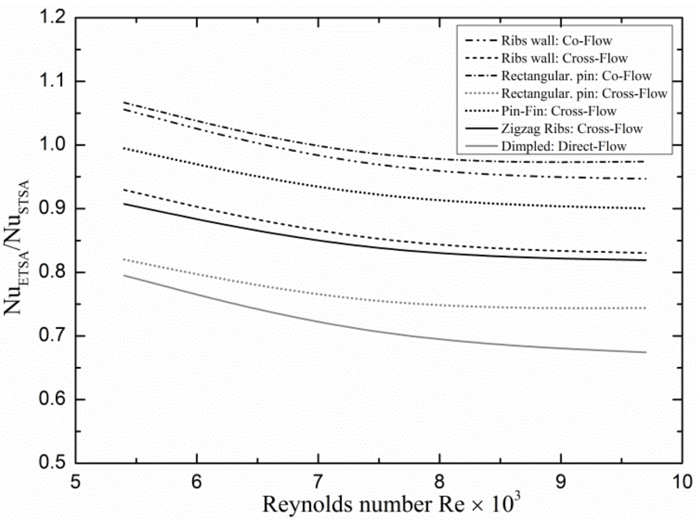

Figure 7.21: Comparison of predicted target surface average Nu of enhanced over smooth

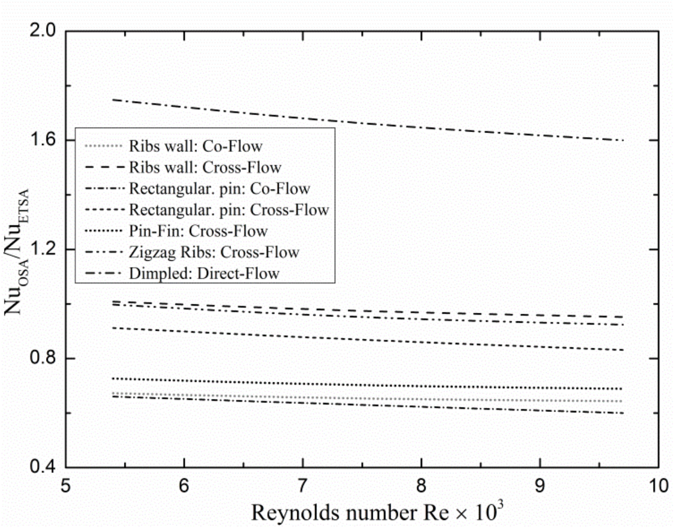

Figure 7.22: CFD predicted obstacles surface average Nu over their target average Nu

The predicted surface averaged Nusselt number variations averaged over the smooth target average Nu for range of Reynolds number for all the types of obstacle walls are shown in Figure 7.21. The co-flow obstacles predicted the average Nu to be above that of the smooth target walls, while every other obstacles was below that of a smooth wall. The lowest surface average Nu was the dimpled averaged Nu. By averaging the target surface Nu to the obstacle Nu Figure 7.22 shows that the dimpled surface was predicted to have the highest Nu relative to the flat surface Nu. For the other obstacles the heat transfer to the obstacle surface was less than to the flat target surface.

7.10 Heating of the Impingement Target Wall

Impingement jet plate heating by the reverse flow has previously been reported [25, 46] and has been shown to influence the cooling of the target walls. By using the dimensionless temperatures T^* of Equation 2.6 that has been used to predict the target wall and the coolant air temperatures, Figure 7.23 and 7.24 shows the dimensionless temperature flow in the symetry planes of half holes and the planes between row of holes. A clear picture of the reverse flow heated jet is shown here where the flow between the obstacles walls and jet plate looks severe. The smooth target wall shows clearly the impingement jet and the reverse flow jet and its deflection by the cross-flow between the impingement jets. However, with the obstacles present this reverse flow jet is indicates higher deflections by the cross-flow and does not impinge on the target surface, but on the ribs.

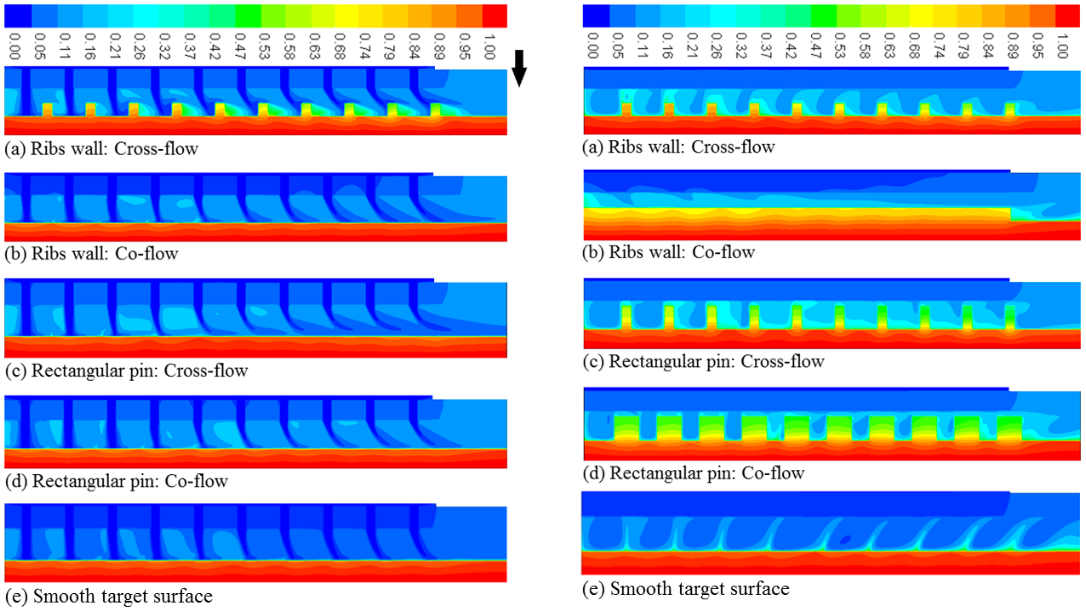

(i) Rows of half holes symmetry plane (ii) Symmetry plane between rows of holes

Figure 7.23: Contours of T^* in the impingement gap for the experimental geometries modelled for G of 1.93 kg/sm^2bar

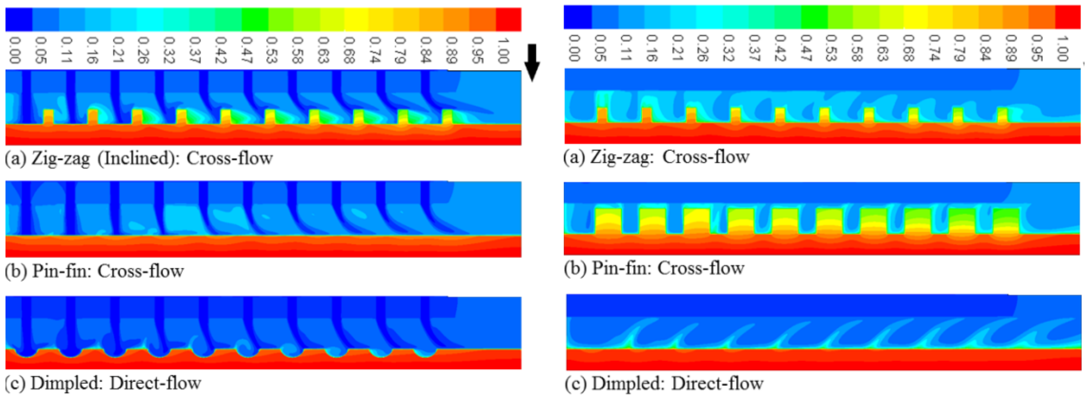

(i) Rows of half holes symmetry plane (ii) Symmetry plane between rows of holes

Figure 7.24: Contours of normalized temperature in the impingement gap for the new obstacles geometries modelled for G of 1.93 kg/sm^2bar

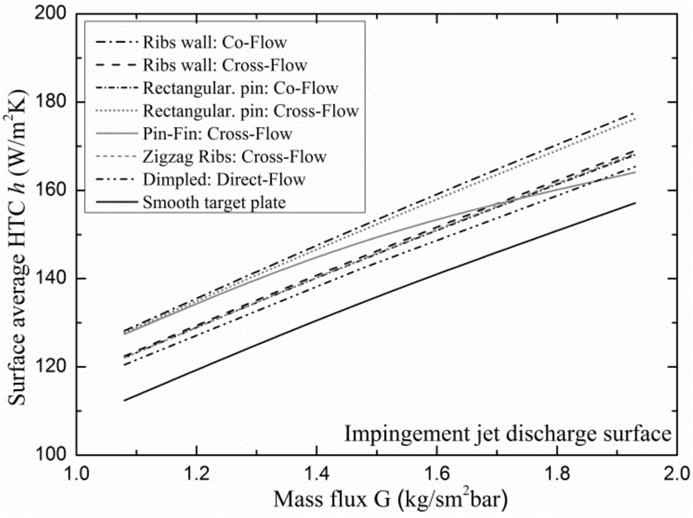

Figure 7.25: Comparison of predicted HTC on the impingement jet plates for the obstacles

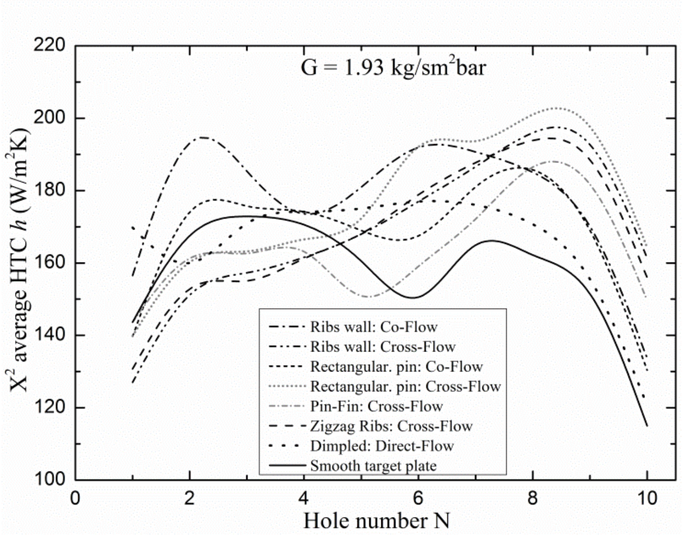

Figure 7.26: Comparison of predicted obstacles locally X^2 average *h* on impingement jet plate for a fixed G of 1.93 kg/sm^{2}bar

The heated reverse flow jet impinges on the impingement jet wall surface and heats this surface. The predicted surface average HTC of impingement jet wall are compared in Figure 7.25 for a range of G and in Figure 7.26 as X^2 average HTC as a function of distance for G = 1.93 kg/sm^{2}bar. In both cases, the smooth target plate predictions gave lower HTC with downstream lower X^2 average HTC. This shows the influence of the high jet flow interactions between the jet plates, the obstacles walls shows to also enhanced the heat transfer to the impingement jet wall rather than to the target wall.

7.11 Temperature Gradients in the Target and Fins

Figure 7.27 shows the target wall surface distribution of normalised temperature T^* for all the obstacles configurations. This shows that the smooth and dimpled target walls gave the lowest surface distribution of T^*. The region of lowest distributions of T^* indicates the region with the higher HTC or Nu. Figure 7.28 shows that the smooth wall had the lowest surface temperatures and temperature distribution. This was due to the reduced impingement cooling by the various obstacles. Figure 7.28 shows the X^2 surface average T^* was lowest for the standard smooth wall impingement cooling. The thermal gradients through the combined target and obstacles walls for the obstacles at the hole 9 position are predicted in Figure 7.29. The smooth wall predictions are shown for comparison.

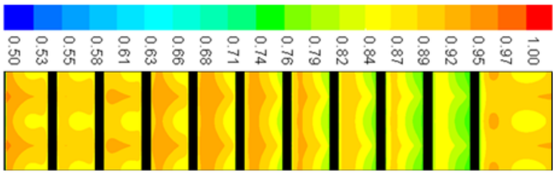

(a) Ribs wall: Cross-flow

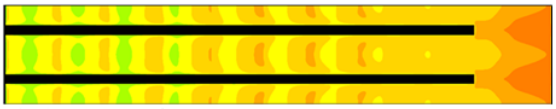

(b) Ribs wall: Co-flow

(c) Rectangular pin: Cross-flow

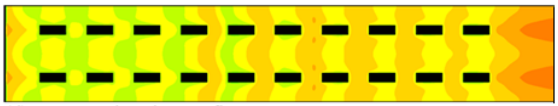

(d) Rectangular pin: Co-flow

(e) Smooth target surface

(i) Ribs and rectangular pin in co and cross-flow compared with the smooth wall predictions

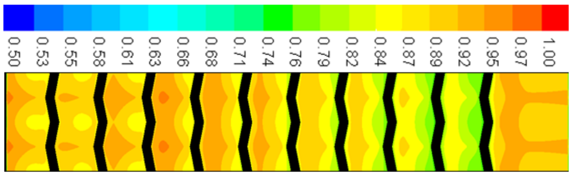

(a) Zig-zag: Cross-flow

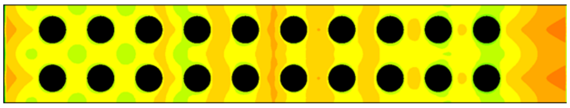

(b) Pin-fin: Cross-flow

(c) Dimpled: Direct-flow

(ii) Zig-zag, cylindrical pin-fins and dimple surfaces.

Figure 7.27: Target surface distribution of T^* for the obstacle walls at G of 1.93 kg/sm^2bar

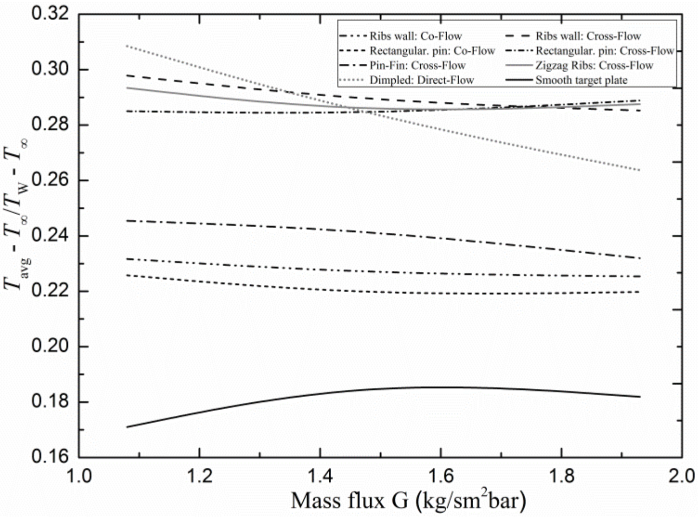

Figure 7.28: Comparison of predicted rough walls target surface T* for ranged of G values

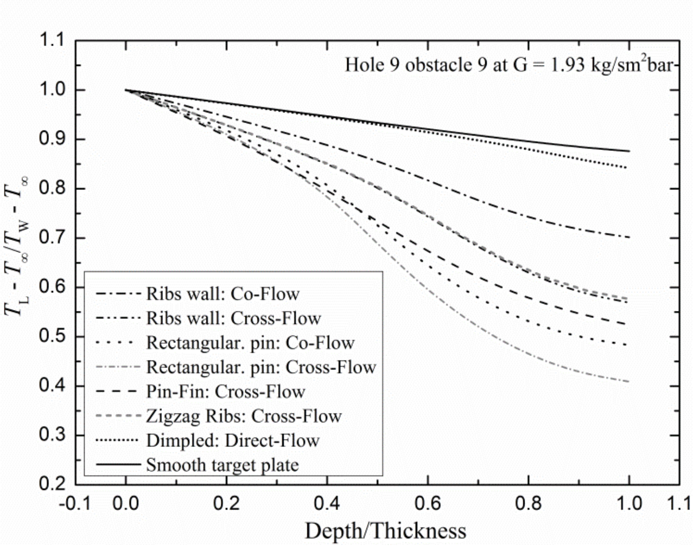

Figure 7.29: Comparison of predicted T* target wall hot side through the obstacle walls

The lowest thermal gradients T* are predicted in Figure 7.29 to be in the region close to the jet plates. The ribs obstacles gave lower thermal gradients with the pin-fin being much lower than zig-zag. The smooth wall had the lowest thermal gradients as a result of its high HTC. The decrease in HTC with obstacles results in an increase in thermal gradient.

7.12 Conclusions

The CHT CFD predictions for enhanced impingement heat transfer for G of 1.08, 1.48 and 1.93 kg/sm^{2}bar at fixed X/D of 4.66 and Z/D of 3.06 showed good agreement with the experimental surface and locally X^2 averaged HTC.

The predictions of the pressure loss were in very good agreement with the measurements, indicating that the aerodynamics were adequately predicted.

The predictions showed that it was difficult to enhance the smooth wall impingement heat transfer and that obstacles could deteriorate the heat transfer. The main effect of the obstacles was to enhance the heat transfer to the impingement jet wall and decrease it to the target wall. A small increase in the overall surface averaged heat transfer was predicted for the co-flow configuration with ribs.

CHAPTER EIGTH

IMPINGEMENT/EFFUSION COOLING HEAT TRANSFER RESULTS

Chapter 8

Impingement/Effusion Cooling Heat Transfer Results

8.1 Introduction

Impingement/effusion cooling as shown in Figure 2.3 (b), is one of the most effective cooling system for GT combustor and turbine blades walls that enables lower coolant mass flow to be used [4, 19, 23, 44]. The impingement/effusion arrays of holes are usually designed based on the equal number of holes [4, 23] but unequal number of holes have also been used [6, 7, 41, 44, 172], the present work investigates both cases. In impingement/effusion internal wall heat transfer, the variation of n is most significant for the effusion film cooling and a high value of n may be require for best overall film cooling effectiveness [4, 44]. A large number of effusion holes is advantageous for effusion cooling effectiveness, whereas a large number of impingement holes may not be necessary [32] and a lower number could reduce manufacturing costs. A very large number of effusion holes approaches the ideal film cooling of transpiration cooling using a porous wall [7, 19, 44], hence the optimum could be as many as can be manufactured [44]. This investigations concentrate on usinge conjugate heat transfer (CHT) CFD, in understanding the aerodynamics and wall conductive heat transfer in the choice of geometries with effusion number of holes that have no implications of structural strength.

8.2 Impingement/Effusion Experimental Geometries

Al Dabagh *et al* [4], Andrews *et al* [23] and Nazari [41] experimentally investigated the wall heat transfer for impingement/effusion cooling for a range of number of holes m^{-2}, n. The present work uses CHT CFD to model their experimental work, for a constant isothermal effusion wall measured with embedded thermocouples (Figure 4.1c and d) and varied coolant mass flux G from 0.1 - 0.94 kg/sm^2bar. The aim was to develop CHT CFD design procedures that could be used in combustor and turbine blade heat transfer optimisation.

Square arrays of 10, 15 and 25 holes for the impingement wall were investigated with the effusion holes located half a hole pitch displaced from the impingement jets. The values of n were 4306, 9687 and 26910 m^{-2} for both impingement and effusion walls (equal n) as Table 4.4 showed. A fixed X/D of 11 for the impingement wall and 4.7 for the effusion wall was used. The unequal n geometries have a fixed impingement wall of 1076 m^{-2} and varied effusion walls of 4306, 9687 and 26910 m^{-2}, whereby for the two walls their X/D are the same as the equal *n* geoemetries. This gives fewer impingement holes, 1 per 4, 9 and 25 effusion holes, respectively as Table 4.5 showed. For optimum performance of impingement/effusion cooling, the effusion wall should have a low blowing ratio (BR), which means a low jet velocity and this in turn requires a low relative pressure loss ΔP/P. The design requirement for this is a low X/D with relatively large effusion holes. In contrast, the impingement wall requires a high jet velocity for best effusion wall backside cooling and this requires a higher X/D. The combination of the impingement X/D of 11 and effusion X/D of 4.7 walls, has been found experimentally to be a practical combination in terms of the overall cooling effectiveness with a practical wall pressure loss at low overall coolant mass flux [4, 19, 23, 41, 44].

Previous CFD investigation by El-jummah *et al* [32] have investigated the internal wall heat transfer of the impingement cooling only. For both gas turbine combustor and turbine blade walls cooling, backside only impingement cooling is a design option. The backside wall cooling application, is used in combustors to regeneratively cool the combustor and in this case all the combustion air flow is used first to cool the walls. This requires a high G of about 2 kg/sm^{2}bar and for a low pressures loss this requires a low X/D. The high G low pressure loss is required as the air has to have enough pressure energy for most of the combustor pressure loss to be at the low NOx flame stabiliser. A problem with impingement only backside cooling is that the air has to flow out of the impingement gap and this cross-flow generates complex interactions that lead to the deterioration of the heat transfer in the cross-flow direction [25, 32, 33]. With impingement/effusion cooling and equal or unequal number of holes, there is no cross-flow as each impingement jet air flow emerges through adjacent effusion hole or holes, these geometries were investigated here.

8.3 Impingement/Effusion Configurations

Andrews *et al* [19, 23, 61, 174], showed that the combustor design requirements for impingement/effusion system are that ~70% of the pressure loss occurs at the impingement wall, with the effusion wall pressure loss relatively low as this gives low BR and a high film cooling effectiveness. For turbine blades, the large static pressure variations around the blade surfaces makes the relative pressure loss between the two plates very complex. In the leading edge of the stator vane, due to high static pressure at the hole outlet film cooling system, a low pressure loss is desirable at both the impingement and effusion holes [4, 23].

The geometries investigated in Table 4.4 all had equal number of impingement and effusion holes, while that of Table 4.5 were all having unequal number of constant impingement and varied number of effusion holes. Figure 4.3 (a - d) show the computational domains that were used in modelling the geometries shown in Tables 4.4 and 4.5, respectively. For the equal *n* geometries shown in Figure 4.3 (a), the impingement holes were offset half a pitch relative to the effusion holes, so that an impingement jet hole was located on the centre of each of four effusion holes. But for unequal *n* geometries shown in Figure 4.3 (a, b and c), the impingement holes were offset 1/4, 1/6 and 1/10 a pitch relative to the effusion holes, respectively. This implies that the location of the impingement jet hole was at the centre of six, sixteen and thirty effusion 10 × 10, 15 × 15 and 25 × 25 holes. The requirements for optimum film cooling effectiveness are that the impingement jet size be small or large X/D (or high ΔP/P), while the effusion film cooling hole size is larger or the X/D is small (or low ΔP/P) [4, 44]. Not all investigations of impingement/effusion cooling have used this ratio of the X/D for the two walls, as in the work of Hong *et al* [188]. The number of holes was a key variable, as for the same hole porosity A and pressure loss ratio ΔP/P, the internal hole

Table 8.1: Equal Hole Density Impingement Wall Flow Conditions

G (kg/sm^{2}bar)	***n*** **(m^{-2})/N**					
	4306		9687		26910	
	10 × 10		15 × 15		25 × 25	
	V_j (m/s)	**Re (× 10^3)**	**V_j (m/s)**	**Re (× 10^3)**	**V_j (m/s)**	**Re(× 10^3)**
0.94	114.5	10.98	115.2	7.28	89.4	3.83
0.77	93.4	8.96	93.9	5.94	72.9	3.13
0.63	76.3	7.32	76.8	4.86	59.6	2.55
0.50	60.6	5.81	60.9	3.86	47.3	2.03
0.30	36.4	3.49	36.6	2.32	28.4	1.22
0.10	12.2	1.17	12.4	0.78	9.5	0.41

Table 8.2: Equal Hole Density Effusion Wall Flow Conditions

G (kg/sm^{2}bar)	**V_h (m/s)**	***n*** **(m^{-2})/N**		
		4306	9687	26910
		10 × 10	15 × 15	25 × 25
		Re (× 10^3)		
0.94	21.7	4.83	3.29	1.92
0.77	17.7	3.94	2.68	1.57
0.63	14.5	3.22	2.19	1.28
0.50	11.5	2.55	1.74	1.02
0.30	6.9	1.53	1.05	0.61
0.10	2.3	0.51	0.35	0.21

Table 8.3: Unequal Hole Density Impingement and Effusion Walls Flow Conditions

G (kg/sm^{2}bar)	***n*** **(m^{-2})/N**					
	Impingement			Effusion		
	1076			4306	9688	26910
	V_j (m/s)	**Re (× 10^3)**	**V_h (m/s)**	**Re (× 10^3)**		
0.94	109.9	21.53	21.7	4.83	3.29	1.92
0.77	89.7	17.56	17.7	3.94	2.69	1.57
0.63	73.3	14.35	14.5	3.22	2.19	1.28
0.50	58.2	11.39	11.5	2.55	1.75	1.02
0.30	34.9	6.84	6.9	1.53	1.05	0.61
0.10	11.7	2.29	2.3	0.52	0.35	0.21

surface area scales with $n^{0.5}$. Thus for equal hole numbers investigated has relative internal surface areas of 1: 1.5: 2.5 or increases in internal hole surface area of 50 and 150%.

The computational domain shown in Figure 4.3 (a - d) were transformed into the grid model geometries shown in Figure 4.6 (a - d), by which Figure 4.6 (a) represent the model for all equal *n* and Figure 4.6 (b, c and d) are the grid models for each unequal *n* of 1076/4306, 1076/9687 and 1076/26910 m^{-2}, respectively. For each *n* (m^{-2}) shown in Tables 4.4 and 4.5, six ranged of G geometries were modelled, which are G from 0.1 - 0.94 kg/sm^2bar. This varied the total number of grid cells of all *n* geometries that were shown Tables 4.9 and 4.10, as the cell in the gap and impingement/effusion holes also varied. The flow variables of Table 8.1/8.2 and

Table 8.3 have been calculated based on air temperature T_∞ of 288K, density ρ of 1.225 kg/m^3 and imposed hot wall side temperature T_w of 360K and were used in this steady state CHT CFD investigations [22, 25]. The CHT computations were carried out using the wall function standard k - ε turbulence model, for which the first cell size near the target wall was kept at $y^+ \sim 35$ for all the G values.

8.4 Aerodynamics in the Impingement and Effusion Plates Gap

The aerodynamics in the impingement/effusion geometry are complex and they cannot adequately be shown in a 2D plane, as several investigators have shown [4, 6, 7, 242, 260, 261, 283, 314]. Figure 8.1 shows the 3D velocity pathline of a 4306/4306 and all three unequal *n* geometries for a G of 0.5 kg/sm^2bar. Figure 8.1 also compares the impingement/effusion velocity pathlines (8.1 a - d) with those for impingement-only flow (8.1 e). This shows that the air jet interactions of the impingement-only flow disappears with the effusion hole. This helps to increase the heat transfer as the impingement flow is sucked into the effusion hole which enhances the heat transfer on the back side of the effusion wall. Figure 8.1 (a) show that the flow recirculation in the impingement gap for impingement-only aerodynamics is changed when effusion jets are added. Instead of the reverse flow jet being in the centre of the four impingement jets, it moves to be in the plane of the impingement jets midway between two jets. This ensures that even with the flow extracted through effusion holes, there is still a reverse flow that heats the impingement wall. These reverse flow jets reduce as the number of effusion holes are increased as Figure 8.1 (b - d) show, which also show that the jet interactions between the impingement and effusion plates are significantly reduced.

The key aerodynamic feature that significantly influences heat transfer in the short hole of the GT test walls and jet approach surfaces is the flow turbulence [17, 80, 83, 85, 94, 187], which has been shown to be adequately predicted by the turbulent kinetic energy [25, 46].

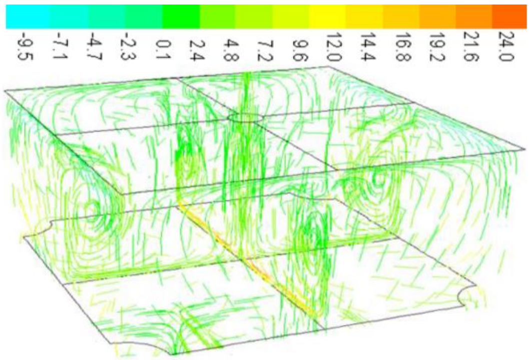

(a) 4306/4306

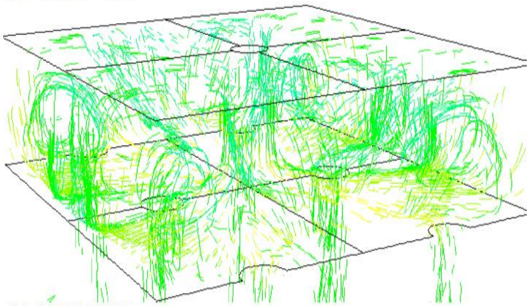

(b) 1076/4306

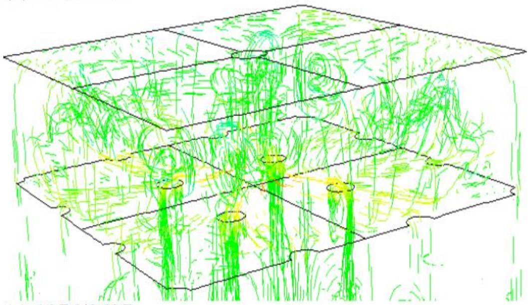

(c) 1076/9687

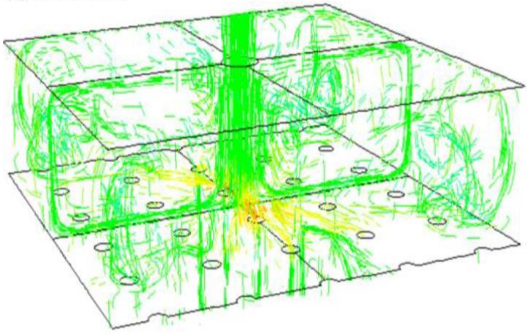

(d) 1076/26910

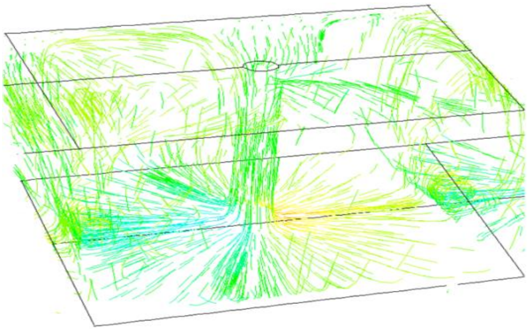

(e) Impingement jet only *n* = 4306

Figure 8.1: Gap flow velocity pathlines (m/s) for impingement/effusion and impingement *n*

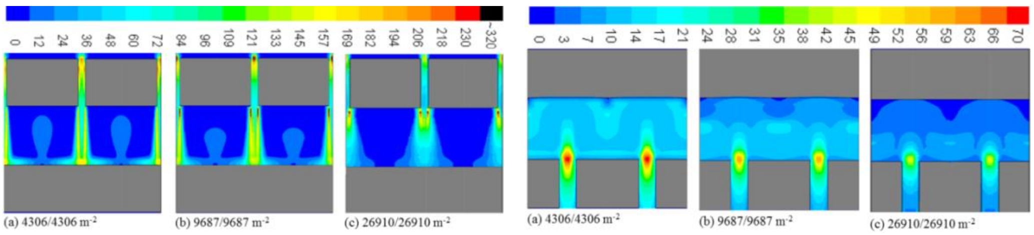

(a) 4306/4306 m^{-2} (b) 9687/9687 m^{-2} (c) 26910/26910 m^{-2}

(a) 4306/4306 m^{-2} (b) 9687/9687 m^{-2} (c) 26910/26910 m^{-2}

(i) In-line with impingement jets

(ii) Between impingement jets

(A) Equal *n* (m^{-2}) geometries

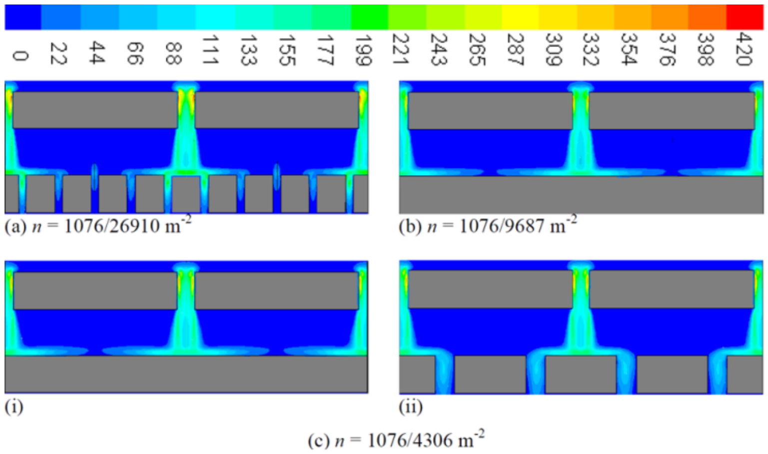

(a) *n* = 1076/26910 m^{-2}

(b) *n* = 1076/9687 m^{-2}

(i)

(ii)

(c) *n* = 1076/4306 m^{-2}

(B) Unequal *n* (m^{-2}) geometries

Figure 8.2: Surface distribution of TKE (m^2/s^2) for G of 0.5 kg/sm^{2}bar at fixed X/D

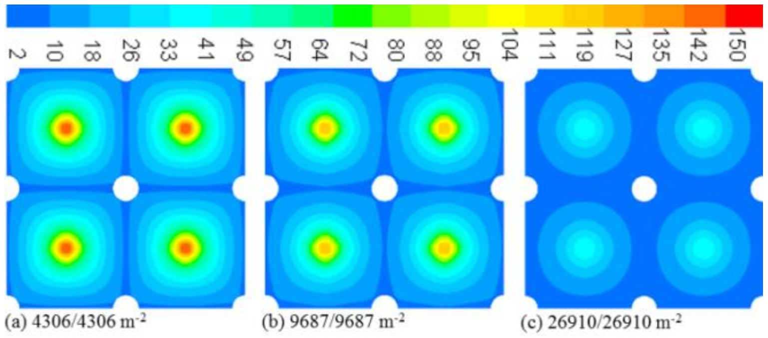

(a) 4306/4306 m^{-2} (b) 9687/9687 m^{-2} (c) 26910/26910 m^{-2}

(i) Equal *n* (m^{-2}) geometries

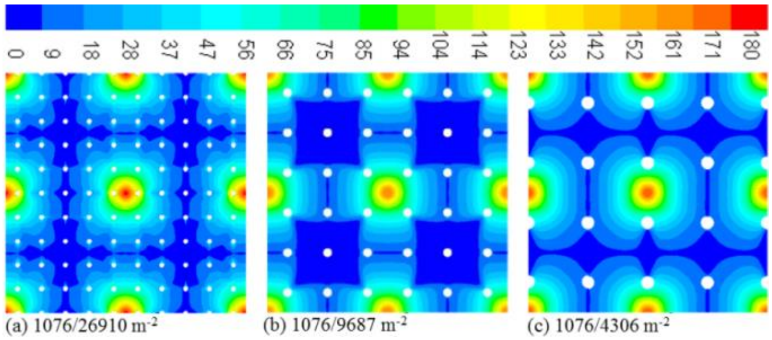

(a) 1076/26910 m^{-2} (b) 1076/9687 m^{-2} (c) 1076/4306 m^{-2}

(ii) Unequal *n* (m^{-2}) geometries

Figure 8.3: Contours of TKE (m^2/s^2) on effusion walls for G of 0.5 kg/sm^{2}bar at fixed X/D

Figure 8.2A (i a - c) and (ii a - c) show the equal *n* TKE (m^2/s^2) for G of 0.5 kg/sm^2bar, which are for the planes of the impingement jet and effusion holes, shows the effects of turbulence in the holes and in the gap between the plates. Whereby Figure 8.2A (i) shows the TKE for the impingement jets, whilst Figure 8.2A (ii) is for the effusion jets. Figure 8.2B (a, b and c) are the TKE (m^2/s^2) for G of 0.5 kg/sm^2bar of unequal *n*, by which only the *n* of 1076/4306 m^{-2}

TKE of Figure 8.2B (ci and ii) are for the planes of the impingement jet and effusion holes based on their symmetries. For unequal *n* of 1076/26910 m^{-2} and 1076/9687 m^{-2}, only TKE in the symmetric planes in-lined with effusion holes and in-lined with impingement jets, respectively are shown in Figure 8.2B (a and c). This shows that the impact of the increase in number of holes at constant impingement gap Z, is to increase the Z/D as the holes are a smaller diameter for larger *n*. Impingement gap to diameter ratio Z/D increases from 2.7 to 12.5 as *n* increases, as Table 4.4 and 4.5 showed. Figure 8.2A show that for the higher *n* with Z/D = 12.5 the peak turbulence of the impingement jet does not reach the surface, thus the surface heat transfer will be lower. Figure 8.2A (ii) show that the peak turbulence for the effusion holes occurs in the hole inlet due to the flow separation that occurs there. Figure 8.2B shows that all the flow features due to separation, reattachment and developing flow are well resolved. Figure 8.2B (a and cii), shows that there is significant amount of turbulence in the effusion holes coming directly from the jets flow, this could enhance hole surfaces heat transfer.

The surface distribution of TKE (m^2/s^2) for G of 0.5 kg/sm^2bar on the effusion approach walls are shown in Figure 8.3 (ia - c) and (iia - c) for both equal and unequal *n* geometries. Figure 8.3 (i) show that a higher TKE is predicted for *n* of 4306/4306 m^{-2} with the lowest value for *n* of 26910/26910 m^{-2}. This is partially because of differences in Reynolds number, as 4306/4306 m^{-2} has the highest Reynolds number. But for unequal *n* geometries that all have the same Re which is equivalent to twice that for an equal *n* with the highest Re, higher TKE was predicted for the 1076/26910 m^{-2} geometries, although the difference is not much. This could be based on minimal jets interactions that was shown in Figure 8.1 (d). Overall, the unequal *n* geometries had the highest hole Reynolds number, which gave the highest predicted surface TKE. Of interest are the shapes displayed by the lowest predicted regions of surface TKE for all the unequal *n* geometries as Figure 8.3 (ii) show, where 1076/26910 m^{-2} gave quatrefoil, 1076/9687 m^{-2} is square and 1076/26910 m^{-2} is rhombus. This insures that the regions with the higher predicted TKE are dominated by certain number of effusion holes coverage, 1076/26910 m^{-2} were 20, 1076/9687 m^{-2} were 12 and 1076/4306 m^{-2} were 4 effusion holes. These TKE values could also affect the surface coverage of the average heat transfer.

8.5 Impingement/Effusion Heat Transfer

Validation of the present work was carried out from the measured surface averaged *h* of Al Dabagh *et al* [4], Andrews *et al* [19, 23] and Nazari [41]. These were found from Equations 2.24 and 2.25, while the $NuPr^{-0.33}$ was found from the Nusselt number of Equation 2.35. The effusion approach surface and effusion holes surface HTCs were computed using Equation 2.24, but the hole *h* again appears in Equation 2.25 [158] in order to calculate the correct surface *h* of the hole, which together gives the total surface *h*. The reason for these HTC additions is based on the diagonal flow velocity through the effusion holes that was shown in Figure 8.1 (a - d). The predicted CHT CFD total surface HTC *h* is compared with the measurements in Figure 8.4 for the equal 8.4 (a) and unequal 8.4(b) *n* geometries. This show

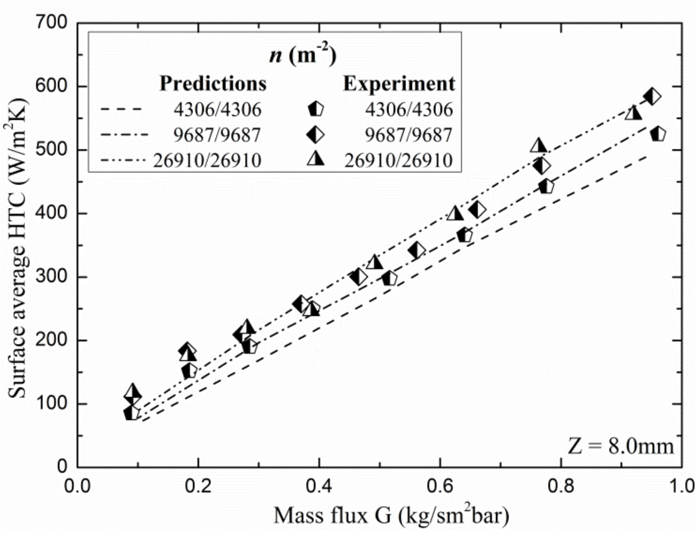

(a) Equal *n* (m^{-2}) at fixed X/D and Z/D

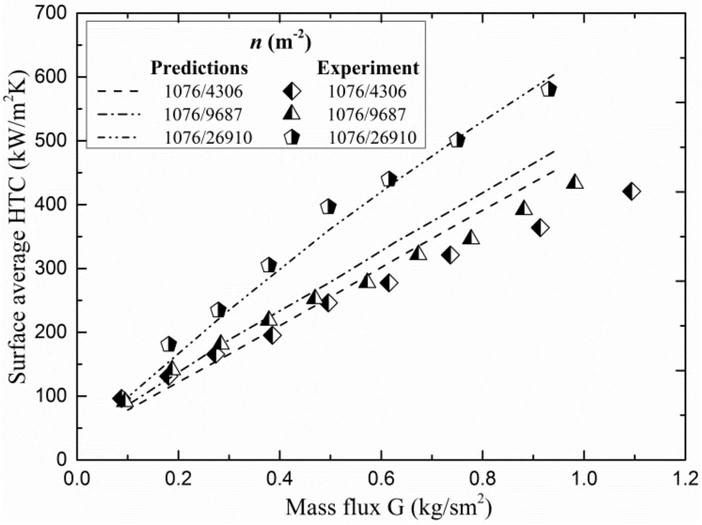

(b) Unequal *n* (m^{-2}) at fixed X/D and Z/D

Figure 8.4: Predicted and experimental comparison of HTC on effusion walls with varied G

very good agreement of the predictions and measurement as a function of G and for all three *n* of each equal and unequal geometries. The best agreement were for the highest two *n*, the other two *n* of equal impingement and effusion holes were slightly lower than the measurements, while that of unequal *n* geometries gave higher predictions than the measured data for G between 0.63 - 0.94 kg/sm^{2}bar values. Figure 8.5 compares the predicted surface averaged HTC *h* of equal and unequal *n* geometries, the highest *h* is for *n* of 1076/26910 m^{-2} followed by *n* of 26910/26910 m^{-2} even though the difference is not much. This must be based on the influence of surface turbulence that was explained on Figure 8.3 above, although the surface X^2 area covered by the unequal *n* impingement jets was 5 times larger. The greatest surprise is for the lowest predicted surface averaged *h* that was given by *n* of 1076/4306 m^{-2} and lower than even 4306/4306 m^{-2}, for G between 0.5 - 0.94 kg/sm^{2}bar, where the hole Re is the as 1076/26910 m^{-2}. So is the surface TKE that is important as Figure 8.3 showed that both their TKE are in the same peak range, hence the obvious reason should be X^2 area coverage of the TKE as 4306/4306 m^{-2} has the full. This explanation is also appropriate for 1076/9687 m^{-2} and 9687/9687 m^{-2} and on average, all the four geometries have approximately the same predicted HTC *h*.

Figure 8.6 show the predictions of *h* for the impingement jet wall, due to the reverse flow shown in Figure 8.1 (a - d). Although there were no measurements of this heat transfer, the agreement of the predictions with measurement for the effusion wall surface indicates that the predictions should be reliable. The highest heat transfer to the impingement wall surface was for the highest equal *n*. It is considered that this is due to their greater number which gives more reverse flow jets per surface area. While the lowest predicted heat transfer were for all the unequal *n*, which were due to the reduced reverse jets with lower jets interactions in the gap between impingement and effusion walls. Comparison of Figure 8.5 with Figure 8.6 shows that for the highest equal *n*, the heat transfer to the impingement jet surface was only slightly below that to the effusion wall target surface, but for lower *n* there was a greater difference. For the unequal *n*, this comparison shows that the reversed jets shown Figure 8.1 (b - d), were not impacted strongly on the impingement wall due to weakening effects of the jets flowing through the effusion holes.

Figure 8.7 show the predicted *h* for the 4306 m^{-2} impingement/effusion cooling compared with impingement only cooling with single sided flow exit. This has a minimum cross-flow and is close to the no cross-flow condition of impingement effusion cooling. Figure 8.7 shows that the impingement/effusion has significantly higher *h* for the effusion target wall than for impingement cooling only. Thus the presence of the effusion jets enhances the heat transfer of the impingement flow. This is due to the extra heat transfer at the inlet to the effusion holes and inside the effusion holes.

The effusion wall has also been predicted as a heat transfer surface without the presence of the impingement flow. The results are shown in Figure 8.7 and are much lower than those for impingement jet cooling only. However, if the separate measurements of *h* for the impingement and effusion walls are added together, Figure 8.7 shows that the total is greater than measured for impingement/effusion combined heat transfer. This shows that there is an adverse interaction between the impingement and effusion walls. This may be due to the impingement flow changing the hole entry and internal aerodynamics of the effusion wall. This was also shown by the experimental investigations of Andrews *et al* [23].

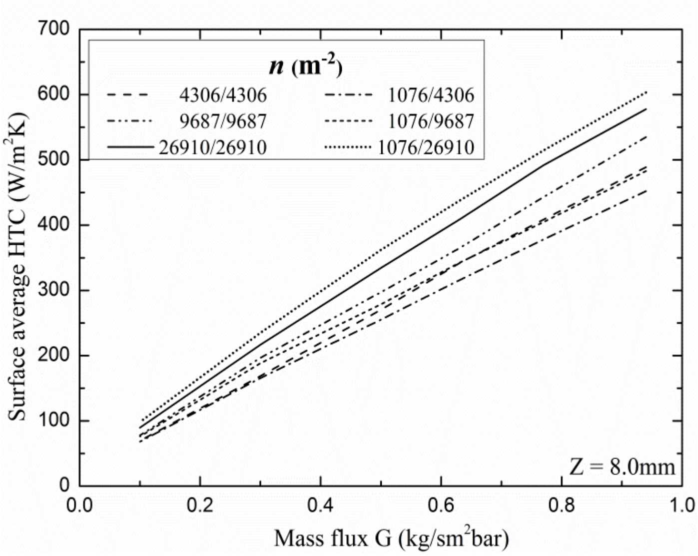

Figure 8.5: Comparison of equal and unequal *n* (m^{-2}) predicted HTC on effusion approach and hole surfaces for the ranged of G at fixed X/D and Z/D

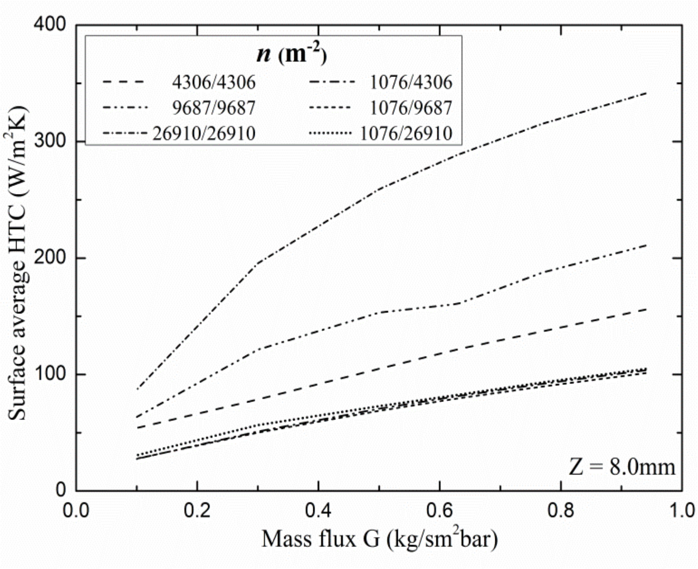

Figure 8.6: Comparison of equal and unequal *n* (m^{-2}) predicted heat transfer on impingement jet side surfaces for the ranged of G at fixed X/D and Z/D

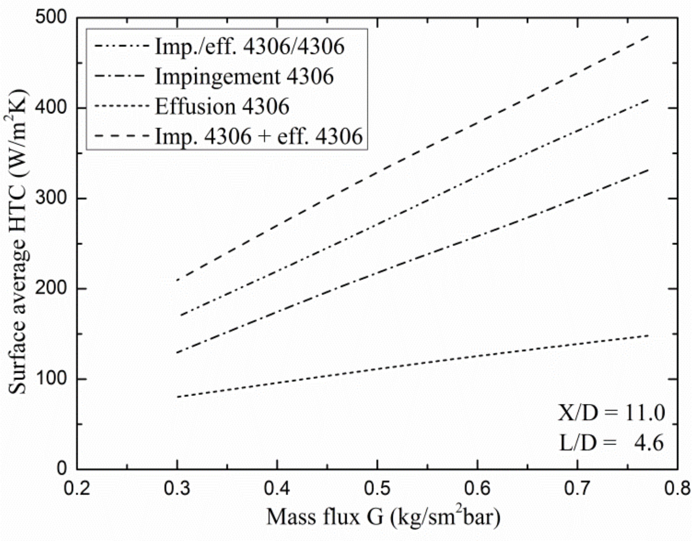

Figure 8.7: Comparison of predicted cooling heat transfer on target or effusion approach surfaces of three different type of cooling with similar *n* (m^{-2}) for varied G at fixed X/D

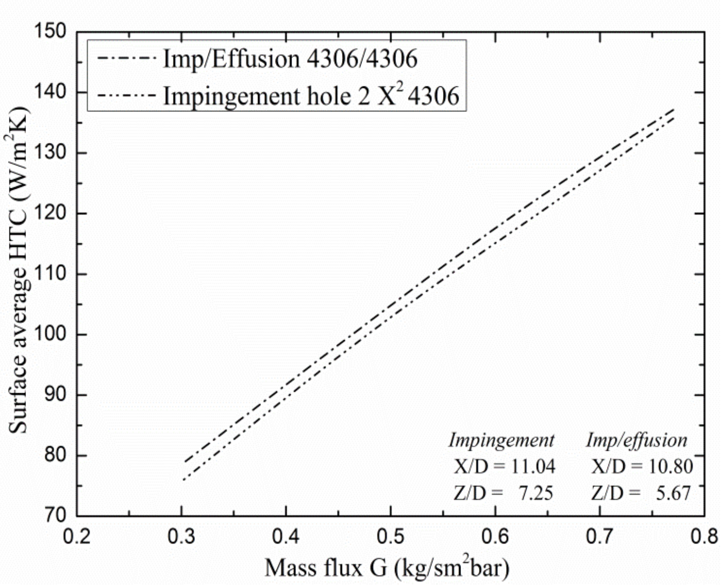

Figure 8.8: Comparison of predicted heat transfer on impingement jet surfaces for impingement/effusion and impingement single exit flow of the same *n* (m^{-2}) with varied G

Figure 8.8 is the comparison of the predicted impingement jet surface averaged HTC *h* for impingement/effusion cooling with that of impingement only cooling, using the second hole for impingement cooling with single sided flow exit [25]. Figure 8.8 show good agreement with the two predicted *h*. The impingement/effusion case was slightly higher than for the impingement cooling only. This indicates that the addition of effusion cooling does not significantly reduce the reverse flow of these *n* geometries. Figure 8.1 (e) show that there is still flow recirculation in the impingement gap, but now with four recirculation zones.

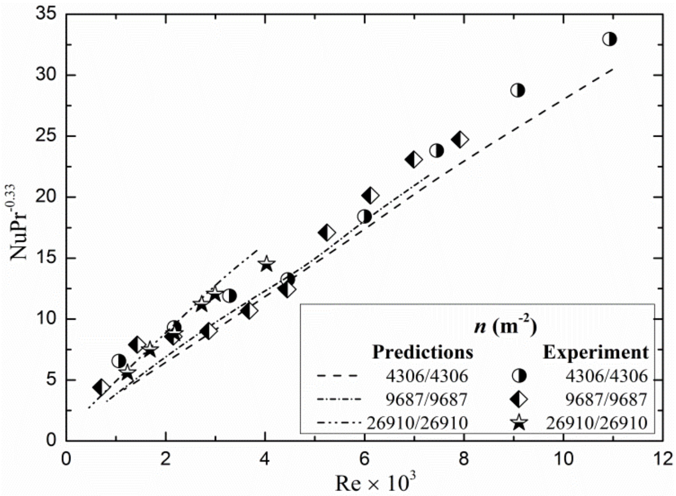

(a) Equal n (m^{-2}) at fixed X/D and Z/D

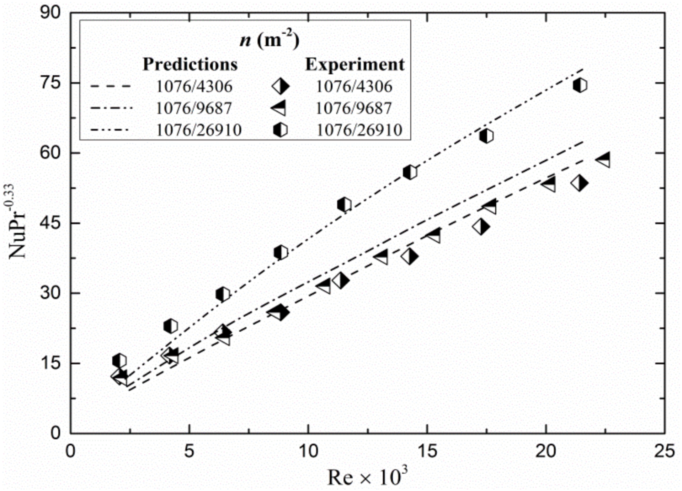

(b) Unequal n (m^{-2}) at fixed X/D and Z/D

Figure 8.9: Comparison of predicted and experimental Nu on effusion walls with varied G

8.5.1 Influence of Reynolds number on Heat Transfer

The heat transfer on the effusion approach wall is shown as a Nu versus Re plot in Figure 8.9, Figure 8.9 (a) is for the equal n and Figure 8.9 (b) is for the unequal n. The best agreement with the experimental measurements [4, 23] in Figure 8.9 (a) is for the largest n and for the lower two n, the predictions are slightly lower than the measurements. Similarly, in Figure 8.9 (b), the best agreement is for the largest effusion n, while the lower n were predicted to be slightly above the measured data [41]. These similar heat transfer comparisons have been explained for the surface averaged HTC h in Figure 8.4 above.

The surface distribution of Nusselt number on the effusion approach wall is shown in Figure 8.10 (ia - c and iia - c) for G of 0.5 kg/sm^2bar, this is similar to surface distribution of TKE in Figure 8.3. The highest Nu in Figure 8.10 (ia - c) is for n of 4306/4306 m^{-2} with the lowest for 26910/26910 m^{-2} of Figure 8.10 (ic), this might be the influenced of the low Re at

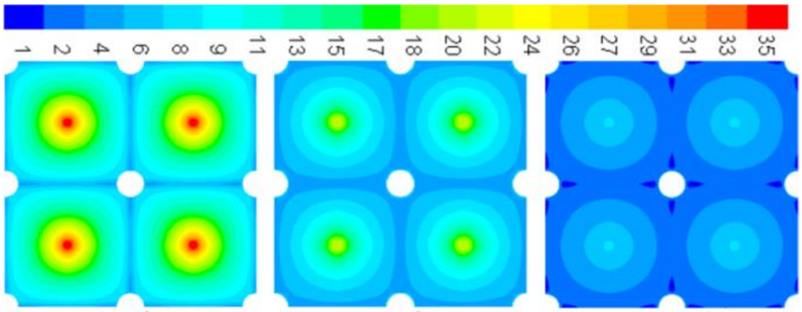

(a) 4306/4306 m^{-2} (b) 9687/9687 m^{-2} (c) 26910/26910 m^{-2}

(i) Equal *n* (m^{-2}) geometries at fixed X/D

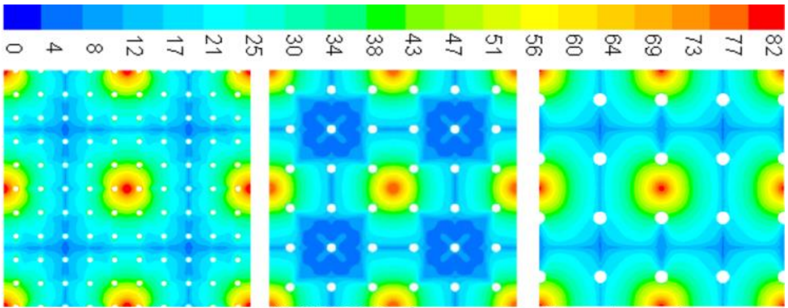

(a) 1076/26910 m^{-2} (b) 1076/9687 m^{-2} (c) 1076/4306 m^{-2}

(ii) Unequal *n* (m^{-2}) geometries at fixed X/D

Figure 8.10: Contours of Nusselt number on effusion wall for G of 0.5 kg/sm^{2}bar

low G. For the fixed impingement holes Re of unequal *n* geometries, the predicted Nu for the largest effusion wall *n* of 1076/26910 m^{-2} is the highest, which also has better heat transfer X^2 coverage as was shown by TKE in Figure 8.3 (ii). Ideally, the unequal *n* of 1076/9687 m^{-2} should have higher Nu than does 1076/4306 m^{-2} based on the X^2 coverage, as the two are having the lower Nu in Figure 8.10 (ii). But the reverse was the case and the reason could be based on the averaged heat transfer in the effusion holes, which resulted to a slightly higher Nu for 1076/4306 m^{-2} than does 1076/9687 m^{-2} of Figure 8.10 (ii). Overall the predicted Nu of the unequal *n* were the highest as compared the equal *n* data.

8.5.2 Heating of the Impingement Jet Wall

The dimensionless temperatures that were shown by Equations 2.44 and 2.6 have been used to measure [4, 19] or predict [25, 46] wall temperatures on impingement test walls. Figure 8.11 compares the measured and predicted impingement jet plates dimensionless temperature T_z for the ranged of impingement/effusion cooling geometries. The geometries of n = 9687 m^{-2} gave good agreement with the measurements for the upstream part of the jet plates. While the predicted T_z for n = 4306 m^{-2} has a poor agreement with the measured data, even though they have the same *n* with closely similar D and Z, as only at the exit plate side that they agreed.

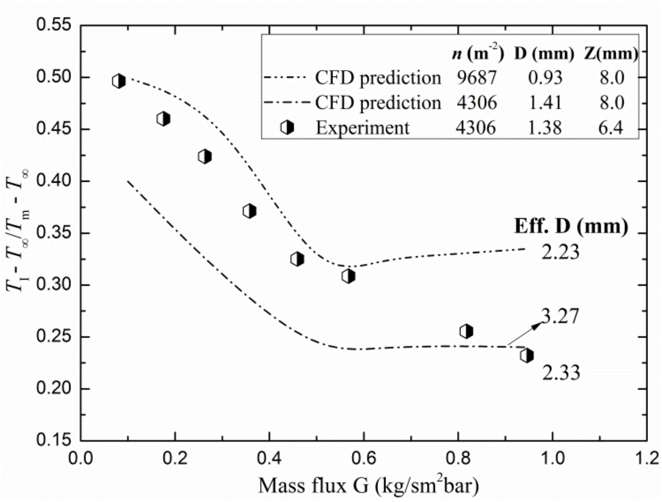

Figure 8.11: Predicted and experimental T_Z comparison on impingement wall for varied G

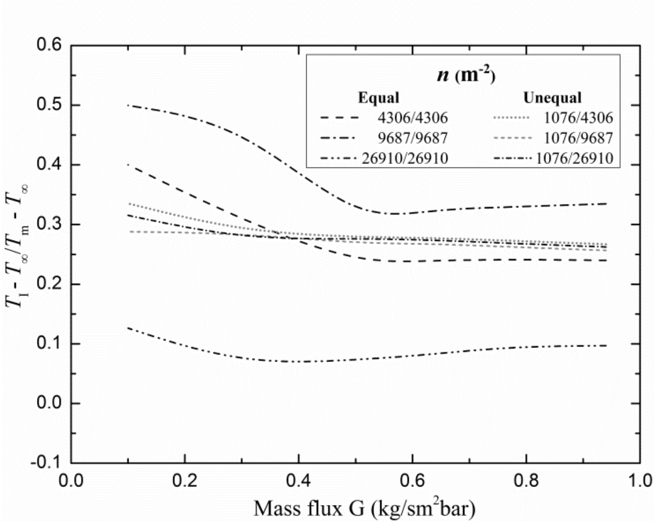

Figure 8.12: Comparisons of predicted equal and unequal *n* (m^{-2}) surface average T_Z on the impingement jet plates for the ranged of G values at fixed X/D and Z/D

Figure 8.12 show the comparisons of the predicted T_Z on the impingement jets plates for the equal and unequal *n* geometries. These predictions show that by averaging out the effusion approach surface temperatures and taken the mean T_m, the predicted T_Z of the unequal *n* that all agreed to each other are on averaged slightly close to the 4306/4306 m^{-2}. This show that the X^2 area average influences the T_Z predictions, as the X^2 of 4306/4306 m^{-2} are only twice the unequal *n* one, this could influence the T_m even though the Re is much more significant. Possibly, this could be the reason why all the unequal *n* predicted T_Z nearly the same, which further indicates that the jets reversal of Figure 8.1 (a - d) are not strong on the jet plates.

A method of predicting and seeing clearly the influence of the heated jet and the interactions of this jet in the gap, is the use of Equation 2.6 and this is shown in Figure 8.13 (A and B) for the equal *n*. Figure 8.13A (ia - c) are normalized temperature T^* for the symmetry plane

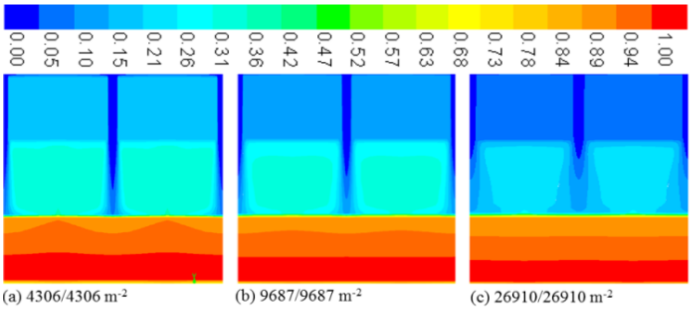

(i) In-line with jets

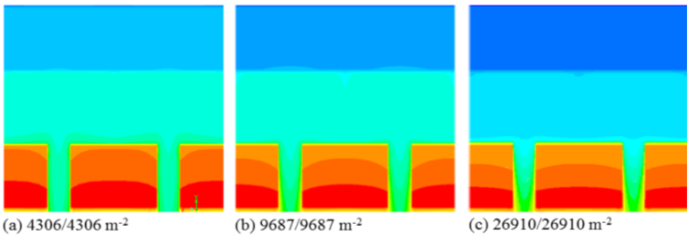

(ii) Between jets

(A) Equal *n* (m^{-2}) geometries

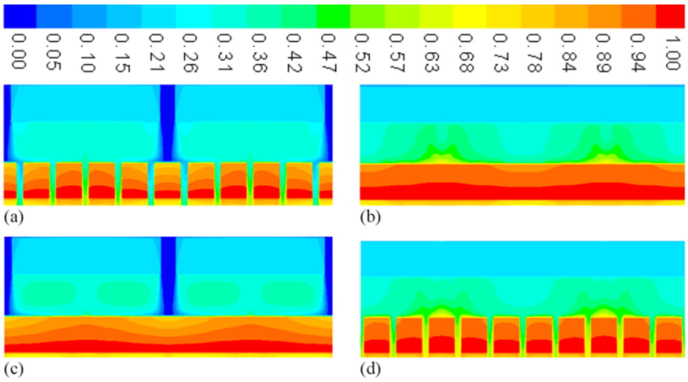

(i) 1076/26910 m^{-2}

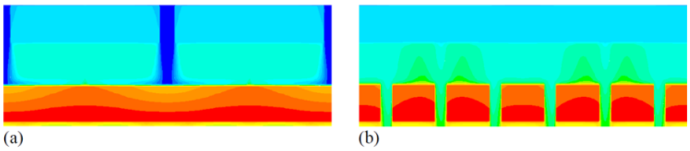

(ii) 1076/9687 m^{-2}

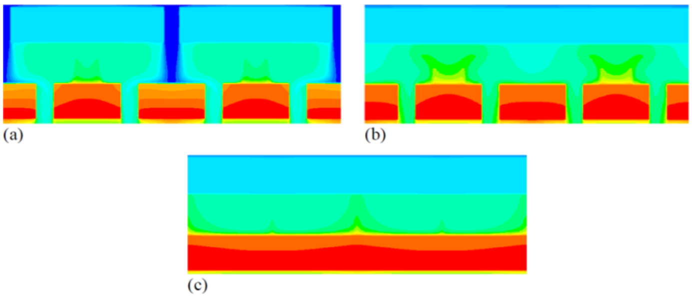

(iii) 1076/4306 m^{-2}

(B) Unequal *n* (m^{-2}) geometries

Figure 8.13: Contours of normalized temperature T^* for G of 0.5 kg/sm^{2}bar

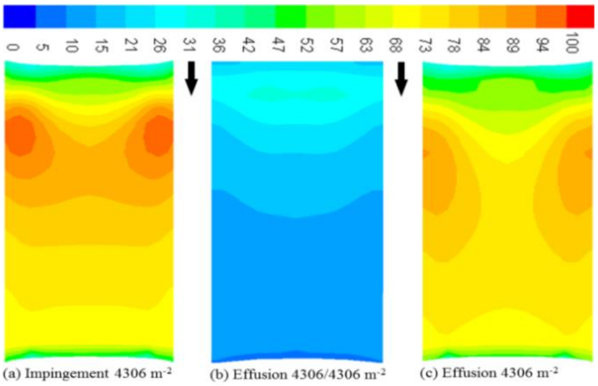

(a) Impingement 4306 m^{-2} (b) Effusion 4306/4306 m^{-2} (c) Effusion 4306 m^{-2}

Figure 8.14: Comparisons of predicted holes TKE (m^2/s^2) contours for G of 0.5 kg/sm^2bar

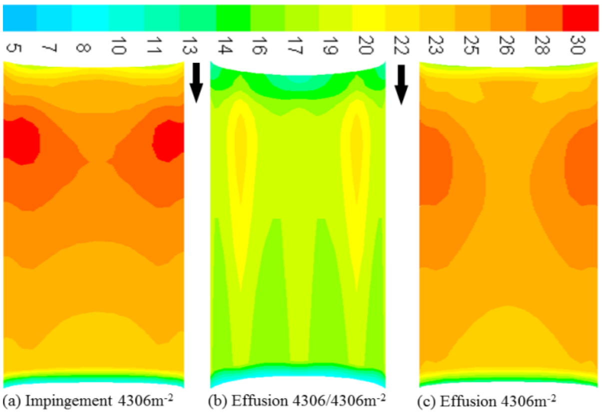

(a) Impingement 4306m^{-2} (b) Effusion 4306/4306m^{-2} (c) Effusion 4306m^{-2}

Figure 8.15: Comparisons of Nu contours on hole walls for G of 0.5 kg/sm^2bar

of the jet wall, while Figure 8.13A (iia - c) are for the symmetry plane of the effusion walls. The impingement jet is shown clearly in Figure 8.13A (i). However, the reverse flow jets shown in Figure 8.1 are not shown in the planes of Figure 8.13A. Figure 8.13A (ii) shows that the air at the entrance to the effusion hole is heated by the impingement jet heat transfer. Figure 8.13B (i - ii) are the T^* for the unequal *n* geometries, which show that these *n* were better cooled than the does the equal *n* geometries. The effusion walls in-lined to the impingement jets planes are shown in Figure 8.13B (ia and c), (iia and c) and (iiia), respectively, those between the jets are shown in 8.13B (ib and d), (iib and d) and (iiib and c), respectively. For the planes between the jets, it shows that the reversed jets do not strongly hit the impingement plates and most of the heat are in the effusion holes, which could be additional reason for the uniformity and lower T_Z of the unequal *n* in Figure 8.12.

8.5.3 Test Walls Holes Entry Length Effects

Figure 8.14 show the hole internal surface distribution of TKE (m^2/s^2) for *n* of 4306 m^{-2}, for which the impingement, impingement/effusion and effusion are compared. The results in Figure 8.14 (a - c) show for a fixed G of 0.5 kg/sm^2bar that the turbulence in the effusion hole is much lower for impingement/effusion cooling than for effusion cooling. This indicates an adverse interaction of the impingement jet on the effusion wall that influences the internal flow inside the impingement wall.

Figure 8.15 (a - c) show the internal effusion hole surface area distribution of the Nu for impingement alone and for impingement/effusion and effusion alone. Figure 8.15 (b) show a complex thermal effects on the hole surface as a results of the weak flow effects coming from the effusion approach surface. This has been shown experimentally to influence the effusion hole suction effects [23] on the impingement jet heat transfer. For the separately jets impingement and effusion walls, there is the classic inlet flow separation and reattachment inside the holes. But for the combined impingement and effusion, the impingement jet flow to the effusion hole inlet creates the complex Nu distribution inside the hole.

Figure 8.15 show the internal effusion hole surface area distribution of the Nu for impingement alone and for impingement/effusion and effusion alone. Figure 8.15 (b) show a complex thermal effects, on the hole surface as a results of the weak flow effects coming from the effusion approach surface. This has been shown experimentally to be the influence of the effusion hole ‘suction’ effects [23] on the impingement jet heat transfer. For the separately impingement and effusion walls, there is the classic inlet flow separation and reattachment inside the holes. But for the combined impingement and effusion, the impingement jet flow to the effusion hole inlet creates the complex Nu distribution inside the effusion hole.

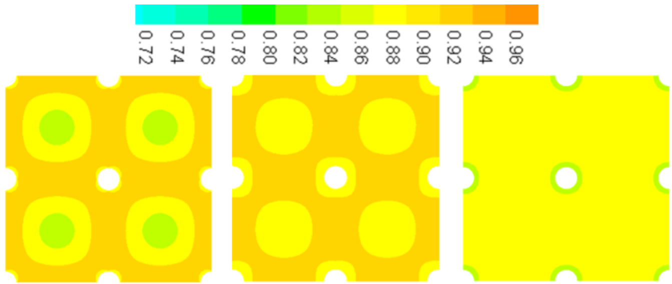

(a) 4306/4306 m^{-2} (b) 9687/9687 m^{-2} (c) 26910/26910 m^{-2}

(i) Equal *n* (m^{-2}) geometries

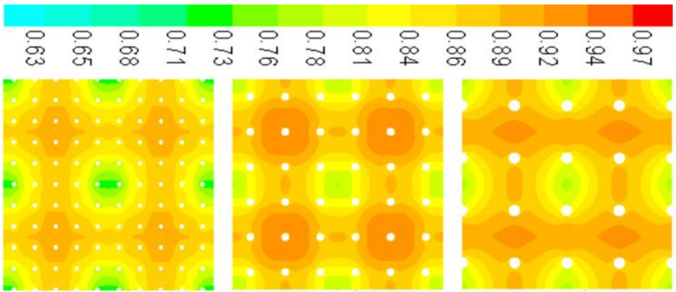

(a) 1076/26910 m^{-2} (b) 1076/9687 m^{-2} (c) 1076/4306 m^{-2}

(ii) Unequal *n* (m^{-2}) geometries

Figure 8.16: Contours of normalized temperature on effusion wall for G of 0.5 kg/sm^{2}bar

8.6 Effusion Walls Thermal Gradients

Figure 8.16 (ia - c) and (iia - b)show the surface distribution of normalized temperature T^* for a fixed G of 0.5 kg/sm^{2}bar. By surface averaging the distributions in Figure 8.16, the surface averaged dimensionless temperature T^* is transformed into Figure 8.17 (a and b) as a function of G. The lower the T^* value, the higher the HTC *h*, this indicates that the results for the HTC *h* in Figure 8.5 would thus predict that 26910/26910 and 1076/26910 m^{-2} would have the lowest T^* as in Figure 8.16 (ic). This is true for 26910/26910 m^{-2} as it has the smallest X^2 coverage with the same number of effusion holes/jets to the other two equal *n*. But this is not the case with 1076/26910 m^{-2} that has the same X^2 coverage with different number of effusion holes/jets to the other two unequal *n*, so most of the cooling will be in the effusion holes. Figure 8.16 (ic) and (iia) gave the lowest T^* each in Figure 8.17 (a) and (b) even though the difference in Figure 8.17 (b) is slightly small. Comparing T^* of the equal and unequal *n* as shown in Figure 8.18 shows that all the unequal *n* predicted the highest T^*. Ideally this should not be so, as the unequal *n* has the highest HTC *h*, but because most of the cooling is in the effusion holes (Figure 8.13) and only the surface T^* of Figure 8.16 (ii) were averaged out, implies that this difference in Figure 8.18 is correct. Figure 8.16 (ia) show that *n* of 4306/4306 m^{-2} has the highest T^* with the lowest spot at the middle, while *n* of 9687/9687 m^{-2} of Figure 8.16 (ib) is in between the two *n* (m^{-2}). Figure 8.17 (a) show that the coolest wall is for the highest *n* which is in agreement with Figure 8.4 (a) for the surface averaged *h*. Figure 8.17 (b) show that the predicted T^* for the unequal *n* are in agreement, with *n* of 1076/26910 m^{-2} having the lowest T^* spot at the middle in Figure 8.16 (ii), which also correspond to the predictions of Figure 8.17 (b).

The T^* comparisons of impingement jet only *n* of 4306 m^{-2} at hole 2 with impingement/effusion of similar *n* are made in Figure 8.19. This show that the impingement/effusion surface temperatures are lower than for impingement alone, due to the additional effusion wall heat transfer. Figure 8.20 (a and b) show the effusion walls predicted thermal gradients through the metal thickness. At both locations of between the jet flow and in-lined to the jet, shows that 26910/26910 and 1076/26910 m^{-2} still gives the lowest value of T^* and n = 4306/4306 and 1076/4306 m^{-2} have the highest T^*. These two *n* geometries are compared in Figure 8.21 for *n* of 4306/4306 and 1076/4306 m^{-2}, the wall predicted T^* between the jets show that *n* of 1076/4306 m^{-2} has the highest gradients, which should be based on the influence of the effusion holes. The lowest gradient in the region in-lined with the jets is also given by the same *n* and was based on the absent of the effusion holes there. This further indicates the importance of combining the heat transfer of the effusion approach and holes surfaces to actualize the correct HTC *h* data.

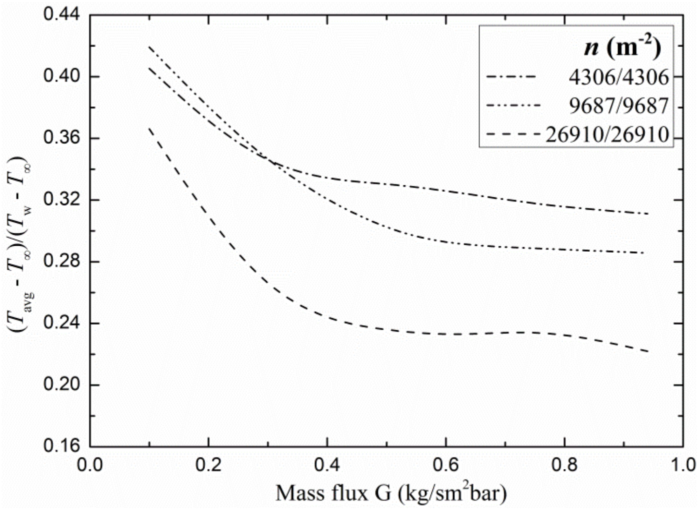

(a) Equal *n* (m^{-2}) at fixed X/D and Z/D

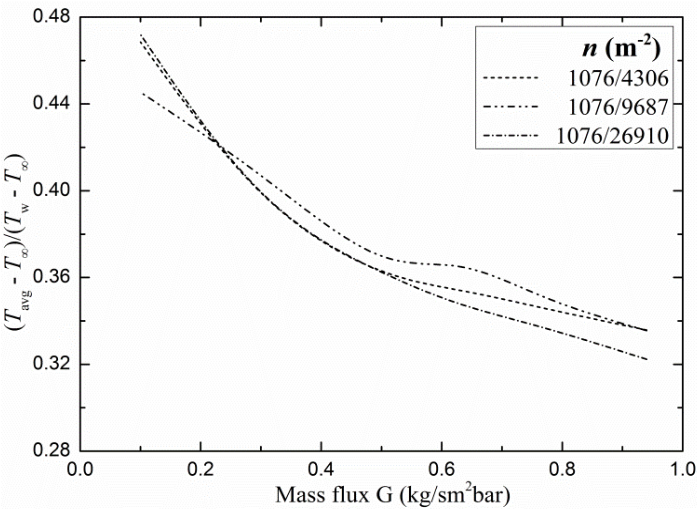

(b) Unequal *n* (m^{-2}) at fixed X/D and Z/D

Figure 8.17: Comparison of predicted surface average T* on effusion walls as function of G

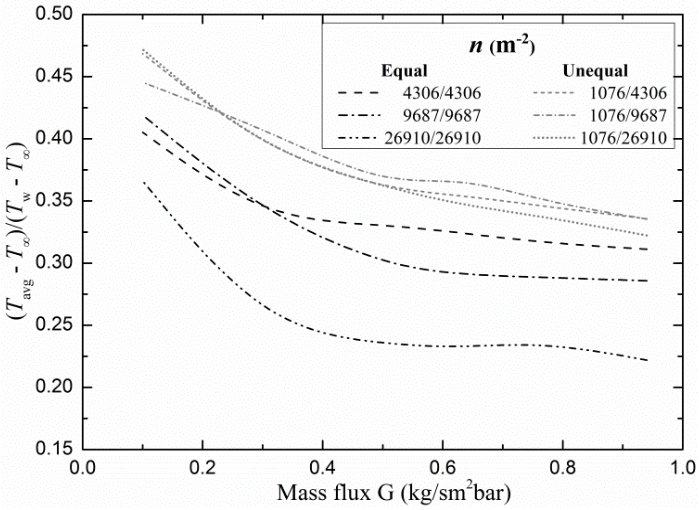

Figure 8.18: Comparison of predicted equal and unequal *n* (m^{-2}) surface average T* on the effusion walls for varied G values

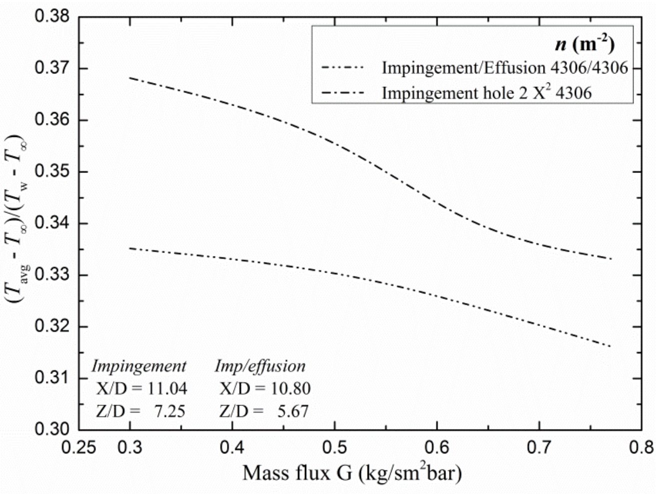

Figure 8.19: Comparison of predicted average normalized temperature on target surface of impingement/effusion and impingement single exit flow for fixed *n* (m^{-2}) with G.

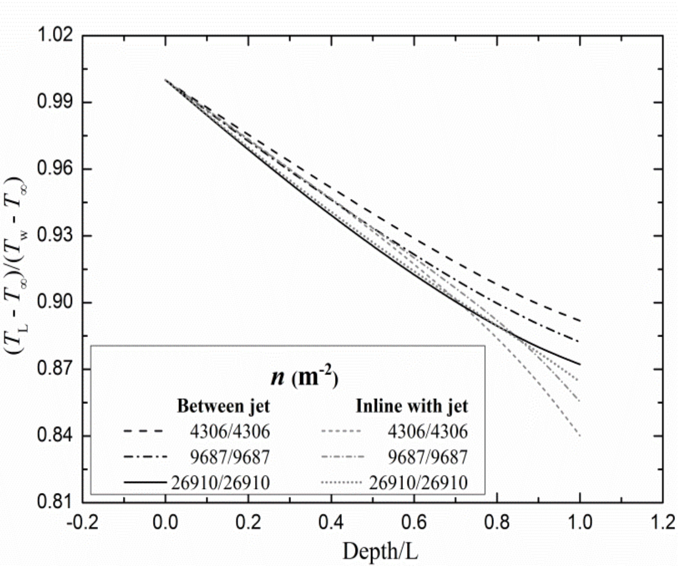

(a) Equal *n* (m^{-2}) at fixed X/D and Z/D

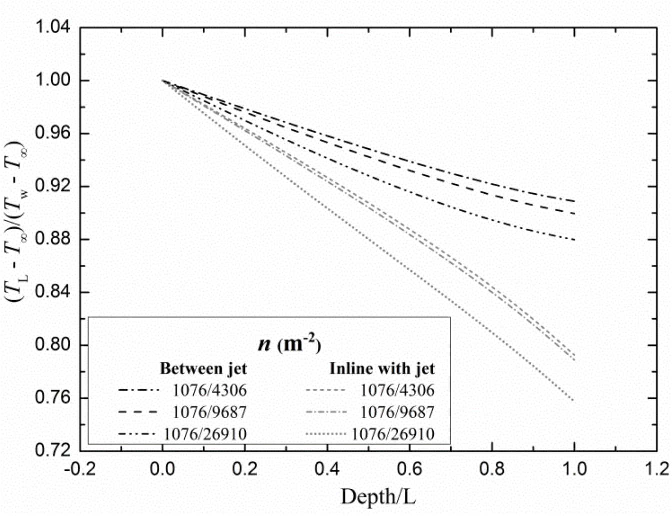

(b) Unequal *n* (m^{-2}) at fixed X/D and Z/D

Figure 8.20: Predicted locally T* through the effusion walls for G of 0.5 kg/sm^{2}bar

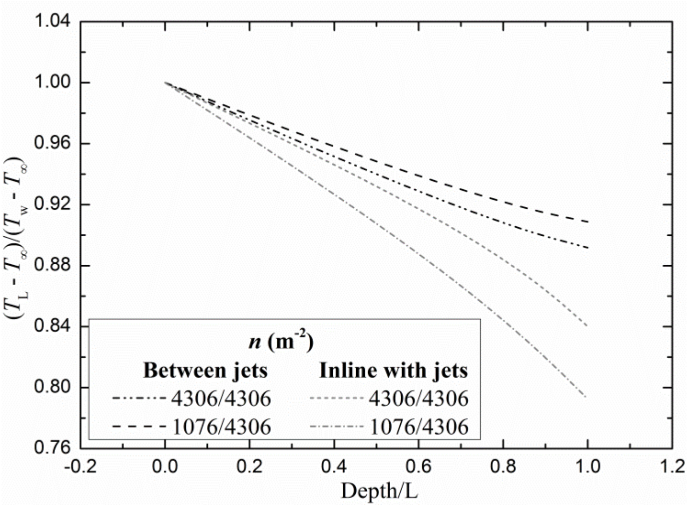

Figure 8.21: Comparison of predicted equal and unequal *n* (m^{-2}) locally T* through the 4306 m^{-2} effusion walls for a fixed G of 0.5 kg/sm^{2}bar at fixed X/D and Z/D

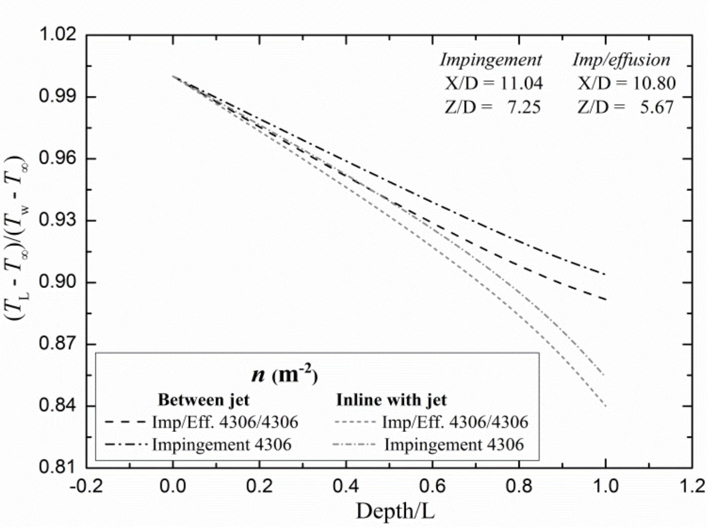

Figure 8.22: Comparison of predicted target wall locally normalized temperature of impingement/effusion and hole 2 X^2 impingement single exit flow for G of 0.5 kg/sm^{2}bar

Figure 8.22 compares the predicted thermal gradient T* of *n* = 4306/4306 m^{-2} and impingement hole 2 X^2 of *n* = 4306 m^{-2}. This comparison between impingement/effusion and the equivalent impingement only cooling shows that the thermal gradients are greatest for the impingement/effusion cooling, which is due to the higher HTC *h*. This show that the best cooling could be achieve using the impingement/effusion geometries.

8.7 Conclusions

The predicted surface average heat transfer coefficient *h* and the NuPr$^{-0.33}$ have been shown to agree very well with the experimental measurements. This shows that the present CHT CFD procedures are adequate for the design of impingement/effusion cooling system for gas turbines engines.

Impingement/effusion cooling was shown to give a higher cooling heat transfer coefficient h than for impingement only cooling with a single exit flow. The heat transfer was also higher than for effusion only geometries.

The n of 26910/26910 and 1076/26910 m^{-2} that have the largest number of holes N with the smallest effusion X were predicted to have the best cooling.

The CHT CFD predictions of the effusion wall thermal gradients showed that the largest n of 26910/26910 m^{-2} gave lowest surface average temperature and the lowest wall thermal gradient, while n = 4306/4306 m^{-2} with the lowest number of holes n gave the highest.

Overall, the best cooling can be achieved using unequal n (m^{-2}) impingement/effusion cooling system as it gives higher HTC h and better thermal gradients.

CHAPTER NINE

CONCLUSION AND RECOMMENDED FUTURE WORK

Chapter 9

Conclusion and Recommended Future Work

9.1 Conclusions

The internal wall cooling of gas turbine components is an important part of the overall wall and film cooling in gas turbines. This work explored the use of regenerative cooling of combustors using impingement cooled walls only with very high coolant mass flow rates and low pressure loss. Two major features of such heat transfer were predicted: the flow-maldistribution caused by the cross-flow when the impingement wall pressure loss was low (low X/D) and the deterioration of heat transfer along the length of the wall for configurations where the impingement wall pressure loss was high and flow-maldistribution was low (high X/D). In the absence of published measurement of velocity and turbulence profiles in the impingement gap, the prediction of measured pressure loss was used as an indicator that the CFD predicted aerodynamics was correct. The most important part of the pressure loss was internal impingement jet hole flow separation and reattachment and some turbulence models could not predict this well-known effect at the sharp edged entry to a short tube.

It was shown that an important part of the impingement target wall cooling (the combustor wall) was the heat recirculated back to the impingement hole wall. This led to work on the predictions of heat transfer in a relatively thin wall with an array of holes through which a coolant passes. As this is also the geometry for effusion film cooled walls, both applications were investigated from a wall heat transfer viewpoint. The acceleration of the coolant flow into the holes was an important part of this overall heat transfer. Finally the combination of impingement and effusion cooling was investigated in terms of the overall wall heat transfer. The presence of the effusion hole jet flows were predicted to reduce the reverse flow to the impingement jet wall and hence to reduce the heat transfer to this wall. The addition of the effusion cooled wall to the impingement cooling did lead to an enhanced overall internal wall cooling, but not by an amount that would have been the two wall heat transfers added together.

Conjugate heat transfer (CHT) computational fluid dynamics (CFD) was successfully applied to the design of impingement, effusion and impingement/effusion metal conductive wall heat transfer systems. Validations of the predictions were carried out by comparison with experimental data for two grid types (tetrahedral and hexahedral) using wall function ($y^+ \sim 35$) RANS and RSM turbulence models on impingement heat transfer with single sided exit flow geometry. The judgement of the acceptability of the grid used and the turbulence model was the ability to predict the measured flow pressure loss and the measured surface averaged heat transfer coefficient or surface averaged measured temperature. On this basis for the impingement cooling application the comparison of the predictions with experimental results showed that the hexahedral grid with the standard k - ε turbulence model with standard wall functions better predicted the pressure loss and the surface average heat transfer coefficients than alternative grids and turbulence models. The range of y^+ values from 30 - 35 were used, which showed good predictions of the measured surface averaged metal wall heat transfer data.

For an array of short holes in a thin metal wall (impingement jet wall and effusion wall) a similar validation was carried out for low Re (y^+ from 1 - 2) and wall function ($y^+ \sim 35$) with RANS and RSM turbulence models using hexahedral grids. The application of a hexahedral grid with the aid of symmetric boundary conditions and the use of wall function standard k - ε turbulence model, were shown to give a good prediction of the overall pressure loss, which indicates that all the aerodynmics were correctly predicted. The agreement of predictions and hot metal wall measurements for the locally surface averaged heat transfer was good. Thus there was no advantage for abandoning the wall function approach and using y^+ values of ~ 1 and a very large number of grids in the wall region. Also there was no advantage and considerable disadvantage in using more complex turbulence models, as they could not predict the flow separation and reattachment of the flow in the short holes. This was also fundamental to why they were so poor at predicting impingement heat transfer.

Experimental results for the wall heat transfer for impingement, effusion and impingement/effusion cooling systems compared well with the CHT/CFD predictions for pressure loss $\Delta P/P$ and locally/surfaced averaged heat transfer coefficient (HTC) *h* (W/m^2K). The impingement jet and target or effusion metal walls were Nimonic-75 of 6.35mm metal thickness. Square array impingement jets and effusion holes were investigated for a range of X/D, Z/D, *n* (m^{-2}) and G (kg/sm^2bar) which were varied by changing the hole diameter D, X, Z, *n* or G. By varying D or G, the Reynolds number was also changed, which also influenced the impingement jet or effusion holes and impingement gap turbulent flow.

The heating of the impingement jet plate that resulted from flow reversal of the impingement jets were shown to carry heat from the cooled target surface to the impingement wall surface and for the first time the heat transfer coefficient to the impingement jet wall surface was predicted. These predictions compared well with the limited experimental data for this surface temperature. The impingement jet wall recirculated flow surface averaged heat transfer coefficient was about 70% of that of the target or effusion approach surface. This high ratio indicates that it is an important part of the overall wall cooling heat transfer and hence a significant feature of the overall process.

The influence of hole density *n* (m^{-2}) in a square array impingement and impingement/effusion cooling geometries has received little study and current design methodology do not include this as a design parameter. This is in spite of the fact that *n* has to be specified in order to determine the impingement hole diameter D, as design correlations for impingement heat transfer predict X/D and Z/D. The specification of X/D and Z/D do not enable the optimum X and D to be specified, as these depend on *n*. For practical reasons the impingement gap Z has a limited range in gas turbine cooling applications. As the impingment cooling is highest at low Z/D in the range 1 - 2, there is a benefit in using the smallest number of holes *n* as these have the largest diameter and hence the lowest Z/D, there is also a manufacturing cost reduction. The factor that limits making *n* very small and X and D very large, is the thermal gradients in the metal wall. These can only be determined from CHT/CFD and hence these predictions should be an important part of the design process. It was shown that thermal gradients become too large if $n < 4306\ m^{-2}$ and hence this is the optimum *n* for impingement cooling.

For impingement/effusion cooling the variation of *n* is most significant for the effusion film cooling and a high value of *n* is required and $n = 26910\ m^{-2}$ was the highest number of holes investigated and had the best overall film cooling effectiveness. Also required for optimum effusion designs is a low hole velocity or low effusion wall pressure loss, which is a low X/D design choice and < 5 was used in the present work. For the impingement wall high jet velocities are desired for best cooling and hence a high pressure loss or high X/D design is required. Thus impingement/effusion walls should have different X/D and combination of low effusion X/D and high impingement X/D were investigated in this work. The CHT/CFD studies showed that the action of effusion cooling was to reduce the reverse flow in the impingement gap. This reduced the heat transfer to the impingement jet wall, but this was more than offset by the gain in heat transfer at the effusion wall. The different optimum *n* for effusion and impingement cooling leads to both *n* and X/D being different in impingement/effusion cooling and 26910/26910 and 1076/26910 m^{-2} were shown to be the optimum designs. The lower optimum *n* for the impingement wall, than for impingement alone was because there were 25 effusion holes for each impingement holes and these reduced the thermal gradients between impingement holes.

The CHT/CFD predictions showed that thermal gradients between impingement holes were low and the greatest thermal gradients were through the Nimonic-75 metal thickness. For an impingement jet cooling, the thermal gradients increased as *n* decreased but were considered acceptable for the optimum *n* of 4306 m^{-2} for maximum *h* and unacceptable for the lower *n* of 1076 m^{-2}. But for impingement/effusion cooling system, thermal gradients between impingement holes on the effusion walls for equal and unequal *n* were all within acceptable limits.

CHT/CFD was also applied to impingement cooling with obstacles in the gap to enhance the heat transfer. The literature survey on this topic showed that it was difficult to get large improvements in an already high heat transfer mode, if there was only one obstacle per impingement jet or per row of impingement jets. The best systems in the literature with 50% enhancement in heat transfer demonstrated were for 6 pin fins per impingement jet and to fit these requires a large X/D of 8 or higher. For the impingement geometries of low pressure loss and high coolant mass flow regenerative combustor cooling applications, only one obstacle per hole is feasible and this was investigated using CHT/CFD. The results gave good agreement with experiments and showed that the main effect of the obstacles was to stop the deterioration of heat transfer with distance and to give a more uniform surface heat transfer. Three new impingement gap obstacle design were investigated, but none were predicted to have higher heat transfer enhancement than the rectangular pin fin geomentry under co-flow and cross-flow gas aerodyamics. However, the CHT/CFD predictions only showed a 12-13% increase in the surface averaged heat transfer coefficient and this was in reasonsonly agreement with the experimental measurements.

9.2 Future Work Recommendations

1. To predict the benefit if any of directing the impingement jets upstream against the cross-flow, so as to minimise downstream deflection.
2. To overcome the flow-maldistribution problem by changing the impingement hole diameter along the length of the cross-flow gap by varying the upstream jet holes diameter. The design of this could be evolved using CHT/CFD.
3. To evaluate using conjugate heat transfer CFD design, the complete hot gas crossflow combustion rig, rather than the present technique of imposing a heat flux on the impingement wall or an imposed gas side wall temperature. This would enable the feedback of the heat removal through the wall on the boundary layer temperature profile to be determined.
4. To extend the impingement/effusion cooling computations to include the hot gas cross-flow film cooling aerodynamics and hence to predict the overall film cooling effectiveness. This requires that for a square array of holes, a complete half row of holes is modelled and is based on the requirement for efflux of the hot gas exit flow. This will considerably increase the grid size required and may require a HPC system.

5. To evaluate using conjugate heat transfer CFD design, the effects of obstacle pins or dimples walls by varying their arrangement as either using an in-lined obstacles to the jet flow and by increasing their number relative to the impingement holes.
6. Further work should be carried out on ribbed wall designs: varying angle, height, width or number, so that their arrangements are varied, these could increase the heat transfer enhancement.
7. Work should be carried out on ribs across the cross-flow that have one or more holes in them to force the cross-flow air to more efficiently cool these ribs. Initial work by the Leeds experimental group showed this had one of the best enhancements and could be higher if the entire gap was used. The hole size would have to increase as the cross-flow mass flow increased.
8. To evaluate using conjugate heat transfer CFD design, the variation of effusion holes angles applied to impingement/effusion cooling with hot gas crossflow.
9. To evaluate using conjugate heat transfer CFD design, the variation of impingement and effusion walls thickness (hole length) or L/D based on varied L. This affects the discharge coefficient C_d, which will also alter the hole exit pressure loss. Once the wall thickness is altered, the conduction through the wall is also affected so also the thermal gradients even though the thermal conductivity remain the same. There is experimental data that exist to validate this area of CHT/CFD predictions.
10. To evaluate using conjugate heat transfer CFD designs, low Re turbulence model solutions for comparison between tetrahedral and hexahedral grids, which can also be compare with hybrid grids. For an effective use of these grids with boundary layer growth, the requirements for HPC must be employed as the grid sizes will be high.
11. To use CHT/CFD to design a complete reverse flow combustor and low NOx burner to show that reverse flow cooling is practical at engine operating conditions, both in terms of pressure loss and wall temperatures.

Appendix A

Ideal and Real Thermodynamics Properties of Gas Turbine

A.1 Gas Turbine Thermal Efficiency and Power

The thermodynamic cycle or the ideal cycle for which a simple cycle gas turbines operates is the Brayton (or Joule) cycle. This cycle is shown as a PV diagram in Figure A.1. Stages; 1 - 2 is adiabatic air compression, 2 - 3 is constant pressure combustion and 3 - 4 is the turbine adiabatic expansion. The temperature and pressure after compression are T_2 and P_2 ($P_3 = P_2$ in an ideal cycle, but in a real cycle the combustor has a pressure loss of about 4%), T_3 is the temperature after combustion, while T_4 and P_4 are the temperature and pressure after the turbine expansion. The Brayton cycle is characterized by two significant parameters: pressure ratio and combustor firing temperature T_3 (or turbine entry temperature). The pressure ratio is the compressor discharge pressure P_2 divided by compressor inlet pressure P_1 (or P_3/P_4 for an ideal cycle), while the turbine entry temperature T_3 is the highest temperature reached in the ideal cycle. The ideal thermal efficiency is defined by Equation 1 below:

$$\eta_i = \frac{Turbine\ \ work\,done - Compressor\ \ work\,done}{Heat\,input\ \ from\,the\ \ fuel}\ or\ \eta_i = \frac{\left\{\dot{m}_2 C_p\left(T_3 - T_4\right) - \dot{m}_1 C_p\left(T_2 - T_1\right)\right\}}{\dot{m}_2 C_p\left(T_3 - T_2\right)} \qquad (1)$$

Where $\dot{m}_1$ is the air mass flow rate (kg/s) through the compressor, $\dot{m}_2$ $(= \dot{m}_1 + \dot{m}_f)$ is the exhaust mass flow rate (kg/s) through the turbine, $\dot{m}_f$ is the fuel mass flow rate (kg/s) and C_p is the specific heat of air at constant pressure (kJ/kg.K).

In an ideal cycle, the working fluid is assumed to be air with a constant C_p that does not vary with temperature or with the composition changing after combustion. This is clearly invalid assumption and the real C_p needs to be used for a real cycle with C_p varying with temperature and composition (i.e. different in the turbine expansion than in the air compression). In an air standard cycle $\dot{m}_1 = \dot{m}_2$ as the air is assumed to be heated by a process that does not increase the mass. With this assumption of the ideal cycle, the C_p and mass terms all cancel out of the η_i equation. This yields Equation 2:

$$\eta_i = 1 - \left[\frac{\left(T_4 - T_1\right)}{\left(T_3 - T_2\right)}\right] \qquad (2)$$

In an ideal cycle $T_4/T_3 = T_1/T_2$; and it may be shown that η_i of a simple gas turbine is given by Equation 3 (from the law of adiabatic compression).

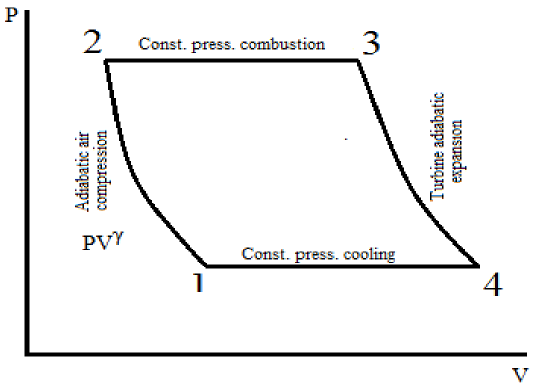

Figure A.1: The pressure-volume, PV-diagram

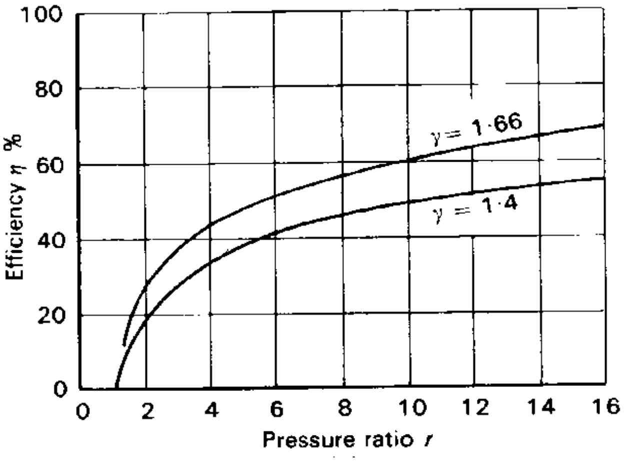

Figure A.2: Gas turbine efficiency versus pressure ratio

$$\eta_i = 1-(T_1/T_2) = 1-(T_4/T_3) = 1-(P_1/P_2)^{\gamma-1/\gamma} = 1-(P_4/P_3)^{\gamma-1/\gamma} \tag{3}$$

Where $\gamma = C_p/C_v$, and C_v is the specific heats at constant volume.

Figure A.2 shows the relation between efficiency and pressure ratio when the working fluid is air ($\gamma = 1.4$). Note that $\gamma = 1.66$ is for helium and this fluid is used in closed cycle gas turbines with a nuclear heat source instead of a combustor.

The consequences of the above ideal equation are:

1. High pressure ratio compressor increase P_2 and T_2 and this increases the thermal efficiency.
2. The thermal efficiency is maximised at the highest T_3 or combustion firing temperature.

This would be the stoichiometric flame temperature but no one can make a turbine blade that will not melt at these temperatures. In reality therefore the progress in the development of gas turbine thermal efficiency has been closely allied with high temperature materials development and with turbine blade cooling techniques. Today the maximum T_3 is 1500°C in an industrial gas turbine (the general electric (GE), H class). In 1950 this was of the order of 800^{o}C.

A.2 Real Thermodynamics Properties

Considering the ideal efficiency equation of Equation 1 above, it is not correct to take all the C_p and mass values as the same and then cancel them out. In reality the C_p for air varies with temperature and the turbine gas flow is the products of combustion (CO_2, H_2O, N_2, and O_2) and this mixture has a different C_p than that of air.

$$\eta_i = \frac{\{\dot{m}_2(C_{p3}T_3 - C_{p4}T_4) - \dot{m}_1(C_{p2}T_2 - C_{p1}T_1)\}}{\dot{m}_2(C_{p3}T_3 - C_{p2}T_2)} \tag{4}$$

At each temperature condition the appropriate specific heat at constant pressure should be used to calculate the accurate ideal efficiency. Also the calculation of pressure and temperature requires the value of γ and this varies with T_3 and composition. C_p is a function of T_3 and Composition in terms of fuel air ratio (F/A). Note the equivalence ratio $\Phi = 1$ for an air fuel ratio A/F = 14.6 and F/A = 0.068. The maximum possible T_3 at ~ 0.07 and gas turbine operate at ~ F/A = 0.025. An example of 700K inlet T_2 implies 1750K T_3 maximum power with a temperature difference ΔT of 1050K, F/A = 0.0324, A/F = 30.9 and $\Phi = 0.47$. T_3 is controlled by the F/A and higher F/A means higher T_3. The real thermodynamics performance properties are found in the work walsh and Fletcher, (2004).

A.3 Gas Turbine Power

Power = work done/second = Force × distance/second = Pressure × Area × Velocity = PAU

Now AU is the volume flow rate $\dot{V} = \dot{m}/\rho$ and $\rho = P/RT$, where $\dot{m}$ is gas mass flow rate (kg/s), ρ is the density (kg/m^3), P is the pressure (Pa) and R is Gas Constant = R_u/MW (R = 287 J/kg.K for air and kerosene combustion products, but for natural gas products is ~292).

Power = $P\dot{m}/\rho$ = $P\dot{m}RT/P$ = $\dot{m}RT$. Maximum available power is at the maximum T and hence maximum power available is given by Equation 5 below;

$$P = \dot{m}RT_3 \quad = \quad 287\dot{m}T_3 \tag{5}$$

Specific Power = Power/mass flow rate = constant × maximum temperature = $287T_3$

A.4 Gas Turbine Compressor and Turbine Efficiencies

The ideal cycle assumes that there are no aerodynamics flow pressure losses in the air flow through the compressor or in the hot gas expansion through the turbine. This is not valid due to aerodynamics pressure losses due to flow friction and gas leakage at the rotor tip seals.

The compressor and turbine flow is then not ideal and their efficiencies are defined as their deviation from the ideal cycle condition.

In the ideal air standard cycle the following temperature and pressure relationships apply under adiabatic conditions: $(T_2/T_1) = (P_2/P_1)^{\gamma-1/\gamma}$. The magnitude of the non-ideal non-adiabatic performance can be measured on a gas turbine by the fact that this equality does not apply and to quantify the difference. Flow friction losses over the blades and air leakages passed the compressor and turbine blade tips results in a non-ideal performance. Extra energy has to be fed into the flow air by the compressor to maintain the exit flow at the required pressure. This additional energy increases the delivery temperature T_2 above the value given by the adiabatic ideal relationship.

The magnitude of the non-ideal performance of the compressor is quantified by the term compressor efficiency η_c. The work done by the compressor is given by Equation 6 below:

$$\text{Compressor Work} = \dot{m}C_p(T_2 - T_1) = \dot{m}C_pT_1(T_2/T_1 - 1) = \dot{m}C_pT_1\left\{(P_2/P_1)^{(\gamma-1)/\gamma} - 1\right\} \qquad (6)$$

The work done by the compressor is controlled by the $(T_2/T_1 - 1)$ term and if the compressor had an ideal performance then the temperature ratio and pressure ratio based work done would be the same, but the compressor outlet temperature is higher than it should be due flow losses and compressor leakage. The compressor efficiency η_c is a measure of the difference in the ideal to actual compressor work given by Equation 7.

$$\eta_c = \frac{\mathit{Ideal\ Compressor\ Work}}{\mathit{Actual\ Compressor\ Work}} = \frac{(P_2/P_1)^{(\gamma-1)/\gamma} - 1}{(T_2/T_1) - 1} \qquad (7)$$

The compressor inefficiencies increase the outlet air temperature. This air is the combustor and turbine blade coolant, so compressor inefficiencies make GT wall cooling less efficient.

In a turbine blade flow friction and blade tip leakage losses result in a non-ideal performance. Thus less energy is extracted from the exhaust gases to achieve the desired pressure drop, this increases T_4 above the ideal value. Turbine work and efficiency η_T are given by Equations 8 and 9 below:

$$\text{Turbine work} = \dot{m}C_p(T_3 - T_4) = \dot{m}C_pT_3(1 - T_4/T_3) \qquad (8)$$

$$\eta_T = \frac{(1 - T_4/T_3)}{(1 - P_4/P_3)^{(\gamma-1)/\gamma}} \qquad (9)$$

It was found that for a range of pressure ratio of a particular application, η_c tends to decrease and η_T to increase as the pressure ratio for which the compressor and turbine are designed increases based on the overall efficiencies [38].

Once the these measured air properties are correctly fixed, the plenum inlet velocity V_i and the air jet velocity V_j for a fixed mass flux G (kg/sm^{2}bar) will be calculated correctly and this predict correctly the flow-maldistribution as well as the pressure loss $\Delta P/P$.

Appendix B

Combustion Duct Heat Transfer Coefficient

Calculations:

Theoretical estimation of temperature drop on the impingement target plate

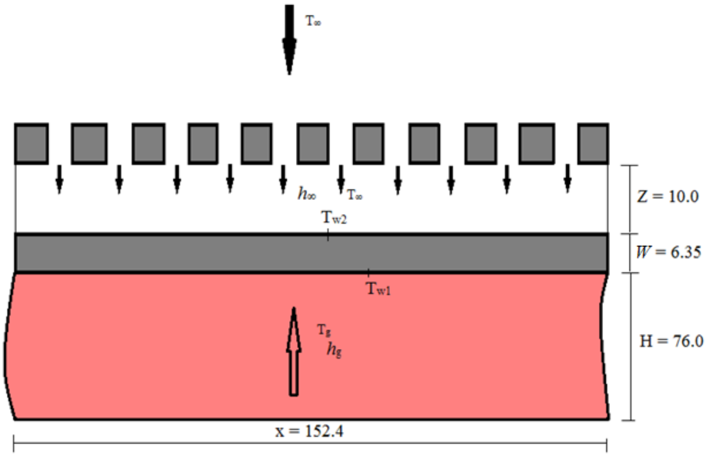

Red ⇒ Combustion Duct and Gray ⇒ Metal Wall

Figure B.1: Impingement cooling heat transfer using high temperature experimental rig

From Figure 1.B, heat transfer from combustion duct to the target plate is by convection

$$q'' = h_g\left(T_g - T_{w1}\right) \tag{1}$$

Heat transfer through the target plate is by conduction

$$q'' = \frac{k_s}{W}\left(T_{w1} - T_{w2}\right) \tag{2}$$

Heat transfer on the target plate in the impingement gap is by convection

$$q'' = h_\infty\left(T_{w2} - T_\infty\right) \tag{3}$$

Correlating between Equations 1, 2 and 3 gives:

$$q'' = \frac{T_g - T_\infty}{\dfrac{1}{h_g} + \dfrac{W}{k_s} + \dfrac{1}{h_\infty}} \tag{4}$$

Or
$$q'' = \frac{T_g - T_{w1}}{\frac{1}{h_g}} = \frac{T_{w1} - T_{w2}}{\frac{W}{k_s}} = \frac{T_{w2} - T_\infty}{\frac{1}{h_\infty}} \tag{5}$$

Correlating between Equations 4 and 5 to solve for T_{w2} gives:

$$q'' = \frac{T_g - T_{w2}}{\frac{1}{h_g} + \frac{W}{k_s}} = \frac{T_g - T_\infty}{\frac{1}{h_1} + \frac{W}{k_s} + \frac{1}{h_\infty}} \tag{6}$$

Solving Equation 6 gives the cooling effectiveness η below:

$$\eta = \frac{T_g - T_{w2}}{T_g - T_\infty} = \frac{\frac{1}{h_g} + \frac{W}{k_s}}{\frac{1}{h_1} + \frac{W}{k_s} + \frac{1}{h_g}} = \frac{1+\beta}{1+\beta+\alpha} \tag{7}$$

$$T_{w2} = T_g - \left\{ \frac{1+\beta}{1+\beta+\alpha} \left(T_g - T_\infty\right) \right\} \tag{8}$$

Correlating between Equations 4 and 5 to solve for T_{w1} gives:

$$\frac{T_g - T_{w1}}{T_g - T_\infty} = \frac{\frac{1}{h_g}}{\frac{1}{h_1} + \frac{W}{k_s} + \frac{1}{h_\infty}} = \frac{1}{1+\beta+\alpha} \tag{9}$$

$$T_{w1} = T_g - \left\{ \frac{1}{1+\beta+\alpha} \left(T_g - T_\infty\right) \right\} \tag{10}$$

$$\Rightarrow \beta = \frac{h_g W}{k_s} = \frac{h_\infty W}{k_s} \tag{11}$$

While, $$\alpha = \frac{h_g}{h_\infty} \tag{12}$$

Evaluating the heat transfer coefficient in the combustion duct using the Dittus-Boelter equation for heating based on the calculated hydraulic diameter D_H = 0.1014 m and properties of fluid at gas (air) temperature T_g = 775 K, given flow velocity V = 27 m/s gives:

$$\mathrm{Re} = \frac{V_m D_h}{\nu} = \frac{27 \times 0.1014}{7.824 \times 10^{-5}} = 34992$$

$$Nu = \frac{h_g D_h}{k_f} = 0.029(\mathrm{Re})^{0.8}(\mathrm{Pr})^{0.4}$$

$$Nu = 0.029(34992)^{0.8}(0.688)^{0.4} = 108$$

$$h_g = \frac{Nu \times k_f}{D_h} = \frac{108 \times 0.05648}{0.1014} = 60.04 \text{ W/m}^2\text{K}$$

Using the relations of jet flow and cross-flow velocities V_j and V_c along the hole and in the impingement gap (Andrews and Hussain, 1987), the velocities are calculated at G = 1.928 kg/sm^{2}bar (or at plenum inlet velocity V_i = 1.57 m/s), X = 15.24 mm and D = 3.27 × 10^{-3} m (or X/D = 4.66) as shown below:

$$V_j = \frac{4G}{\pi\rho}\left(\frac{X}{D}\right)^2 = \frac{4V_i}{\pi}\left(\frac{X}{D}\right)^2 = \frac{4 \times 1.57}{\pi}\left(\frac{0.01524}{3.27 \times 10^{-3}}\right)^2 = 43.4 \text{ m/s}$$

$$V_c = \frac{NV_j}{ZX}\left(\frac{\pi}{4}\right)D^2 = \frac{10 \times 43.4}{0.01 \times 0.01524}\left(\frac{\pi}{4}\right) \times \left(3.27 \times 10^{-3}\right)^2 = 23.9 \text{ m/s}$$

Evaluating the HTC *h* in the impingement gap using the Colburn equation for cooling based on the calculated hydraulic diameter D_H = 0.0188 m and properties of fluid (Appendix C) at the air temperature T_∞ = 288 K for the calculated cross-flow velocity V_c = 23.9 m/s gives:

$$\text{Re} = \frac{V_c D_h}{\nu} = \frac{23.9 \times 0.0188}{1.46 \times 10^{-5}} = 30749$$

$$Nu = \frac{h_\infty D_h}{k_f} = 0.029(\text{Re})^{0.8}(\text{Pr})^{0.3}$$

$$Nu = 0.029(30749)^{0.8}(0.69)^{0.3} = 100.9$$

$$h_\infty = h_{\min} = \frac{Nu \times k_f}{D_h} = \frac{100.9 \times 0.02529}{0.0188} = 135.7 \text{ W/m}^2\text{K}$$

Evaluating the HTC *h* in the impingement hole using the Colburn equation for cooling based on the hole diameter *D* = 3.27 × 10^{-3} m and properties of fluid (Appendix C) at air temperature T_∞= 288K for the calculated jet flow velocity V_j = 43.4m/s gives:

$$\text{Re} = \frac{V_j D}{\nu} = \frac{43.4 \times 0.00327}{1.46 \times 10^{-5}} = 9720 \approx 10^4$$

$$Nu = 0.029(9720)^{0.8}(0.69)^{0.3} = 39.8$$

$$h_\infty = h_{\max} = \frac{Nu \times k_f}{D} = \frac{39.8 \times 0.02529}{3.27 \times 10^{-3}} = 307.4 \text{ W/m}^2\text{K}$$

$$135 \le h_\infty \le 307.4 \text{W/m}^2\text{K}$$

Using Equations 11 and 12, the maximum and minimum values of the Biot number β and gas and fluid HTC's h ratio α are evaluated below and these are shown in Figure B.2, which shows the significances of using lower β to achieve optimum cooling heat transfer.

$$0.07 \le \beta \le 0.17$$

$$0.19 \le \alpha \le 0.44$$

Hence, the cooling target wall temperatures at minimum and maximum values are evaluated using Equation (8) and Equation (10) and is valid when heating temperature is required.

$$356 \le T_{w2} \le 430$$

$$\Rightarrow 0.71 \le \eta \le 0.86$$

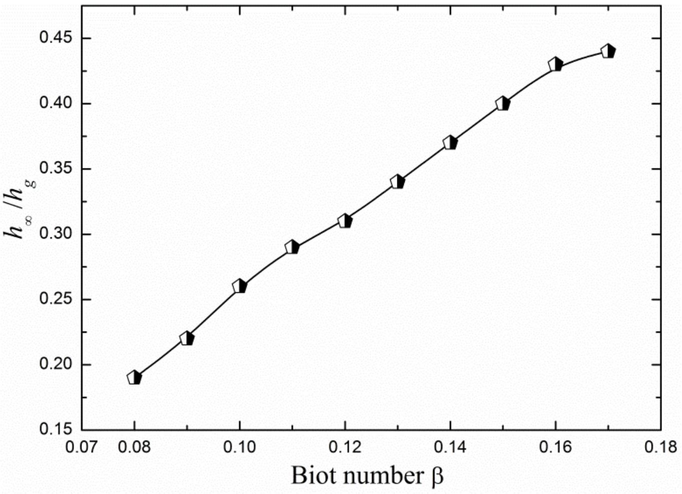

Figure B.2: Relationship between the Biot number and HTC *h* ratio

Appendix C
Air Properties

The specific measured properties of air that have been usually applied in the experimental air jet heat transfer cooling of gas turbine combustor and turbine blades (***), are found to be dependent on the compressor outlet temperature. But occasionally, experimentalist calculates the air properties at either sea level or room temperatures as 15^{o}C (288.15K) or 25^{o}C (298.15K) respectively. These major air properties for constant incompressible flow includes: Kinematic viscosity ν (= μ/ρ) where μ (kg/ms) and ρ (kg/m^3) are the dynamic viscosity and density (m^2/s), the specific heat capacity at constant pressure C_p (J/kgK), thermal conductivity k (W/mK), dimensionless Prandtl number Pr and the air density ρ (kg/m^3). For the purpose of the present conjugate heat transfer (CHT) computational fluid dynamics (CFD) analysis these properties are customised in the ANSYS Fluent commercial software and are fixed (Cengel and Cimbala) as follows:

Air properties at 15^{o}C or 288.15K

$\nu = 1.47 \times 10^{-5}$ m^2/s

$\mu = 1.802 \times 10^{-5}$ kg/ms

C_p = 1007 J/kgK

k = 0.02476 W/mK

Pr = 0.7323

ρ = 1.225 kg/m^3

Air properties at 25^{o}C or 298.15K

$\nu = 1.562 \times 10^{-5}$ m^2/s

$\mu = 1.849 \times 10^{-5}$ kg/ms

C_p = 1007 J/kgK

k = 0.02551 W/mK

Pr = 0.7296

ρ = 1.184 kg/m^3

Once the these measured air properties are correctly fixed, the plenum inlet velocity V_i and the air jet velocity V_j for a fixed mass flux G (kg/sm^{2}bar) will be calculated correctly and this predict correctly the flow-maldistribution as well as the pressure loss $\Delta P/P$.

List of References

[1] Brooks F. J. 2010. "GE Gas Turbine Performance Characteristics". *GE Power Systems,* GER-3567H**,** 1 - 16.

[2] Walsh P. P. and Fletcher P. 2004. "Gas Turbine Performance (Second Edition)". *Backwell Science Ltd., Oxford, UK.*

[3] Andrews G. E. and Hussain C. I. 1984. "Impingement Cooling of Gas Turbine Components". *High Temperature Technology,* 2 (2)**,** 99 - 106.

[4] Al Dabagh A. M., Andrews G. E., Abdul Husain R. A. A., Husain C. I., Nazari A. and Wu J. 1990. "Impingement/ Effusion Cooling: The Influence of Number of Impingement Holes and Pressure Loss on the Heat Transfer Coefficient". *Trans. ASME J. Turbomachinery,* 112**,** 467 - 476.

[5] Abdul Husain R. A. A. and Andrews G. E. 1990. "Full Coverage Impingement Heat Transfer at High Temperature". *Proc. ASME Int. Gas Turbine & Aeroengine Congress & Eposition,* 90-GT-285**,** 1 - 12.

[6] Cho H. H., Rhee D. H. and Goldstein, R. J. 2008. " Effects of Hole Arrangements on Local Heat/Mass Transfer for Impingement/Effusion Cooling With Small Hole Spacing". *Trans. ASME J. Turbomachinery,* 130**,** 1 - 11.

[7] Hollworth, B. R., Lehmann, G. and Rosiczkowski, J. 1983. "Arrays of Impinging Jets with Spent Fluid Removal Through Vent Holes on the Target Surface, Part 2: Local Heat transfer". *Trans. ASME J. Eng. Power,* 105**,** 393 - 402.

[8] Horlock J. H., Watson D. T. and Jones T. V. 2001. "Limitations on Gas Turbine Performance Imposed by Large Turbine Cooling Flows". *Trans. ASME J. Eng. Gas Turbines and Power,* 123**,** 487 - 494.

[9] Huitenga H. and Norster E. R. 2014. "Development Approach to the Dry Low Emission Combustion System of MAN Diesel & Turbo Gas Turbines". *Proc. ASME Turbo Expo,* GT-25164**,** 1 - 10.

[10] Ito E., Okada I., Tsukagoshi K., Muyama A. and Masada J. 2009. "Development of Key Technologies for the Next Generation 1700 C-Class Gas Turbine". *Proc. ASME Turbo Expo,* GT-59783**,** 1 - 11.

[11] Arthur H. L. and Dilip R. B. 2010. "*Gas Turbine Combustion (Third Edition): Alternative Fuels and Emissions,"* New York, CRC Press, Taylor and Francis Group.

[12] Byerley A. R., Jones T. V. and Ireland P. T. 1992. "Internal Cooling Passage Heat Transfer Near the Entrance to a Film Cooling Hole: Experimental and Computational Results". *Proc. ASME Int. Gas Turbine & Aeroengine Congress & Exhibition,* 92-GT-241**,** 969 - 986.

[13] Gillespie D. R. H., Byerley A. R., Ireland P. T., Wang Z., Jones T. V. and Kohler S. T. 1996. "Detailed Measurements of Local Heat Transfer Coefficient in the Entrance to Normal and Inclined Film Cooling Holes". *Trans. ASME J. Turbomachinery,* 118**,** 285 - 290.

[14] Goldstein R. J., Cho H. H. and Jabbari M. Y. 1997. "Effect of Plenum Cross-Flow on Heat (Mass) Transfer Near and Within the Entrance of Film Cooling Holes". *Trans. ASME J. Turbomachinery,* 119**,** 761 - 769.

[15] Ito S., Goldstein R. J. and Eckert E. R. G. 1978. "Film Cooling of a Gas Turbine Blade". *Trans. ASME J. Eng. for Power,* 100**,** 476 - 481.

[16] Metzger D. E. and Bunker R. S. 1990. "Local Heat Transfer in Internally Cooled Turbine Airfoil Leading Edge Regions: Part II - Impingement Cooling With Film Coolant Extraction". *Trans. ASME J. Turbomachinery,* 112**,** 459 - 466.

[17] Andrews G. E., Alikhanizadeh M., Asere A. A., Hussain C. I., Koshkbar Azari M. S. and Mpadi M. C. 1986. "Small Diameter Film Cooling Holes: Wall Convective Heat Transfer". *Trans. ASME J. Turbomachinery,* 108**,** 283 - 289.

[18] Andrews G. E., Alikhanizadeh M., Bazdidi-Tehrani F., Hussain C. I. and Koshkbar Azari M. S. 1988. "Small Diameter Film Cooling Holes: The Influence of Hole Size and Pitch". *Freund Int. J. Turbo and Jet Engines,* 5**,** 61 - 71.

[19] Andrews G. E., Asere A. A., Hussain C. I. and Mkpadi M. C. 1985. "Transpiration and Impingement/Effusion Cooling of Gas Turbine Combustion Chambers". *ISABE and AIAA 7th Propulsion Joint Specialist Conference,* ISABE 85-7095**,** 794 - 803.

[20] Andrews G. E. and Hussain C. I. 1987. "Full Coverage Impingement Heat Transfer: The Influence of Cross-Flow". *AIAA/SAE/ASME/ASEE 23rd Joint Propulsion Conference,* AIAA-87-2010**,** 1 - 9.

[21] Andrews G. E. and Hussain C. I. 1984. "Full Coverage Impingement Heat Transfer: The Influence of Impingement Jet Size". *1st UK National Heat Transfer Conference, IChemE Symposium,* Series No.86**,** 1115 - 1124.

[22] El-jummah A. M., Abdul Hussain R. A. A., Andrews G. E. and Staggs J. E. J. 2014. "Conjugate Heat Transfer CFD Predictions of Impingement Heat Transfer: Influence of the Number of Holes for a Constant Pitch to Diameter Ratio X/D". *Proc. ASME Gas Turbine Conference,* GT-25268**,** 1 - 14.

[23] Andrews G. E., Asere A. A., Hussain C. I., Mkpadi M. C. and Nazari A. 1988. "Impingement/Effusion Cooling: Overall Wall Heat Transfer". *Proc. ASME Int. Gas Turbine and Aeroengine Congress,* 88-GT-290**,** 1 - 9.

[24] Gladden H. J. and Simoneau R. J. 1988. "Review and Assessment of the Database and Numerical Modelling for Turbine Heat Transfer". *Proc. ASME Turbo Expo,* 2.

[25] El-jummah A. M., Abdul Hussain R. A. A., Andrews G. E. and Staggs J. E. J. 2014. "Conjugate Heat Transfer Computational Fluid Dynamic Predictions of Impingement Heat Transfer: The Influence of Hole Pitch to Diameter Ratio X/D at Constant Impingement Gap Z". *Trans. ASME J. Turbomachinery,* 136 (12)**,** 1 - 16.

[26] Sheffler K. D. and Gupta D. K. 1988. "Current Status and Future Trends in Turbine Application of Thermal Barrier Coatings". *Trans. ASME J. Eng. Gas Turbine and Power,* 110**,** 605 - 609.

[27] Padture N. P., Gell M. and Jordan E. H. 2002. "Thermal Barrier Coatings for Gas-Turbine Engine Applications". *Science AAAS J. Review: Materials Science,* 296**,** 280 - 284.

[28] Schilke P. W. 2004. "Advanced Gas Turbine Materials and Coatings". *General Electric Company GE Energy,* GER-3569G [08/04]**,** 1 - 25.

[29] Smith K. O. 1984. "Internal Heat Transfer Characteristics of Silicon Carbide Heat Exchanger Tubes". *Trans. ASME J. Heat Transfer: Technical Brief,* 106**,** 672 - 674.

[30] Kano K., Matsuzaki H., Aoyama K., Aoki S. and Mandai S. 1991. "Development Study of 1500^{O}C Class High Temperature Gas Turbine". *Proc. ASME Int. Gas Turbine & Aeroengine Congress and Exposition,* 91-GT-297**,** 1 - 5.

[31] Pollock T. M. and Tin S. 2006. "Nickel-Based Superalloys for Advanced Turbine Engines: Chemistry, Microstructure and Properties". *AIAA J. Propulsion and Power,* 22 (2)**,** 361 - 374.

[32] El-jummah, A. M., Andrews, G. E. and Staggs, J. E. J. 2013. "Conjugate Heat Transfer CFD Predictions of Impingement Jet Array Flat Wall Cooling Aerodynamics with Single Sided Flow Exit". *Proc. ASME Turbo Expo Conference,* GT-95343**,** 1 - 12.

[33] El-jummah, A. M., Andrews, G. E. and Staggs, J. E. J. 2013. "Conjugate Heat Transfer CFD Predictions of the Influence of the Impingement Gap on the Effect of Cross-Flow". *Proc. ASME Heat Transfer Conference,* HT-17180**,** 1 - 12.

[34] Abdul Husain, R. A. A., Andrews, G. E., Asere, A. A. and Ndiema, C. K. W. 1988. "Full Coverage Impingement Heat Transfer: Cooling Effectiveness". *ASME Int. Gas Turbine Conference,* Paper No.88-GT-270**,** pp.1 - 9.

[35] Trabold T. A. and Obot N. T. 1987. "Impingement Heat Transfer Within Arrays of Circular Jets: Part II - Efects of Cross-Flow in the Presence of Roughness Elements". *Trans. ASME J. Turbomachinery*, 109**,** 594 - 601.

[36] Andrews G. E. and Kim M. N. 2001. "The Influence of Film Cooling on Emissions of a Low NOx Radial Swirler Gas Turbine Combustor". *ASME Int. Gas Turbine & Aeroengine Congress & Exhibition,* GT-71**,** 1 - 11.

[37] Alkabie H. S. and Andrews G. E. 1989. "Ultra Low NOx Emissions for Gas and Liquid Fuels Using Radial Swirlers". *Proc. ASME Gas Turbine and Aeroengine Congress and Exposition,* 89-GT-322**,** 1 - 10.

[38] Saravanamuttoo H. I. H., Rogers G. F. C. and Cohen H. 2001. "Gas Turbine Theory (Fifth Edition)". *Pearson, Prentice Hall Inc.*

[39] Andrews, G. E. and Khalifa, I. M. 2007. "Planar Duct Heat Transfer with Turbulence Enhancing Obstacles for Combustor Liner External Cooling". *Proceeding of ASME,* GT2007-27418, pp.1-10

[40] Cerri G., Giovannelli A., Battisti L. and Fedrizzi R. 2007. "Advances in Effusive Cooling Techniques of Gas Turbines". *Elsevier J. Applied Thermal Engineering,* 27**,** 692 - 698.

[41] Nazari A. 1991. "*The Impingement/Effusion Cooling of Gas Turbine Combustor Walls". PhD Thesis, University of Leeds.

[42] Cengel Y. A. and Cimbala J. M. 2010. "*Fluid Mechanics: Fundamentals and Application (Second Edition in SI Units),"* McGraw-Hill Co., Int. NY.

[43] Abdul Husain R. A. A., Andrews G. E., Asere A. A. and Ndiema C. K. W. 1988. "Full Coverage Impingement Heat Transfer: Cooling Effectiveness". *Proc. ASME Int. Gas Turbine & Aeroengine Congress,* 88-GT-270**,** 1 - 9.

[44] Andrews G. E. and Nazari, A. 1999. "Impingement/Effusion Cooling: Influence of Number of Holes on the Cooling Effectiveness for an Impingement X/D of 10.5 and

Effusion X/D of 7.0". *Proc. GTSJ Int. Gas Turbine Congress,* Vol. II, IGTC TS-51**,** 639 - 646.

[45] Andrews G. E., Durance J., Hussain C. I. and Ojobor S. N. 1987. "Full Coverage Impingement Heat Transfer: Influence of the Number of Holes". *Trans. ASME J. Turbomachinery,* 109**,** 557 - 563.

[46] El-jummah, A. M., Abdul Hussain R. A. A., Andrews G. E. and Staggs J. E. J. 2013. "Conjugate Heat Transfer CFD Predictions of the Surface Averaged Impingement Heat Transfer Coefficients for Impingement Cooling with Backside Cross-flow". *Proc. ASME IMECE Conference,* IMECE-63580**,** 1 - 14.

[47] Obot N. T. and Trabold T. A. 1987. "Impingement Heat Transfer within Arrays of Circular Jets: Part 1-Efects of Minimum, Intermediate and Complete Cross-Flow for Small and Large Spacings". *Trans. ASME J. Heat Transfer,* 109**,** 872 - 879.

[48] Incropera, F. P., Dewitt, D. P., Bergman, T. L. and Lavine, A. S. 2007. "*Fundamentals of Heat and Mass Transfer,"* Hoboken, USA, John Wiley & Sons.

[49] Mills, A. F. 1999. "*Basic Heat and Mass Transfer,"* New Jersey, USA, Prentice Hall.

[50] Goldstein R. J. 1971. "Film Cooling". *Advances in Heat Transfer, Academic Press, New York and London,* 7**,** 321 - 379.

[51] Wilson D. G. and Pope J. A. 1954. "Convective Heat Transfer to Gas Turbine Blade Surfaces". *Proc. IMechE,* 168 (36)**,** 861 - 874.

[52] Sparrow E. M. 1965. "Radiation Heat Transfer Between Surfaces". *Advances in Heat Transfer, Academic Press, New York and London,* 2**,** 399 - 452.

[53] Eckert E. R. G., Sparrow E. M., Goldstein R. J., Pfender E., Patankar S. V., Ramsey J. W. and Teichman K. Y. 1981. "Heat Transfer – A Review of 1979 Literature". *Pergamon Int. J. Heat Mass Transfer,* 24**,** 1 - 34.

[54] Kays W. M. 1994. "Turbulent Prandtl Number - Where Are We?". *Trans. ASME J. Heat Transfer,* 116**,** 284 - 295.

[55] Gustafsson K. M. B. and Johansson T. G. 2001. "An Experimental Study of Surface Temperature Distribution on Effusion-Cooled Plates". *Trans. ASME J. Eng. Gas Turbines and Power,* 123**,** 308 - 316.

[56] Chance J. L. 1974. "Experimental Investigation of Air Impingement Heat Transfer Under an Array of Round Jets". *Tappi,* 57 (6)**,** 108 - 112.

[57] Kercher D. M. and Tabakoff W. 1970. "Heat Transfer by a Square Array of Round Air Jets Impinging Perpendicular to a Flat Surface Including Effect of Spent Air". *Trans. ASME J. Eng. Power***,** 73 - 82.

[58] Janbunathan K., Lai E., Moss M. A. and Button B. L. 1992. "A Review of Heat Transfer Data for Single Circular Jet Impingement". *Elsevier Int. J. Heat and Fluid Flow,* 13 (2)**,** 106 - 115.

[59] Kumada M. and Mabuchi I. 1970. "Studies on the Heat Transfer of Impinging Jet (1st Report, Mass Transfer for Two-Dimensional Jet of Air impinging Normally on a Flat Plate)". *Bulletin of the JSME,* 13 (55)**,** 77 - 85.

[60] Chupp R. E., Helms H. E., McFadden P. W. and Brown T. R. 1968. "Evaluation of Internal Heat Transfer Coefficients for Impingement Cooled Turbine Airfoils". *AIAA 4th Propulsion Joint Specialist Conference,* Paper No. 68-564**,** 1 - 7.

[61] Andrews G. E., Asere A. A., Hussain C. I. and Mkpadi M. C. 1985. "Full Coverage Impingement Heat Transfer: The Variation in Pitch to Diameter Ratio at a Constant Gap". *Proportion and Energetics Panel of AGARD, 65th Symposium, 'Heat Transfer and Cooling in Gas Turbines',* Paper 26**,** 1 - 12.

[62] Andrews G. E. and Hussain C. I. 1984. "Impingement Cooling Using Large Arrays of Holes". *IChemE 11th Annual Research Meeting***,** 86 - 91.

[63] Hollworth B. R. and Berry R. D. 1978. "Heat Transfer from Arrays of Impinging Jets with Large Jet-to-Jet Spacing". *Trans. ASME J. Heat Transfer,* 100**,** 352 - 357.

[64] Hollworth B. R. and Cole G. H. 1987. "Heat Transfer to Arrays of Impinging Jets in a Cross-Flow". *Trans. ASME J. Heat Transfer,* 109**,** 564 - 571.

[65] Hilgeroth S. J. 1965. "Heat Transfer in Jet Flow Perpendicular to the Transfer Surface". *Chem. Ing. Tech.,* 37 (12)**,** 1264 - 1272.

[66] Friedman S.J. and Mueller A.C. 1951. "Heat Transfer to flat surfaces ". *Proc. IMechE: General Discussions on Heat Transfer***,** 138 - 142.

[67] Gauntner J. W., Gladden H. J., Gauntner D. J. and Yeh F. C. 1974. "Cross-Flow Effects on Impingement Cooling of a Turbine Vane". *NASA,Langley* E-7768**,** 1 - 19.

[68] Freidman, S. J. and Mueller, A. C. 1951. Heat Transfer to Flat Surfaces. *ASME Proc. General Discussion on Heat Transfer. Inst. Mech. Engineers, pp.138-142.*

[69] Hollworth, B. R. and Berry, R. D. 1978. "Heat Transfer from Arrays of Impinging Jets with Large Jet-to-Jet Spacing". *ASME Paper No. 78-GT-117***,** 1-6.

[70] Andrews, G. E., Asere, A. A., Hussain, C. I. and Mkpadi, M. C. 1985. "Full Coverage Impingement Heat Transfer: The Variation in Pitch to Diameter Ratio at a Constant Gap". *Proportion and Energetics Panel of AGARD, 65th Symposium, 'Heat Transfer and Cooling in Gas Turbines',* Paper 26**,** 1-12.

[71] Lee J., Ren Z., Haegele J., Potts G., Jin J. S., Ligrani P., Fox M. D. and Moon H-K. 2013. "Effects of Jet-to-Target Plate Distance and Reynolds Number on Jet Array Impingement Heat Transfer". *Proc. ASME Turbo Expo,* GT-94651**,** 1 - 17.

[72] Terzis A., Cochet M., Wolfersdorf J., Weigand B. and Ott P. 2014. "Detailed Heat Transfer Distributions of Narrow Impingement Channels With Varying Jet Diameter". *Proc. ASME Turbo Expo,* GT-25910**,** 1 - 11.

[73] Ward Smith A. J. 1971. "Pressure Losses in Ducted Flows: A Unified Treatment of the Flow and Pressure Drop Characteristics of Constrictions Having Orifices With Square Edges". *Butterworths, London,* Part 4**,** 135 - 191.

[74] Lutum E. and Johnson B. V. 1998. "Influence of the Hole Length-to-Diameter Ratio on Film Cooling With Cylindrical Holes". *Proc. ASME Int. Gas Turbine & Aeroengine Congress & Exhibition,* 98-GT-10**,** 1 - 10.

[75] Bazdidi-Tehrani F. and Andrews G. E. 1994. "Full-Coverage Discrete Hole Film Cooling: Investigation of the Effect of Variable Density Ratio". *Trans. ASME J. Eng. Gas Turbine and Power,* 116**,** 587 - 596.

[76] Andrews G. E., Bazdidi-Tehrani F., Hussain C. I. and Pearson J. P. 1991. "Small Diameter Film Cooling Hole Heat Transfer: The Influence of the Hole Length". *Proc. ASME Int. Gas Turbine & Aeroengine Congress and Exposition,* 91-GT-344**,** 1 - 13.

[77] Sparrow E. M., Kang S. S. and Chuck W. 1987. " Relation between the Points of Flow reattachment and Maximum Heat Transfer for Regions of Flow Separation". 30 (7)**,** 1237 - 1246.

[78] Krall K. M. and Sparrow E. M. 1966. "Turbulent Heat Transfer in the Seperated, Reattached and Redevelopment Regions of a Circular Tube". *Trans. ASME J. Heat Transfer,* Paper No. 65-WA/HT-12**,** 131 - 136.

[79] Cho H. H., Jabbari M. Y. and Goldstein R. J. 1997. "Experimental Mass (Heat) Transfer in and Near a Circular Hole in a Flat Plate". *Elsevier Int. J. Heat Mass Transfer,* 40 (10)**,** 2431 - 2443.

[80] Cho H. H. and Goldstein R. J. 1997. "Total-Coverage Discrete Hole Wall Cooling". *Trans. ASME J. Turbomachinery,* 119**,** 320 - 329.

[81] Andrews G. E. and Hussain C. I. 1986. "Full Coverage Impingement Heat Transfer: Influence of Channel Height". *Proc. 8th International Heat Transfer Conference***,** 1205 - 1211.

[82] Andrews G. E. and Bazdidi-Tehrani F. 1989. "Small Diameter Film Cooling Hole Heat Transfer: The Influence of Number of Holes". *Proc. Int. Gas Turbine & Aeroengine Congress & Exhibition,* 89-GT-7**,** 1 - 11.

[83] Andrews G. E. and Mpadi M. C. 1984. "Full-Coverage Discrete Hole Wall Cooling: Discharge Coefficients". *Trans. ASME J. Eng. Gas Turbines and Power,* 106 183 - 192.

[84] Boelter L. M. K., Young G. and Iversen H. W. 1948. "An Investigation of Aircraft Heaters: XXVII - Distribution of Heat Transfer Rate in the Entrance Section of a Circular Tube". *Report by National Advisory Committee for Aeronautics* NACA TN No. 1451**,** 1 - 53.

[85] Mills A. F. 1962. "Experimental Investigation of Turbulent Heat Transfer in the Entrance Region of a Circular Conduit". *SAGE IMechE J. Mechanical Eng. Science,* 4 (1)**,** 63 - 77.

[86] Sparrow E. M. and Ortiz M. C. 1982. "Heat Transfer Coefficients for the Upstream Face of a Perforated Plate Positioned Normal to an Oncoming Flow". *Pergamon Int. J. Heat Mass Transfer,* 25 (1) 127 - 135.

[87] Sparrow E. M. and Chaboki A. 1984. "Swirl-Affected Turbulent Fluid Flow Heat Transfer in a Circular Tube". *Trans. ASME J. Heat Transfer,* 106**,** 766 - 773.

[88] Donohue G. L., Tiederman W. G. and Reischman M. M. 1972. "Flow Visualization of the Near-Wall Region in a Drag-Reducing Channel Flow". *Cambridge J. Fluid Mechanics,* 56, Part 3**,** 559 - 575.

[89] Hale C. A., Plesniak M. W. and Ramadhyani S. 2000. "Film Cooling Effectiveness for Short Film Cooling Holes Fed by a Narrow Plenum". *Trans. ASME J. Turbomachinery,* 122**,** 553 - 557.

[90] Metzger D. E. and Cordaro J. V. 1980. "Heat Transfer in Short Tubes Supplies from a Cross-Flowing Stream". *ASME Heat Transfer Div. Winter Annual Meeting, NY,* 79-WA/HT-16**,** 1 - 6.

[91] Van Treuren K. W., Wang Z., Ireland P. T. and Jones T. V. 1994. "Detailed Measurements of Local Heat Transfer Coefficient and Adiabatic Wall Temperature Beneath an Array of Impinging Jets". *Trans. ASME J. Turbomachinery,* 116**,** 369 - 374.

[92] Cho H. H., Jabbari M. Y. and Goldstein R. J. 1997. "Effect of Plenum Cross-flow on Heat (Mass) Transfer Near and Within Entrance of Film Cooling Holes". *Trans. ASME J. Turbomachinery,* 119**,** 761 - 769.

[93] Sparrow E. M. and Siegel R. 1960. "Unsteady Turbulent Heat Transfer in Tubes". *Trans. ASME J. Heat Transfer,* Paper No. 59-HT-16**,** 170 - 180.

[94] Baines W. D. and Peterson E. G. 1951. "An Investigation of Flow through Screens". *Trans. ASME Hydraulic Div,* Paper No.50-A-23**,** 467 - 480.

[95] Siegel R. and Sparrow E. M. 1959. "Turbulent Flow in a Circular Tube With Arbitrary Internal Heat Sources and Wall Heat Transfer". *Trans. ASME J. Heat Transfer,* Paper No. 59-SA-19**,** 280 - 290.

[96] Oguntade H. I., Andrews G. E., Burns A., Ingham D. and Pourkashanian M. 2011. "Predictions of Effusion Cooling with Conjugate Heat Transfer". *Proc. ASME Turbo Expo,* GT-45417**,** 1 - 11.

[97] Dann A. G., Thorpe S. J., Lewis L. V. and Ireland P. T. 2014. "Innovative Measurement Techniques for a Cooled Turbine Casing Operating at Engine Representative Thermal Conditions". *Proc. ASME Turbo Expo,* GT-26092**,** 1 - 12.

[98] Metzger D. E. and Korstad R. J. 1972. "Effects of Cross-Flow on Impingement Heat Transfer". *Trans. ASME J. Eng. Power,* Paper No. 71-GT-1**,** 35 - 41.

[99] Abdul Husain R. A. A. 1990. "*Impingement Cooling of Gas Turbine Components".* PhD Thesis, Department of Fuel and Energy, University of Leeds.

[100] Asere A. A. 1986. "*Gas Turbine Combustor Wall Cooling".* PhD Thesis, Department of Fuel and Energy, University of Leeds.

[101] Sparrow E. M. and Gurdal U. 1981. "Heat Transfer at an Upstream-Facing Surface Washed by Fluid En Route to an Aperture in the Surface". *Pergamon Int. J. Heat Mass Transfer,* 24 (5)**,** 851 - 857.

[102] Sparrow E. M., Altemani C. A. C. and Chaboki A. 1984. "Jet-Impingement Heat Transfer for Circular Jet Impinging in Cross-Flow on a Cylinder". *Trans. ASME J. Heat Transfer,* 106**,** 570 - 577.

[103] Sparrow E. M. and Lovell B. J. 1980. "Heat Transfer Characteristics of an Obliquely Impinging Circular Jet". *Trans. ASME J. Heat Transfer,* 102**,** 202 - 209.

[104] Koopman R. N. and Sparrow E. M. 1976. "Local and Average Heat Transfer Coefficients Due to an Impinging Row of Jets ". *Pergamon Int. J. Heat Mass Transfer,* 19**,** 673 - 683.

[105] Haring M. and Weigand B. 1995. "A New Analogy Function for the Naphthalene Sublimation Technique to Measure Heat Transfer Coefficients on Turbine Airfoils". *Proc. ASME Int. Gas Turbine & Aeroengine Congress & Eposition*, 95-GT-17**,** 1 - 8.

[106] Goldstein R. J. and Taylor J. R. 1982. "Mass Transfer in the Neighbourhood of Jets Entering a Cross-Flow". *Trans. ASME J. Heat Transfer,* 104**,** 715 - 721.

[107] Goldstein R. J. and Cho H. H. 1995. "A Review of Mass Transfer Measurements Using Naphthalene Sublimation". *Elsevier J. Experimental Thermal and Fluid Science,* 10**,** 416 - 434.

[108] Mendes P. R. S. 1991. "The Naphthalene Subblimation Technique". *Elsevier J. Thermal and Fluid Science,* 4**,** 510 - 523.

[109] Dyban E. P., Mazur A. I. and Golovanov V. P. 1980. "Heat Transfer and Hydrodynamics of an Array of Round Impinging Jets with One-sided Exhaust of the Spent Air". *Pergamon Int. J. Heat Mass Transfer,* 23**,** 667 - 676.

[110] Ireland, P. T. and Jones T. V. 2000. " Liquid Crystal Measurements of Heat Transfer and Surface Shear Stress". *IOP Science Meas. Sci. technology,* 11**,** 969 - 986.

[111] Wang Z., Ireland P. T. and Jones T. V. 1991. "A technique for Measuring Convective Heat Transfer at Rough Surfaces". *Trans. Inst. Measurement and Control,* 13 (3)**,** 145 - 154.

[112] Huber A. M. and Viskanta R. 1994. "Effect of Jet-Jet Spacing on Convective Heat Transfer to Confined, Impinging Arrays of Axisymmetric Air Jets". *Elsevier Int. J. Heat Mass Transfer,* 37 (18)**,** 2859 - 2869.

[113] Arcangeli L., Facchini B., Surace M. and Tarchi L. 2008. "Correlation Analysis of Effusion Cooling Systems". *Trans. ASME J. Turbomachinery,* 130**,** 1 - 7.

[114] Ireland, P. T. and Jones T. V. 1987. " The Response Time of a Surface Thermometer Employing Encapsulated Thermochromic Liquid Crystals". *IOP Science J. Phys. E: Sci. Instrum.,* 20**,** 1195 - 1199.

[115] Ireland P. T., Neely A. J., Gillespie D. R. H. and Robertson A. J. 1999. "Turbulent Heat Transfer Measurements using Liquid Crystals". *Elsevier. Int. J. Heat and Fluid Flow,* 20**,** 355 - 367.

[116] Ireland, P. T. and Jones T. V. 1986. " Detailed Measurement of Heat Transfer on and Around a Pedastal in Fully-Developed Channel Flow". *Proc. 8th Int. Heat Transfer Conference,* 20**,** 975 - 986.

[117] Byerley A. R., Ireland P. T., Jones T. V. and Graham C. G. 1988. "Detailed Heat Transfer Measurements Near the Entrance to an Inclined Film Cooling Hole Inside a Gas Turbine Blade". *Second UK National Conference on Heat Transfer (IMechE),* Paper No. C164/88**,** 1029 - 1040.

[118] Byerley A. R., Ireland P. T., Jones T. V. and Ashton S. A. 1988. "Detailed Heat Transfer Measurements Near and Within the Entrance of a Film Cooling Hole". *Proc. ASME Int. Gas Turbine & Aeroengine Congress & Exhibition,* 88-GT-155**,** 1 - 8.

[119] Tapinlis O., Choi M., Gillespie D. R. H., Lewis L. V. and Ciccomascolo C. 2014. "The Effect of Impingement Jet Heat Transfer on Casing Contraction in a Turbine Case Cooling System". *Proc. ASME Turbo Expo,* GT-26749**,** 1 - 11.

[120] Palafox P., Oldfield M. L. G., Ireland P. T., Jones T. V. and LaGraff J. E. 2012. "Blade Tip Heat Transfer and Aerodynamics in a Large Scale Turbine Cascade With Moving Endwall". *Trans. ASME J. Turbomachinery,* 134**,** 1 - 11.

[121] Bunker R. S., Bailey J. C. and Ameri A. A. 2000. "Heat Transfer and Flow on the First-Stage Blade Tip of a Power Generation Gas Turbine: Part 1-Experimental Results". *Trans. ASME J. Turbomachinery,* 122**,** 263 - 271.

[122] Bailey J. C., Intile J., Fric T. F., Tolpadi A. K., Nirmalan N. V. and Bunker R. S. 2003. "Experimental and Numerical Study of Heat Transfer in a Gas Turbine Combustor Liner". *Trans. ASME J. Eng. Gas Turbines and Power,* 125**,** 994 - 1002.

[123] Facchini B. and Surace M. 2006. "Impingement Cooling for Modern Combustors: Experimental Analysis of Heat Transfer and Effectiveness". *Springer J. Experiments in Fluids,* 40**,** 601 - 611.

[124] Baughn J. W. 1995. "Liquid Crystal Methods for Studying Turbulent Heat Transfer (Review)". *Elsevier Int. J. Heat and Fluid Flow,* 16**,** 365 - 375.

[125] Bunker R. S. and Metzger D. E. 1990. "Local Heat Transfer in Internally Cooled Turbine Airfoil Leading Edge Regions: Part I - Impingement Cooling Without Film Coolant Extraction". *Trans. ASME J. Turbomachinery,* 112**,** 451 - 458.

[126] Van Treuren K. W., Wang Z., Ireland P. T., Jones T. V. and Kohler S. T. 1994. "Local Heat Transfer Coefficient and Adiabatic Wall Temperature Measurement

Beneath Arrays of Staggered and Inline Impinging Jets". *Proc. ASME Int. Gas Turbine & Aeroengine Congress & Eposition*, 94-GT-181**,** 1 - 10.

[127] Chambers A. C., Gillespie D. R. H., Ireland P. T. and Dailey G. M. 2005. "The Effect of Initial Cross-flow on the Cooling Performance of Narrow Impingement Channel". *Trans. ASME J. Heat Transfer,* 127 358 - 365.

[128] Abu Talib A., Neely A. J., Ireland P. T. and Mullender A. J. 2004. " A Novel Liquid Crystal Image Processing Technique Using Multiple Gas Temperature Steps to Determine Heat Transfer Coefficient Distribution and Adiabatic Wall Temperature". *Trans. ASME J. Turbomachinery,* 126**,** 587 - 596.

[129] Wang L., Sunden B., Borg A. and Abrahamsson H. 2011. "Heat Transfer Characteristics of an Impingement Jet in Cross-Flow". *Trans. ASME J. Heat Transfer,* 133**,** 1 - 10.

[130] Chambers A. C., Gillespie D. R. H., Ireland P. T. and Dailey G. M. 2003. "A Novel Transient Liquid Crystal Technique to Determine Heat Transfer Coefficient Distributions and Adiabatic Wall Temperature in a Three-Temperature Problem". *Trans. ASME J. Turbomachinery,* 125**,** 538 - 546.

[131] Schueren S., Hoefler F., Wolfersdorf J. and Naik S. 2013. "Heat Transfer in an Oblique Jet Impingement Configuration With Varying Jet Geometries". *Trans. ASME J. Turbomachinery,* 135**,** 1 - 10.

[132] Bailey J. C. and Bunker R. S. 2002. "Local Heat Transfer and Flow Distributions for Impinging Jet Arrays of Dence and Sparse Extent.". *Proc. ASME Turbo Expo,* GT-30473**,** 1 - 10.

[133] Spring S., Xing Y. and Weigand B. 2012. "Experimental and Numerical Study of Heat Transfer from Arrays of Impinging Jets With Surface Ribs". *ASME J. Heat Transfer,* 134**,** 1 - 11.

[134] Xing Y. and Weigand B. 2013. "Optimum Jet-to-Plate Spacing of Inline Impingement Heat Transfer for Different Cross-Flow Schemes". *Trans. ASME J. Heat Transfer,* 135 1 - 8.

[135] Xing Y., Spring S. and Weigand B. 2010. "Experimental and Numerical Investigation of Heat Transfer Characteristics of Inline and Staggered Arrays of Impinging Jets". *Trans. ASME J. Heat Transfer,* 132**,** 1 - 11.

[136] Lamont J. A. and Ekkad S. V. 2011. "Effects of Rotation on Jet Impingement Channel Heat Transfer". *Proc. ASME Turbo Expo,* GT-45744**,** 1 - 10.

[137] Hoefler F., Schueren S., Wolfersdorf J. and Naik S. 2012. "Heat Transfer Characteristics of an Oblique Jet Impingement Configuration in a Passage With Ribbed Surfaces". *Trans. ASME J. Turbomachinery,* 134**,** 1 - 9.

[138] Wang Z., Ireland P. T. and Jones T. V. 1995. "Detailed Heat Transfer Coefficient Measurements and Thermal Analysis at Engine Conditions of a Pedestal With Fillet Radii". *Trans. ASME J. Turbomachinery,* 117**,** 290 - 297.

[139] Lee J. and Lee S-J. 2000. "The Effect of Nozzle Aspect Ratio on Stagnation Region Heat Transfer Characteristics of Elliptic Impinging Jet". *Elsevier Int. J. Heat and Mass Transfer,* 43**,** 555 - 575.

[140] Metzger D. E., Florschuetz L. W., Takeuchi D. I., Behee R. D. and Berry R. A. 1979. "Heat Transfer Characteristics for Inline and Staggered Arrays of Circular Jets With Cross-Flow of Spent Air". *Trans. ASME J. Heat Transfer,* 101**,** 526 - 531.

[141] Florschuetz L. W., Berry R. A. and Metzger D. E. 1980. "Periodic Streamwise Variations of Heat Transfer Coefficients for Inline and Staggered Arrays of Circular Jets With Cross-Flow of Spent Air". *Trans. ASME J. Heat Transfer,* 102**,** 132 - 137.

[142] Florschuetz L. W., Truman C. R. and Metzger D. E. 1981. "Streamwise Flow and Heat Transfer Distributions for Jet Array Impingement With Cross-Flow". *Trans. ASME J. Heat Transfer,* 103**,** 337 - 342.

[143] Florschuetz L. W., Metzger D. E. and Su C. C. 1984. "Heat Transfer Characteristics for Jet Array Impingement With Initial Cross-Flow". *ASME J. Heat Transfer,* 106**,** 34 - 41.

[144] Gardon R. and Akfirat J. C. 1966. "Heat Transfer Characteristics of Impinging Two-Dimensional Air Jets". *Trans. ASME J. Heat Transfer,* Paper No. 65-HT-20**,** 101 - 108.

[145] Taslim M. E. and Khanicheh A. 2006. "Experimental and Numerical Study of Impingement on an Airfoil Leading-Edge With and Without Showerhead and Gill Film Holes". *Trans. ASME J. Turbomachinery,* 128**,** 310 - 320.

[146] Taslim M. E. and Bethka D. 2009. "Experimental and Numerical Jet Impingement Heat Transfer in an Airfoil Leading-Edge Cooling Channel With Cross-Flow". *Trans. ASME J. Turbomachinery,* 131**,** 1 - 7.

[147] Hollworth B. R. and Wilson S. I. 1984. "Entrainment Effects on Impingement Heat Transfer: Part I - Measurements of Heated Jet Velocity and Temperature Distributions and Recovery Temperatures on Target Surface". *Trans. ASME J. Heat Transfer,* 106**,** 797 - 803.

[148] Hollworth B. R. and Gero L. R. 1985. "Entrainment Effects on Impingement Heat Transfer: Part II - Local Heat Transfer Measurements". *Trans. ASME J. Heat Transfer,* 107**,** 910 - 915.

[149] Hollworth B. R. and Durbin M. 1992. "Impingement Cooling of Electronics". *Trans. ASME J. Heat Transfer,* 114**,** 607 - 613.

[150] Saad N. R., Mujumdar A. S., Abdel Messah W. and Douglas W. J. M. 1981. "Local Heat Transfer Characteristics for Staggered Arrays of Circular Impinging Jets with Cross-Flow of Spent Air". *Joint ASME/AIChE National Heat Transfer Conference,* paper No. 80-HT-23**,** 1 - 8.

[151] Lee J., Ren Z., Ligrani P., Fox M. D. and Moon H-K. 2014. "Cross-Flows from Jet Array Impingement Cooling: Effects of Hole Array Spacing, Jet-to-Target Plate Distance and Reynolds Number". *Proc. ASME Turbo Expo,* GT-26426**,** 1 - 13.

[152] Nakamata C., Okita Y., Yamane T., Fukuyama Y. and Yoshida T. 2011. "Effect of Roughened Elements on Target Surface and Cooling Hole Shape on Impingement Cooling Effectiveness". *Proc. GTSJ Int. Gas Turbine Congress* IGTC-0003**,** 1 - 7.

[153] Scherer V., Wittig S., Bittlinger G. and Pfeiffer A. 1993. "Thermographic Heat Transfer Measurements in Separated Flows". *Springer-Verlag J. Experiments in Fluids,* 14**,** 17 - 24.

[154] Hedlund C. R., Ligrani P. M., Moon H. -K. and Glezer B. 1999. "Heat Transfer and Flow Phenomena in a Swirl Chamber Simulating Turbine Blade Internal Cooling". *Trans. ASME J. Turbomachinery,* 121**,** 804 - 813.

[155] Oh S. H., Lee D. H., Kim K. M., Kim M. Y. and Cho H. H. 2008. "Enhanced Cooling Effectiveness in Full-Coverage Film Cooling System With Impingement Jets". *Proc. ASME Turbo Expo,* GT-50784**,** 1 - 10.

[156] Boyle R. J., Spuckler C. M., Lucci B. L. and Camperchioli W. P. 2001. "Infrared Low-Temperature Turbine Vane Rough Surface Heat Transfer Measurements". *Trans. ASME J. Turbomachinery,* 123**,** 168 - 177.

[157] Leger B., Miron P. and Emidio J. M. 2003. "Geometric and Aero-Thermal Influences on Multiholed Plate Temperature: Application on Combustor Wall". *Elsevier Int. J. Heat and Mass Transfer,* 46**,** 1215 - 1222.

[158] El-jummah A. M., Andrews G. E. and Staggs J. E. J. 2015. "Conjugate Heat Transfer CFD Predictions of Metal Walls with Arrays of Short Holes as Used in Impingement and Effusion Cooling". *CHT'15 6th Int. Symposium on Advances in Computational Heat Transfer,* Unpublished**,** 1 - 12.

[159] Narzary D. P., Liu K. C., Rallabandi A. P. and Han J-C. 2012. "Influence of Coolant Density on Turbine Blade Film-Cooling Using Pressure Sensitive Paint Technique". *Trans. ASME J. Turbomachinery,* 134**,** 1 - 10.

[160] Zhang L. J. and Jaiswal R. S. 2001. "Turbine Nozzle Endwall Film Cooling Study Using Pressure Sensitive Paint". *Trans. ASME J. Turbomachinery,* 123**,** 730 - 738.

[161] Suryanarayanan A., Ozturk B., Schobeiri M. T. and Han J. C. 2010. "Film-Cooling Effectiveness on a Rotating Turbine Platform Using Pressure Sensitive Paint Technique". *Trans. ASME J. Turbomachinery,* 132**,** 1 - 13.

[162] Luque S. and Povey T. 2011. "A Novel Technique for Assessing Turbine Cooling System Performance". *Trans. ASME J. Turbomachinery,* 133**,** 1 - 9.

[163] Harasgama S. P. and Burton C. D. 1992. "Film Cooling Research on the Endwall of a Turbine Nozzle Guide Vane in a Short Duration Annular Cascade: Part 1 - Experimental Technique and Results". *Trans. ASME J. Turbomachinery,* 114**,** 734 - 740.

[164] Huang G. C. 1963. "Investigations of Heat Transfer Coefficients for Air Flow Through Round Jets Impinging Normal to a Heat-Transfer Surface". *Trans. ASME J. Heat Transfer***,** 237 - 245.

[165] Tabakoff W. and Clevenger W 1972. "Gas Turbine Blade Heat Transfer Augmentation by Impingement of Air Jets having Various Configurations". *Trans. ASME J. Eng. Power,* Paper No. 71-GT-9**,** 51 - 60.

[166] Stoy R. L. and Ben-Haim Y. 1973. "Turbulent Jets in a Confined Cross-flow". *Trans. ASME J. Fluids Eng.,* Paper No. 73-FE-15**,** 551 - 556.

[167] Hrycak P. 1981. "Heat Transfer from Row of Impinging Jets to Concave Cylindrical Surfaces". *Pergamon Int. J. Heat Mass Transfer,* 24**,** 407 - 418.

[168] Metzger D. E., Yamashita T. and Jenkins C. W. 1969. " Impingement Cooling of Concave Surfaces With Lines of Circular Air Jets". *Trans. ASME J. Eng. Power,* Paper No. 68-WA/GT-1**,** 149 - 155.

[169] Kayansayan N. and Küçüka S. 2001. "Impingement Cooling of Semi-Cylindrical Concave Channel by Confined Slot-Air-Jet". *Elsevier Experimental Thermal and Fluid Science,* 25**,** 383 - 396.

[170] Perry K. P. 1954. "Heat Transfer by Convection from a Hot Gas Jet to a Plane Surface". *Proc. IMechE* 168**,** 775 - 780.

[171] Goldstein R. J. and Behbahani A. I. 1982. "Impingement of Circular Jet With and Without Cross-Flow". 25 (9), 1377 - 1382.

[172] Hollworth B. R. and Dagan L. 1980. "Arrays of Impingement Jets with Spent Fluid Removal through Vent Holes on the Target Surface, Part 1: Average Heat Transfer". *Trans. ASME J. Eng. Power,* 102, 994 - 999.

[173] Florschuetz L. W. and Su C. C. 1987. "Effects of Cross-Flow Temperature on Heat Transfer Within an Array of Impinging Jets". *Trans. ASME J. Heat Transfer,* 109 74 - 82.

[174] Andrews G. E., Asere A. A., Gupta M. L. and Mpadi M. C. 1990. "Effusion Cooling: The Influence of the Number of Holes". *IMechE J. Power and Energy: Part A,* 204, 175 - 182.

[175] Andrews G. E. 2013. "Effusion Cooling With Backside Cross-Flow Cooling and the Backside Coolant Mass Flow Rate Greater than the Effusion Cooling Mass Flow". *Proc. ASME Turbo Expo,* GT-95355, 1 - 13.

[176] Andrews G. E., Khalifa I. M., Asere A. A. and Bazdidi-Tehrani F. 1995. "Full-Coverage Effusion Film Cooling With Inclined Holes". *Proc. ASME Turbo Expo,* 95-GT-274, 1 - 12.

[177] Ligrani P. M., Ciriello S. and Bishop D. T. 1992. "Heat Transfer, Adiabatic Effectiveness and Injectant Distributions Downstream of a Single Row and Two Staggered Rows of Compound Angle Film Cooling Holes". *Trans. ASME J. Turbomachinery,* 114, 687 - 700.

[178] Ligrani P. M. and Ramsey A. E. 1997. "Film Cooling From Spanwise-Oriented Holes in Two Staggered Rows". *Trans. ASME J. Turbomachinery,* 119, 562 - 567.

[179] Schmidt D. L., Sen B. and Bogard D. G. 1996. "Film Cooling With Compound Angle Holes: Adiabatic Effectiveness". *Trans. ASME J. Turbomachinery,* 118, 807 - 813.

[180] Sinha A. K., Bogard D. G. and Crawford M. E. 1991. "Film Cooling Effectiveness Downstream of a Single Row of Holes With Variable Density Ratio". *Trans. ASME J. Turbomachinery,* 113, 442 - 449.

[181] Krewinkel R. 2013. "A Review of Gas Turbine Effusion Cooling Studies". *Elsevier Int. J. Heat and Mass Transfer,* 66, 706 - 722.

[182] Ligrani P. M. and Lee J. S. 1996. "Film Cooling from a Single Row of Compound Angle Holes at High Blowing Ratios". *OPA Int. J. Rotating Machinery,* 2**,** 259 - 267.

[183] Scrittore J. J., Thole K. A. and Burd S. W. 2007. "Investigation of Velocity Profiles for Effusion Cooling of a Combustor Liner". *Trans. ASME J. Turbomachinery,* 129**,** 518 - 526.

[184] Oguntade H. I., Andrews G. E., Burns A. D., Ingham D. B. and Pourkashanian M. M. 2010. "CFD Predictions of Single Row Film Cooling With Inclined Holes: Influence of Hole Outlet Geometry". *Proc. ASME Turbo Expo,* GT-22308**,** 1 - 15.

[185] Oguntade H. I., Andrews G. E., Burns A. D., Ingham D. B. and Pourkashanian M. M. 2013. "Improved Trench Film Cooling WIth Shaped Trench Outlets". *Trans. ASME J. Turbomachinery,* 135**,** 1 - 10.

[186] Oguntade H. I., Andrews G. E., Burns A. D., Ingham D. B. and Pourkashanian M. 2012. "Conjugate Heat Transfer Predictions of Effusion Cooling: The Influence of the Injection Hole Size on Cooling Performance". *Proc. ASME Turbo Expo,* GT-68516**,** 1 - 12.

[187] Bayley F. J. and Turner A. B. 1970. "The Transpiration-Cooled Gas Turbine". *Trans. ASME J. Eng. for Power,* Paper No. 70-GT-56**,** 351 - 358.

[188] Hong S. K., Lee D. H., Cho H. H. and Rhee D. H. 2010. "Local Heat/Mass Transfer Measurements on Effusion Plates in Impingement/Effusion Cooling With Rotation". *Elsevier Int. J. Heat and Mass Transfer,* 53**,** 1373 - 1379.

[189] Andrews G. E. and Khalifa I. M. 2007. "Planar Duct Heat Transfer with Turbulence Enhancing Obstacles for Combustor Liner External Cooling". *Proc. ASME Turbo Expo,* GT-27418**,** 1 - 10.

[190] Rolls-Royce RR. 2007. "Gas Turbine Technology, Introduction to Jet Engine". *Rolls-Royce Plc (RR),* VCOM13797.

[191] Livingood J. N. B. and Hrycak P. 1973. "Impingement Heat Transfer from Turbulent Air Jets to Flat Plates - A Literature Survey". *NASA Technical Memorandum,* TM X-2778**,** 1 - 42.

[192] Gardon R. and Akfirat J. C. 1965. "The Role of Turbulence in Determining the Heat-Transfer Characteristics of Impinging Jets". *Pergamon Int. J. Heat Mass Transfer,* 8**,** 1261 - 1272.

[193] Myers G. E., Schauer J. J. and Eustis R. H. 1963. "Heat Transfer to Plane Turbulent Wall Jets". *Trans. ASME J. Heat Transfer,* Paper No. 62-HT-33**,** 209 - 214.

[194] Andrews G. E., Abdul Husain R. A. A. and Mkpadi M. C. 2003. "Enhanced Impingement Heat Transfer: Comparison of Co-Flow and Cross-flow with Rib Turbulators". *Proc. GTSJ Int. Gas Turbine Congress,* IGTC TS-075 1 - 8.

[195] Huang L. and El-Genk M. 1994. "Heat Transfer of an Impinging Jet on a Flat Surface". *Elsevier Science Int. J. Heat Mass Transfer,* 37 (13)**,** 1915 - 1923.

[196] Huang L., Lee C. H. and Cho H. H. 2001. "Heat Transfer and flow structures in axisymmetric Impinging Jet Controlled by Vortex Pairing". *Elsevier Int. J. Heat and Fluid Flow,* 22**,** 293 - 300.

[197] Metzger, D. E., Yamashita, T. and Jenkins, C. W. 1969. "Impingement Cooling of Concave Surfaces with Lines of Circular Air Jets". *J. Eng. for Power. Transaction of the ASME,* 91 (3)**,** 149 - 158.

[198] Miller N., Siw S. C., Chyu M. K.. and Alvin M. A. 2013. "Effects of Jet Diameter and Surface Roughness on Internal Cooling With Single Array of Jets". *Proc. ASME Turbo Expo,* GT-95400**,** 1 - 9.

[199] Al-Hadhrami L. M., Shaahid S. M. and Al-Mubarak A. A. 2007. "Effect of Orifice Jet Configuration on Heat Transfer Characteristics in a Channel With In-Clined Target Surface Cooled by Single Array of Impinging Jets With Outflow Parallel to Entry Flow". *Proc. GTSJ Int. Gas Turbine Congress,* IGTC TS-118**,** 1 - 8.

[200] Behbahani A. I. and Goldstein R. J. 1983. "Local Heat Transfer to Staggered Arrays of Impinging Circular Air Jets". *Trans. ASME J. Eng. Power,* 105**,** 354 - 360.

[201] Nuntadusit C. and Wae-hayee M. 2011. "Heat Transfer Characteristics of Some Multiple Impinging Jets with Swirling Flow Effect". *Proc. GTSJ Int. Gas Turbine Congress,* IGTC-0257**,** 1 - 7.

[202] Andreini A., Da Soghe R., Faccini B., Maiuolo F., Tarchi L. and Coutandin D. 2013. "Experimental and Numerical Analysis of Multiple Impingement Jet Arrays for an Active Clearance Control System". *Trans. ASME J. Turbomachinery,* 135**,** 1 - 9.

[203] Yamane Y., Ichikawa Y., Yamamota M. and Honami S. 2011. "Effect of Injection Parameters on Jet Array Impingement Heat Transfer". *Proc. GTSJ Int. Gas Turbine Congress* IGTC-228**,** 1 - 8.

[204] Kanokjaruvijit K. and Martinez-Botas R. F. 2003. "Jet Impingement onto a Dimpled Surface With Different Cross-Flow Schemes". *Proc. GTSJ Int. Gas Turbine Congress,* IGTC TS-074**,** 1 - 8.

[205] kanokjaruvijit K. and Martinez-Botas R. F. 2005. "Jet Impingement on a Dimpled Surface With Different Cross-Flow Schemes". *Elsevier Int. J. Heat and Mass Transfer,* 48**,** 161 - 170.

[206] El-jummah A. M., Andrews G. E. and Staggs J. E. J. 2015. "CHT/CFD Predictions of Impingement Cooling With Four Sided Flow Exit". *Proc. ASME Turbo Expo,* GT-42256 1 - 11.

[207] Sparrow E. M., Goldstein R. J. and Rouf M. A. 1975. "Effect of Nozzle–Surface Separation Distance on Impingement Heat Transfer for a Jet in a Cross_Flow". *Trans. ASME J. Heat Transfer,* Paper No. 76-HT-F 528 - 533.

[208] Taslim M. E. and Rosso N. 2012. "Experimental/Numerical Study of Multiple Rows of Confined Jet Impingement Normal to a Surface at Close Distances". *Proc. ASME Turbo Expo* GT-68634**,** 1 - 13.

[209] Consonni S. 1995. "Cooling Flow Prediction for Fully Impingement Cooled Gas Turbine Blades". *Proc. ASME Int. Gas Turbine & Aeroengine Congress and Exposition,* 95-GT-22**,** 1 - 12.

[210] Andrews G. E., Abdul Husain R. A. A. and Mkpadi M. C. 2006. "Enhanced Impingement Heat Transfer: The Influence of Impingement X/D for Interrupted Rib Obstacles (Rectangular Pin Fins)". *Trans. ASME J. Turbomachinery,* 128**,** 321 - 331.

[211] Goldstein R. J. and Timmers J. F. 1982. "Visualization of Heat Transfer from Arrays of Impinging Jets". *Pergamon Int. J. Heat Mass Transfer,* 25 (12)**,** 1857 - 1868.

[212] Goldstein R. J., Behbahani A. I. and Heppelmann K. 1986. "Streamwise Distribution of the Recovery Factor and the Local Heat Transfer Coefficient to an Impinging Circular Airjet". *Pergamon Int. J. Heat Mass Transfer,* 29 (8)**,** 1227 - 1235.

[213] Daane R. A. and Han S. T. 1961. "An Analysis of Air-Impingement Drying". *Tappi,* 44 (1)**,** 73 - 80.

[214] Abdul Husain R. A. A. and Andrews G. E. 1991. "Enhanced Full Coverage Impingement Heat Transfer With Obstacle in the Gap". *Proc. ASME Int. Gas Turbine & Aeroengine Congress & Eposition,* 91-GT-346**,** 1 - 12.

[215] Taslim M. E. and Fong M. K. H. 2011. "Experimental and Numerical Crossover Jet Impingement in a Rib-Roughened Airfoil Trailing-Edge Cooling Channel". *Proc. ASME Turbo Expo,* GT-45995**,** 1 - 12.

[216] Taslim M. E., Pan Y. and Spring S. D. 2001. "An Experimental Study of Impingement on Roughened Airfoil Leading-Edge Walls With Film Holes". *Trans. ASME J. Turbomachinery,* 123**,** 766 - 773.

[217] Rundstrom D. and Moshfegh B. 2008. "Investigation of Heat Transfer and Pressure Drop of an Impinging Jet in a Cross-Flow for Cooling of Heated Cube". *Trans. ASME J. Heat Transfer,* 130**,** 1 - 13.

[218] Chang B. H. and Mills A. F. 1993. "Turbulent Flow in a Channel with Transverse Rib Heat Transfer Augmentation". *Pergamon Int. J. Heat Mass Transfer,* 36 (6)**,** 1459 - 1469.

[219] Schuler M., Dreher H. M., Neumann S. O., Weigand B. and Elfert M. 2012. "Numerical Predictions of the Effect of Rotation on Fluid Flow and Heat Transfer in an Engine-Similar Two-Pass Internal Cooling Channel With Smooth and Ribbed Walls". *Trans. ASME J. Turbomachinery,* 134**,** 1 - 10.

[220] Han J. C. 1984. "Heat Transfer and Friction in Channels With Two Opposite Rib-Roughened Walls". *Trans. ASME J. Heat Transfer,* 106**,** 774 - 781.

[221] Chung H., Park S. J., Park S., Choi S. M., Cho H. H. and Rhee D. H. 2014. "Augmentated Heat Transfer for a Angled Rib With Intersecting Rib in Rectangular Channels of Different Aspect Ratios". *Proc. ASME Turbo Expo,* GT-26924**,** 1 - 13.

[222] Sparrow E. M. and Tao W. Q. 1983. "Enhanced Heat Transfer in a Flat Rectangular Duct With Streamwise-Periodic Disturbances at One Principal Wall". *Trans. ASME J. Heat Transfer,* 105**,** 851 - 861.

[223] Kadle D. S and Sparrow E. M. 1986. "Numerical and Experimental Study of Turbulent Heat Transfer and Fluid Flow in Longitudinal Fin Arrays". *Trans. ASME J. Heat Transfer,* 108**,** 16 - 23.

[224] Wang Z., Ireland P. T., Kohler S. T. and Chew J. W. 1998. "Heat Transfer Measurements to a Gas Turbine Cooling Passage With Inclined Ribs". *Trans. ASME J. Turbomachinery,* 120**,** 63 - 69.

[225] Shen J. R., Wang Z., Ireland P. T., Jones T. V. and Byerley A. R. 1996. "Heat Transfer Enhancement Within a Turbine Blade Cooling Passage Using Ribs and Combinations of Ribs With Film Cooling Holes". *Trans. ASME J. Turbomachinery,* 118**,** 428 - 434.

[226] Andreini A., Caciolli G., Soghe R. D., Facchini B. and Mazzei L. 2014. "Numerical Investigation on the Heat Transfer Enhancement Due to Coolant Extraction on the Cold Side of Film Cooling Holes". *Proc. ASME Turbo Expo,* GT-25460**,** 1 - 9.

[227] McGilvray M., Gillespie D. and Ryley J. 2014. "Investigation of Wrapping Ribs onto Smooth Walls for Mid-Chord Internal Cooling Passages". *Proc. ASME Turbo Expo,* GT-26800**,** 1 - 11.

[228] Shizuya M. and Kawaike K. 1987. "Experimental Investigation of Blade Internal Cooling Methods Using Ribs and Fins". *Proc. GTSJ Int. Gas Turbine Congress,* IGTC-65**,** 159 - 166.

[229] Azad G. M. S., Huang Y. and Han J. 2002. "Jet Impingement Heat Transfer on Pinned Surfaces Using a Transient Liquid Crystal Technique". *Taylor & Franscis Int. J. Rotating Machinery,* 8 (3)**,** 161 - 173.

[230] Al Dabagh A. M. and Andrews G. E. 1992. "Pin-Fin Heat Transfer: Contribution of the Wall and the Pin to the Overall Heat Transfer". *Proc. ASME Int. Gas Turbine & Aeroengine Congress and Exposition,* 92-GT-242**,** 1 - 10.

[231] Baughn J. W., Ireland P. T., Jones T. V. and Saniei N. 1989. "A Comparison of the Transient and Heated-Coating Methods for the Measurement of Local Heat Transfer Coefficients on a Pin Fin". *Trans. ASME J. Heat Transfer,* 111**,** 877 - 881.

[232] Sparrow E. M., Ramsey J. W. and Altemani C. A. C. 1980. "Experiments on In-line Pin-Fin Arrays and Performance Comparisons With Staggered Arrays". *Trans. ASME J. Heat Transfer,* 102**,** 44 - 50.

[233] Metzger D. E., Berry R. A. and Bronson J. P. 1982. "Developing Heat Transfer in Rectangular Ducts with Staggered Arrays of Short Pin Fins". *Trans. ASME J. Heat Transfer,* 104**,** 700 - 706.

[234] Armstrong J. and Winstanley D. 1988. "A Review of Staggered Array Pin-Fin Heat Transfer for Turbine Cooling Applications". *Trans. ASME J. Turbomachinery,* 110**,** 94 - 103.

[235] Lee D. H., Lee Y. M., Kim Y. T., Won S. Y. and Chung Y. S. 2002. "Heat Transfer Enhancement by the Perforated Plate Installed Between an Impinging Jet and the Target Plate". *Elsevier Int. J. Heat and Mass Transfer,* 45**,** 213 - 217.

[236] Xie Y., Li P., Lan J. and Zhang D. 2013. "Flow and Heat Transfer Characteristics of Single Jet Impinging on Dimpled Surface ". *Trans. ASME J. Heat Transfer,* 135**,** 1 - 15.

[237] Azad G. S., Huang Y. and Han J. C. 2000. "Impingement Heat Transfer on Dimpled Surfaces Using a Transient Liquid Crystal Technique". *AIAA J. Thermophysics and Heat Transfer,* 14 (2)**,** 186 -193.

[238] Kanokjaruvijit K. and Martinez-Botas R. F. 2005. "Heat Transfer and Pressure Investigation of Dimple Impingement". *Proc. ASME Turbo Expo,* GT-68823**,** 1 - 12.

[239] kanokjaruvijit K. and Martinez-Botas R. F. 2005. "Parametric Effects on Heat Transfer of Impingement on Dimpled Surface". *Trans. ASME J. Turbomachinery,* 127**,** 287 - 296.

[240] Ligrani P. M., Oliveira M. M. and Blaskovich T. 2003. "Comparison of Heat Transfer Augmentation Techniques". *AIAA Journal,* 41 (3)**,** 337 - 362.

[241] Ligrani P. M. 2013. "Review Article: Heat Transfer Augmentation Technologies for Internal Cooling of Turbine Components of Gas Turbine Engines". *Hindawi Int. J. Rotating Machinery,* 2013, ID. 275653**,** 1 - 32.

[242] Rhee D. H., Choi J. H. and Cho H. H. 2003. "Flow and Heat (Mass) Transfer Characteristics in an Impingement/Effusion Cooling System With Crossflow". *Trans. ASME J. Turbomachinery,* 125**,** 74 - 82.

[243] Goodro M., Park J., Ligrani P., Fox M. and Moon H. 2008. "Effects of Hole Spacing on Spatially-Resolved Jet Array Impingement Heat Transfer". *Elsevier Int. J. Heat and Mass Transfer,* 51**,** 6243 - 6253.

[244] Miller M. W., Claretti R., Ricklick M. and Kapat J. S. 2011. "Heat Transfer to Impingement Jets in a Narrow Channel". *Proc. GTSJ Int. Gas Turbine Congress,* IGTC TS-00151**,** 1 - 6.

[245] Spring S., Lauffer D., Weigand B. and Hase M. 2010. "Experimental and Numerical Investigation of Impingement Cooling in a Combusor Liner Heat Shield". *ASME J. Turbomachinery,* 132**,** 1 - 10.

[246] Zimmer V. J., Rutledge J. L. and Knieriem C. 2014. "The Influence of Coolant Unsteadiness on Impingement Heat Transfer". *Proc. ASME Turbo Expo,* GT-25897**,** 1 - 8.

[247] Yamane Y., Motosuke M., Yamamoto M. and Honami S. 2013. "Effect of Jet Shape of Square Array of Multi-Impinging Jets on Heat Transfer". *Proc. ASME Turbo Expo,* GT-94452**,** 1 - 10.

[248] Parsons J. A., Han J. C. and Lee C. P. 1998. "Rotation Effect on Jet Impingement Heat Transfer in Smooth Rectangular Channels With Four Heated Walls and Radially Outward Cross-Flow". *Trans. ASME J. Turbomachinery,* 120**,** 79 - 85.

[249] Bergeles G., Gosman A. D. and Launder B. E. 1981. "The Prediction of Three-Dimensional Discrete-Hole Cooling Processes - Part 2: Turbulent Flow". *Trans. ASME J. Heat Transfer,* 103**,** 141 - 145.

[250] Heyerichs K. and Pollard A. 1996. "Heat Transfer in Seperated and Impinging Turbulent Flows". *Elsevier Int. J. Heat Mass Transfer,* 39 (12)**,** 2385 - 2400.

[251] Debruge L. L. and Han L. S. 1972. "Heat transfer in a Channel with a Porous Wall for Turbine Cooling Application". *Trans. ASME J. Heat Transfer,* 72-HT-39**,** 385 - 390.

[252] Launder B. E. and Spalding D. B. 1974. "The Numerical Computation of Turbulent Flows". *North-Holland Computer Methods in Applied Mechanics and Engineering,* 3**,** 269 - 289.

[253] Brosh A., Dagani D. and Zalmanovich S. 1982. "Conjugate Heat Transfer in a Laminar Boundary Layer With Heat Source at the Wall". *Trans. ASME J. Heat Transfer,* 104**,** 90 - 95.

[254] Bohn D. E., Becker V. J. and Kusterer K. A. 1997. "3-D Conjugate Flow and Heat Transfer Calculations of a Film-Cooled Turbine Guide Vane at Different Operation Conditions". *Proc. ASME Int. Gas Turbine & Aeroengine Congress & Exhibition,* 97-GT-23**,** 1 - 10.

[255] Dunn M. G. 2001. "Convective Heat Transfer and Aerodynamics in Axial Flow Turbines". *Trans. ASME J. Turbomachinery,* 123**,** 637 - 686.

[256] Badcock K. J., Richards B. E. and Woodgate M. A. 2000. "Elements of Computational Fluid Dynamics on Block Structured Grids using Implicit Solvers". *Elsevier J. Progress in Aerospace Sciences,* 36**,** 351 - 392.

[257] Nuutinen M., Kaario O. and Larmi M. 2009. "Advances in Variable Density Wall Functions for Turbulent Flow CFD-Simulations, Emphasis on Heat Transfer". *SAE International,* 2009-01-1975**,** 1 - 16.

[258] Ahmed F. B., Tucholke R., Weigand B. and Meier K. 2011. "Numerical Investigation of Heat Transfer and Pressure Drop Characteristics for Different Hole Geometries of a Turbine Casing Impingement Cooling System". *Proc. ASME Turbo Expo,* GT-45251**,** 1 - 13.

[259] Oguntade H. I., Andrews G. E., Burns, A. D., Ingham D. B. and Pourkashanian M. 2012. "Conjugate Heat Transfer Predictions of Effusion Cooling: The Influence of the Coolant Jet Flow Direction on the Cooling Effectiveness". *Proc. ASME Turbo Expo,* GT-68517**,** 1 - 11.

[260] Hong S. K., Rhee D. H. and Cho H. H. 2007. " Effects of Fin Shapes and Arrangements on Heat Transfer for Impingement/Effusion Cooling With Crossflow". *Trans. ASME J. Heat Transfer,* 129**,** 1697 - 1707.

[261] Rhee D. H., Nam Y. W. and Cho H. H. 2004. " Local Heat/Mass Transfer With Various Rib Arrangements in Impingement/Effusion Cooling Systems With Crossflow". *Trans. ASME J. Turbomachinery,* 126**,** 615 - 626.

[262] Shih T. I-P., Lin Y. -L., Chyu M. K. and Gogineni S. 1999. "Computations of Film Cooling from Holes With Struts". *Proc. Int. Gas Turbine & Aeroengine Congress & Exhibition,* 99-GT-282**,** 1 - 8.

[263] ASME V & V. 2009. "Standard for Verification and Validation in Computational Fluid Dynamics and Heat Transfer: An American National Standard". *The American Society of Mechanical Engineers, USA,* 20.

[264] Fluent, I. 2009. "ANSYS Fluent User's Gude". *Release 12.0, Fluent In., Lebanon, NH.*

[265] Sharif M. A. R. and Mothe K. K. 2009. "Evaluation of Turbulent Models in the Prediction of Heat Transfer Due to Slot-Jet Impingement on Plane Concave Surfaces". *Taylor & Franscis Numerical Heat Transfer, Part B,* 55**,** 273 - 294.

[266] Sharif M. A. R. and Mothe K. K. 2010. "Parametric Study of Turbulent Slot-Jet Impingement Heat transfer from Concave Cylindrical Surfaces". *Elsevier Int. J. Thermal Sciences,* 49**,** 428 - 442.

[267] Ariff M., Salim S.M. and Cheah S.C. 2009. "Wall y^+ Approach for Dealing With Turbulent Flow Over a Surface Mounted Cube: Part 1 - Low Reynolds Number". *Proc. Seventh Int. Conference on CFD in the Minerals and Process Industries, CSIRO***,** 1 - 6.

[268] Ariff M., Salim S.M. and Cheah S.C. 2009. "Wall y^+ Approach for Dealing With Turbulent Flow Over a Surface Mounted Cube: Part 2 - High Reynolds Number". *Proc. Seventh Int. Conference on CFD in the Minerals and Process Industries, CSIRO***,** 1 - 6.

[269] Behnia M., Parneix S., Shabany Y. and Durbin P. A. 1999. "Numerical Study of Turbulent Heat Transfer in Confined and Unconfined Impinging Jets". *Elsevier Int. J. Heat and Fluid Flow,* 20**,** 1 - 9.

[270] Kuznetsov A. V. 2004. "Numerical Modelling of Turbulent Flow in a Composite Porous/Fluid Duct Utilizing a Two-Layer k - ε Model to Account for Interface Roughness". *Elsevier Int. J. Thermal Science,* 43**,** 1047 - 1056.

[271] Garg V. K. and Ameri A. A. 1997. "Comparison of Two-Equation Turbulence Models for Prediction of Heat Transfer on Film-Cooled Turbine Blades". *Proc. Int. Gas Turbine & Aeroengine Congress & Exhibition,* 97-GT-24**,** 1 - 12.

[272] Iyer G. R. and Yavuzkurt S. 1996. "Comparison of k - e Models in Predicting Heat transfer and Skin Friction Under High Free Stream Turbulence". *Proc. ASME Int. Gas Turbine & Aeroengine Congress & Exhibition,* 96-GT-537**,** 1 - 8.

[273] Andrews G. E., Wang J. and Abdul Husain R. A. A. 2011. "CFD Predictions of the Aerodynamics and Heat Transfer from Arrays of Impingement Jets with crossflow". *Proc. GTSJ Int. Gas Turbine Congress,* IGTC-0141**,** 1 - 18.

[274] Hossain J., Tran L. V., Kapat J. S., Fernandez E. and Kumar R. 2014. "An Experimental Study of Detailed Flow and Heat Transfer Analysis in a Single Row Narrow Impingement Channel". *Proc. ASME Turbo Expo,* GT-26498**,** 1 - 10.

[275] Wang X., Liu R., Bai X. and Yao J. 2011. "Numerical Study on Flow and Heat Transfer Characteristics of Jet Impingement". *Proc. ASME Turbo Expo.,* GT-45287**,** 1 - 10.

[276] Abishek S. and Narayanaswamy R. 2012. "Coupled Effects of Surface-Radiation and Buoyancy on Jet-Impingement Heat Transfer". *Trans. ASME J. Heat Transfer,* 134**,** 1 - 14.

[277] Hyams D. G., McGovern K. T. and Laylek J. H. 1996. "Effects of Geoometry on Slot-Jet Film Cooling Performance". *Proc. ASME Int. Gas Turbine & Aeroengine Congress & Exhibition,* 96-GT-187**,** 1 - 10.

[278] Ma C., Wang J., Zang S. and Ji Y. 2014. "Comparative Study of Impinging Jet Array Heat Transfer on a Flat Plate Cooled by Superheated Steam and Air". *Proc. ASME Turbo Expo,* GT-25493**,** 1 - 9.

[279] Liu Z., Ye L. and Feng Z. 2014. "Numerical Study of Impingement and Film Composite Cooling on Blade Leading Edge". *Proc. ASME Turbo Expo,* GT-26643**,** 1 - 10.

[280] Keenan M., Amano R. S. and Olu S. 2013. "Study of an Impingement Cooling Jet Array for Turbine Blade Cooling With Single and Double Exit Cases". *Proc. ASME Turbo Expo,* GT-94116**,** 1 - 12.

[281] Kini C. R., Shenoy B. S. and Sharma N. Y. 2011. "A Computational Conjugate Thermal Analysis of HP Stage Turbine Blade Cooling with Innovative Cooling Passage Geometries". *Proc. Worid Congress Eng.,* WCE III**,** 1 - 6.

[282] Yamane Y., Yamamoto M. and Honami S. 2012. "Effect of Cross-shaped Circular Jet Array on Impingement Heat Transfer". *Proc. ASME Turbo Expo,* GT-68199**,** 1 - 9.

[283] Cho H. H. and Rhee D. H. 2001. "Local Heat/Mass Transfer Measurement on the Effusion Plate in Impingement/Effusion Cooling Systems". *Trans. ASME J. Turbomachinery,* 123**,** 601 - 608.

[284] Zhang C., Wang Z., Liu J. and An B. 2013. "The Effects Biot Number on the Conjugate Film Cooling Effectiveness Under Different Blowing Ratios". *Proc. ASME Turbo Expo,* GT-94041**,** 1 - 9.

[285] Johnson J. J., King P. I., Ni R. H., Humber W. and Clark J. P. 2013. "Conjugate CFD Simulations of an Optimized Turbine Vane Film Cooling Array on Flat Plate Models". *Proc. ASME Turbo Expo,* GT-94383**,** 1 - 11.

[286] Lad B. and He L. 2013. "An Immersed Mesh Block (I.M.B) Approach for Conjugate Heat Transfer Predictions". *Proc. ASME Turbo Expo,* GT-94053**,** 1 - 12.

[287] Panda R. K. and Prasad B. V. S. S. S. 2012. "Conjugate Heat Transfer from Flat Plate with Combined Impingement and Film Cooling". *Proc. ASME Turbo Expo,* GT-68830**,** 1 - 10.

[288] Sidwell T. G., Lawson S. A., Straub D. L., Casleton K. H. and Beer S. 2013. "Conjugate Heat Transfer Modelling of a Film-Cooled Flat-Plate Test Specimen in a Gas Turbine Aerothermal Test Facility". *Proc. ASME Turbo Expo,* GT-94687**,** 1 - 16.

[289] Lawson S. A., Straub D. L., Beer S., Casleton K. H. and Sidwell T. G. 2013. "Direct Measurement of Overall Effectiveness and Heat Flux on a Film Cooled Test Article at High Temperatures and Pressures". *Proc. ASME Turbo Expo,* GT-94685**,** 1 - 12.

[290] Hao Z., Ren X., Song Y. and Gu C. 2013. "An Investigation of Conjugate Heat Transfer Simulations Based on Discontinuous Galerkin Methods on Unstructured Grids". *Proc. ASME Turbo Expo,* GT-94498**,** 1 - 12.

[291] Ni R., Clark J. P., Humber W., Anthony R. J., Fan G. and Johnson J. J. 2013. "Comparison of Predictions from Conjugate Heat Transfer Analysis of a Film-Cooled Turbine Vane to Experimental Data". GT-94716**,** 1 - 13.

[292] Tennehill, J. C., Anderson, D. A. and Pletcher, R. H. 1997. "*Computational Fluid Mechanics and Heat Transfer, Second Edition,"* USA, Taylor & Franscis.

[293] Versteeg, H. K. and Malalasekera, W. 2007. "*An Introduction to Computational Fluid Dynamics: The Finite Volume Method,"* Harlow, England, Pearson, Prentice Hall.

[294] Tennekes, H. and Lumley, J. L. 1992. "*A First Course in Turbulence,"* Cambridge, England, The MIT Press.

[295] Pope, S. B. 2000. "*Turbulent Flows,"* UK, Cambridge University Press.

[296] Jackson J. D. 2011. "Mechanisms for impairment of heat transfer in strongly heated turbulent flow of air through a tube". *UK National Heat Transfer Conference,* 0092 (2)**,** 1 - 15.

[297] Hussain A. K. M. F. and Reynolds W. C. 1975. "Measurements in Fully Developed Turbulent Channel Flow". *Trans. ASME J. Fluids Eng.*, Paper No. 75-FE-5**,** 568 - 578.

[298] Bernard P. S. and Wallace J. M. 2002. "*Turbulent Flows: Analysis, Measurement and Prediction,"* New Jersey, USA, John Wiley & Sons, Inc.

[299] Chen C. -J. and Jaw S. -Y. 1998. "Fundamentals of Turbulence Modelling". *Taylor and Francis*.

[300] Chen H. C. and Patel V. C. 1988. "Near-Wall Turbulence Models for Complex Flows Including Seperation". *AIAA Journal,* 26 (6)**,** 641 - 648.

[301] Andrews, G. E. and I., H. C. 1984. Impingement Cooling of Gas Turbine Components. *High Temperature Technology*. Butterworth & Co (Publisher) Ltd.

[302] Obot, N. T. and A., T. T. 1987. Impingement Heat Transfer within Arrays of Circular Jets: Part 1-Efects of Minimum, Intermediate and Complete Crossflow for Small and Large Spacings. *Trans. ASME J. Heat Transfer*

[303] Facchini, B. and M., S. 2006. Impingement Cooling for Modern Combustors: Experimental Analysis of Heat Transfer and Effectiveness. *Springer-Verlag, Experiments in Fluids.*

[304] Facchini, B. and Surace, M. 2006. "Impingement Cooling for Modern Combustors: Experimental Analysis of Heat Transfer and Effectiveness". *Experiments in Fluids. Springer,* Vol.40**,** pp.601-611.

[305] Kercher, D. M. and Tabakoff, W. 1970. "Heat Transfer by a Square Array of Round Air Jets Impinging Perpendicular to a Flat Surface including Effects of Spent Air". *ASME J. Eng. Power***,** 73-82.

[306] Chance, J. L. 1974. "Experimental Investigation of Air Impingement Heat Transfer under an Array of Round Jets". *Tappi,* 57, No.6**,** 108-112.

[307] Florschuetz, L. W., Truman, C. R. and Metzger, D. E. 1981. "Streamwise Flow and Heat Transfer Distributions for Jet Array Impingement with Crossflow". *Trans. ASME, J. Heat Transfer,* 103**,** 337-342.

[308] El-jummah, A. M., Andrews, G. E. and Staggs, J. E. J. "Conjugate Heat Transfer CFD Predictions of Impingement Jet Array Flat Wall Cooling Aerodynamics with Single Sided Flow Exit". Proceedings of ASME Turbo Expo 2013, 2013 Texas, USA. ASME, 1-12.

[309] El-jummah, A. M., Andrews, G. E. and Staggs, J. E. J. "Conjugate Heat Transfer CFD Predictions of the Influence of the Impingement Gap on the Effect of Crossflow". Proceedings of the ASME Heat Transfer, 2013 Minneapolis MN. ASME, 1-12.

[310] Andrews, G. E. and Hussain, C. I. 1987. "Full Coverage Impingement Heat Transfer: The Influence of Crossflow". *AIAA-87-2010***,** 1-9.

[311] Andrews, G. E. and Hussain, C. I. "Full Coverage Impingement Heat Transfer: Influence of Channel Height". Proc. of the 8th International Heat Transfer Conference, 1986. Hemisphere Pub. Corp., 1205-1211.

[312] El-jummah A. M., Abdul Hussain R. A. A., Andrews G. E. and Staggs J. E. J. 2014. "Conjugate Heat Transfer Computational Fluid Dynamics Predictions of Impingement Heat Transfer: The Influence of Hole Pitch to Diameter Ratio X/D at Constant Impingement Gap Z". *Trans. ASME J. Turbomachinery,* TURBO-14-1118**,** 1 - 16.

[313] Feng X., Tian S., Bai J., Zhang H., Wang K. and Wang H. 2014. "Numerical Investigation of an Integrated Impingement and Pin_Fin Cooling Configuration in a Wedge Duct". *Proc. ASME Turbo Expo,* GT-26185**,** 1 - 10.

[314] Miller M., Natsui G., Ricklick M. and Kapat J. 2014. "Heat Transfer in aCoupled Impinge-Effusion Cooling System". *Proc. ASME Turbo Expo,* GT-26416**,** 1 - 10.